UNIVERSIDADE ESTADUAL DE CAMPINAS
Faculdade de Engenharia Química

ALINE GALLO DE MITRI

DESENVOLVIMENTO DE NOVA ABORDAGEM DA VELOCIMETRIA POR IMAGEM DE PARTÍCULA PARA A ESTIMATIVA DA ENERGIA CINÉTICA TURBULENTA EM TANQUES AGITADOS

DEVELOPMENT OF A NOVEL PARTICLE IMAGE VELOCIMETRY APPROACH FOR TURBULENT KINETIC ENERGY ESTIMATION IN STIRRED TANKS

CAMPINAS
2024

ALINE GALLO DE MITRI

DESENVOLVIMENTO DE NOVA ABORDAGEM DA VELOCIMETRIA POR IMAGEM DE PARTÍCULA PARA A ESTIMATIVA DA ENERGIA CINÉTICA TURBULENTA EM TANQUES AGITADOS

DEVELOPMENT OF A NOVEL PARTICLE IMAGE VELOCIMETRY APPROACH FOR TURBULENT KINETIC ENERGY ESTIMATION IN STIRRED TANKS

Tese apresentada à Faculdade de Engenharia Química da Universidade Estadual de Campinas como parte dos requisitos exigidos para a obtenção do título de Doutora em Engenharia Química.

Orientador: Prof. Dr. Guilherme José de Castilho
Coorientador: Prof. Dr. Rodrigo de Lima Amaral

ESTE TRABALHO CORRESPONDE À VERSÃO FINAL DA TESE DEFENDIDA PELA ALUNA ALINE GALLO DE MITRI, ORIENTADA PELO PROF. DR. GUILHERME JOSÉ DE CASTILHO E COORIENTADA PELO PROF. DR. RODRIGO DE LIMA AMARAL

CAMPINAS
2024

Ficha catalográfica
Universidade Estadual de Campinas
Biblioteca da Área de Engenharia e Arquitetura
Rose Meire da Silva - CRB 8/5974

D594d

De Mitri, Aline Gallo, 1990-
Development of a novel particle image velocimetry approach for turbulent kinetic energy estimation in stirred tanks / Aline Gallo De Mitri. – Campinas, SP : [s.n.], 2024.

Orientador: Guilherme José de Castilho.
Coorientador: Rodrigo de Lima Amaral.
Tese (doutorado) – Universidade Estadual de Campinas, Faculdade de Engenharia Química.

1. Escoamento turbulento. 2. Dinâmica dos fluidos - medição. 3. Tanques. I. Castilho, Guilherme José de, 1983-. II. Amaral, Rodrigo de Lima, 1988-. III. Universidade Estadual de Campinas. Faculdade de Engenharia Química. IV. Título.

Informações Complementares

Título em outro idioma: Desenvolvimento de nova abordagem da velocimetria por imagem de partícula para a estimativa da energia cinética turbulenta em tanques agitados
Palavras-chave em inglês:
Turbulent flow
Fluid dynamics - Measurement
Tanks
Área de concentração: Engenharia Química
Titulação: Doutora em Engenharia Química
Banca examinadora:
Guilherme José de Castilho [Orientador]
Henry França Meier
João Lameu da Silva Júnior
Marco Aurélio Cremasco
Nicolas Spogis
Data de defesa: 05-02-2024
Programa de Pós-Graduação: Engenharia Química

Identificação e informações acadêmicas do(a) aluno(a)
- ORCID do autor: https://orcid.org/0000-0002-5412-3706
- Currículo Lattes do autor: http://lattes.cnpq.br/4894245383473105

Folha de Aprovação da Defesa de Tese de Doutorado defendida por Aline Gallo De Mitri e aprovada em 05 de fevereiro de 2024 pela Comissão Examinadora constituída pelos doutores:

Prof. Dr. Guilherme José de Castilho
Presidente e Orientador
FEQ/UNICAMP

Prof. Dr. Henry França Meier
Fundação Universidade Regional de Blumenau (FURB)
Blumenau/SC

Prof. Dr. João Lameu da Silva Júnior
Universidade Federal do ABC (UFABC)
São Bernardo do Campo/SP

Prof. Dr. Marco Aurélio Cremasco
FEQ/UNICAMP

Prof. Dr. Nicolas Spogis
FEQ/UNICAMP

A Ata da defesa com as respectivas assinaturas dos membros encontra-se no SIGA/Sistema de Fluxo de Dissertação/Tese e na Secretaria do Programa da Unidade.

Dedico este trabalho à memória
do vô Ademar, que me ensinou sobre o zelo
da nonna Oriedes, que me ensinou a amar os livros
do nonno Amleto, que me ensinou a ter coragem e atravessar oceanos
e da vó Lázara, que me ensinou sobre o amor.
Ensinamentos indispensáveis para a realização desta tese.

AGRADECIMENTOS

Agradeço primeiramente à Deus, por ter guiado meu caminho até aqui e por todas as oportunidades que surgiram no percurso.

Agradeço aos meus pais, Adriana e Giuseppe, e à minha irmã, Alicia, pelo amor e apoio incondicional em todos os momentos da minha vida.

Agradeço ao Professor Guilherme pela confiança em meu trabalho, pela orientação e ensinamentos compartilhados e pela amizade.

Agradeço ao Professor Rodrigo por ter compartilhado comigo seus grandes conhecimentos sobre PIV e por ter me guiado nos desafios técnicos deste trabalho. Também agradeço ao Dr. Helder e ao grupo PIV_br pela ajuda no processamento das imagens, por me ensinar sobre o procedimento experimental e a escrever algoritmos em MATLAB.

Agradeço aos membros das bancas de qualificação I, qualificação II e de defesa da tese pelas valiosas contribuições ao trabalho.

Agradeço aos familiares e amigos de longa data pelo carinho e companheirismo que me motivam e suportam no dia a dia. Agradeço aos companheiros de laboratório e aos amigos que fiz nesta jornada: vocês tornaram meus dias muito melhores!

Agradeço ao Felipe, pela paciência, amor e suporte nos momentos difíceis e, principalmente, por sempre acreditar em mim, mesmo quando eu mesma não acredito.

O presente trabalho foi realizado com apoio do Conselho Nacional de Desenvolvimento Científico e Tecnológico (CNPq, processo n°142604/2019-4), da Coordenação de Aperfeiçoamento de Pessoal de Nível Superior (CAPES, Código de Financiamento 001) e da empresa Petróleo Brasileiro S/A (PETROBRAS, processo 2017/00376-1).

RESUMO

Tanques de agitação e mistura estão presentes nos mais diversos processos industriais e frequentemente operam em regime turbulento. A dinâmica do escoamento e a distribuição de energia cinética turbulenta nestes equipamentos ainda não é totalmente conhecida, mas muitos esforços já foram feitos a partir da aplicação da Velocimetria por Imagem de Partícula (PIV). Esta técnica, porém, ainda apresenta aspectos a serem consolidados para que as medidas apresentem um nível de acurácia e precisão adequado à operação. Este trabalho visa desenvolver e aplicar uma nova abordagem PIV para a estimativa da distribuição de energia cinética turbulenta em tanques agitados. Nesta nova abordagem, denominada *Tilted PIV*, as medições foram feitas por uma câmera posicionada a 45º da folha de luz para registrar o deslocamento combinado das partículas traçadoras nas direções dentro e fora do plano. O desempenho da nova abordagem foi avaliado utilizando diferentes modelos de impelidores (turbinas Rushton e de pás inclinadas) e foi comparado com outras abordagens PIV (*Stereo-PIV* e *Classic PIV*). Os resultados mostraram que *Tilted PIV* é uma abordagem adequada para estimar a energia cinética turbulenta em tanques agitados, pois apresentou campos muito similares aos obtidos pelas técnicas *Stereo-PIV* e *Classic PIV* levando em consideração da aproximação pseudoisotrópica, com diferenças menores que 15%. A nova abordagem *Tilted PIV* facilita a aplicação da tecnologia PIV na estimativa da energia cinética turbulenta em operações nas quais o acesso óptico é restrito ou um maior controle de ruído é necessário.

Palavras-chave: parâmetros turbulentos, tanque agitado, velocimetria por imagem de partícula

ABSTRACT

Agitation and mixing tanks are present in a wide variety of industrial processes and often operate in a turbulent regime. The fluid dynamics and the distribution of turbulent kinetic energy in these operations are not yet fully known, but many efforts have already been made by employing Particle Image Velocimetry (PIV). This technique, however, still presents aspects to be consolidated to ensure that the measurements achieve the necessary accuracy and precision for these operations. This work aims to develop and apply a novel PIV approach for estimating turbulent kinetic energy distribution in stirred tanks. In this novel approach, named Tilted PIV, measurements were taken by a camera positioned at 45º from the light sheet to record the combined displacement of tracer particles in the in-plane and out-of-plane directions. The performance of the novel approach was evaluated using different impeller models (Rushton and pitched blade turbines) and was compared with other PIV approaches (Stereo-PIV and Classic PIV). The results showed that Tilted PIV is a suitable approach for estimating turbulent kinetic energy in stirred tanks because it yielded results very similar to those obtained by the Stereo-PIV and Classic PIV taking into account the pseudo-isotropic approximation, with differences less than 15%. Tilted PIV approach facilitates the application of PIV technology to estimate turbulent kinetic energy in operations where optical access is restricted, or higher noise control is required.

Keywords: turbulent parameters, stirred tank, particle image velocimetry

NOMENCLATURE

A	Constant of proportionality	[-]
A_I, A_{II}, A_{III}	Anisotropic invariants	[-]
a_{ij}	Anisotropic Reynolds stress	[-]
a_i, b_i	Coefficients of the mapping function	[-]
B	Baffle width	[m]
C	Number of velocity components	[-]
C_2	The second tallest correlation peak	[-]
C_{max}	The highest correlation peak	[-]
C_T	Clearance	[mm]
D	Number of spatial dimensions	[-]
D_T	impeller diameter	[m]
d_p	Tracer particles diameter	[μm]
dx	Displacement in the in-plane direction	[m]
dz	Displacement in the out-of-plane direction	[m]
F_Δ	Loss-of-correlation due to displacement gradients	[-]
F_I	Loss-of-correlation due to in-plane motion	[-]
F_O	Loss-of-correlation due to out-of-plane motion	[-]
F_σ	Loss-of-correlation due to image noise	[-]
f^{a_i}	Function of a variable i	[-]
H	height of the liquid	[m]
h_M	Recording time	[-]
I_l	Integral length scale	[m]
I_t	Integral time scale	[s]
K_η	Kolmogorov length scale	[m]
K_ϑ	Kolmogorov velocity scale	[m/s]
K_τ	Kolmogorov time scale	[s]
k	Turbulent kinetic energy	[m²/s²]
k_{2C}	Turbulent kinetic energy with 2 components	[m²/s²]
k_{3C}	Turbulent kinetic energy with 3 components	[m²/s²]

k_{iso}	Turbulent kinetic energy considering the pseudo-isotropic approximation	[m²/s²]
$k_{iso\,tPIV}$	Turbulent kinetic energy considering the pseudo-isotropic approximation for Tilted PIV data	[m²/s²]
L_{exp}	Experimental length scale	[m]
l	Eddy size	[m]
l_{DI}	Length scale at the beginning of the dissipation range	[m]
l_{EI}	Length scale at the beginning of the universal equilibrium range	[m]
N	Number of samples	[-]
N_E	Effective number of particle images	[-]
N_i	Number of particles within the interrogation window	[-]
N_T	Impeller rotational speed	[1/s]
n	Number of variables	[-]
n_B	Number of baffles	[-]
n_P	Number of blades	[-]
P	Power input	[W]
P_I, P_{II}, P_{III}, P_{IV}, P_V	Gradient ratios of the velocity fluctuations	[-]
R	Internal radius of the vessel	[m]
Re	Reynolds number	[-]
Re_l	Reynolds number of an eddy	[-]
Re_{K_η}	Reynolds number of the Kolmogorov scale	[-]
R_{uu}	Normal Reynolds stress	[m²/s²]
s_C	Radial normalized coordinate	[px]
T	Internal diameter of the vessel	[m]
t_C	Axial normalized coordinate	[px]
t_D	Blade thickness	[m]
t_{exp}	Experimental time scale	[s]
t_i	Interframe time	[s]
U	Transport velocity of the integral scale	[m/s]
UQ_k	Uncertainty of the turbulent kinetic energy	[m²/s²]
UQ_{uu}	Uncertainty of the velocity component	[m/s]
U_{tip}	Impeller tip velocity	[m/s]

u	Radial velocity component	[m/s]
u'	Radial velocity fluctuations	[m/s]
u'^2	Root-mean-square of the radial velocity fluctuations	[m²/s³]
$u_i'^2$	Instantaneous root-mean-square of the radial velocity fluctuations	[m²/s³]
u_i	Instantaneous radial velocity component	[m/s]
$u_c'^2$	Root-mean-square of the combined-radial velocity fluctuations	[m²/s³]
u_p	Projection of the reconstructed velocity component	[m/s]
V	Volume of the tank	[m³]
v	Axial velocity component	[m/s]
v'	Axial velocity fluctuations	[m/s]
v'^2	Root-mean-square of the axial velocity fluctuations	[m²/s²]
w	Out-of-plane velocity component	[m/s]
w'	Out-of-plane velocity fluctuations	[m/s]
w'^2	Root-mean-square of the out-of-plane velocity fluctuations	[m²/s²]
w_T	Impeller blade width	[m]
(x, y, z)	Radial, axial and out-of-plane image coordinates	[px]
(X', Y', Z')	Radial, axial and out-of-plane object coordinates	[px]

Greek letters

α_P	Angle of the blades	[º]
β	Camera 2 angle	[º]
γ_B	Angle between baffles	[º]
Δ	Size of the interrogation window	[mm]
Δ_x	Image size in x direction	[px]
Δ_y	Image size in y direction	[px]
δ_{ij}	unitary tensor	[-]
ε	Energy dissipation rate	[m²/s³]
$\bar{\varepsilon}$	Mean energy dissipation rate	[m²/s³]

ϑ_l	Characteristic velocity	[m/s]
λ_c	Cut off wave number	[1/m]
λ_l	Integral scale wave number	[1/m]
λ_N	Wave number	[1/m]
λ_η	Kolmogorov scale wave number	[1/m]
μ	Dynamic viscosity	[Pa.s]
ν	Kinematic viscosity	[m^2/s]
ρ	Density	[kg/m^3]
σ	Camera 1 angle	[º]
$\bar{\tau}$	Boussinesq-Reynolds tensor	[m^2/s^2]

Abbreviations

AR	Angle-resolved
CFD	Computational fluid dynamics
EDR	Energy Dissipation Rate
FEQ	School of Chemical Engineering
LACEM	Laboratory of Multiphase Flow Characterization
LDA	Laser Doppler Anemometry
LDV	Laser Doppler Velocimetry
NACA	National Advisory Committee for Aeronautics
OGW	Otsu–Gauss–Wiener method
PBT	Pitched blade turbine
PIV	Particle Image Velocimetry
PSD	Power spectrum density
ppp	Particle per pixel
rms	Root-mean-square
rpm	Rotation per minute
SCC	Standard cross-correlation
SNR	Signal-to-noise ratio
TKE	Turbulent Kinetic Energy
UNICAMP	Universidade Estadual de Campinas
VDP	Valid detection probability

CONTENTS

1. INTRODUCTION

The unit operation of agitation and mixing is one of the most used within industrial facilities, whether in a batch process for producing pharmaceutical ingredients on a small scale, or in the storage of oil in a gigantic tank, known in Brazil as *Maracanã*, in allusion to the Brazilian soccer stadium. At the same time, the understanding of the phenomena of heat, mass and momentum transfer within these devices is limited, and many process still rely on trial-and-error experiments. Knowing the fluid dynamics of these systems is crucial to obtain quality products and optimized operations.

The characterization of the turbulent flow within these devices is very relevant to examine different types and configurations of impellers (DELBRIDGE *et al.*, 2023; LI *et al.*, 2013; LIU *et al.*, 2008; MARTÍNEZ-DELGADILLO *et al.*, 2019; MENDOZA-ESCAMILLA *et al.*, 2023; STELMACH *et al.*, 2022) and investigate variations in tank arrangement, e.g. with and without baffles (CHUNG; SIMMONS; BARIGOU, 2009; FAN *et al.*, 2022). In addition, the evaluation of turbulent parameters allows to compute the turbulent kinetic energy dissipation rate caused by the impeller movement (BALDI; YIANNESKIS, 2003; BUGAY; ESCUDIÉ; LINÉ, 2002; ESCUDIÉ; LINÉ, 2003; KILANDER; RASMUSON, 2005; MICHELETTI *et al.*, 2004; SHENG; MENG; FOX, 2000) and analyze different flow structures that can form in this type of regime (DE LAMOTTE *et al.*, 2017; SCHÄFER *et al.*, 1998; SHARP; ADRIAN, 2001; WANG *et al.*, 2022). Another very common application of the study of turbulent flows is in the validation of numerical models (ALONZO-GARCIA *et al.*, 2019; FANG; LING; SANG, 2011; HOQUE *et al.*, 2014; JÄHRLING *et al.*, 2017; RANADE *et al.*, 2001).

One of the ways to experimentally investigate turbulent flow in stirred tanks is through techniques involving Particle Image Velocimetry (PIV), which allows obtaining flow fields from the analysis of images of tracer particles immersed in the fluid, following its movement. The approach presents as a positive aspect the measurement of instantaneous and simultaneous velocity vector fields, rather than providing point values, as is common with other techniques. However, it also has disadvantages associated with problems when performing optical measurements, such as optical distortion and noise interference (RAFFEL *et al.*, 2018).

In this context, the Multiphase Flow Characterization Laboratory (LACEM) of the School of Chemical Engineering (FEQ) at the Universidade Estadual de Campinas (UNICAMP) investigates, in one of its lines of research, the flow patterns and the

distribution of energy parameters in stirred tanks. Currently, LACEM research team is working on a case study consisting of a partnership with the *Petróleo Brasileiro S/A* company (cooperation term 5850.0106772.18.9) to optimize the homogenization of crude oil storage tanks and minimize the formation of sludge, which is difficult to remove, damages the integrity of the equipment and can contaminate the stored product. However, in order to carry out the investigation of the storage tank through experiments that reproduce the multiphase system under analysis, it is necessary to consolidate some aspects of the flow in stirred tanks, even in single-phase systems.

One of the most important parameters to assess the homogenization and agitation efficiency is the turbulent kinetic energy (TKE). This energy is related to the large-scale flow structures where the high turbulence levels are concentrated, which are responsible for pumping and mixing (POPE, 2000; SOUZA et al., 2011). Consequently, the knowledge of the distribution of TKE in the vessel is important to optimize the mixing time and to identify the best feed location and potential dead zones (KRESTA; WOOD, 1993). In this context, one of the challenges regarding PIV measurements is the impact of the out-of-plane component on the flow and on the turbulent kinetic energy distribution, since the technique generally evaluates a two-dimensional plane, while the flow in the device is three-dimensional. Besides, the out-of-plane movement can introduce a perspective error in the in-plane velocity components.

In the case of the TKE estimation, several researchers consider the pseudo-isotropic approximation, in which the out-of-plane component is valued as the arithmetic mean of the other two components measured. However, this assumption is unplausible (KRESTA, 1998) especially in regions close to the impeller, where energy gradients are higher, and the out-of-plane component can have significant effects. Thus, evaluating the effect of the out-of-plane component is relevant not only for a more realistic description of the flow patterns inside the equipment, but also to estimate the turbulent kinetic energy distribution more accurately, putting to the test the pseudo-isotropic approximation.

Much effort was made by different research groups to deal with the issue of the lack of the out-of-plane component and its consequences on the flow evaluation. There are arrangements such as Tomographic PIV, that employ a set of at least four cameras to register the particle images. It can measure precisely the three dimensions and the three velocity components but presents a very high computational and experimental costs. Other approaches that can be employed are Stereo-PIV, that uses only two cameras to register the same plane of view, or the combination of planes measured by Classic PIV.

However, these methods add complex and costly steps in computational processing, in addition to introduce error sources in the experimental arrangement. The simplest solution in terms of these costs is the application of Classic PIV technique along with the consideration of the pseudo-isotropic approximation, previously mentioned, which is unsuitable for complex flows. The different PIV approaches found in the literature for evaluating the fluid dynamics and the turbulence distribution in stirred tanks lead to questioning whether there is an optimal way to assess this system. The approach should combine precise measurements of the velocity components with a technique that has lower operational and data processing costs.

Our proposal is to change the way of seeing the out-of-plane displacement and to improve the TKE estimation of a three-dimensional flow using two-dimensional fields. Instead of just considering the out-of-plane displacement as a perspective error, we suggest expanding its capture through a more tilted camera to measure the combined effect of the in-plane and out-of-plane velocity component on TKE of a three-dimensional flow. In order to analyze our proposal, some variables were identified and evaluated: impeller geometry; the velocity components of the flow, especially the out-of-plane component; the position and arrangement of cameras during image acquisition and the consideration of the pseudo-isotropic approximation on TKE estimation. By this investigation, a novel PIV approach had been developed, named Tilted PIV, in which the measurements were made by one camera positioned at 45° from the light sheet.

Therefore, the main objective of this thesis is to develop and apply this novel PIV approach to enhance the accuracy of flow and turbulent kinetic energy measurements in stirred tanks. With this improvement, more complex flows, such as the one promoted in the oil storage tank, can be better reproduced and evaluated experimentally.

2. GENERAL OBJETIVE

This work aims to develop and apply a novel Particle Image Velocimetry approach, referred to as Tilted PIV, in which the measurements are made by a single camera positioned at 45º relative to the light sheet. Tilted PIV performance was investigated in two different flow patterns in a stirred tank: one predominantly radial, promoted by a Rushton turbine, and another predominantly axial, promoted by a 45º pitched blade turbine (PBT). Turbulent kinetic energy (TKE) fields estimated from Stereo-PIV and Classic PIV measurements were used as a reference to support the assessment of the alternative approach, as well as the evaluation of uncertainty quantities. In addition, we also investigated the effect of the pseudo-isotropic approximation on the TKE estimated from Tilted PIV measurements.

2.1. Specific Objectives

To achieve the general objective, the following specific objectives have been established:

- Investigate the impact of the out-of-plane component on the flow pattern and on the estimation of the turbulent parameters.
- Estimate TKE fields using Stereo-PIV, Classic PIV and Tilted PIV approaches.
- Assess the limitations and validity of the pseudo-isotropic approximation in TKE estimation.
- Evaluate the quality of the PIV measurements by the signal-to-noise ratio (SNR), the out-of-plane component reconstruction error and the uncertainty quantification.

3. LITERATURE REVIEW

3.1. Fluid Dynamics in Stirred Tanks

Turbulent flow in stirred tanks is extensively used across various industrial processes, including the suspension of solids, dispersion of gases, and the mixing and emulsification of liquids (KRESTA; BRODKEY, 2003). Examples of applications for this type of operation can be found in the fermentation of biomass for sugar production, in the synthesis of pharmaceuticals in the drug manufacturing industry, in various polymerization reactions, in the storage of fuels in the petrochemical industry, among others. The diversity of applications, the growing demand for high-quality products at reduced costs and the advancement of manufacturing systems make necessary continual enhancements in agitation efficiency (EDWARDS; BAKER, 1992). These improvements are directly related to understanding the fluid dynamics inside this equipment.

Agitation efficiency is defined differently based on the specific process under evaluation. In general, the operation must ensure good circulation inside the equipment. However, in the case of multiphase systems, it is also crucial to ensure that the mixture of components is adequate not only in the region close to the impeller, but also in more remote positions, such as at the bottom and sides of the equipment. Based on this, agitation efficiency can be evaluated by analyzing the distribution of velocity components in different directions of the flow, as well as the flow patterns developed by the impeller (GÓMEZ; BENNINGTON; TAGHIPOUR, 2010).

The type of impeller, its geometry and its positioning in the tank are the main factors to be considered in the evaluation of the velocity fields and the flow pattern. Additional factors influencing these parameters include the presence of baffles and the fluid's properties, like viscosity (BATES; FONDY; FENIC, 1966). There are two main flow patterns that can be developed by the impeller in the agitation system. Axial-flow impellers produce a flow pattern typically discharging at 90° from the blades and circulating through the entire tank in a single stage, returning to the impeller through the central region (Figure 3.1a). Radial-flow impellers create a two-stage flow pattern: one circulating above the impeller and another below it (Figure 3.1b) *(*GENCK *et al.*, 2008).

Figure 3.1: Axial (a) and radial (b) flow patterns.

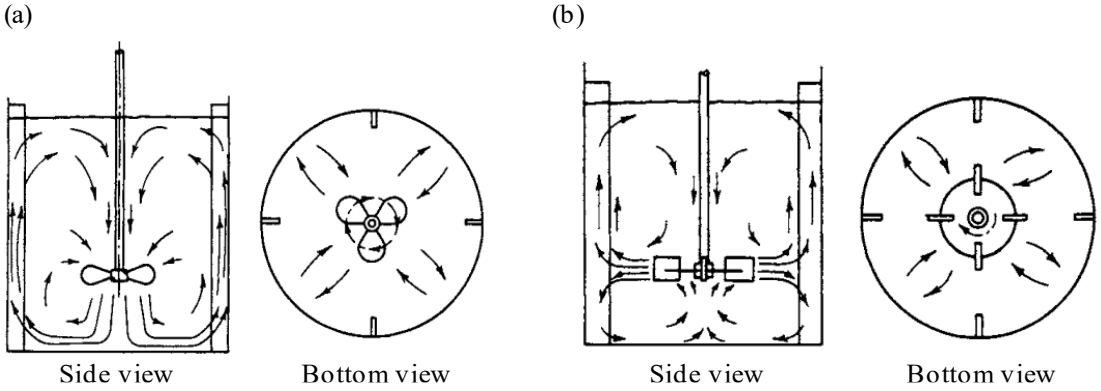

Source: Adapted from Genck *et al.* (2008).

In this context, a briefly discuss of the use of baffles in the tank is important. Baffles, flat vertical strips placed along the tank wall, serve to minimize the swirling in the bulk fluid, facilitate fluid circulation between the top and the bottom of the equipment and stabilize the impeller shaft (FAN *et al.*, 2022; GENCK *et al.*, 2008). Due to the significant advantages offered by baffles, there are relatively few studies focused on the investigation of unbaffled stirred tanks in turbulent flow. In general, the turbulence in unbaffled stirred tanks is strongly anisotropic and the studies concentrate on the evaluation and prediction of the central eddies (ALCAMO *et al.*, 2005; BERTRAND *et al.*, 2012).

In a recent study, Brůha, Prochákza and Uruba (2021) explored the impact of the baffles on the flow pattern by the assessment of quasi-periodical and periodical low-frequency phenomena in the flow promoted by a 45° PBT with 6 blades. They verified that the primary circulation loop is induced and stabilized by the ascent stream adjacent to the baffles. In addition, the authors studied the flow in front and behind this accessory and verified a significant tangential flow around it. Thus, the results indicated that the application of baffles is important for the agitation mechanism. In light of these findings, baffles were incorporated in our investigation of flow patterns in stirred tanks.

The most commonly used impellers in agitation and mixing processes are the disc flat blade turbine, also known as the Rushton turbine (Figure 3.2a) and the pitched blade turbine (PBT, Figure 3.2b). However, in recent decades, new impeller designs have emerged aiming to optimize fluid agitation and component mixing in specific applications, in addition to reduce energy consumption (EDWARDS; BAKER, 1992; GENCK *et al.*, 2008; JOAQUIM JUNIOR *et al.*, 2007; WYROBNIK *et al.*, 2022). In

general, disc flat blade turbines promote radial flow patterns and are used when the working fluid has lower viscosity and requires high levels of turbulence and shear stress. Conversely, pitched blade turbines, which develop axial flow patterns, are better suited for pumping more viscous fluids (JOAQUIM JUNIOR *et al.*, 2007). It is crucial to note that the selection of an impeller is inherently linked to the specific requirements of the mixing process (MACHADO *et al.*, 2012).

Figure 3.2: Illustration of the (a) Rushton turbine with 6 blades, (b) 45° pitched blade turbine with 4 blades and (c) cross-sectional view of the vessel with its characteristic dimensions.

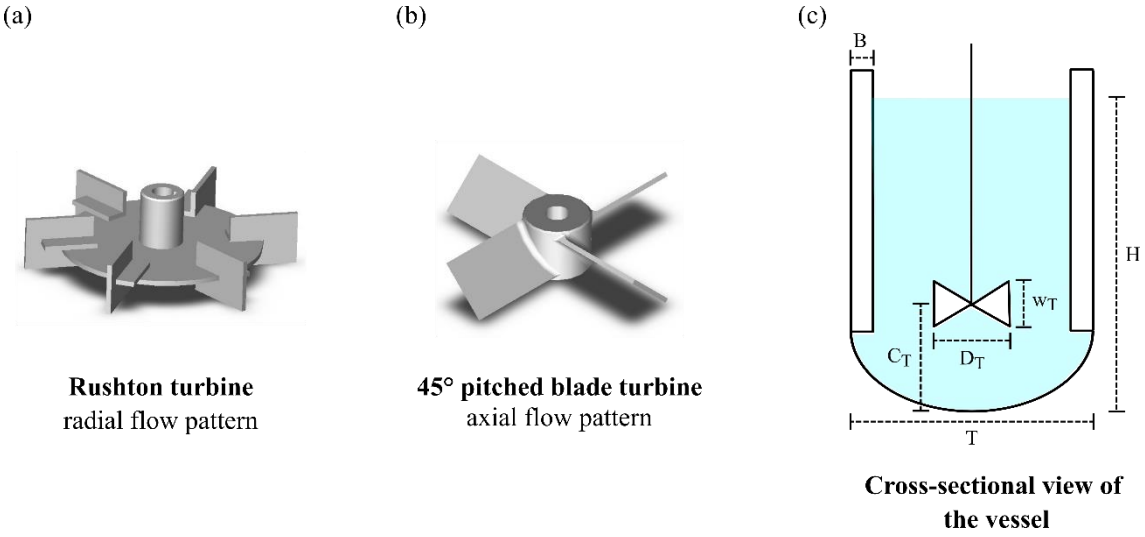

Source: Both illustrations of the impellers were made by Peter Czizar. Available in: https://www.postmixing.com/mixing%20forum/images/rt6.jpg (Rushton turbine); https://www.postmixing.com/mixing%20forum/images/pbtdown.jpg (PBT). Accessed on 16 May 2023. The illustration of the vessel was made by the author.

The agitation system is typically characterized by the following dimensions (Figure 3.2c): internal diameter of the vessel (T), impeller diameter (D_T), impeller blade width (w_T), clearance (C_T), height of the liquid (H) and width of baffles (B). The geometric relationships between these dimensions vary depending on the application and the fluid involved (JOAQUIM JUNIOR *et al.*, 2007). As mentioned before, they also have an impact on the flow pattern and on the velocity distribution. For example, with Rushton turbines, the reduction of the clearance can result in a transition from the two-stage flow pattern (as described in Figure 3.1) to a single stage flow pattern (LI; BAO; GAO, 2011; MONTANTE *et al.*, 1999).

The authors who evaluated the distribution of velocity components in flows promoted by the Rushton turbine observed that the axial component exhibits significantly lower values compared to the radial and out-of-plane components, while the latter two components demonstrate comparable magnitudes (ESCUDIÉ; LINÉ, 2003; MONTANTE *et al.*, 1999; RANADE *et al.*, 2001; WU; PATTERSON, 1989). Figure 3.3 presents examples of this type of profile obtained by Escudié and Liné (2003) in the study of a flow induced by this impeller. In the graphs of this figure, the average velocities in each direction, as obtained through Classic PIV measurements, were contrasted with data from other literature sources, which applied the Laser Doppler Velocimetry technique (LDV). The authors verified that the maximum velocities correspond to 80% and 73% of U_{tip} (impeller tip velocity) for the radial and out-of-plane components, respectively. Comparison with other studies indicated some differences between the profiles, which were explained by divergences in systems' geometries.

Figure 3.3: Axial profiles of (a) radial, (b) out-of-plane and (c) axial velocity components normalized by U_{tip}. Comparison among values from different studies in literature: ♦ Escudié and Liné (2003), □ Zhou and Kresta (1996), Δ Wu and Patterson (1989), × Rutherford *et al.* (1996) t_D/D = 0,01 and ● Rutherford *et al.* (1996) t_D/D = 0,2.

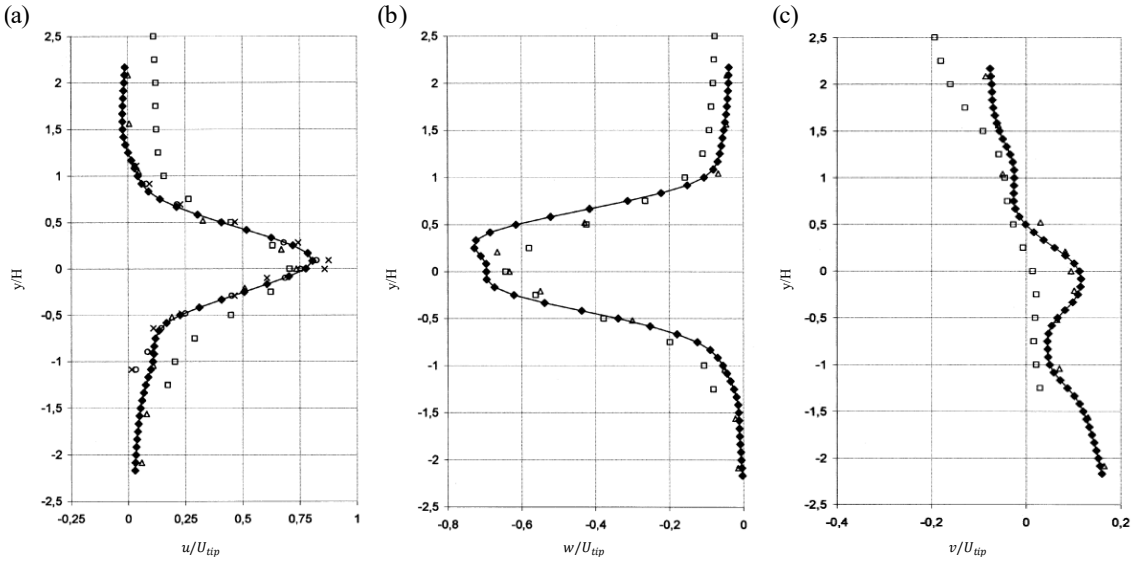

Source: adapted from Escudié and Liné (2003).

Regarding the flow pattern, these studies reported the emergence of two primary circulation stages, one above the impeller region and the other below it, in addition to the formation of secondary circulation zones (BALDI; YIANNESKIS, 2004; GALLETTI *et al.*, 2004; LEE; YIANNESKIS, 1998; PERRARD *et al.*, 2000; WANG *et*

al., 2022). An example of a flow field promoted by a Rushton turbine can be seen in Figure 3.4, extracted from Baldi and Yianneskis (2004). The vector field depicts a slight upward inclination of approximately 5°. The out-of-plane velocity distribution follows the shape of the impeller stream, with the highest values near the blade and a decrease in velocity with radial distance from the impeller.

Figure 3.4: Time-averaged velocity field of the flow promoted by Rushton turbine obtained by Baldi and Yianneskis (2004). The vectors indicate de distribution of the radial and axial velocity components, while the grey scale map shows the distribution of the out-of-plane velocity component.

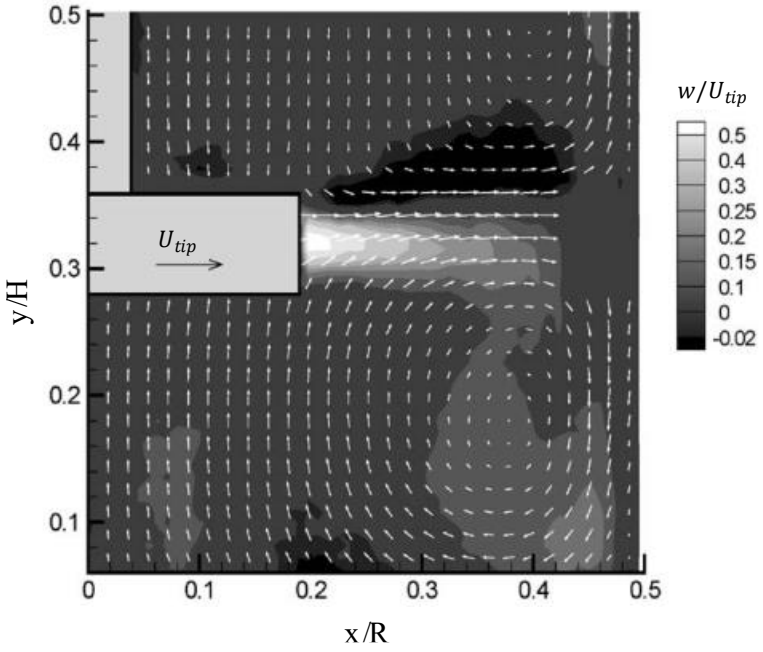

Source: Adapted from Baldi and Yianneskis (2004).

Unadkat *et al.* (2011) investigated the turbulent flow promoted by a sawtooth impeller using Stereo-PIV measurements in two positions, one closer to the impeller (1) and other farther from it (2). This type of impeller also promotes a radial flow pattern. The distribution of the mean velocities at position 1 indicated a maximum radial component of $0.12 \times U_{tip}$ at the blade edge, whereas the axial component presented a maximum of $0.03 \times U_{tip}$ in the regions above and below the impeller. The out-of-plane component showed a range of values marginally exceeds that of the radial component, reaching a maximum of $0.14 \times U_{tip}$; however, it is not uniformly distributed in the field of view, as the largest values are confined to the impeller discharge region. Consequently, the radial mean velocity component remains dominant in the impeller's discharge stream.

In general, despite the differences in geometry observed by researchers, the flow induced by pitched blade turbines follows a predominantly axial movement pattern with a slight deviation downwards due to the inclination of the blade. (CHUNG; BARIGOU; SIMMONS, 2007; HOCKEY; NOURI, 1996; KHAN; RIELLY; BROWN, 2006; SCHÄFER *et al.*, 1998; WANG *et al.*, 2022). Hockey and Nouri (1996) investigated a tank stirred by 60º pitched blade turbine with 6 blades. The authors observed, from the vector fields in the y-x plane (horizontal), that the axial velocity component is predominant near the impeller. For regions close to the base of the tank, the out-of-plane and radial velocity components are similar.

Khan *et al.* (2006) used Classic PIV and Stereo-PIV techniques to obtain velocity fields and turbulent parameters of the flow promoted by a 45º pitched blade turbine with 4 blades. They verified that the out-of-plane velocity component is higher in the drag vortices region, reaching up to 67% of U_{tip} (Figure 3.5). To check the validity of the out-of-plane velocity component, these values were compared with Laser Doppler Anemometry (LDA) measurements made in a stirring system similar to the one employed in their work. The two sets of data showed reasonable agreement.

Figure 3.5: Mean velocity fields for the flow induced by a 45° PBT with 4 blades obtained by Stereo-PIV measurements at different blade angles.

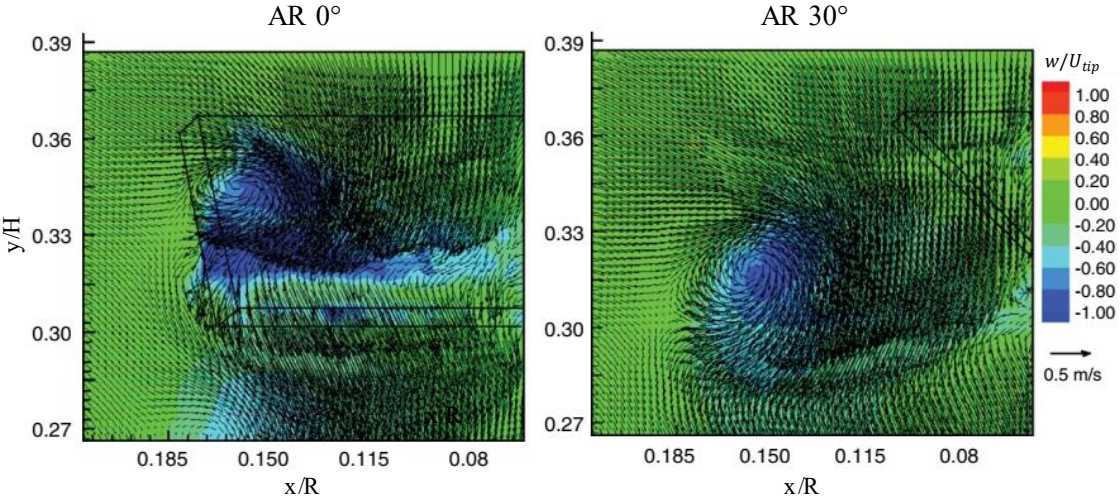

Fonte: Adapted from Khan *et al.* (2006).

Alonzo-Garcia *et al.* (2019) also assessed the flow induced by a 45º pitched blade turbine with 4 blades using the Classic PIV method, in order to validate diverse turbulence models employing unstructured meshing schemes. The radial and axial velocity component fields normalized by the impeller tip velocity ($U_{tip} = 2{,}18\ m/s$) at

the angle-resolved of 0° are shown in Figure 3.6. The authors observed a strong swirl motion near the blade tips and a sign change of the velocity components, which was related to the presence of a recirculation region near the impeller. The flow pattern also presented a slightly deflection outwards in the discharge region, which was associated with the blade angle. They verified a maximum value of $0.50 \times U_{tip}$ for the axial component in the region above the impeller and a maximum of $0.20 \times U_{tip}$ for the radial component in the discharge region.

Figure 3.6: Axial (v/U_{tip}) and radial (u/U_{tip}) time-averaged velocity components obtained from Classic PIV measurements at blade angle of 0° by Alonzo-Garcia *et al.* (2019) for the flow induced by PBT.

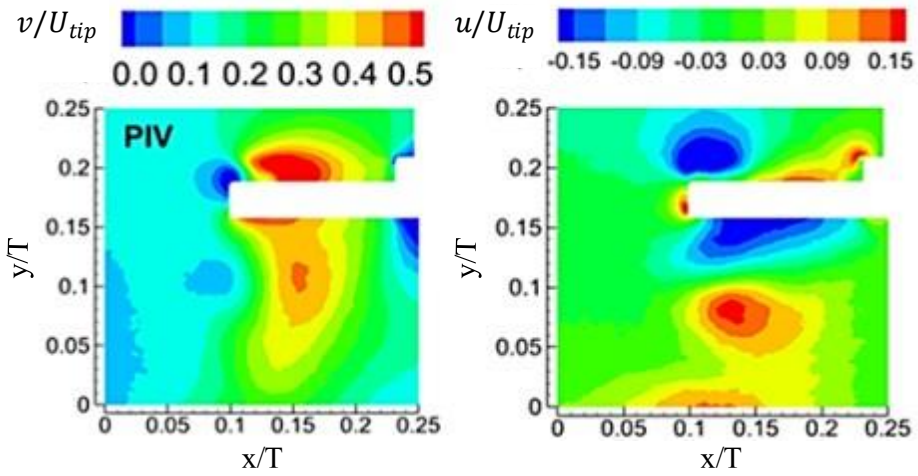

Source: Adapted from Alonzo-Garcia *et al.* (2019).

Ge *et al.* (2014) compared the flow promoted by PBT with modified blades. They evaluated the effect of the blade shape and angle on the mean radial and axial velocity profiles, in addition to the TKE profiles. The results indicated that the change of the blade shape can increase the radial velocity close to the impeller and rise the axial velocity in poorly mixed areas, for instance, the center of the tank. Furthermore, the increase in the blade angle improved the velocity components, pumping and power numbers, but decreased the efficiency of pumping capacity. The authors concluded that the relation between the geometric parameters of the impellers and the macroscopic flow is significant to obtain optimized impellers.

Bugay *et al.* (2002) evaluated the flow promoted by a Lightnin A310 impeller. The authors obtained the three velocity components from measurements in different planes parallel and perpendicular to the impeller blade. The evaluation of radial profiles

of the average velocity components normalized by U_{tip} for different heights of the tank allowed to verify that the vertical flow is pumped downwards and circulates upwards along the lateral wall. The magnitude of the axial velocity reaches 30% of U_{tip} near the tip of the impeller. The magnitude of the radial velocity is smaller ($< 0.03 \times U_{tip}$) and the out-of-plane velocity reaches between 10 and 15% of U_{tip}. Similar results were observed by Shekhar *et al.* (2012) when investigating the flow generated by a HR-100 impeller, which also has 3 blades as the Lightnin A310, but with a different shape.

Recently, Stelmach *et al.* (2022) compared the performance of a 45° PBT with 6 blades and of three NACA impellers with airfoil blades using Classic PIV and torque measurements. All the impellers presented similar flow patterns and Figure 3.7 provides an example of the velocity fields obtained by the researchers. The discharge stream flows downwards with a 45° deviation due to the pitched inclination. This stream reaches the bottom of the tank and changes direction, flowing radially towards the wall. At the wall, the flow changes its direction one more time and flows upwards until reaches the height of the impeller, and then moves toward the tank axis, closing the circulation loop. The authors verified that the impellers with airfoil paddles showed a reduction in mixing power and presented higher efficiency when compared with the 45° PBT. They believe that impellers with profiled blades (instead of flat) can be used more often in future due to the rise of 3D printers.

Figure 3.7: Velocity components field of the flow promoted by 45° PBT with 6 blades. The point where radial and axial velocities marked as two intersecting red lines are equal to zero.

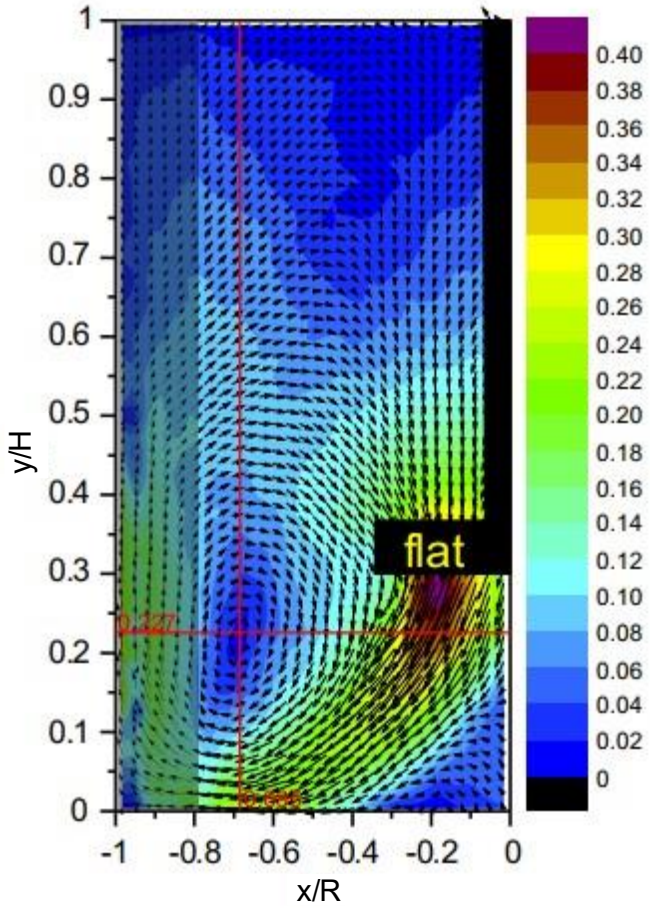

Source: Adapted from Stelmach *et al.* (2022).

Table 3.1 describes the main findings in literature regarding the fluid dynamics in stirred tanks. What stands out in the table is the wide range of results showing the flow pattern and the distribution of the velocity components in the flows promoted by the most diverse impellers. The out-of-plane component, although neglected when methods such as the Classic PIV are applied, plays an important role in the dynamics of circulation and tank mixing. Thus, one of the objectives of this work is to investigate the impact of the out-of-plane component not only on the flow pattern developed inside the tank, considering different types of impellers, but also on the estimation of the turbulent parameters, in order to contribute to the consolidation of the knowledge about fluid dynamics in a stirred tank.

Table 3.1: Summary of the main works in the literature on fluid dynamics of stirred tanks.

Author	Impeller	Tank's Geometry	Technique	Re ($\times 10^4$)	Main conclusions and comments
Wu and Patterson (1989)	Rushton turbine	T = 0.270 m D_T = T/3 C = T/3	LDV	1.4, 2.9 and 4.3	The authors measured the three velocity components and their fluctuations. They observed a radial flow pattern and that the axial component is smaller than the other components. The authors discussed the effect of the periodic fluctuation caused by the impeller movement, which is negligible nowadays due to angle-resolved measurements. The velocity profiles presented in this work are widely used in validation of CFD simulations.
Hockey and Nouri (1996)	60° PBT 6-blades	T = 0.294 m D_T = T/3 C = T/3	LDV	4.8	The power number decreased by 12% for 200 < Re < 1200 and stabilized for higher numbers, which was attributed to a flow pattern change. Currently, this is related to a flow regime change. The velocity fields showed the single stage pattern. The axial velocity fluctuations were up to 50% higher in the discharge region. The 60º PBT generated 2.5 times more flow per energy input than a Rushton turbine, thus it can be better for higher flow rate applications.
Montante *et al.* (1999)	Rushton turbine	T = 0.290 m D_T = T/3 C variable	LDV	From 1.2 to 5.6	For clearances of T/3 and T/4 the expected radial flow pattern with the double stage formation was observed. However, for clearances below T/5, a transition to single stage was verified, with an inclination of the discharge stream in the bottom direction. The results also showed that the rotational speed has no effect on the flow pattern, the normalized velocity fields and the normalized turbulence levels.
Bugay *et al.* (2002)	Lightinin A310	T = 0.450 m D_T = T/3 C = T/3	Classic PIV	7.5	The Profiles of velocity components and Reynolds tensors are presented, indicating a predominantly axial flow pattern. The energy dissipation rate was estimated from energy balance equations and compared with empirical correlations.

Table 3.1: Summary of the main works in the literature on fluid dynamics of stirred tanks.

Author	Impeller	Tank's Geometry	Technique	Re ($\times 10^4$)	Main conclusions and comments
Escudié and Liné (2003)	Rushton turbine	T = 0.450 m D_T = T/3 C = T/3	Classic PIV	5.6	It is one of the most cited papers on PIV measurements in stirred tanks. The authors characterized the mean flow, the periodic fluctuations and the turbulent fluctuations. The mean flow energy is transferred to the periodic and turbulent fluctuations in the impeller stream jet.
Galletti *et al.* (2004)	Rushton turbine	T = 0.290 m D_T = 0.32T C = T/2	LDV	2.8	The radial and out-of-plane velocity fluctuations were similar and approximately three times greater than the axial component. Rod-shaped turbulence regions were identified near the impeller stream and in the circulation loops, while disc-shaped turbulence was found near the tank's bottom.
Khan *et al.* (2006)	45° PBT 4-blades	T = 0.290 m D_T = T/3 C = T/3	Stereo-PIV	4.75	Both in-plane and out-of-plane mean velocity fields were validated against previous works. Close to the impeller, the out-of-plane velocity component can be up to 67% of the U_{tip}. The pseudo-isotropic approximation was considered a reasonable assumption for most of the field. From this work, many authors started to assume the pseudo-isotropic approximation to evaluate TKE.
Gabriele *et al.* (2009)	45° PBT 6-blades	T = 0.150 m D_T = 0.45T C = T/4	Classic PIV	2.28	Comparison between up and down pumping flows. Assessment of the flow pattern, TKE fields and EDR estimated with different models. The results showed that the mean flow with up pumping generally developed lower values than the down pumping. The up pumping led to a more radial discharge profile with a strong lower flow loop and weak upper flow loop, while the down pumping yielded only one main flow loop, which encompassed most of the vessel.

Table 3.1: Summary of the main works in the literature on fluid dynamics of stirred tanks.

Author	Impeller	Tank's Geometry	Technique	Re ($\times 10^4$)	Main conclusions and comments
Li *et al.* (2011)	Rushton turbine	T = 0.150 m D_T = T/3, T/2 and 2T/5 C = 0.15T	Classic PIV	4.0, 6.4 and 7.5	The effect of the impeller diameter and the Reynolds number were evaluated using PIV measurements and large eddy simulations. It was found that Reynolds number has little effect on the mean flow. At low clearance, the single-loop flow pattern is changed into a double-loop one if the impeller diameter is increased from T/3 to T/2.
Zhao *et al.* (2011)	Four types of 6-blades disc turbines	T = 0.480 m D_T = 0.190 m C = T/3	Classic PIV	5.4	The authors examined the effect of blade shape on the structure of trailing vortices and turbulent properties in the stirred tank. As the blade turns more curved, the inclination of the impeller stream becomes smaller, and the radial jet becomes weaker. The large curvature leads to a longer residence time of the eddies at the impeller tip, a bigger distance between the upper and lower eddies.
Unadkat *et al.* (2011)	Sawtooth impeller	T = 0.305 m D_T = T/3.21 C = T/3	Stereo-PIV	23	The authors evaluated a different type of impeller that promotes radial flow pattern. The out-of-plane velocity component exceeded the radial velocities at the blade but decayed more rapidly than the radial flow further away from the blade. Consequently, the radial mean velocity component is the predominant flow direction. The out-of-plane velocity fluctuations are larger than the axial and radial components.
Shekhar *et al.* (2012)	HR-100 3 blades at 120°	T = 0.300 m D_T = T/3	Stereo-PIV	5.94	A different impeller model was evaluated, which promotes an axial flow pattern. The Stereo-PIV measurements were comparable with the Classic PIV and made it possible to observe the out-of-plane velocity component, which presented a dominant contribution to the flow, mainly in the region of eddies formation. Also, it was found that this component contributed to 96% of the turbulent kinetic energy

Table 3.1: Summary of the main works in the literature on fluid dynamics of stirred tanks.

Author	Impeller	Tank's Geometry	Technique	Re ($\times 10^4$)	Main conclusions and comments
Li *et al.* (2013)	Three types of 6-blades disc turbines	T = 0.480 m D_T = 0.190 m C = T/3	Stereo-PIV	4.0, 5.0, 6.0, 7.5 and 9.0	Three of the four blade shapes evaluated by Zhao et al. (2011) were used in this work to assess the effect of Reynolds number and blade shape on flow pattern and TKE distribution using Stereo-PIV measurements. The Reynolds number has no influence on the velocity and TKE distributions. Also, the absolute TKE fields are similar for all impellers at the same power input.
Ge *et al.* (2014)	Six types of PBT	T = 0.340 m D_T = 0.144 m C = 0.113 m	Classic PIV	5.0	The change of the blade shape can increase the radial velocity close to the impeller and the axial velocity in poorly mixed areas. The increase in the blade angle improved velocity, pumping and power numbers, but it decreased the efficiency of pumping capacity. The relation among the geometric parameters of the impellers and the macroscopic flow are important to obtain optimized impellers.
Wang *et al.* (2022)	Five types of impellers	T = 0.234 m D_T = T/3 C = T/3	Classic PIV	From 3.33 to 4.47	Shear rate distribution characteristics are investigated for five different impellers at the same power consumption per unit volume. For radial impellers, the larger shear rates are distributed around the blades; while for axial impellers, they are in the impeller discharge region. These higher zones provide reference for feed locations.
Stelmach *et al.* (2022)	Four types of PBT	T = 0.292 m D_T = T/3 C = T/3	Classic PIV	4.0	All impellers presented similar flow patterns. Two dead zones were observed: a conical region below the impeller and in the contact region of the tank's bottom with the wall. The inverted asymmetric impeller profile presented lower velocities and larger dead zones. Impellers with airfoil blades presented axial velocities similar to those of the standard impeller, despite the lower mixing power. They believe that impellers with profiled blades can be used in future due to the rise of 3D printers.

3.2. Turbulent Flow

This thesis proposed to study turbulent flow in stirred tanks. To develop this study, it is necessary to keep in mind what turbulent flow means, its definition, implications and particularities. A turbulent flow exists within a turbulent regime, as opposed to a laminar regime. The laminar regime is characterized by the aligned and coherent movement of fluid layers. The turbulent regime, in turn, is characterized by the irregular, unstable and apparently random movement of fluid elements, resulting in fluctuations in the properties of the flow. It is important to remember that a turbulent flow is considered a continuous medium, where the characteristic length of a fluid element significantly exceeds the mean free path of its molecules (POPE, 2000). Therefore, in this thesis we do not deal with the discrete molecular nature of the fluid, and we do not discuss molecular scales. It is also noteworthy that the behavior of a continuous medium can be modeled using the Navier-Stokes equations.

As here we were interested in the velocity and energy distribution fields of the flow inside the tank, our study of turbulence focuses on characterizing the irregular fluctuations in instantaneous velocity, generated by the shear promoted by the irregular, unstable and apparently random movement of fluid elements. Clusters of instabilities of different frequencies form eddies, which coexist in space and time, interacting non-linearly with each other (SILVEIRA NETO, 2020). Due to this unstable nature, velocity fields lack a singular, consistent value, meaning they vary with each repetition of the experiment under identical conditions, and only statistical properties can be recognized and analyzed. Consequently, turbulent flow is much more sensitive to perturbations in experimental conditions. Even if efforts are made to reduce these disturbances, they will always exist (FROST; MOULDEN, 1977; POPE, 2000; SOUZA et al., 2011). This highlights the complexity and challenge of characterizing this type of flow.

Regarding the flow in stirred tanks, the turbulent flow has an essential ability to transport and mix fluids much more efficiently than the laminar flow. The knowledge of the eddies location and size is important to optimize the mixing time. The high concentration of turbulence levels generated in this zone could be exploited to reduce the mixing times if this location is used, for instance, as a feed location (SCHÄFER *et al.*, 1998). In addition, the comprehension of how the turbulent structures is distributed along the tank provides insights into the agitation efficiency and helps identify potential dead zones.

The turbulence must be seen as an entity that can be produced, dissipated and transported through the flow (SOUZA et al., 2011). A steady-state turbulence promotes the formation of eddies at different scales. The large structures are unstable and break, transferring energy to smaller structures. These structures go through a similar process of breakdown and transfer their energy to even smaller structures. The energy cascade persists until the eddy motion stabilizes, and viscous effects become significant enough to dissipate the kinetic energy (MORY, 2011; POPE, 2000).

Figure 3.8 provides a schematic model of energy production and dissipation as a function of wave number (λ_N). We can observe that turbulent kinetic energy is mainly generated in the integral scale wave number (λ_l), and then the same amount of energy is dissipated near the Kolmogorov scale wave number (λ_η). In the middle, there is a large region, called the inertial subinterval, in which the turbulent structures transfer energy from the large structures to the small-scale ones, without significatively changes (SHENG; MENG; FOX, 2000). To have a steady-state turbulent flow, it is necessary that all the injected energy over the integral scale (λ_l) is transformed by viscous effects in the Kolmogorov scale (λ_η).

Figure 3.8: Schematic model of production and dissipation of turbulent kinetic energy, according to Sheng *et al*. (2000).

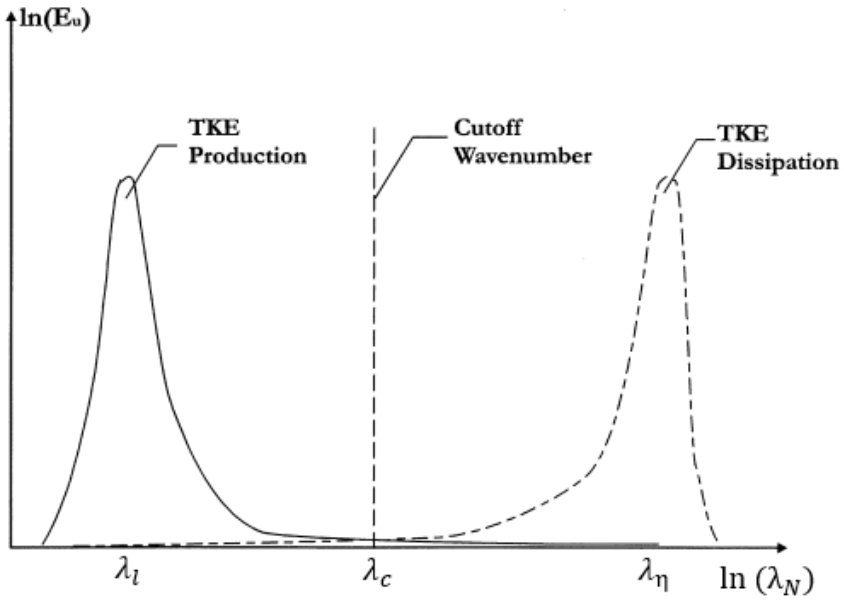

Source: Sheng *et al*. (2000).

3.2.1. Kolmogorov Theory and Scales

As was mentioned in the previous section, the energy distribution promoted by turbulent flow is characterized by eddies of different scales. Thus, there is a need to understand and measure these scales, which is directly related to Kolmogorov's Theory and its hypotheses.

Kolmogorov's Theory (1991) aims to characterize the local turbulence structure of incompressible and viscous fluid flows with high Reynolds numbers. Kolmogorov employs two definitions: homogeneous turbulence and locally isotropic turbulence. Turbulence is considered homogeneous when the velocity fluctuations field is statistically invariant in a translation of the coordinate system, that is, it is independent of an initial coordinate system. Turbulence is locally isotropic if it is locally homogeneous and invariant with respect to rotations and reflections of the coordinate axes. The author argues that during the process of reducing scales in the energy cascade there is a loss of the directional bias of the large scales (POPE, 2000).

From these two definitions, Kolmogorov develops two hypotheses of similarity. The first hypothesis deals with the universal equilibrium range (Figure 3.9). In all turbulent flow with a sufficiently high Reynolds number, considering an eddy size l, the statistics of small-scale motions ($l < l_{EI}$) have a universal form uniquely determined by fluid viscosity ν and by energy dissipation rate ε. The second hypothesis deals with a range within universal equilibrium ($l_{EI} \gg l \gg l_{DI}$) in which all turbulent flow with a sufficiently high Reynolds number can have movement statistics solely determined by ε and independent of ν. This range is called the inertial subrange and is delimited by the beginning of the dissipation range l_{DI} and the beginning of the universal equilibrium range l_{EI} (POPE, 2000).

Figure 3.9: The various ranges and length scales that an eddy structure can present in a turbulent flow with a high Reynolds number.

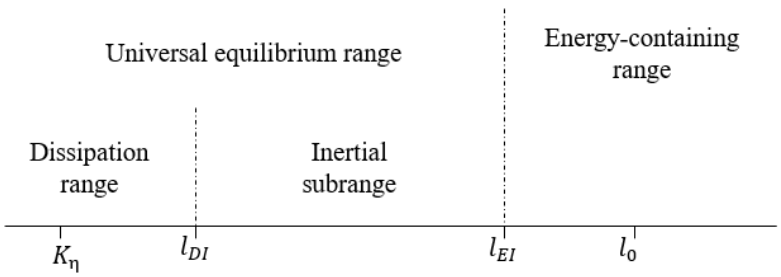

Source: Adapted from Pope (2000).

Consider an eddy of a characteristic length l, that is originated in the turbulent flow of a fluid with viscosity ν, with a characteristic velocity ϑ_l. The local Reynolds number is defined as (SILVEIRA NETO, 2020):

$$Re_l = \frac{\vartheta_l l}{\nu} \tag{3.1}$$

By Kolmogorov's theory:

$$\vartheta_l = (\varepsilon l)^{1/3} \tag{3.2}$$

By substituting this result in Equation (3.1, we have:

$$Re_l = \frac{(\varepsilon l^4)^{1/3}}{\nu} \tag{3.3}$$

A characteristic length K_η is defined so that the Reynolds number in this situation is equal to a unit:

$$Re_{K_\eta} = \frac{\left(\varepsilon K_\eta^4\right)^{1/3}}{\nu} = 1 \tag{3.4}$$

Then, we have the Kolmogorov viscous transformation length scale:

$$K_\eta = \left(\frac{\nu^3}{\varepsilon}\right)^{1/4} \tag{3.5}$$

Perturbations with wavelengths shorter than K_η cannot be amplified due to the predominance of viscous effects. The Kolmogorov time scale is defined as:

$$K_\tau = \left(\frac{\nu}{\varepsilon}\right)^{1/2} \tag{3.6}$$

And the Kolmogorov velocity scale:

$$K_\vartheta = (\nu\varepsilon)^{1/4} \tag{3.7}$$

These quantities refer to the smallest possible turbulent structures that make up the energy cascade of a turbulent flow. For a fully developed flow, the energy dissipation rate is equal to the rate at which energy is supplied to the large vortices by the average flow (SILVEIRA NETO, 2020):

$$\varepsilon \approx \frac{U^3}{I_l} \tag{3.8}$$

where U is the transport velocity of the integral scale and I_l is the integral length of the most energize eddies. The ratios between the smallest scales (the Kolmogorov ones) to largest scales (known as integral scales) can be determined from this definition. The results are, for the length scales:

$$\frac{K_\eta}{I_l} = Re^{-3/4} \tag{3.9}$$

For the time scales:

$$\frac{K_\tau}{I_t} = Re^{-1/2} \tag{3.10}$$

And for the velocity scales:

$$\frac{K_\vartheta}{U} = Re^{-1/4} \tag{3.11}$$

Clearly, the characteristic Kolmogorov scales are much smaller than the integral scales. Moreover, the difference is greater the higher the Reynolds number of the mean flow (POPE, 2000; SILVEIRA NETO, 2020).

It is noteworthy that the Kolmogorov's hypotheses have some limitations. Firstly, the definition of what is a sufficiently high Reynolds number is unclear. Secondly, there is a simplification of the complex turbulent phenomena with the assumption that the energy cascade is unidirectional, with energy transfer going from larger to smaller structures. Furthermore, a number of studies shows that statistical moments of order greater than 2 may not be well predicted by the Kolmogorov's hypotheses. Despite this, it remains the best theory available to date, and its resulting scales are widely to discuss the limitations of models and characterizations of turbulent flow.

Particle image velocimetry acquires instantaneous velocity fields, which allows resolving the spatial structure of eddies (DIETERLE, L.; WEICHERT, R., 1996). However, the spatial resolution of the images must be able to measure turbulent structures at different scales, from the integral scales to the Kolmogorov ones.

3.2.2. Turbulent Kinetic Energy

As explained earlier, one way to analyze the turbulent flow in stirred tanks is through the evaluation of velocity fluctuations in a cross section of the flow (MORY, 2011; WESTERWEEL; ELSINGA; ADRIAN, 2013). These fluctuations give rise to Kelvin–Helmholtz instabilities, which are linked to the shear nature of the flow and are independent of viscous effects. Kelvin-Helmholtz instabilities carry large amounts of turbulent kinetic energy (SILVEIRA NETO, 2020).

A statistical moment of order n is defined by the ensemble average of the product of the n variables f^{a_i} involved in a study object:

$$[f^{a_1} f^{a_2} \dots f^{a_n}](\vec{x}, t) = \lim_{N \to \infty} \frac{1}{N} \sum_{i=1}^{N} f^{a_1} f^{a_2} \dots f^{a_n} \tag{3.12}$$

Considering the turbulent flow our study object, we can define n equals to 2 and these two variables as the velocity fluctuations of one of the velocity components u'. Thus, the statistical moment of second order provides the relative turbulent intensity:

$$[u'u'] = \overline{u'^2} \tag{3.13}$$

The term on the right side of the equation is the variance of the velocity fluctuations, defined as time average of the velocity fluctuations (MORY, 2011):

$$\overline{u'^2} = \frac{1}{\mathrm{N}}\sum_{\mathrm{i}=1}^{\mathrm{N}}(\mathrm{u_i} - \bar{u})^2 \tag{3.14}$$

where $\mathrm{u_i}$ and $\bar{u}$ are the instantaneous and mean velocities, respectively, and N is the number of acquired samples. This definition derives from the Reynolds decomposition. It is important to notice that the equality described by Equation (3.13 consider the ergodicity hypothesis, in which the ensemble averaged of a variable can be obtained by its temporal average. Extending this example to the three velocity components, we can obtain the Boussinesq–Reynolds tensor, composed of nine second-order statistical elements (SILVEIRA NETO, 2020):

$$\bar{\bar{\tau}}(\vec{x}) = \begin{bmatrix} \overline{u'^2} & \overline{u'v'} & \overline{u'w'} \\ \overline{v'u'} & \overline{v'^2} & \overline{u'w'} \\ \overline{w'u'} & \overline{w'v'} & \overline{w'^2} \end{bmatrix} \tag{3.15}$$

The turbulent kinetic energy is defined as half of the trace of the Boussinesq-Reynolds tensor:

$$k \equiv \frac{1}{2}\overline{u_i'u_i'} = \frac{1}{2}\left(\overline{u'^2} + \overline{v'^2} + \overline{w'^2}\right) \tag{3.16}$$

This is the average kinetic energy per unit mass in the velocity fluctuations field (POPE, 2000; SILVEIRA NETO, 2020). The variance of the velocity fluctuations $\overline{u'^2}$, $\overline{v'^2}$ and $\overline{w'^2}$ are also known as the root-mean-square of the radial, axial and out-of-plane velocity fluctuations, respectively. For Classic PIV measurements, in which the out-of-plane velocity component is unknown, the pseudo-isotropic approximation is assumed, in which the root-mean-square of the out-of-plane velocity fluctuations is the

arithmetic mean of the two other fluctuations (radial and axial), and then the turbulent kinetic energy can be calculated according to Equation (3.17:

$$k_{iso} = \frac{1}{2}\left[\overline{u'^2} + \overline{v'^2} + \frac{1}{2}\left(\overline{u'^2} + \overline{v'^2}\right)\right] = \frac{3}{4}\left(\overline{u'^2} + \overline{v'^2}\right) \quad (3.17)$$

Table 3.2 summarizes studies in literature regarding the evaluation of the turbulent kinetic energy fields in stirred tanks and the TKE ranges found in the main investigations for different types of impellers and measurement techniques. What is interesting about the data in this table is that most articles assessed the flow promoted by PBT and Rushton turbine, due to their industrial importance. The TKE ranges reaches a maximum of $0.1 \times U_{tip}^2$ and $0.12 \times U_{tip}^2$ for the flow induced by 45° PBT with 4 blades and with 6 blades, respectively. The ranges obtained with the Rushton turbine are wider and can reach a maximum of $0.18 \times U_{tip}^2$, which is expected since this impeller has, in general, a higher power number.

Table 3.2: Turbulent kinetic energy (TKE) ranges of different types of impellers and methods reported in literature.

Author	Impeller	Tank's Geometry	Technique	Re ($\times 10^4$)	Spatial Resolution (mm)	k/U_{tip}^2
Kresta and Wood (1993)	45° PBT 4-blades	T = 0.152 m, D_T = T/2	LDA	3.85	-	$0.01 < k/U_{tip}^2 < 0.10$
Schäfer *et al.* (1998)	45° PBT 4-blades	T = 0.152 m, D_T = 0.329T	LDA	0.73	-	$0.00 < k/U_{tip}^2 < 0.06$
Khan *et al.* (2006)	45° PBT 4-blades	T = 0.290 m, D_T = T/3	PIV, Stereo-PIV	4.75	1.25	$0.00 < k/U_{tip}^2 < 0.06$
Roy *et al.* (2010)	45° PBT 4-blades	T = 0.44 m, D_T = 0.51T	PIV	4.4	1	$0.01 < k/U_{tip}^2 < 0.06$
				13.2		$0.01 < k/U_{tip}^2 < 0.06$
Alonzo-Garcia *et al.* (2019)	45° PBT 4-blades	T = 0.250 m, D_T = T/3	PIV	5.2	0.64	$0.00 < k/U_{tip}^2 < 0.04$
Martinez-Delgadillo *et al.* (2019)	45° PBT 4-blades	T = 0.250 m, D_T = T/3	PIV	5.2	0.69	$0.00 < k/U_{tip}^2 < 0.04$
Chung *et al.* (2009)	45° PBT 6-blades	T = 0.045 m, D_T = 0.54T	PIV	0.82	1	$0.00 < k/U_{tip}^2 < 0.05$
Gabriele *et al.* (2009)	45° PBT 6-blades	T = 0.150 m, D_T = 0.45T	PIV	2.28	0.69	$0.00 < k/U_{tip}^2 < 0.07$
Guida *et al.* (2010)	45° PBT 6-blades	T = 0.190 m, D_T = 0.55T	PIV	4.0	1.04	$0.00 < k/U_{tip}^2 < 0.11$
Savari *et al.* (2022)	45° PBT 6-blades	T = 0.190 m, D_T = T/2	PIV	4.0	1.04	$0.00 < k/U_{tip}^2 < 0.12$

Table 3.2: Turbulent kinetic energy (TKE) ranges of different types of impellers and methods reported in literature.

Author	Impeller	Tank's Geometry	Technique	Re ($\times 10^4$)	Spatial Resolution (mm)	k/U_{tip}^2
Lee and Yianneskis (1998)	Rushton turbine	T = 0.100 m, D_T = T/3	LDA	4.0	-	$0.00 < k/U_{tip}^2 < 0.18$
Derksen *et al.*(1999)	Rushton turbine	T = 0.288 m, D_T = T/3	LDA	2.9	0.1	$0.00 < k/U_{tip}^2 < 0.15$
Escudié and Liné (2003)	Rushton turbine	T = 0.450 m, D_T = T/3	PIV	5.63	1.1	$0.00 < k/U_{tip}^2 < 0.13$
Li *et al.* (2011)	Rushton turbine	T = 0.476 m, D_T = T/3	PIV	6.4	0.6	$0.03 < k/U_{tip}^2 < 0.10$
		T = 0.476 m, D_T = T/2.5				$0.03 < k/U_{tip}^2 < 0.15$
		T = 0.476 m, D_T = T/2				$0.03 < k/U_{tip}^2 < 0.15$
Bugay *et al.* (2002)	Hydrofoil	T = 0.450 m, D_T = T/3	PIV	7.5	1.5	$0.00 < k/U_{tip}^2 < 0.11$
Unadkat *et al.* (2011)	Sawtooth imp.	T = 0.305 m, D_T = T/3.21	Stereo-PIV	23.0	1	$0.00< k/U_{tip}^2 < 0.01$
Liang *et al.* (2018)	curved-rigid imp.	T = 0.480 m, D_T = T/2	PIV	~10	1.4	$0.06 < k/U_{tip}^2 < 0.14$
	flat-rigid impeller					$0.06 < k/U_{tip}^2 < 0.14$
	flexible impeller					$0.06 < k/U_{tip}^2 < 0.14$
Martinez-Delgadillo *et al.* (2019)	U-groove turbine	T = 0.250 m, D_T = T/3	PIV	5.2	0.69	$0.00 < k/U_{tip}^2 < 0.04$
	V-groove turbine					$0.00 < k/U_{tip}^2 < 0.04$

Some studies bring interesting discussions about the distribution of kinetic energy in stirred tanks. Gabriele *et al.* (2009) explored the flow induced by a 45° PBT with 6 blades employing Classic PIV measurements (Figure 3.10). They observed two areas of higher TKE, one close to the impeller tip ($y/H = 0.16$ and $x/R = 0.42$) and another in the discharge region ($y/H = 0.07$ and $x/R = 0.55$). The first area was associated with the eddies generated by the impeller. The second area was, in turn, the eddies from the previous blade. The maximum TKE value was $0.06 \times U_{tip}^2$ at the blade angle of 39°.

Figure 3.10: Normalized turbulent kinetic energy obtained from Classic PIV measurements for different angles relative to the blade of the flow promoted by a 45° PBT with 6 blades.

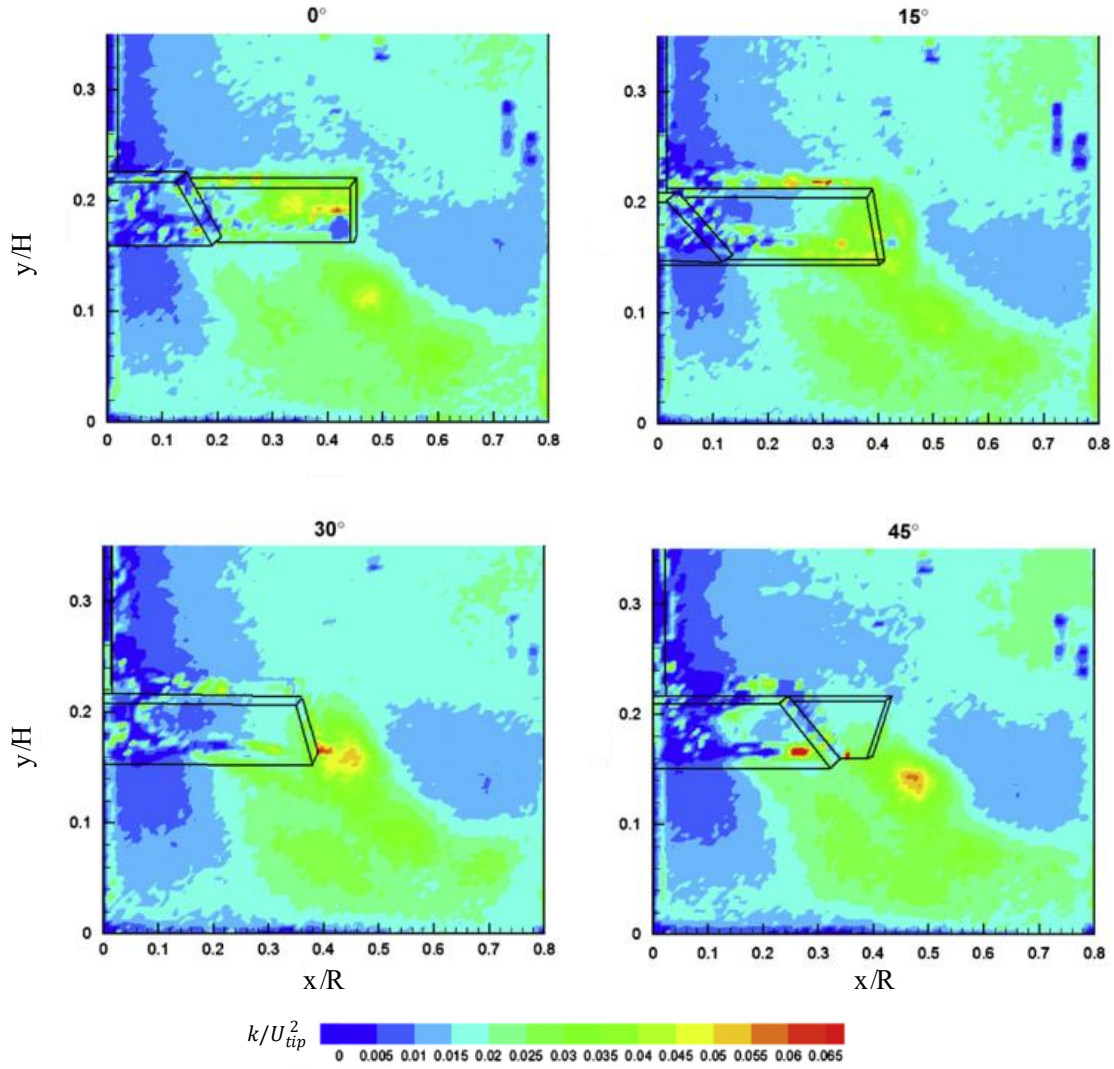

Source: Adapted from Gabriele *et al.* (2009).

Alonzo-Garcia *et al.* (2019) assessed the flow promoted by the same impeller using Classic PIV and verified values of normalized TKE (k_{iso}/U_{tip}^2) between $0.01 \times U_{tip}^2$ and $0.04 \times U_{tip}^2$. They observed an elongated pattern in the pumping direction that spreads out covering almost all the discharge region (Figure 3.11).

Figure 3.11: Normalized turbulent kinetic energy obtained from Classic PIV measurements considering the pseudo-isotropic approximation for blade angle 0° of PBT by Alonzo-Garcia *et al.* (2019).

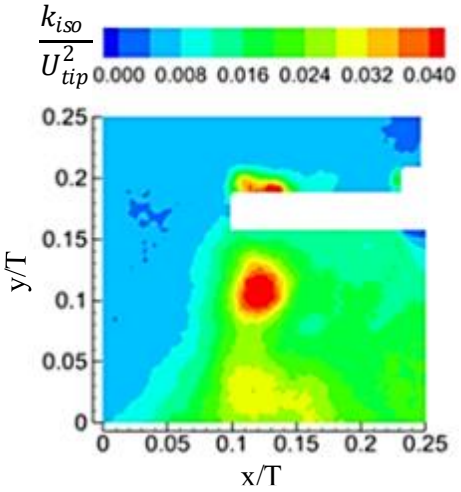

Source: Adapted from Alonzo-Garcia *et al.* (2019).

Escudié and Liné (2003) used the Classic PIV technique to evaluate the turbulent kinetic energy distribution of the flow promoted by a Rushton turbine. The three velocity components were determined from the evaluation of different planes: 1 radial plane, parallel to the impeller, 9 vertical planes and 9 horizontal planes. From these parameters, the authors identified and quantified the transfer of kinetic energy between the different forms of movement in the tank (mean flow, periodic fluctuation and turbulent fluctuation). The turbulent kinetic energy showed an increase near the impeller tip, followed by a rapid decrease, while the periodic kinetic energy showed the opposite behavior. Thus, the authors inferred that the energy was transferred from the periodic portion to the turbulent portion.

Li *et al.* (2011) focused on the investigation of the effects of the clearance on the flow promoted by a Rushton turbine. The authors employed a lower clearance than usual (C_T = 0.15T instead of C_T = T/3) and studied the formation of a single-loop flow pattern. In this situation, they also investigated the effect of the impeller diameter in this formation. Three different diameters were used: D_T = 0.158 m (RT158), D_T = 0.190 m (RT190) and D_T = 0.238 m. (RT238). The phase-average velocity and TKE fields for all the impellers are

presented in Figure 3.12. The results indicated that the discharge stream changed significantly with the increase of the impeller diameter. The smaller impeller induced a downward stream that reached the bottom of the tank. With the increase of the impeller size, the single-loop flow pattern became a two-stage loop, in which the discharge stream moved to the side wall of the tank and divided into two circulations. The TKE distribution also changed in a similar way.

Figure 3.12: Phase-average velocity components and TKE fields obtained by Classic PIV considering different impeller diameters (a) D_T = 0.158 m (RT158), (b) D_T = 0.190 m (RT190) and (c) D_T = 0.238 m. (RT238).

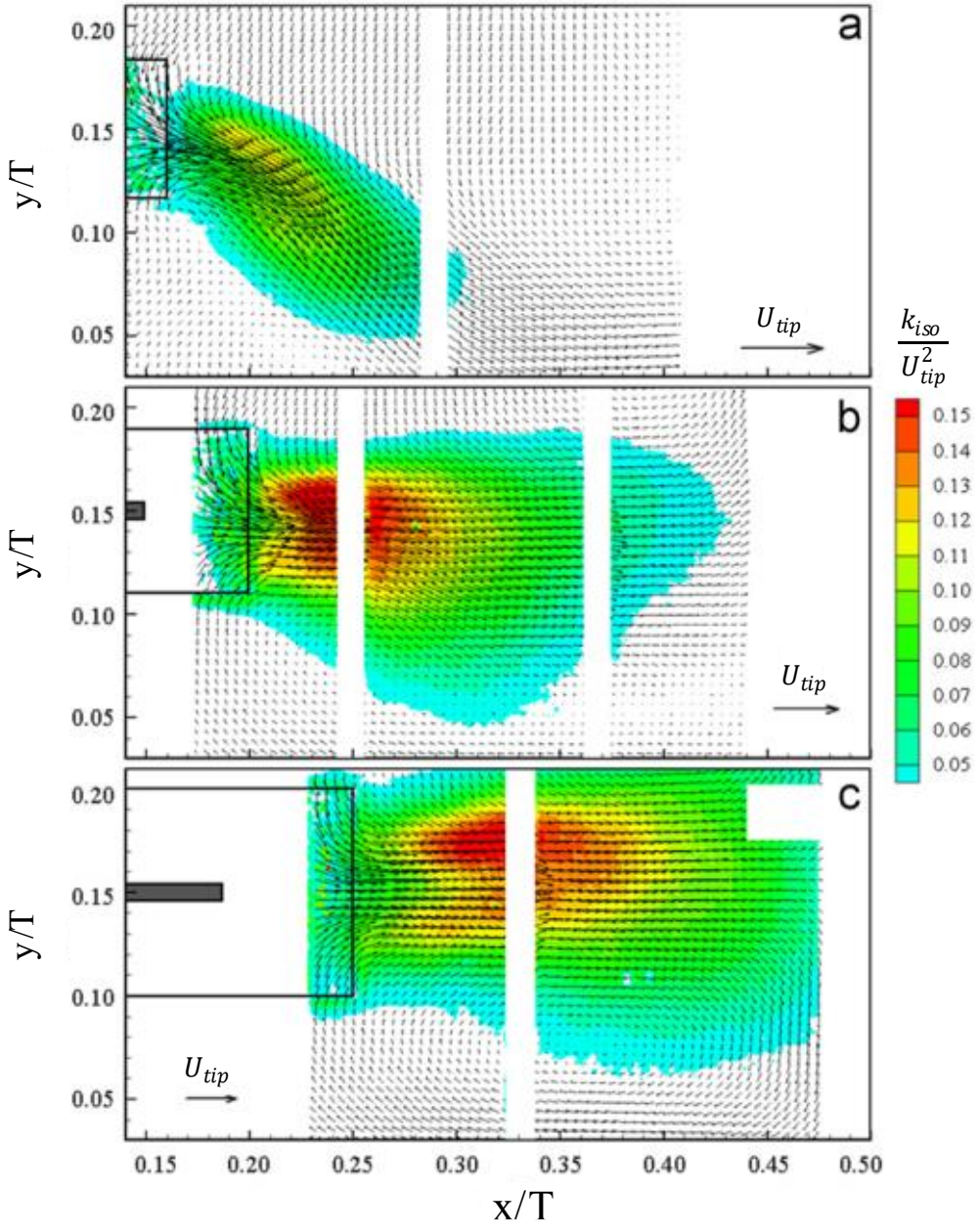

Source: Adapted from Li *et al.* (2011).

Fan *et al.* (2022) also studied the flow promoted by a Rushton turbine; however, the authors focused on the comparison of unbaffled and baffled tanks. The TKE fields obtained by Classic PIV with angle-resolved measurements showed higher values at angle-resolved (AR) of 40° (Figure 3.13). These higher values were observed near the impeller stream and were related to the increased presence of large-scale fluctuations. The higher value region of TKE were larger in baffled tank than in the unbaffled arrangement due to the shear effect promoted by the use of the accessory, that enhance the distribution of energy.

Figure 3.13: Normalized turbulent kinetic energy obtained from Classic PIV measurements at angle-resolved of 0°, 20° and 40º of Rushton turbine by Fan *et al.* (2022).

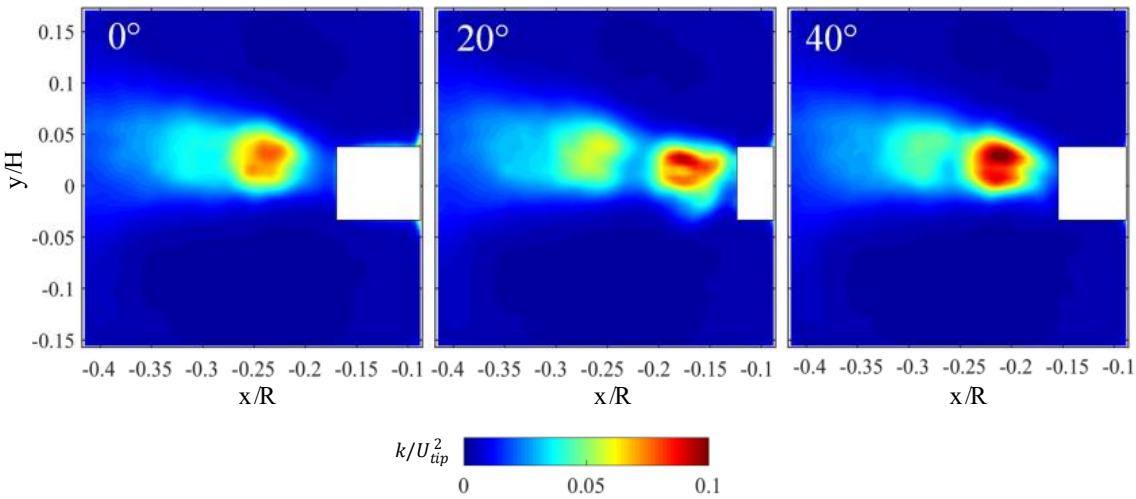

Source: Adapted from Fan *et al*. (2022)

In this section, we presented an overview of how the turbulent kinetic energy in stirred tanks is measured and discussed in the literature, with a greater focus on studies of the flow promoted by PBT and Rushton turbines. We found that regions of higher energy are intrinsically associated with regions of higher flow, where large-scale structures are formed. An interesting aspect to be considered is that few studies in the literature used the Stereo-PIV technique and were concerned with evaluating the effect of the out-of-plane component of TKE measurements. In general, works that use Classic PIV measurements simply consider the pseudo-isotropic approximation in estimating TKE without further discussions. Thus, a more detailed evaluation of this approximation is necessary for a better understanding of the energy distribution in the tank flow and some studies on this issue are presented in the following section.

3.2.3. Pseudo-isotropic Approximation

A hypothesis widely used in the literature in the attempt of compensating the absence of measurements of the out-of-plane velocity component is the pseudo-isotropic approximation (ALONZO-GARCIA et al., 2019; CHUNG; BARIGOU; SIMMONS, 2007; CHUNG; SIMMONS; BARIGOU, 2009; GABRIELE; NIENOW; SIMMONS, 2009; GUIDA; NIENOW; BARIGOU, 2010; KHAN; RIELLY; BROWN, 2006; LI; BAO; GAO, 2011; LIANG et al., 2018; MARTÍNEZ-DELGADILLO et al., 2019; SAVARI; LI; BARIGOU, 2022; UNADKAT; RIELLY; NAGY, 2011; WANG et al., 2018; ZHAO; GAO; BAO, 2011). This assumption considers that the velocity components are independent of the measurement direction, then the out-of-plane component can be computed as the arithmetic mean of the two measured velocities.

The main problem of this assumption in the analysis of the turbulent flow in stirred tanks is the fact that the drag vortices generated by the impeller have a clearly defined orientation, making the approximation not very consistent with the reality of the phenomenon. For eddies in a smaller scale and with a very high Reynolds number, it is possible to consider a local isotropy, in which the energy is dissipated without the influence of the large-scale movements provided by the drag vortices and of the shear effect of the main flow (KRESTA, 1998; MÖLLER, S. V.; SILVESTRINI, J. H., 2004). However, in the evaluation of the turbulent kinetic energy, this assumption is not possible because we are concerned with large-scales eddies.

Khan *et al*. (2006) employed the Classic PIV and Stereo-PIV techniques to evaluate the turbulent kinetic energy field of the flow induced by a 45º PBT with 4 blades (Figure 3.14). The authors compared the TKE estimated by the three velocity components and the fields obtained from the pseudo-isotropic approximation. The fields showed that the TKE distribution and its values are very similar in both cases. Small differences were observed in the center of the eddies, where the TKE estimated by the three components is slightly higher than that estimated considering the pseudo-isotropic approximation, which indicates that the contribution of the out-of-plane component in the turbulent structures is greater than that estimated by the assumption. From this work, many authors started to assume the pseudo-isotropic approximation to evaluate the distribution of TKE (GUIDA; NIENOW; BARIGOU, 2010; LI; BAO; GAO, 2011; ALONZO-GARCIA et al., 2019; MARTÍNEZ-DELGADILLO et al., 2019; ZHAO; GAO; BAO, 2011).

However, Unadkat *et al.* (2011) evaluated the isotropy of the turbulent flow promoted by a sawtooth impeller from Stereo-PIV measurements and found that the flow is anisotropic close to the impeller, but isotropic in the most distant regions (Figure 3.15). The evaluation of turbulent kinetic energy considering the pseudo-isotropic approximation led to values on average 45% lower than those obtained from the three root-mean-square (rms) of the velocity fluctuations.

Figure 3.14: Turbulent kinetic energy obtained by Khan *et al.* (2006) considering (a) Classic PIV and (b) Stereo-PIV measurements.

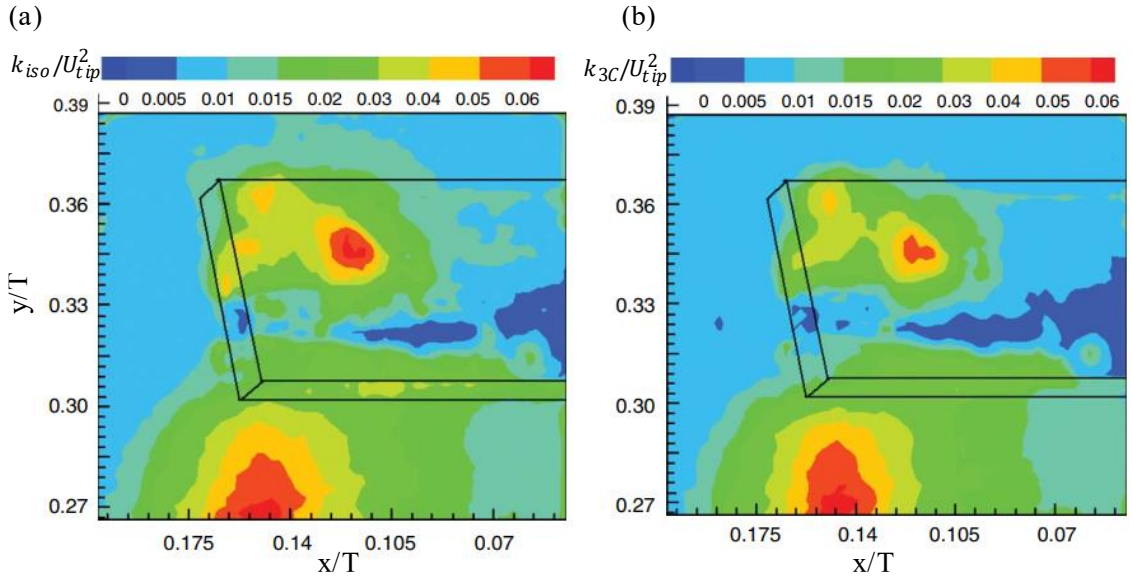

Source: Adapted from Khan *et al.* (2006).

Figure 3.15: Turbulent kinetic energy obtained by Unadkat *et al*. (2011) considering (a) Classic PIV and (b) Stereo-PIV measurements.

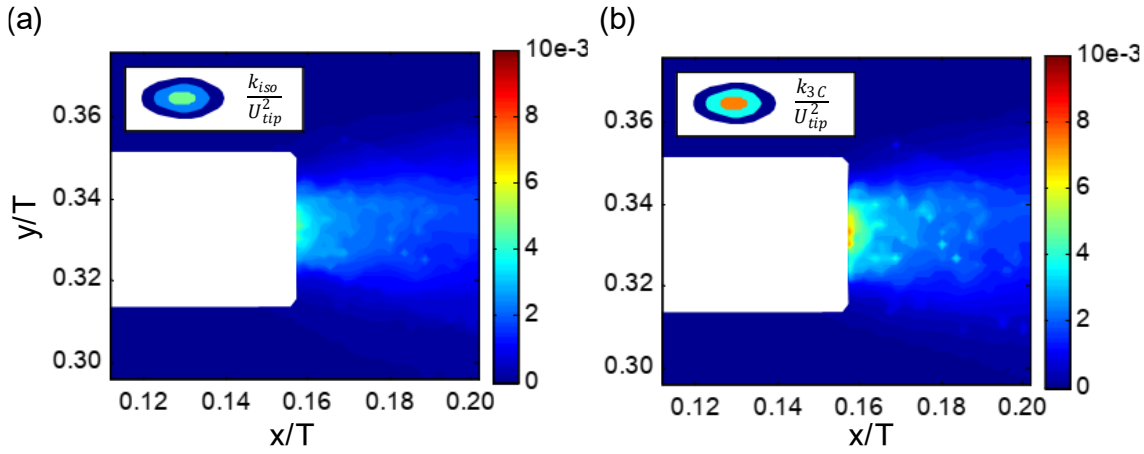

Source: Adapted from Unadkat (2010).

Liang *et al.* (2018) compared TKE profiles computed by the three rms of the velocity fluctuations and considering the pseudo-isotropic assumption of the flow induced by different types of impellers with flat-rigid, flexible and curve-rigid blades. The results showed that the TKE estimation based on the pseudo-isotropic approximation was higher than the TKE computed with all three rms of the velocity fluctuations because the out-of-plane component is lower than the in-plane components. The difference reached 20% in the region close to the impeller.

Taken together, these studies differ between the validity of the pseudo-isotropic approximation for the estimation of the turbulent kinetic energy. While some researchers exhibited satisfactory results when comparing the values obtained from this assumption with numerical simulations or when performing a direct comparison of fields with and without the pseudo-isotropy approximation, as in the case of Khan *et al*.(2006), other authors verified that the flows presented regions of strong anisotropy, mainly close to the impeller. Thus, the evaluation of the isotropy or anisotropy of the flow becomes relevant. This evaluation was made by several approaches in the literature, as described in Table 3.3.

Sharp and Adrian (2001) evaluated the turbulent flow structures in flow induced by a Rushton turbine. The degree of isotropy of the small-scale eddies was evaluated from different ratios of (P_I to P_V) of radial (u') and axial (v') velocity fluctuations gradients, where x and y are the radial and axial directions, respectively.

$$P_I = \frac{\overline{\left(\frac{\partial u'}{\partial x}\right)^2}}{\overline{\left(\frac{\partial v'}{\partial y}\right)^2}} \tag{3.18}$$

$$P_{II} = \frac{\overline{\left(\frac{\partial u'}{\partial y}\right)^2}}{\overline{\left(\frac{\partial v'}{\partial x}\right)^2}} \tag{3.19}$$

$$P_{III} = \frac{1}{2}\frac{\overline{\left(\frac{\partial u'}{\partial y}\right)^2}}{\overline{\left(\frac{\partial u'}{\partial x}\right)^2}} \tag{3.20}$$

$$P_{IV} = \frac{1}{2}\frac{\overline{\left(\frac{\partial v'}{\partial x}\right)^2}}{\overline{\left(\frac{\partial u'}{\partial x}\right)^2}} \tag{3.21}$$

$$P_V = -2\frac{\overline{\left(\frac{\partial u'}{\partial y}\right)\left(\frac{\partial v'}{\partial x}\right)}}{\overline{\left(\frac{\partial u'}{\partial x}\right)^2}} \quad (3.22)$$

Table 3.3: Different ways of evaluating isotropy/ anisotropy discussed in the literature.

Method for Evaluating Isotropy/ Anisotropy	**Authors**
Root-mean-square of the velocity fluctuations	Kresta (1998) and Chung *et al.* (2007).
Root-mean-square of the velocity fluctuations normalized by impeller tip velocity	Montante *et al.* (1999, 2001) , Pinho *et al.* (2000), Sharp and Adrian (2001), Bugay *et al.* (2002)., Baldi and Yianneskis (2004), Khan *et al.* (2006), Unadkat (2010), Liang *et al.* (2018) and Stelmach *et al.* (2019).
Absolute difference between the root-mean-square of the velocity fluctuations normalized by impeller tip velocity	Lee and Yianneskis (1998), Lee *et al.* (2000), Yeoh *et al.* (2004), Khan (2005), Li *et al.* (2011), Wang *et al.* (2018).
Comparison of turbulent kinetic energy estimation considering or not the pseudo-isotropic assumption	Khan (2005), Chung *et al.* (2007), Unadkat (2010), Zhang *et al.* (2017) and Liang *et al.* (2018), Laine *et al.* (2023)
Ratios of velocity fluctuations gradients	Sharp and Adrian (2001), Ducci and Yianneskis (2005), Unadkat (2010) and Delafosse *et al.* (2011).
Lumley's triangle	Derksen *et al.* (1999), Galletti *et al.* (2004), Hartmann *et al.* (2004), Escudié and Liné (2006), Lamarque *et al.* (2010), Roy *et al.* (2010), Unadkat *et al.* (2011), Bertrand *et al.* (2012) and Zamiri and Chung (2018).
Other methods	Perrard *et al.* (2000), Brunazzi *et al.* (2005) and Escudié and Liné (2006).

The gradient ratios must all equal 1 if the isotropic assumptions are fully valid for the small scales of turbulent flow. The system evaluated by Sharp and Adrian (2001) presented proportions between 0.2 and 1.8, corresponding to isotropy deviations of up to 80%. Thus, the authors suggested that isotropic turbulence relations should not be used to estimate turbulent dissipation or other statistics dominated by small scales. The ratios between the gradients of the velocity fluctuations were also applied by Ducci and Yianneskis (2005) to also evaluate the flow promoted by Rushton impeller; by Unadkat (2010) in the analysis of the flow induced by

sawtooth impeller and by Delafosse *et al*. (2011) to assess the flow promoted by an axial pumping impeller. In this last study, gradients were evaluated at the intersection of three different planes (horizontal, vertical and tangential to the impeller blades) using Classic PIV measurements. Once more, the gradients ratios indicated that the turbulence is far from isotropy in the impeller discharge region.

As described in Table 3.3, there are some studies in the literature that employed the Lumley's triangle or other methods on the investigation of the isotropic issue. These works evaluate the anisotropy of the flow, which means how far this flow is from isotropy. In general, statistical tools based on measurements of Reynolds tensors are used. The anisotropic part of the Reynolds stress tensors is (LUMLEY, 1978; POPE, 2000):

,

$$a_{ij} = \frac{\overline{u'v'}}{k} - \frac{3}{2}\delta_{ij} \tag{3.23}$$

where δ_{ij} is a unitary tensor. These tensors have three invariants A_I, A_{II} and A_{III}. By definition, $A_I = 0$. The other invariants are evaluated as (LUMLEY, 1978):

$$A_{II} = a_{ij}a_{ji} \tag{3.24}$$

$$A_{III} = a_{ij}a_{jk}a_{ki} \tag{3.25}$$

The limits of these invariants make up the so-called Lumley's triangle (Figure 3.16). The distribution of the invariants within this triangle enables the evaluation of turbulence states, and consequently, the degree of anisotropy of the flow: the closer to the vertex indicating 3D isotropy, the more isotropic the phenomenon (LUMLEY, 1978).

Derksen *et al*. (1999) performed angle-resolved three-dimensional LDA measurements of the turbulent flow induced by a Rushton impeller. From the evaluation of the distribution of the invariants in Lumley's triangle, it was verified that the turbulent structure of the flow can be associated with a strong anisotropic activity. Galletti *et al*. (2004) evaluated a larger region of a tank stirred by the same type of impeller and observed that turbulence significantly deviates from the isotropic state, not only in the region of the impeller, but also near the bottom of the tank.

Figure 3.16: Lumley's triangle, its limits and states of turbulence.

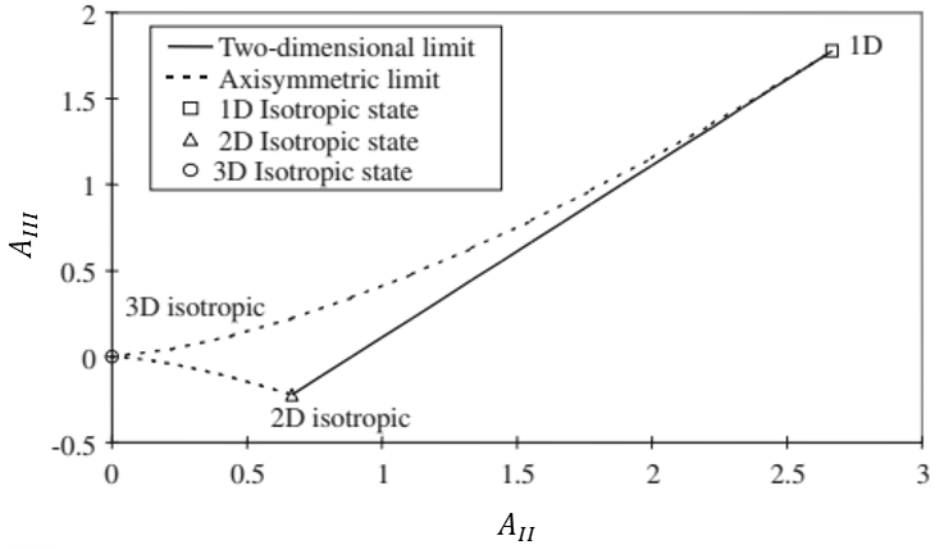

Source: Escudié and Liné (2006).

Unadkat *et al*. (2011) studied the distribution of invariants for the flow promoted by a sawtooth-type impeller considering two distinct regions: a region closer to the impeller and a more distant one. Furthermore, these regions were divided into 5 sections considering different distances from the impeller. The authors verified that, for the region close to the impeller, the turbulence is axisymmetric, and no section satisfied the condition of isotropy. The sections closer to the impeller are more anisotropic, while the more distant ones indicate a tendency towards isotropy, but without actually reaching it. On the other hand, the region farthest from the impeller presented sections that reached the three-dimensional isotropic condition, and the invariants are distributed in a region between the 3D isotropic limit and the axisymmetric limit.

Perrard *et al.* (2000) employed a different methodology to assess the anisotropy of the flow induced by a Rushton turbine. The authors compared the macro length scales of turbulence calculated from the root-mean-square of the radial, axial and out-of-plane velocity fluctuations. The results indicated that the out-of-plane macro scales are two times higher than radial and axial scales, which are, in turn, similar to each other.

A quick and easy way to estimate the degree of anisotropy in stirred tanks was the proposal presented by Brunazzi et al. (2005). The estimation of the anisotropy was made from measurements of the root-mean-square (rms) of the velocity fluctuations, using the following relationship:

$$A = \sum_{i=1}^{3} \frac{\left| u_i'^2 - \overline{u'^2} \right|}{\overline{u'^2}} \tag{3.26}$$

where $u_i'^2$ is the instantaneous root-mean-square of the velocity fluctuations and $\overline{u'^2}$ its average value. The authors compared the results obtained by this tool with those estimated by the Lumley's triangle from LDA measurements of a flow generated by the Rushton turbine with and without baffless. It was found that the flow presents considerable degrees of anisotropy near the tip of the impeller, in the region of the bottom of the tank and in the centers of the circulation loops. The flow without baffles is more anisotropic than with this accessory. The tool proposed by the authors proved to be suitable for a preliminary check of the degree of anisotropy of the flow, but presented, in general, overestimated values in relation to the results computed by the Lumley's triangle.

Moreover, Escudié and Liné (2006) investigated the anisotropy of the flow developed by a Rushton turbine not only by the Lumley's triangle method, but also by other graphical representations of turbulence such as the distribution of the eigenvalues of the anisotropy tensors and the distribution of the axisymmetric and two-dimensional invariants. The three methods were applied in three different regions of the tank: close to the impeller, in the impeller stream region and in the region external to the axis of the stream. It was verified that the turbulence is considerably anisotropic near the impeller. However, in the stream region, it was observed that the turbulence is close to three-dimensional isotropy. In addition, the region outside the stream showed turbulence close to the axisymmetric limit.

The critical analysis of the different studies that aim to evaluate the isotropy or anisotropy of the flow provide evidence that, regardless of the methodology, all the researchers verify a deviation from the concept of isotropy in several regions, especially close to the impeller. However, the pseudo-isotropic approximation is widely used in the estimation of turbulent kinetic energy, and presents, in fact, reasonable results comparable to those obtained when the three velocity components are measured. Some questions arise from this analysis: is the pseudo-isotropic approximation applicable because the degree of anisotropy of the flow in stirred tanks is not high enough to cause significant impact on the turbulent kinetic energy? Does this approach have an application limit? Would it also be applicable to more complex and highly anisotropic flows? In this work we aimed to contribute to the investigation of the validity of the pseudo-isotropic assumption on the estimation of turbulent kinetic energy, considering different impeller geometries and PIV approaches.

3.3. Particle Image Velocimetry and Its Challenges

Different measurement systems can be considered when Particle Image Velocimetry (PIV) is applied. Hinsch (1995) proposed a classification to differentiate them, which considers the number of velocity components, C, (1, 2 or 3) that can be obtained, the number of spatial dimensions of the measurement, D, (1, 2 or 3) and whether the form of recording time, $\mathrm{h_M}$, is instantaneous or continuous (0 or 1, respectively). In this work we evaluated only instantaneous records, so the value of the classification $\mathrm{h_M}$ is always 0. In relation to the other classifications, three systems are addressed: Classic PIV and Tilted PIV, in which two velocity components ($\mathrm{C} = 2$) are obtained from planes of 2 dimensions ($\mathrm{D} = 2$); and the Stereoscopic PIV, in which two cameras are used in a stereoscopic arrangement, in order to obtain 3 velocity components ($C = 3$) in planes of 2 dimensions ($\mathrm{D} = 2$). This technique is referred to in this work as Stereo-PIV.

Particle Image Velocimetry is a non-intrusive technique applied in the evaluation of fluid flow. Its operation is based on the analysis of tracer particle images, which faithfully follow the fluid movement, and is performed from the recording of light scattering caused by these particles in high-speed cameras and with high-quality lenses. Obtaining the image of the particles in two different moments allows the evaluation of the velocity vectors in the field of analysis. The technique arose from the need to study the flow of gases and liquids globally, in contrast to the point approach of other techniques (e.g., Laser Doppler Anemometry), in order to obtain fields that allow the instantaneous evaluation of the velocity. Another main advantage of this technique is the possibility of performing a non-intrusive analysis of the flow (RAFFEL *et al.*, 2018).

The vector field in two dimensions (2D) has two shortcomings. First, the loss of the out-of-plane component. Second, in-plane components are affected by a perspective error resulting from the out-of-plane displacement. This error is proportional to the magnitude of the ratio between the out-of-plane and in-plane component and the angle between the orthogonal axis and the final position of the particle (PRASAD; JENSEN, 1995). However, this technique is the most widely accepted in the literature for evaluating the flow of stirred tanks (WANG *et al.*, 2021). The systems that provide 3D measurements (three dimensions and three velocity components, known as Tomographic PIV) are more expensive, require higher noise control and are more complex than the Classic PIV system. Optical access, data storage and computational cost are other problems directly related to 3D PIV systems.

The evaluation at different angles of view allows solving the problem of not knowing the out-of-plane component. In a generic situation, there are three unknown variables. The evaluation in only one plane provides only two equations for the determination of these variables, making the system indeterminate. When two different planes are evaluated, we have a total of four equations, and thus it is possible to solve the system and define all the variables (PRASAD, 2000). This is the principle of the Stereo-PIV, in which two cameras obtain stereoscopic images using the Classic PIV system (2D) but provide the measurement of all three velocity components (3C).

In general, two stereoscopic configurations are addressed: translational (Figure 3.17a) and angular (Figure 3.17b). In the first case, the axes of both cameras are oriented parallel to be orthogonal to the plane of light. The advantages of this configuration are the simplicity of the construction of the array and the guarantee of a uniform magnification. However, the setting may limit the size of the field of view. In the second case, the camera axes have a concurrent orientation, so that they intersect in the middle of the object's plane. With this setup, the restrictions on the angle between the object and the lens, imposed by the translational array, are eliminated, but the magnification is no longer uniform, leading to stretches in opposite directions in the image field. (PRASAD, 2000; PRASAD; JENSEN, 1995).

Figure 3.17: Stereoscopic translational (a) and angular (b) configurations.

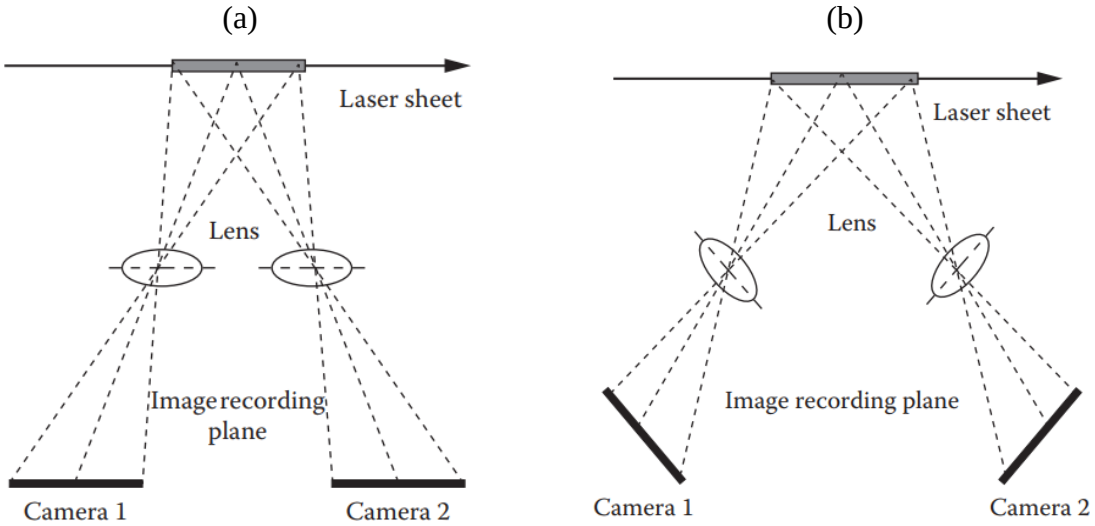

Source: Hu (2013).

An essential consideration when positioning cameras for stereoscopic measurements is to ensure the Scheimpflug condition, which requires rotating the image plane by an angle relative to the lens plane. This alignment ensures that the object, lens, and image are collinear. This condition guarantees that all particles in the object plane are in focus, but at the same time increases the magnification variation (PRASAD, 2000; SOLOFF; ADRIAN; LIU, 1997).

Yoon and Lee (2002) brought into contrast Classic PIV and Stereo-PIV measurements. The authors evaluated the flow behind a forward-swept axial-fan with five blades in a water tank, which has a predominantly axial and well-defined flow pattern. The measurements were performed by three cameras simultaneously, that is, all cameras received the activation signal at the same time. Despite differences between the study conditions of Yoon and Lee's work and our investigation, the authors presented an interesting correlation between the perspective effect and the error between Classic PIV and Stereo-PIV measurements, as they verified that the difference between the measurements is proportional to the out-of-plane velocity component. Thus, the velocity fluctuations used in our work for the estimation of the TKE can lead to different results when the two approaches are compared due to not only the contribution of the out-of-plane component, but also the perspective error in the in-plane velocity components caused by the out-of-plane movement.

Baldi and Yianneskis (2004) carried out Stereo-PIV measurements of the flow generated by a Rushton turbine. However, for the study of the energy dissipation rate distribution, the authors preferred the use of Classic PIV measurements, as this technique obtains data with higher spatial resolution, which is necessary to analyze the smaller length scales associated to energy dissipation, as described previously. In order to increase the spatial resolution of the Stereo-PIV system, changes in the experimental arrangement would be necessary, which made the procedure unfeasible due to the introduction of uncertainties.

Moreover, Khan *et al.* (2006) employed the Stereo-PIV technique to obtain the flow fields and turbulent parameters of a tank stirred by a 4-bladed 45º pitched blade turbine. The authors compared Stereo-PIV measurements of the radial and axial components with Classic PIV measurements obtained by Khan *et al.* (2004). They also confronted Stereo-PIV measurements of the out-of-plane component with values measured by Laser Doppler Anemometry (LDA). The components showed good agreement between the different measurement techniques in both cases. Shekhar *et al.* (2012) also found good agreement when compared Stereo-PIV and Classic PIV measurements of a flow promoted by a water-flow mixer (HR-100).

Järhling *et al*. (2017) compared Classic and Stereo-PIV measurements of a flow promoted by Rushton turbine and by PBT with 4 blades. They employed a helical coil to also evaluate the heat exchange. The results showed that the Stereo-PIV data is harder to obtain than the Classic PIV measurements, because of stronger reflections on the non-orthogonal view on the light sheet (Figure 3.18). They also verified that the 3C reconstruction lead the processing more complex; however, the acquisition of the out-of-plane motion promote a more precise evaluation of the velocity field inside the vessel.

Figure 3.18 Comparison of (a) Classic PIV measurements, (b) CFD simulation and (c) Stereo-PIV data of the flow induced by PBT. The white areas represent zones with high reflections.

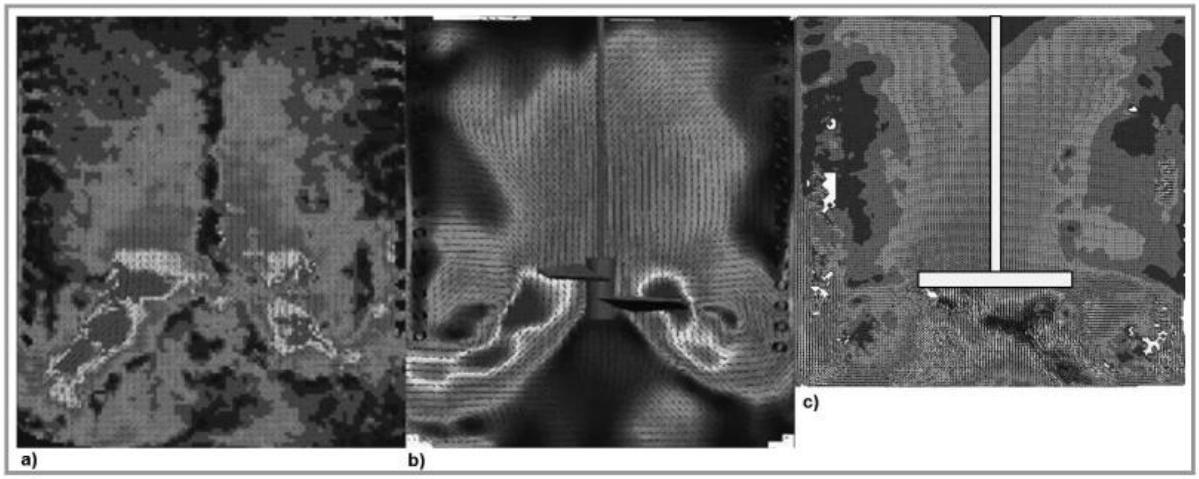

Source: Järhling *et al*. (2017).

Lee *et al.* (2022) developed a method for estimating and correcting the perspective error due to the presence of the out-of-plane component in 2D measurements. The equation was derived from geometric relationships between the position in the physical domain and the position measured by the sensor. The authors demonstrated that the effect of the perspective error on velocity is inversely proportional to the distance from the lens to the camera sensor and proportional to the displacement in the out-of-plane direction and the relative position of the sensor center. The correction model was evaluated using synthetic fields of a homogeneous isotropic turbulence with different levels of perspective error. In addition, the model was also applied to estimate TKE fields from Classic PIV measurements performed in a wind tunnel. In both cases, the model showed significant reductions in perspective error and was considered suitable for this application.

Spatial resolution and seeding density are other aspects that need to be taken into account when discussing different techniques for measuring turbulent parameters in stirred

tanks. Spatial resolution can be defined by the concentration of particles within the measurement field. A Classic PIV or Stereo-PIV system can accommodate a high concentration of tracers in the interrogation window without the noise caused by particle image overlap and opacity, as often observed in the interrogation box of a 3D PIV system. (ELSINGA, 2008; RAFFEL *et al*., 2018; SCHARNOWSKI; KÄHLER, 2020). Thus, the 2D system supports measurements with higher spatial resolution compared to the 3D system, ensuring higher quality and accuracy in data. Examples of this difference in particle detection can be observed when PTV (Particle Tracking Velocimetry) systems are considered. Raffel *et al.* (2018) reports that a 2D system with a particle concentration of 0.06 ppp (particle per pixel) detected more than 95% of tracers correctly. For 3D systems the correct reconstruction reached only 75% considering a maximum possible concentration of 0.05 ppp. Under controlled conditions, it is still possible to obtain 3D measurements by Tomographic PIV with 0.2 ppp and 2D measurements by Classic PIV with 0.5 ppp (ADRIAN; WESTERWEEL, 2011; RAFFEL *et al*., 2018).

3.3.1. Image Distortion

Particle Image Velocimetry (PIV) has been used as a powerful tool in the investigation of turbulent flow in stirred tanks. The accurate imaging of these particles, ensuring the good performance of the technique, is directly related to the rigorous mapping of the region of interest, that is, the precise relationship of the physical space with the image plane (SOLOFF; ADRIAN; LIU, 1997).

However, inaccuracies in this mapping can happen when stirred tanks are evaluated. Distortions in PIV images are caused by factors such as the curvature of the tank and the significant difference between the refractive indices of the tank material and the working fluid. These distortions affect the scattering of light by the particles and therefore their recording in the images. In addition, they can lead to variation of the magnification factor (ratio between the distance of the image and the object in relation to the camera lens) as function of the position in the image field (SOLOFF; ADRIAN; LIU, 1997) which invalidates the hypothesis of this value being constant in a PIV evaluation (RAFFEL *et al*., 2018)

Different distortion compensation strategies are addressed in attempt to minimize its effects and to rise the accurate level of PIV measurements. These strategies can be divided into two groups: the first is related to changes in the physical aspect of the experimental apparatus and the second refers to changes in the characterization of the image plane.

Prasad (1995) was the first to suggest a strategy associated with physical space by simulating between the object and the lens a prism filled with liquid, in order to potentially reduce radial distortion by an order of magnitude. In studies in stirred tanks, an approximate technique is applied in an attempt to correct the distortions caused by the curvature of the tank. Transparent structures filled with the working fluid are built around the tank in the square shape (ALONZO-GARCIA *et al*., 2019; CHUNG; SIMMONS; BARIGOU, 2009; GABRIELE *et al*., 2011; LI; BAO; GAO, 2011; MICHELETTI *et al*., 2004) rectangular (CHUNG; BARIGOU; SIMMONS, 2007; CHUNG; SIMMONS; BARIGOU, 2009; FANG; LING; SANG, 2011; SHARP; ADRIAN, 2001; STELMACH *et al*., 2019) pentagonal (KHAN; RIELLY; BROWN, 2006; UNADKAT; RIELLY; NAGY, 2011) or with a combination of a rectangular box and prism (LI *et al*., 2013). This strategy, however, has as main problems the complexity of construction, which makes its application often unfeasible, in addition to the high cost of installation and use, especially if the fluid applied is not water.

Another strategy of compensating for distortion through physical changes is the use of two cameras in a stereoscopic configuration (Stereo-PIV). The arrangement of cameras allows the plane of the object to be recorded in two different directions, providing enough information to reduce the perspective errors of the components in plane (PRASAD; JENSEN, 1995). Although this condition ensures the adequate focus of the equipment, its configuration can lead to non-uniform magnification of the image plane (PRASAD, 2000), in addition to require the use of two cameras, making the application of the technique more expensive.

In the strategies associated with the characterization of the image plane, an experimental calibration of the camera is done by recording a uniform pattern of points. The comparison between the physical pattern and the recorded image generates a mapping function, which corrects the magnification factor variation and, consequently, compensates for the image deformations (RAFFEL *et al*., 2018). Soloff *et al*. (1997) developed this strategy in order to allow the recombination of stereoscopic images to construct three-dimensional velocity fields. Some authors have applied the strategy in studies of stirred tanks (ALBERINI *et al*., 2017; KHAN; RIELLY; BROWN, 2006; KILANDER; RASMUSON, 2005) mainly to ensure the evaluation of turbulent parameters without measure the out-of-plane velocity component, assuming the pseudo-isotropic approximation. One of the problems of this approach is to ensure that the position of the calibration plate is exactly the same position as the light sheet (WIENEKE, 2005).

The image distortion can be reduced or minimized to some extent by optimizing experimental parameters, but it is quite challenging, especially in situations where the PIV are

employed in the evaluation of a pilot facility like the stirred tank of our work. The PIV arrangement depends on different characteristics, such as the space available for its assembly, the type of equipment and the fluid dynamics inherent to the type of flow under analysis. Moreover, for the turbulent kinetic energy estimation, higher spatial resolution is required in order to obtain accurate values (SAARENRINNE; PIIRTO; ELORANTA, 2001), which demand high noise control.

In order to obtain accurate velocity fields, we need a high valid detection probability (VDP) of the PIV correlation, which indicates the probability of the highest correlation peak really corresponds to the true displacement of the particle images (SCHARNOWSKI; SCIACCHITANO; KAHLER, 2019). At first, Keane and Adrian (1992) had showed that a high VDP is related to an effective number of particle images (N_E). This parameter, in turn, depends on the number of particles within the interrogation window (N_i) and the loss-of-correlation due to in-plane motion (F_I) and out-of-plane motion (F_O). Then, Scharnowski and Kähler (2016) discussed that N_E also depends on the loss-of-correlation due to displacement gradients (F_Δ) and image noise (F_σ). They recommended the following relation to evaluate the effective number of particle images (Equation (3.27):

$$N_E = N_i F_I F_O F_\Delta F_\sigma > 7 \tag{3.27}$$

All these parameters must be considered when applying PIV technique for evaluation of the flow, especially when we assess a region in which the displacement is high heterogeneous, for instance, in the region close to the impeller in a stirred tank. The differences of the motion in different zones of the field of view also change the value of these parameters, making them unfeasible to be measured and controlled. However, based on the study of Scharnowski, Sciacchitano and Kähler (2019), it is possible reduced the effects of the loss-of-correlation parameters by increasing the particle density and choosing an optimum interframe time and light sheet thickness. Moreover, the processing procedure can be designed to control and reduce the interrogation window, particle image size and image noise level in order to minimize the post-processing stage, which can lead to smoothing and artificial fields.

Based on this, we were concerned in obtaining high quality PIV measurements and few works were found in literature that deal with this worry when applying the technique in study cases. Thus, we aimed to contribute to this discussion by applying some of the strategies described in this section on the assessment of the flow in stirred tanks. Firstly, we employed

the Classic PIV and Stereo-PIV approaches to verify if the addition of a camera can improve the measurements. We calibrated the set of cameras using a methodology based on the work of Soloff *et al.* (1997). On data acquisition, we controlled the particle density and the interframe time. Finally, on processing, we applied some filters to reduce the image noise level and employed a multi-pass strategy of improve the spatial resolution of the measurements. More details on each feature can be found in Section 4.

3.4. Concluding Remarks

Based on the information set out in the Literature Review's section, we can highlight some relevant points for the development of this thesis:

- The out-of-plane component, although neglected when methods such as the Classic PIV are applied, plays an important role in the dynamics of circulation and tank mixing.
- The study of turbulence can be restricted to the characterization of irregular fluctuations in instantaneous velocity, generated by the shear promoted by the movement of fluid elements.
- The spatial resolution of the PIV measurements must assure the measurement of turbulent structures at different scales, from the integral scales to the Kolmogorov ones.
- Most articles in literature assessed the turbulent kinetic energy (TKE) of the flow promoted by PBT and Rushton turbine, due to their industrial importance.
- The regions of higher energy are intrinsically associated with regions of greater flow, where large-scale structures are formed.
- Few studies in the literature used the Stereo-PIV technique and were concerned with evaluating the effect of the out-of-plane component of TKE measurements.
- Works in the literature differ between the validity of the pseudo-isotropic approximation for the estimation of the turbulent kinetic energy.
- Some strategies on the assessment of the flow in stirred tanks by PIV measurements can be employed to ensure high quality.

4. EXPERIMENTAL

4.1. Stirred Tank

The experiments were carried out in a pilot scale stirred system with a commercial set of cameras and laser (Dantec Dynamics) for application of different PIV approaches measured simultaneously (Figure 4.1a). The system comprised a cylindrical acrylic tank with a standard ASME 10% torispherical base and four equally spaced metal baffles (Figure 4.1b). Four types of impellers were employed: two Rushton turbines with diameters $D_T = T/3$ (RU01) and $D_T = 2T/5$ (RU02), and two 45º pitched blade turbines with 4 blades with diameters $D_T = T/3$ (PBT01) and $D_T = 2T/5$ (PBT02). These impellers were chosen because they are widely employed in the most diverse industrial processes. Besides, the Rushton turbine promotes a predominantly radial flow, while the pitched blade turbine induces a predominantly axial flow, thus we were able not only to investigate different flow patterns but also to assess the effect of the impeller diameter on the fluid dynamics. The pilot unit is set up on the Laboratory of Multiphase Flow Characterization (LACEM) of the Chemical Engineering School (FEQ) of the Universidade Estadual de Campinas (UNICAMP).

The dimensions of each part of the system and the impellers are shown in Table 4.1. The working fluid was water (density $\rho = 998.2\ \mathrm{kg/m^3}$, and dynamic viscosity $\mu = 1.003 \times 10^{-3}\ \mathrm{Pa.s}$). The performance characteristics of the impellers are presented in Table 4.2. Different rotational speeds were adopted for the impellers with Reynolds numbers between 9.24×10^4 and 1.85×10^5, thus ensuring that the system operated in a turbulent regime ($\mathrm{Re} > 2 \times 10^4$). The Reynolds number was computed as:

$$Re = \frac{\rho N_T D_T^2}{\mu} \tag{4.1}$$

The power input (P) was obtained by torque transducer measurement (MAGTROL system). More details of the process of collecting power data and the curves of the power number (N_P) versus Reynolds number can be found in other works of the research group (AYALA, 2022; BARBUTTI, 2021; FREITAS, 2020; SILVA, 2020). The power number (N_P) was determined by Equation (4.2:

$$N_P = \frac{P}{\rho N_T^3 D_T^5} \tag{4.2}$$

The impeller tip velocity (U_{tip}) was computed according to the Equation (4.5:

$$U_{tip} = \pi D_T N_T \tag{4.3}$$

The scale of agitation (N_A) is defined by the ratio between the power consumed and the volume of fluid (in our case, $V_l = 0.043\ m^3$), as described in Equation (4.6:

$$N_A = \frac{P}{V_l} \tag{4.4}$$

The results described in Table 4.2 for the scale of agitation were classified according to the scale proposed by Cremasco (2012). The reported values of 1.48 and 1.13 for RU01 and RU02, respectively, correspond to an intense agitation. For the PBT impellers, the result was 2.13 for PBT01, revealing a very strong agitation, and 1.90 for PBT02, which can be classify as an intense agitation.

Figure 4.1: Pilot-scale system at LACEM/FEQ/UNICAMP: (a) experimental setup, (b) stirred tank apparatus, (c) vertical and (d) lateral view of the camera positions relative to the light sheet. Legend: 1. Motor, 2. Torquemeter, 3. Stirred tank, 4. Camera 1 (at σ = 45º from the light sheet), 5. Camera 2 (at σ + β = 80º from the light sheet), 6. Light sheet, 7. Laser, 8. Baffles, 9. Shaft, 10. Impeller.

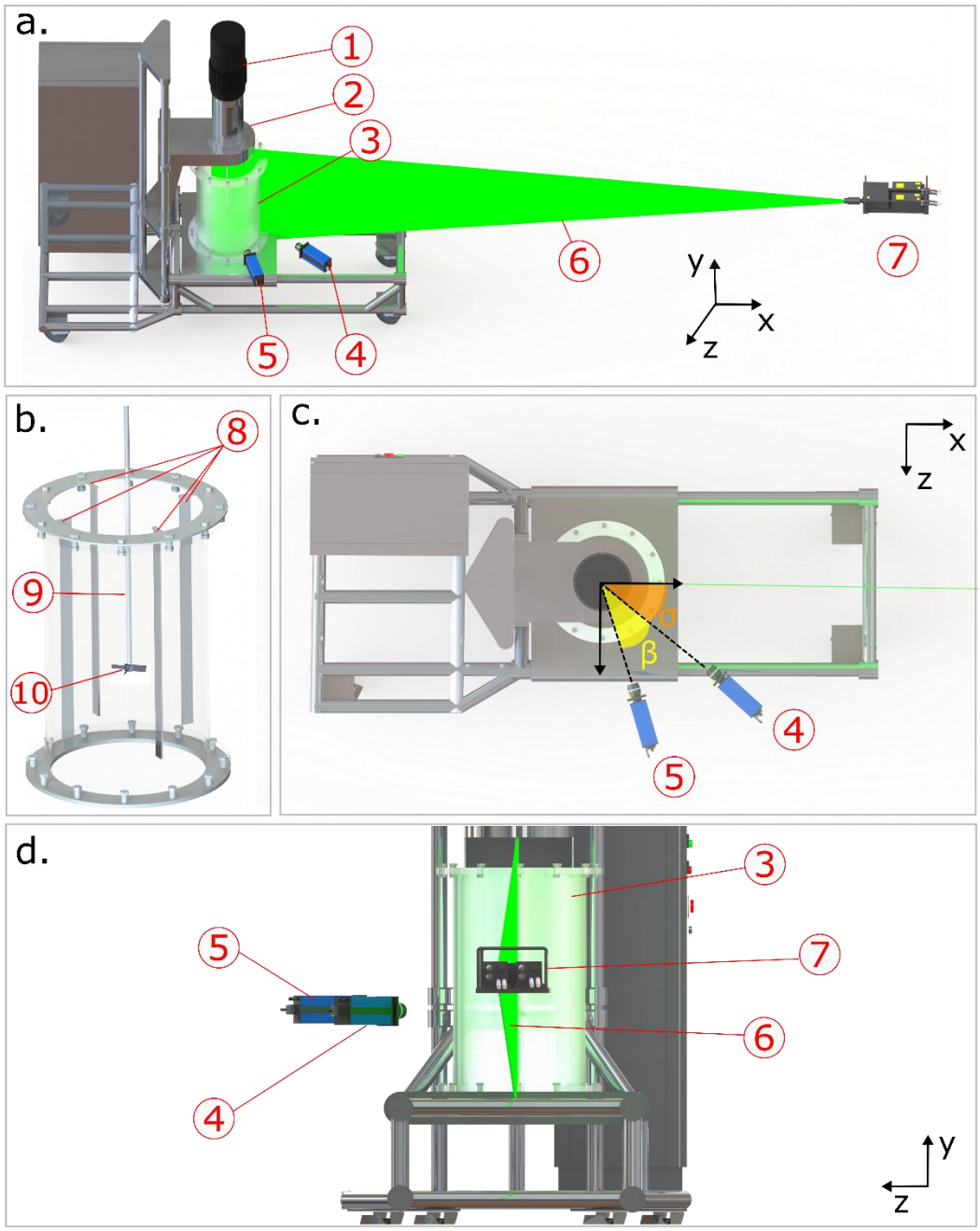

Table 4.1: Geometric configuration of the stirred system.

Property	Notation	RU01	RU02	PBT01	PBT02
Tank diameter (m)	T	0.38 m			
Liquid height (m)	H	T			
Number of baffles	n_B	4			
Baffle width (m)	B	T/10			
Angle between baffles	γ_B	90º			
Clearance	C_T	T/3			
Impeller diameter (m)	D_T	T/3	2T/5	T/3	2T/5
Number of blades	n_P	6	6	4	4
Angle of the blades	α_P	-	-	45º	45º

Table 4.2: Performance parameters of the impellers.

Property	Notation	RU01	RU02	PBT01	PBT02
Rotational speed (rpm)	N_T	360	240	660	480
Power (W)	P	47.75	36.48	68.48	61.03
Impeller tip velocity (m/s)	U_{tip}	2.36	1.91	4.33	3.82
Reynolds number	Re	9.44×10^4	9.24×10^4	1.73×10^5	1.85×10^5
Power number	N_P	7.14	7.04	1.66	1.47
Scale of agitation (HP/m³)	N_A	1.48	1.13	2.13	1.90
Agitation level		Intense	Intense	Very strong	Intense

4.2. Measurement System

The PIV system comprised a Nd:YAG laser (532 nm, 200 mJ, Dantec Dynamics), which provided a 2 mm thick light sheet, and two FlowSense EO 8M-21 cameras (3312 x 2488 pixels, Dantec Dynamics). The cameras were arranged according to Figure 4.1c, with camera 1 being positioned at $\sigma = 45º$ and camera 2 at $\sigma + \beta = 80º$ from the light sheet. The images recorded by camera 1 and camera 2 were used for Tilted PIV and Classic PIV measurements, respectively. Besides, the images obtained by both cameras were employed for Stereo-PIV data processing. It is important to notice that both cameras are in the same plane x-z, in other words, they were positioned in the same height of the impeller position (Figure 4.1d).

Despite the unusual configuration, the principle of Scheimpflug was respected; that is, the collinearity among the planes of the object, lens and image was ensured to guarantee the focus on the object plane (PRASAD, 2000). This configuration was chosen in order to minimize the distortion caused by the curvature of the tank and to avoid the interference of the baffle in the field of view. Silver-coated glass spheres ($d_p = 10\ \mu m$) were used as tracer particles (Dantec Dynamics), with a density of 1100 kg/m³, close to the density of the fluid, to ensure that the movement of the particles faithfully follows the flow induced by the impeller (RAFFEL *et al*., 2018). The impeller blades were painted black to minimize the reflection of laser light.

Different blade angles were evaluated by angle-resolved measurements (AR) to assess the orientation of the blade and to distinguish turbulent fluctuations from the periodic flow (ESCUDIÉ; LINÉ, 2003; GABRIELE; NIENOW; SIMMONS, 2009; GUIDA; NIENOW; BARIGOU, 2010). Images were recorded from the impeller position halfway between baffles at the angles of 0º, 15º, 30º, 45º for the Rushton turbines and at the angles of 0º, 22.5º, 45º and 67.5º for the two PBT. The light sheet was displaced 0.5º in relation to the blade angle of 0° to avoid the baffle reflection. The angle-resolved measurements were performed by a torque sensor (Magtrol), microcontroller (Arduino) and a synchronizer (Dantec Dynamics). The microcontroller received the rotational speed signal of the torque sensor, calculated the revolution time of the impeller to obtain images on the frequency of one pulse per revolution and sent this signal to the synchronizer of the measurement system. This device adjusted the laser and camera activation. More details of the synchronization can be found in the work of Ayala (2022).

4.3. Tilted PIV: a Novel Approach

Before assessing the results of the PIV measurements, it is important to understand the consequences of the tilted view on the acquired images. Figure 4.2 presents a schematic diagram of how the cameras can record the displacement of tracer particles in the out-of-plane direction. Camera 1 is able to register the combined displacement of the tracer particle in the in-plane (dx) and out-of-plane direction (dz) in the light sheet. Camera 2, in turn, records a lower out-of-plane displacement when compared to the camera 1, because its position is almost 90º from the light sheet. This displacement is known as the perspective error in Classic PIV measurements (ADRIAN; WESTERWEEL, 2011; RAFFEL *et al*., 2018).

Figure 4.2: Schematic representation of the out-of-plane motion of the tracer particle recorded by camera 1 (Tilted PIV) and camera 2 (Classic PIV). The combined in-plane and out-of-plane displacement is recorded in camera 1 (dx_1). On the other hand, the out-of-plane displacement is minimally recorded in camera 2 (dx_2).

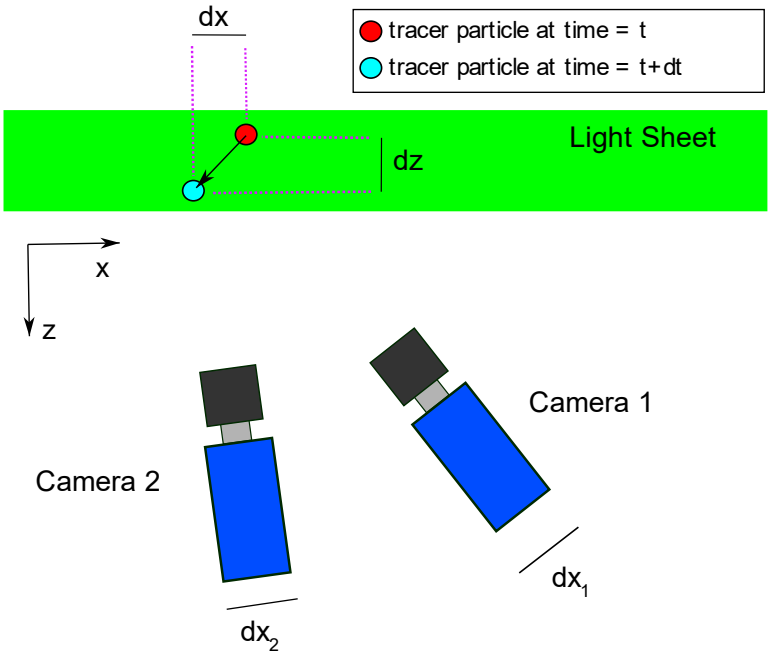

More details about the field of view of each camera can be observed in Figure 4.3-6, which show examples of the raw images obtained from the cameras at the blade angles considered in this work for the flows generated by RU01, RU02, PBT01 and PBT02, respectively. It is noteworthy that the positioning of the impeller blades varied slightly between camera 1 and camera 2. Because of this, different impeller drawings were added to the figures presented in this work, trying to follow the image observed by each camera as best as possible. In the case of the fields obtained by Stereo-PIV, we chose to use the impeller drawings of the two views in superposition, to improve the presentation of the results.

Figure 4.3: Raw images of camera 1 and camera 2 at different blade angles of RU01. Highlighted in pink: noisy zone.

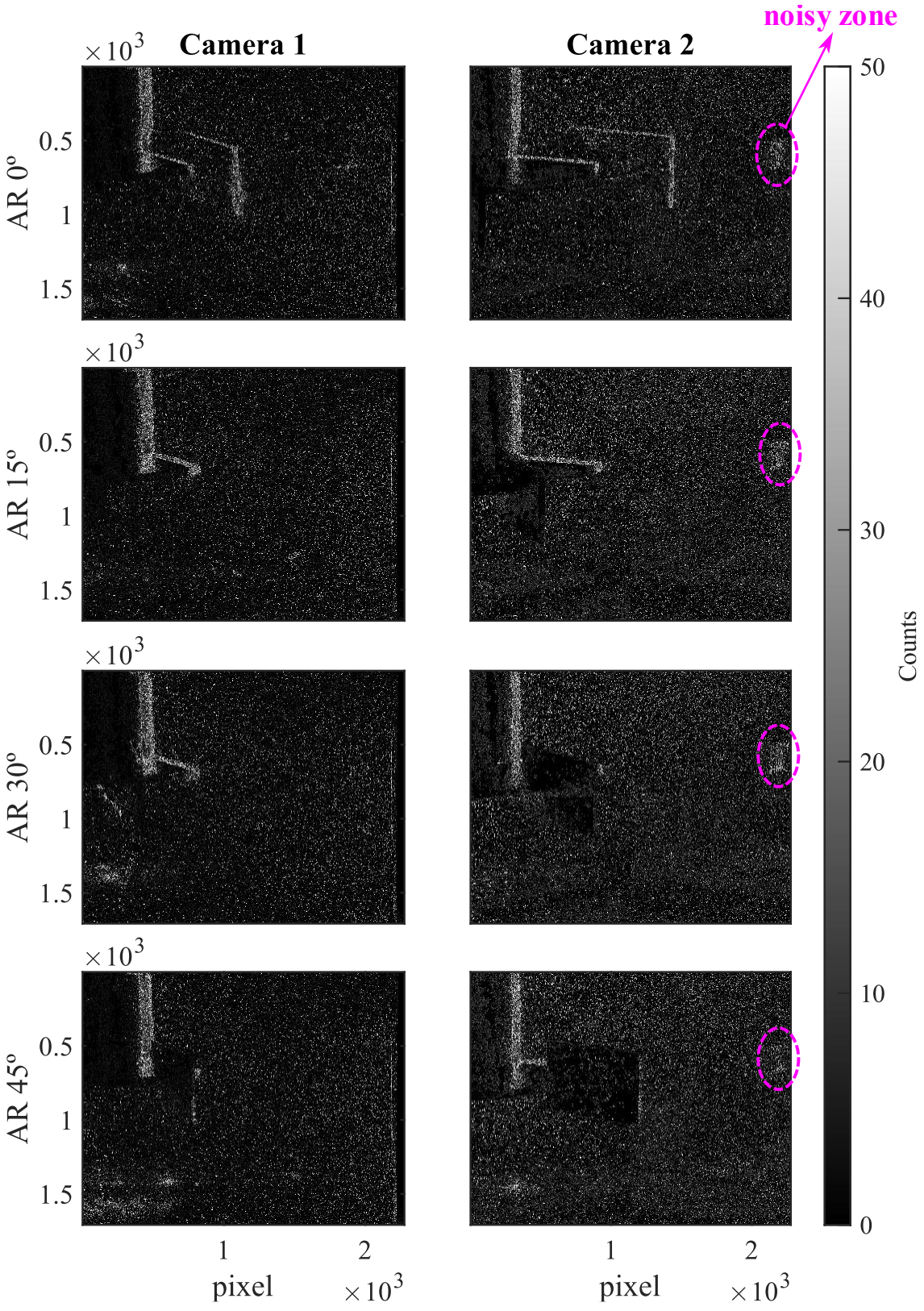

Figure 4.4: Raw images of camera 1 and camera 2 at different blade angles of RU02. Highlighted in pink: noisy zone.

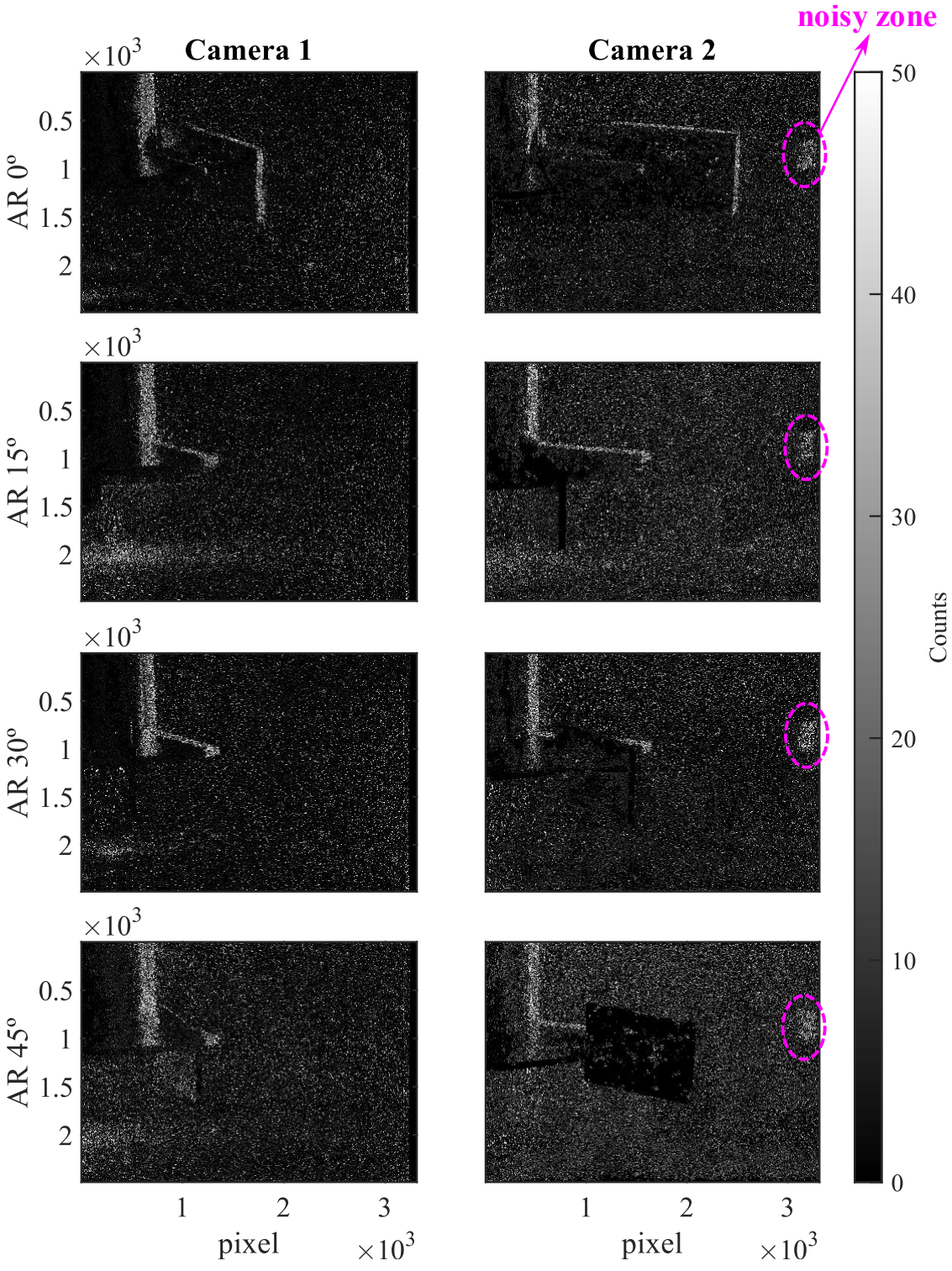

Figure 4.5: Raw images of camera 1 and camera 2 at different blade angles of PBT01.

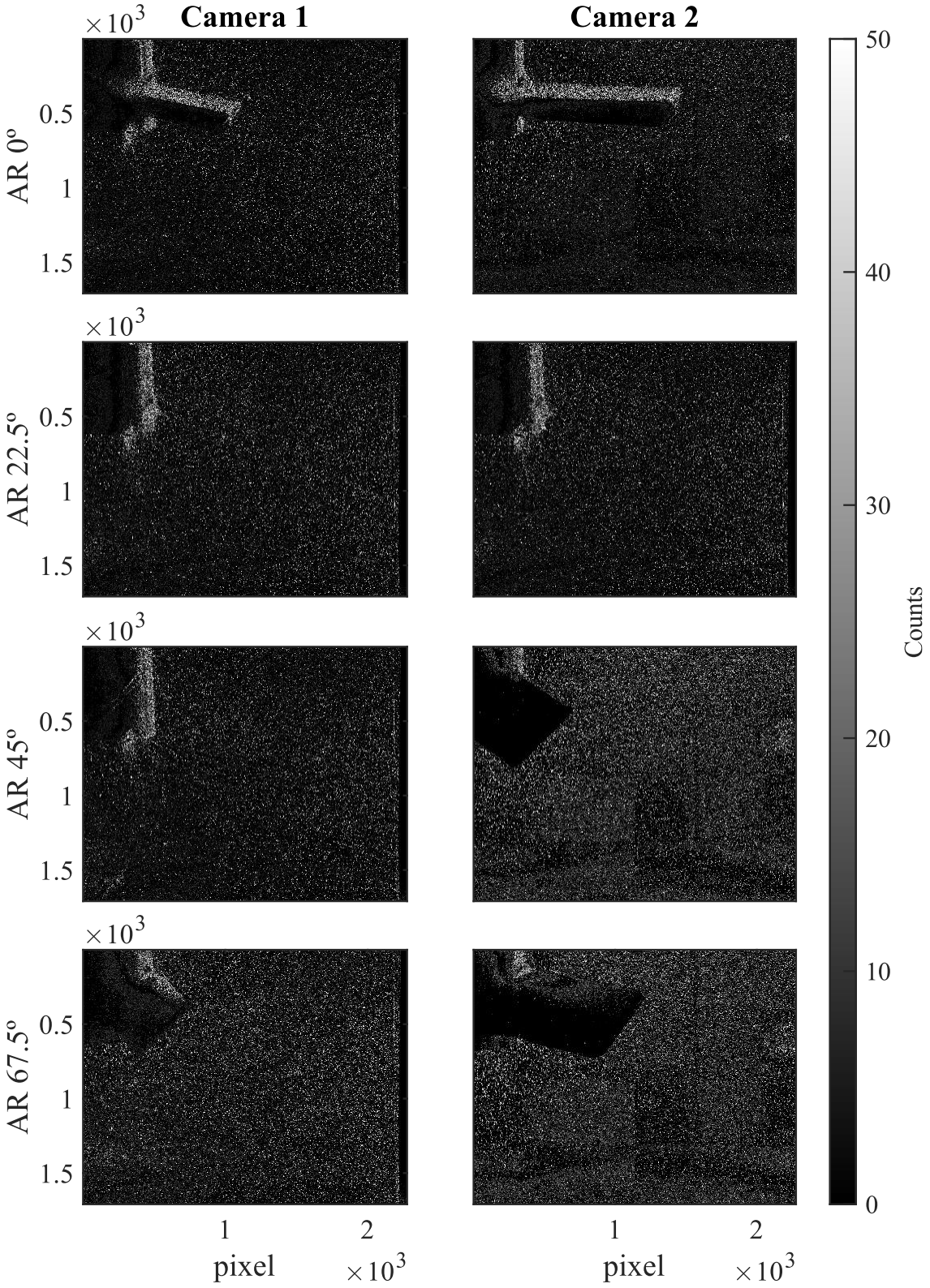

Figure 4.6: Raw images of camera 1 and camera 2 at different blade angles of PBT02. Highlighted in pink: noisy zone.

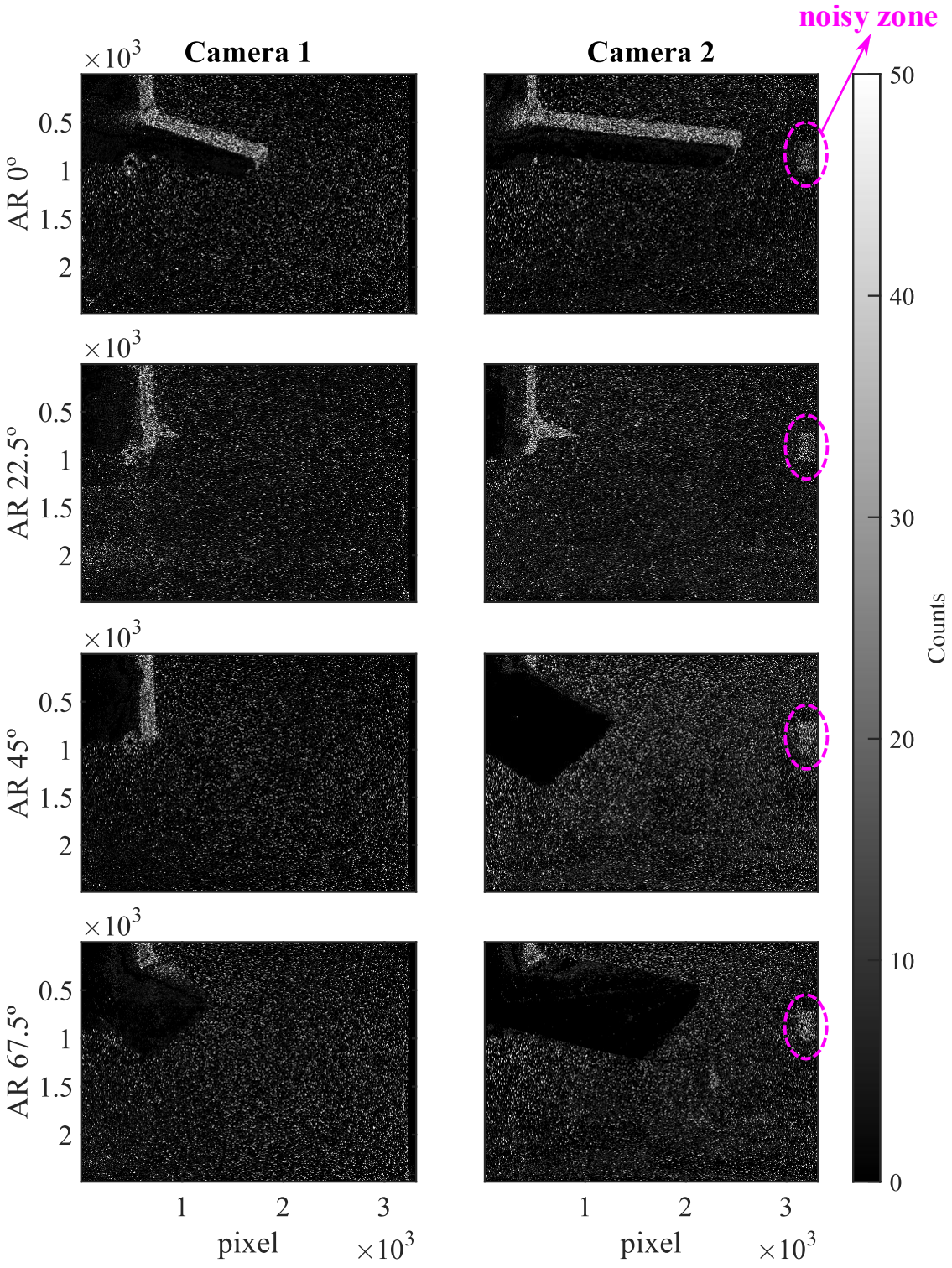

4.4. Calibration of the Cameras and Data Acquisition

A very important step before the acquisition of the images is to perform the calibration of the cameras in order to determine the accuracy of the velocity vectors, define the magnification in each of the directions of analysis (UNADKAT; RIELLY; NAGY, 2011) and compensate optical distortions due to focusing and alignment problems, lens imperfections and refractions caused by different parts of the equipment other than particles (SOLOFF; ADRIAN; LIU, 1997). Especially in the analysis of the flow in a stirred tank, the calibration is essential to compensate the curvature of the tank wall. The size of the facility (50 L) made unfeasible the use of transparent structures full of the working fluid to compensate de wall curvature distortion and avoid optical deviations, as employed by other authors (CHUNG; BARIGOU; SIMMONS, 2007; ESCUDIÉ; LINÉ, 2003; KHAN; RIELLY; BROWN, 2006).

The procedure was based on the work of Soloff *et al*. (1997). The calibration target was an ABS (Acrylonitrile Butadiene Styrene) polymer plate of dimensions 210 x 750 mm containing equally spaced points of 0.5 mm diameter with a distance between centers of 1.5 mm. The cameras recorded the target images in the positions to focus on the light sheet, as described by Figure 4.1c. For the Classic and Tilted PIV measurements, each camera was calibrated individually, while for the Stereo-PIV the images of both cameras were taken into consideration.

The Davis 8.0 software (LaVision) was employed to compute the mapping function corresponding to the variation of the plane magnification. The mapping function is the relationship between the physical coordinates (X′, Y′) and the image coordinates (x, y). The function is obtained by fitting the points identified on the plate to a third-order polynomial (Equation (4.5). This model was considered to be more suitable for situations with high error of global or local perspective (WIENEKE, 2005).

$$\begin{pmatrix} x \\ y \end{pmatrix} = \begin{bmatrix} X' + \partial X(X', Y') \\ Y' + \partial Y(X', Y') \end{bmatrix} \tag{4.5}$$

where ∂X’ and ∂Y’ are defined by Equation (4.6:

$$\begin{pmatrix} \partial X' \\ \partial Y' \end{pmatrix} = \begin{bmatrix} a_0 + a_1 s + a_2 s^2 + a_3 s^3 + a_4 t + a_5 t^2 + a_6 t^3 + a_7 st + a_8 s^2 + a_9 s^2 \\ b_0 + b_1 s + b_2 s^2 + b_3 s^3 + b_4 t + b_5 t^2 + b_6 t^3 + b_7 st + b_8 s^2 + b_9 s^2 \end{bmatrix} \tag{4.6}$$

The displacements ∂X´e ∂Y' are determined by normalized coordinates s_C (Equation (4.7) and t_C (Equation (4.8):

$$s_C = 2 \cdot (X'_0 - X'/\Delta_x) \tag{4.7}$$

$$t_C = 2 \cdot \left(Y'_0 - Y'/\Delta_y\right) \tag{4.8}$$

where Δ_x and Δ_y are the image's size in pixel, X'_0 and Y'_0 are the reference points identified in the target image. Thus, the determination of the mapping function is done by recognizing the points on the calibration target (values of X´ and Y´) and estimating the a_i and b_i coefficients of the Equation (4.6 by the method of least squares. More details about the calibration procedure can be consulted in the work of Barbutti *et al*. (2020). For the Classic and Tilted PIV, the calibration error was 1.24 pixels for the camera 1 and less than 1 pixel for the camera 2.

For the Stereo-PIV measurements, an additional correction was made considering the self-calibration method developed by Wieneke (2005). In this method, the mapping function obtained through the images of the target and 1000 pairs of images of the flow were employed in order to correct possible misalignments between the target and the light sheet, besides the distortions uncorrected by the Soloff's method. Thus, the calibration error of the Stereo-PIV measurements was less than 0.1 pixel.

On the data acquisition procedure, images of the turbulent flow were obtained by both cameras simultaneously in double-frame mode and at a frequency of 5 Hz. For each blade angle mentioned above, to ensure the statistical convergence of the results, 1000 pairs of images were recorded with time between frames of 100 μs. This time was chosen considering an average particle displacement between 4 and 6 pixels, according to Adrian (1986), in addition to a preliminary analysis of the signal-to-noise ratio (SNR) distribution. It is important to notice that the choose of the time between frames were made for each impeller individually, as the experiments were carried out independently. The fact of the time between frames is the same for all impellers is a coincidence.

4.5. Image Processing

The same image preprocessing was applied in all datasets to remove recording noise before PIV processing. Initially, the Gaussian filter (3×3 pixels, standard deviation of 0.3) was applied to optimize the shape of particle images; then the local minimum subtraction filter (7×7 pixels) was used to eliminate background noise and an intensity cover filter was employed to homogenize the intensity distribution. Subsequently, the local average subtraction filter was applied three times (11×11 pixels) followed by the Gaussian filter with a greater standard deviation (0.6). In order to remove the reflection of light on baffles and blades the Otsu–Gauss–Wiener (OGW) method was employed (AMARAL *et al*., 2022). The mask was created from the raw images and applied after the other preprocessing steps mentioned previously. After the preprocessing, the images were reconstructed (dewarping approach) by using the mapping function of each camera obtained in the calibration and a cubic interpolation.

In the image processing, the standard cross-correlation (SCC) was applied with an iterative multigrid strategy of image deformation based on decreasing interrogation windows at each pass (KIM; SUNG, 2006; SCARANO, 2002). In this strategy, the processing is done in four passes, as described in Table 4.3. The final analysis area was 18×18 pixels (0.52×0.52 mm). After each pass, simple post-processing was carried out to eliminate outliers based on the approach developed by Westerweel and Scarano (2005). In addition, complete post-processing was also applied based on the mutual information thresholding (BARBUTTI *et al*., 2021).

Table 4.3: Interrogation window and overlap of each pass on the iterative multigrid strategy applied in PIV processing.

Pass	Initial Interrogation Window (pixels)	Overlap	Final Interrogation Window (pixels)
1	64 x 64	25%	48 x 48
2	48 x 48		36 x 36
3	32 x 32		24 x 24
4	24 x 24		18 x 18

4.6. Turbulent Kinetic Energy Estimation

The turbulent kinetic energy (k_{3C}) for Stereo-PIV measurements was estimated from Equation (4.9 (KHAN; RIELLY; BROWN, 2006; UNADKAT; RIELLY; NAGY, 2011):

$$k_{3C} = \frac{1}{2}\left(\overline{u'^2} + \overline{v'^2} + \overline{w'^2}\right) \tag{4.9}$$

where $\overline{u'^2}$, $\overline{v'^2}$ and $\overline{w'^2}$ are the root-mean-square (rms) of the velocity fluctuations for the radial, axial and out-of-plane components, respectively.

For Classic PIV measurements, in which the out-of-plane velocity component is unknown, we take into account the pseudo-isotropic approximation, where it is assumed that the rms of the out-of-plane velocity fluctuations is the arithmetic mean of rms of the radial and axial velocity fluctuations. Then, the turbulent kinetic energy can be calculated according to Equation (4.10:

$$k_{iso} = \frac{3}{4}\left(\overline{u'^2} + \overline{v'^2}\right) \tag{4.10}$$

For the Tilted PIV measurements, because of the tilted acquisition, we assume that the rms of the radial velocity fluctuations is a combination of the radial and the out-of-plane contributions, called in this work as rms of the combined-radial velocity fluctuations ($\overline{u_c'^2}$). Hence, the turbulent kinetic energy was computed considering the pseudo-isotropic approximation (Equation (4.11):

$$k_{iso_{tPIV}} = \frac{3}{4}\left(\overline{u_c'^2} + \overline{v'^2}\right) \tag{4.11}$$

We also estimate the TKE directly from the 2D field obtained by the cameras, without the pseudo-isotropic approximation, considering the rms of the axial and combined-radial velocity fluctuations, as described by Equation (4.12:

$$k_{2C} = \frac{1}{2}\left(\overline{u_c'^2} + \overline{v'^2}\right) \tag{4.12}$$

In this work, the performance of the TKE estimation from the considerations made above ($k_{iso_{tPIV}}$ and k_{2C}) were evaluated by the comparison with the results calculated from Stereo-PIV data, using all three velocity components (k_{3C}), and the results obtained from Classic PIV measurements, considering the pseudo-isotropic approximation (k_{iso}).

4.7. Quality of PIV Measurements

As the arrangement of the cameras used in this procedure has an unusual configuration, analyzes of the quality of the Classic PIV, Tilted PIV and Stereo-PIV measurements were performed by evaluating the signal-to-noise ratio (SNR), the 3C reconstruction error and the uncertainty quantification. In this section we describe the computation of all these quality parameters.

4.7.1. Signal-to-noise Ratio

The first parameter was calculated from the ratio between the highest correlation peak (C_{max}) to the second tallest peak (C_2), as described in Equation (4.13 (HAIN; KÄHLER, 2007; ROY; ACHARYA; CLOETER, 2010):

$$SNR = \frac{C_{max}}{C_2} \tag{4.13}$$

4.7.2. 3C Reconstruction Error

The 3C reconstruction error was computed by considering two parameters. First, the projection of the reconstructed velocity component, calculated for camera 1 (u_{p1}) and camera 2 (u_{p2}). Second, the velocity component obtained for each camera individually (u_1 and u_2). The deviation between these parameters leads to the 3C reconstruction error, as described by the Equation (4.14 (CALLUAUD; DAVID, 2004):

$$Error_{3C} = \sqrt{\left(u_1 - u_{p1}\right)^2 + \left(u_2 - u_{p2}\right)^2} \tag{4.14}$$

4.7.3. Kolmogorov Scales

The accuracy of the turbulent kinetic energy values can be evaluated by the relation among geometric characteristics of the experiments and the Kolmogorov and integral scales. As described in Section 3.2.1, the Kolmogorov length scale is defined as (POPE, 2000):

$$K_\eta = \left(\frac{\nu^3}{\bar{\varepsilon}}\right)^{1/4} \tag{4.15}$$

where ν is the kinematic viscosity of the fluid (for water, the working fluid, it was considered $\nu = 1.005 \times 10^{-6}\ m^2/s$) and ε is the mean energy dissipation rate (m²/s³). This variable can be computed as (ESCUDIÉ; LINÉ, 2003):

$$\bar{\varepsilon} = \frac{P}{\rho V} \tag{4.16}$$

where P is the power input (W), ρ is the density (for the working fluid, $\rho = 998.2\ \mathrm{kg/m^3}$) and V is the volume of the tank (for this study, $V = 5.0 \times 10^{-2}\ m^2$). The Kolmogorov time scale is:

$$K_\tau = \left(\frac{\nu}{\varepsilon}\right)^{1/2} \tag{4.17}$$

The integral scales can be determined from the ratios between the Kolmogorov scales and the Reynolds number, as already described in Section 3.2.1. To resume, the integral length scale is:

$$I_l = K_\eta Re^{3/4} \tag{4.18}$$

And the time integral time scale is:

$$I_t = K_\tau Re^{1/2} \tag{4.19}$$

These scales were compared to the characteristic scales of the experiments, namely the spatial resolution Δ and the interframe time t_i.

Regarding the accuracy of the turbulence measurement with PIV, Saarenrinne *et al*. (2001) evaluated the influence of spatial resolution through the distribution function of the turbulent kinetic energy spectrum (Figure 4.7). The spectral function indicated that to reach 65% of the correct turbulent kinetic energy the spatial resolution must be around $90\mathrm{K}_\eta$, and to reach 95% around $20\mathrm{K}_\eta$. It is noteworthy that the values are related to the spatial resolution; however, the power spectrum density in Figure 4.7 is a function of the wave number λ_N, which is defined by Saarenrinne et al. (2001) as:

$$\lambda_N = \frac{2\pi}{L_{exp}} \tag{4.20}$$

where L_{exp} is the characteristic length scale, in our case, the spatial resolution Δ.

Figure 4.7: Helland's three-dimensional power spectrum density (PSD) of turbulent kinetic energy (TKE) and its distribution.

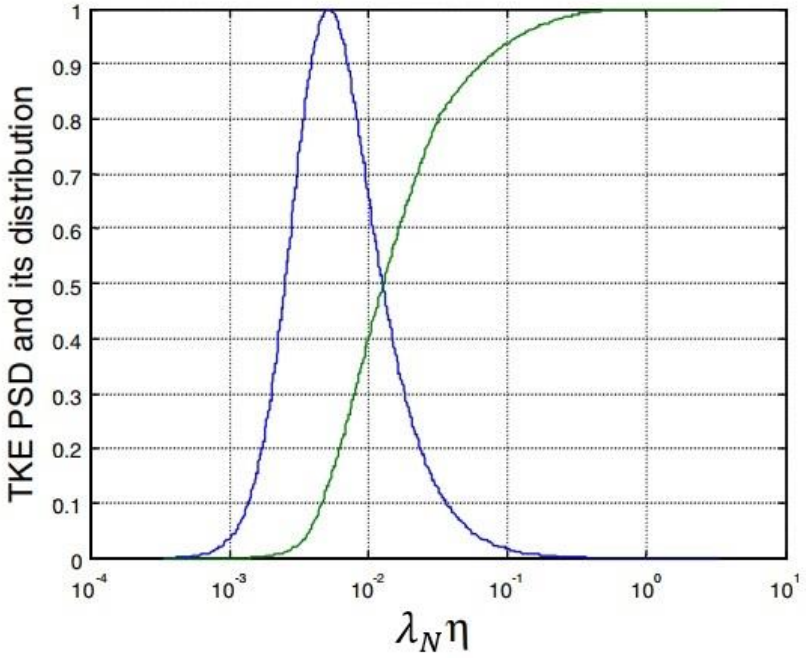

Source: Saarenrinne et al. (2001).

4.7.4. Uncertainty Quantification

Considering the definition of the turbulent kinetic energy (Equation (4.9) and the propagation error (SCIACCHITANO; WIENEKE, 2016), the uncertainty of the TKE is equal to:

$$UQ_{k_{3c}} = \frac{1}{2}\sqrt{UQ_{uu}^2 + UQ_{vv}^2 + UQ_{ww}^2} \tag{4.21}$$

where the uncertainty of each component is computed as the uncertainty of the normal Reynolds stress (R_{uu}) estimated by the Sciacchitano and Wieneke (2016) method of uncertainty quantification:

$$UQ_{uu} = R_{uu}\sqrt{\frac{2}{N}} \tag{4.22}$$

The normal Reynolds stress is computed by the Equation (4.23:

$$R_{uu} = \frac{\sum_{i=1}^{N}(u_i - u)^2}{N - 1} \tag{4.23}$$

Analogous equations are obtained for the axial and out-of-plane velocity components. Replacing the Equation (4.23 on Equation (4.21 for each velocity component and reorganizing the terms, the expression of $UQ_{k_{3c}}$ reduces to:

$$UQ_{k_{3c}} = \sqrt{R_{uu}{}^2 + R_{vv}^2 + R_{ww}^2} \times \sqrt{\frac{1}{2N}} \tag{4.24}$$

When the pseudo-isotropic approximation is taken into consideration, the uncertainty of out-of-plane component can be computed as the arithmetic mean of the two other uncertainties:

$$R_{ww} = \frac{R_{uu} + R_{vv}}{2} \tag{4.25}$$

For k_{2C} estimation, the uncertainty of the out-of-plane component is considered zero ($R_{ww} = 0$).

4.8. General Experimental Procedure

This section describes the general procedure for carrying out PIV measurements in a stirred tank, aiming to present an operational routine so that other researchers can perform the same experiments described in this work. Figure 4.8 describes the routine, which can be divided in four steps: equipment set up, calibration, image acquisition and image processing .

Figure 4.8: Operational routine for carrying out PIV measurements performed in this work.

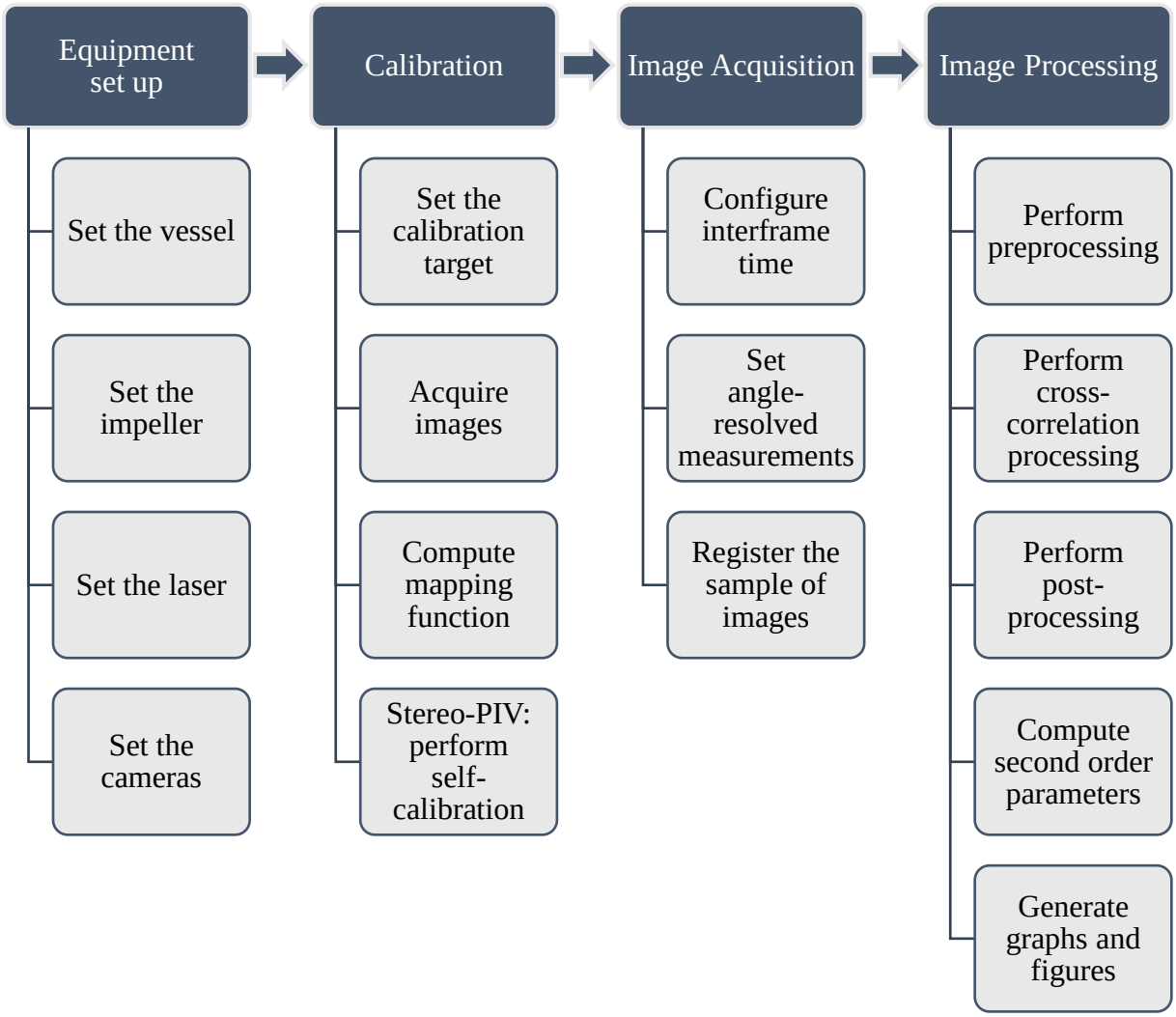

Equipment Set Up

The first step was to set up the stirred tank in its structure, to place the baffles in the right angle, so that it was in the same direction as the light sheet will be placed, and to place the impeller in the right clearance and at the center of the tank. After this, we set up the PIV system. In our laboratory, we have metal structures that help place the laser and cameras in the correct position, according to the desired arrangement. In the case of the experiments described in this work, the laser was spot to provide a light sheet displaced 0.5º in relation to the blade angle of 0° to avoid the baffle reflection. As mentioned before, the cameras were arranged as Figure 4.1c, with camera 1 at $\sigma = 45º$ and camera 2 at $\sigma + \beta = 80º$ from the light sheet, and at the same height of the impeller position.

Calibration

After the equipment set up, we filled the tank with the working fluid (water) and proceeded with the calibration. The calibration procedure was carried out with the smallest PBT impeller and was used for all other experiments. The calibration target was displayed in the object plane inside the tank, that is, in the field of view and at the same plane of the light sheet. Some preliminary tests were conducted to verify the position of the cameras and the intensity of the laser. Then, the cameras registered images of the calibration target. These images were employed by the Davis 8.0 software (LaVision) to compute the mapping function using the Calibration dialog. As described in Section 4.4, for the Classic and Tilted PIV measurements, each camera was calibrated individually. For Stereo-PIV, in turn, the images of both cameras were used and the calibration procedure for 2 cameras by the Davis 8.0 software were employed. The calibration target was removed from the tank.

For the Stereo-PIV measurements, we also performed a self-calibration to adjust the coordinate system and the calibration so that the field of view would be in the middle of the laser light sheet. For this purpose, we added the tracer particles and registered a set of images of the flow by the two cameras. Then, we used the self-calibration procedure by Davis 8.0 software to compute a disparity map and update the Stereo-PIV calibration.

Image Acquisition

For each impeller used in this work, we performed some preliminary acquisitions to configure interframe time. Different interframe times had been tested. For each value, we collected a small sample (10 to 50 pairs of images) and employed the Davis 8.0 software to process this sample considering a single pass iteration with a window size of 32×32 pixels

and 50% overlap. This is the most common cross-correlation mode used in literature for process PIV measurements. Then, we evaluated the fields of SNR and image particle displacement, using as requirements SNR above 1.2 (ROY; ACHARYA; CLOETER, 2010; XUE; CHARONKO; VLACHOS, 2014) and an average particle displacement between 4 and 6 pixels, according to Adrian (1986). At the end, the most suitable interframe time has been selected.

Before the image acquisition, we set up the angle-resolved measurements by the integration of the torque sensor (Magtrol), the microcontroller (Arduino) and the PIV synchronizer (Dantec Dynamics). The microcontroller received the rotational speed signal of the torque sensor, calculated the revolution time of the impeller to obtain images on the frequency of one pulse per revolution and sent this signal to the synchronizer of the measurement system. This device adjusted the laser and camera activation. This set up was made for each blade angle individually. Finally, we registered 1000 pairs of images for each angle-resolved measurement mentioned before (Section 4.2). The sample number was selected based on a statistical convergence analysis performed in previous work (AYALA et al., 2022).

Image Processing

All processing procedure was developed and carried out by Dr. Helder L. de Moura and Dr. Rodrigo de L. Amaral from the PIV_br team (www.piv.eng.br). The algorithms and processing routines were developed on MATLAB programming language, employing the software MATLAB version 2020b. On preprocessing, a routine containing functions of the different filters mentioned before (Section 4.5) was applied on each image. Then, the Otsu–Gauss–Wiener (OGW) method was employed (AMARAL *et al*., 2022). After the preprocessing, the images were reconstructed by using the mapping function of each camera obtained in the calibration procedure and a cubic interpolation.

On processing, the standard cross-correlation (SCC) with an iterative multigrid strategy was performed in the open-source program PRANA (VIRGINIA POLYTECHNIC INSTITUTE AND STATE UNIVERSITY, 2015), in which four passes (Table 4.3) were set and applied. After each pass, simple post-processing was carried out to eliminate outliers (WESTERWEEL; SCARANO, 2005) and a complete post-processing was also applied based on the mutual information thresholding (BARBUTTI *et al*., 2021). This post-processing procedure were also employed through MATLAB algorithms from the PIV_br team.

The processing procedure performed the computation of the matrices (fields) containing the vectors information of the velocity components and root-mean-square of the velocity fluctuations. Other algorithms in MATLAB were created by the PIV_br team and by me in

order to compute second order parameters, for instance, the turbulent kinetic energy, the uncertainty quantities, etc. We also employed MATLAB algorithms for the generation of graphs and figures presented in this work.

5. RESULTS AND DISCUSSION

5.1. Velocity Components Fields and Flow Pattern Analysis

The analysis of the distribution of the velocity components in different directions of the flow, as well as the flow patterns developed by the impellers allow the evaluation of the agitation efficiency. This analysis is also a way to verify the accuracy of the data studied in this work, as there are several studies in literature that perform this type of analysis and allow comparison between distributions. However, it is important to notice that the comparison is not always entirely possible because, as discussed in item 3.1, the velocity parameters and flow pattern depend on the geometry of the tank and impeller, the type of fluid and the impeller rotation speed, which vary across studies.

The fields of the time-averaged (a) radial, (b) axial and (c) out-of-plane velocity components obtained from Stereo-PIV measurements at different blade angles of RU01 and RU02 were presented in Figure 5.1 and Figure A.1 of the APPENDIX A, respectively. All velocity components were normalized by impeller tip velocity (U_{tip}). A radial flow pattern can be observed, typical of the Rushton turbine, which was also noticed by other authors (BALDI; YIANNESKIS, 2004; DERKSEN; DOELMAN; VAN DEN AKKER, 1999; ESCUDIÉ; LINÉ, 2003; GALLETTI *et al*., 2004; RANADE *et al*., 2001; WU; PATTERSON, 1989). There is a predominance of the radial component in relation to the axial and out-of-plane components, which presents lower values, especially in the region of eddies formation. The results showed the movement of the eddies from the region close to the impeller, at AR 0º, toward the tank wall at AR 15°, AR 30° and AR 45º.

Li *et al.* (2013) investigated the flow induced by Rushton turbine with the same diameter as RU02 (D = 2T/5) and observed maximum values of the radial, axial and out-of-plane components of $0.75 \times U_{tip}$, $0.27 \times U_{tip}$ and $0.29 \times U_{tip}$, respectively, at AR 30º. Our maximum absolute values, at the same angle-resolved, were $0.76 \times U_{tip}$ for the radial component, $0.26 \times U_{tip}$ for the axial component, and $0.37 \times U_{tip}$ for the out-of-plane component for RU01 and $0.77 \times U_{tip}$ for the radial, $0.28 \times U_{tip}$ for the axial and $0.39 \times U_{tip}$ for the out-of-plane component for RU02. Thus, the results for both impellers were in good agreement with the literature.

Regarding the diameter effect, we verified that the larger impeller (RU02, Figure A.1 of the APPENDIX A) showed greater eddies formation regions than the smaller impeller (RU01, Figure 5.1) for the radial component at AR 15°, AR 30° and AR 45º. For the axial and out-of-plane components, the greater turbulent structure formation was only identified at AR

15°, while for the other blade angles, similar fields were verified. The eddies formation regions of the larger impeller also seemed to have a greater offset among the angle resolved measurements. Despite these differences, similar maximum values were observed for both impeller diameters. For the RU01, the maximum values of the radial, axial and out-of-plane components were $0.99 \times U_{tip}$, $0.48 \times U_{tip}$ and $0.52 \times U_{tip}$ at AR 15°. For the RU02, in turn, the maximum values were $1.06 \times U_{tip}$, $0.53 \times U_{tip}$ and $0.58 \times U_{tip}$. Thus, an increase of 20% in impeller diameter led to a growth of only 6.7%, 10.6% and 11.5% in the radial, axial and out-of-plane components, which can be considered insignificant to account for effects on agitation and mixing efficiency. It is noteworthy that this comparison is possible because we carried out experiments with similar Reynolds number (9×10^4)

We found a noisy zone in the radial and out-of-plane component fields at y/H = 0.35 and x/R = 0.49 for all blade angles. This zone has also been observed in other fields and it will be discussed in Section 5.5.5.

Figure 5.1: (a) Radial, (b) axial and (c) out-of-plane time-averaged velocity components obtained from Stereo-PIV measurements at different blade angles of RU01. Highlighted in pink: noisy zone.

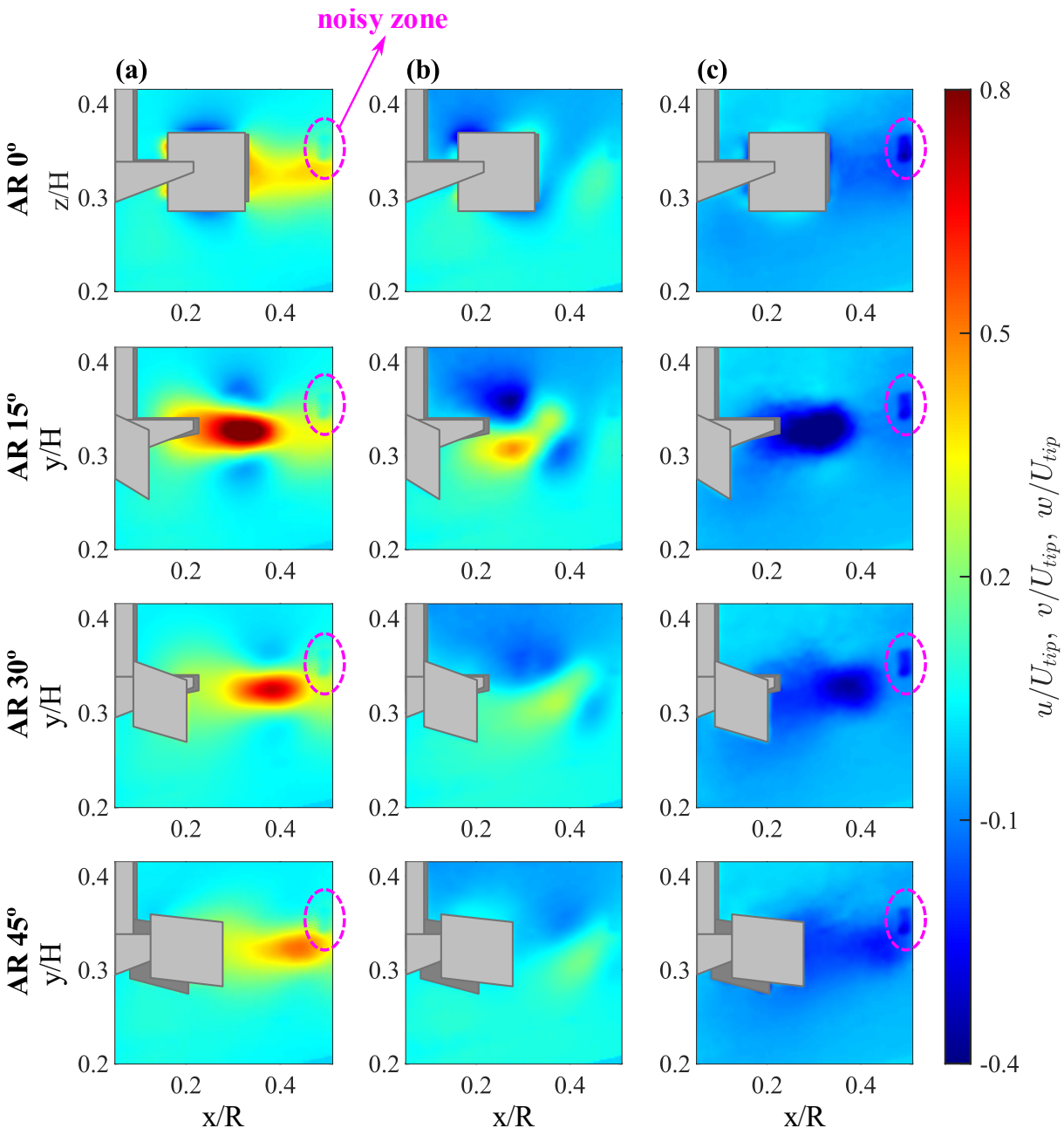

The fields of the time-averaged (a) radial, (b) axial and (c) out-of-plane velocity components obtained from Stereo-PIV measurements at different blade angles of PBT01 and PBT02 were showed in Figure 5.2 and Figure A.2 of the APPENDIX A, respectively. The flow presented a strongly downward axial pattern with a slight deviation downwards the tank due to the inclination of the blade. The same finding was also reported by Hockey and Nouri (1996), Khan *et al*. (2006) and Chung *et al*. (2007). We also observed that the axial velocity component predominated the flow, influenced by the radial and out-of-plane components in the discharge zone below the impeller. In this region, more expressive values of the radial and out-of-plane components were observed, which can be attributed to the blade movement. The comparison between the angle-resolved measurements allows verifying that the highest absolute values of the velocity components followed the trailing vortices induced by the impeller. We also can observe in the figures the movement of the eddies from the suction region at AR 0º to the discharge region at AR 45º.

For the PBT01, the highest absolute value of the radial component was $0.44 \times U_{tip}$ observed at AR 22.5º in the trailing vortices area. The maximum absolute value of the axial component was $0.61 \times U_{tip}$, identified at AR 0º in the suction region. For the out-of-plane velocity component, the uppermost absolute value was $0.34 \times U_{tip}$, verified at discharge region at AR 0º. For the PBT02, the highest absolute values were observed in the same regions, however, the maximum values were $0.56 \times U_{tip}$ at AR 22.5° for the radial component, $0.57 \times U_{tip}$ at AR 0° for the axial component and $0.40 \times U_{tip}$ at AR 0° for the out-of-plane component. Hockey and Nouri (1996) found a maximum value of $0.55 \times U_{tip}$ at AR 0° for the axial velocity component, from Laser Doppler Velocimetry (LDV) measurements, which agree with the values here. For the out-of-plane component, Khan *et al*. (2006) observed a maximum of $0.67 \times U_{tip}$. Despite of carried out angle-resolved experiments, the authors did not specify the blade angle of this peak value.

The increase in PBT diameter led to a larger region of eddies formation and to a greater detachment of the turbulent structures along the discharge region between one angle-resolved and another. However, a 20% increase in the diameter promoted a 27.2% rise in the maximum value of the radial component, a 6.5% decrease in the maximum value of the axial component, and an enhance of 17.6% in the maximum value of the out-of-plane component. Thus, in this case, we verified that the diameter variation has more influence on the radial component than on the other components, probably because the difference in impeller geometry occurs in the radial direction.

Figure 5.2: (a) Radial, (b) axial and (c) out-of-plane time-averaged velocity components obtained from Stereo-PIV measurements at different blade angles of PBT01.

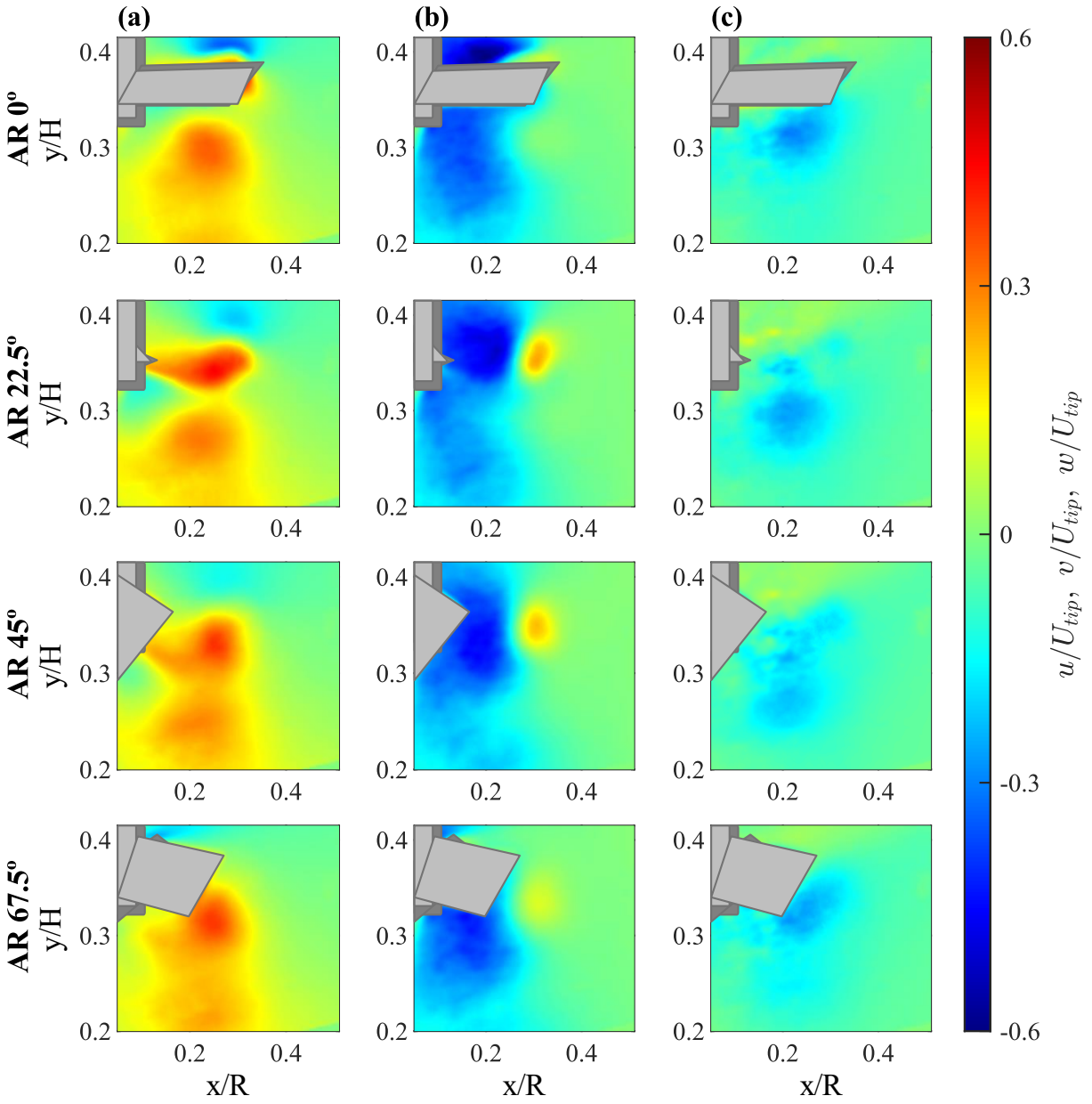

5.2. Root-mean-square of the Velocity Fluctuations Fields

We assessed the fields of the root-mean-square (rms) of the velocity fluctuations to investigate the effect of the different positions of the cameras in the flow parameters. We compared the rms of the radial and axial velocity fluctuations obtained by Classic PIV (camera 1, less tilted), Tilted PIV (camera 2, more tilted) and Stereo-PIV (combination of the two cameras). Moreover, this section discussed the variation on turbulence intensities in different regions of the field of view, as the fields of rms of the velocity fluctuations can be employed as an indicative of the levels of turbulence in different flow regions (HOCKEY; NOURI, 1996; KHAN; RIELLY; BROWN, 2006; KRESTA; WOOD, 1993; PERRARD et al., 2000).

For the flow induced by Rushton turbines, Figure 5.3 and Figure A.3 of the APPENDIX A show the fields of the rms of the radial velocity fluctuations considering the smaller (RU01) and the larger (RU02) impeller, respectively. The results indicated that the rms of the radial velocity fluctuations obtained by the Classic PIV (Figure 5.3a and Figure A.3a) and Stereo-PIV (Figure 5.3c and Figure A.3c) are similar for all blade angles, while the fields obtained by the Tilted PIV (Figure 5.3b and Figure A.3b) present higher values, mainly in the region of the drag vortices displacement, near the impeller blades.

In Table 5.1 are displayed the maximum values of the rms of the radial velocity fluctuations obtained from all the approaches at different blade angles. We can observe that the Classic and Stereo-PIV presented a highest deviation between the maximum values of 20% for RU01 at AR 45°, while the highest deviation between Classic and Tilted PIV were 60% for RU01 at AR 45° and between Stereo and Tilted PIV were 54% for RU02 at AR 45°. However, when comparing the fields of the rms of the axial velocity fluctuations (Figure 5.4 and Figure A.4 of the APPENDIX A), all measurements presented equivalent values. The maximum values presented in Table 5.2 showed that the highest deviation between Classic and Stereo-PIV was 10% for RU01 at AR 15° and among Classic, Tilted and Stereo-PIV was 20% for RU02 at AR 30°.

Figure 5.3: Root-mean-square of the radial velocity fluctuations obtained from (a) Classic PIV, (b) Tilted PIV and (c) Stereo-PIV measurements at different blade angles of RU01. Highlighted in pink: noisy zone.

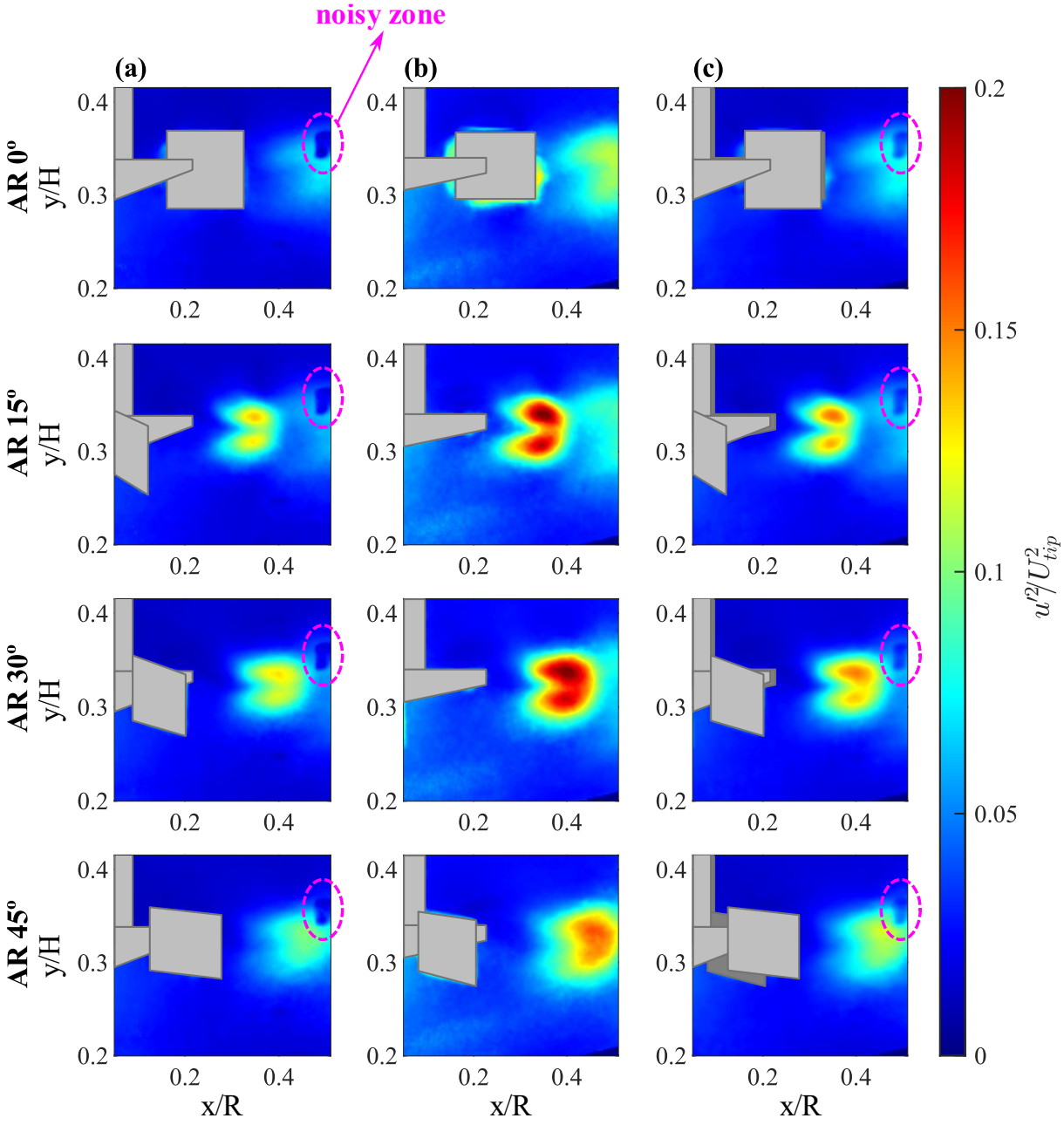

Table 5.1: Maximum values of the rms of the radial velocity fluctuations obtained from Classic PIV, Tilted PIV and Stereo-PIV measurements at different blade angles of RU01 and RU02.

Impeller	AR (°)	Classic PIV	Tilted PIV	Stereo-PIV
RU01	0	$0.08 \times U_{tip}^2$	$0.11 \times U_{tip}^2$	$0.08 \times U_{tip}^2$
	15	$0.14 \times U_{tip}^2$	$0.21 \times U_{tip}^2$	$0.15 \times U_{tip}^2$
	30	$0.13 \times U_{tip}^2$	$0.20 \times U_{tip}^2$	$0.15 \times U_{tip}^2$
	45	$0.10 \times U_{tip}^2$	$0.16 \times U_{tip}^2$	$0.12 \times U_{tip}^2$
RU02	0	$0.07 \times U_{tip}^2$	$0.11 \times U_{tip}^2$	$0.08 \times U_{tip}^2$
	15	$0.15 \times U_{tip}^2$	$0.23 \times U_{tip}^2$	$0.17 \times U_{tip}^2$
	30	$0.17 \times U_{tip}^2$	$0.27 \times U_{tip}^2$	$0.19 \times U_{tip}^2$
	45	$0.13 \times U_{tip}^2$	$0.20 \times U_{tip}^2$	$0.13 \times U_{tip}^2$

Figure 5.4: Root-mean-square of the axial velocity fluctuations obtained from (a) Classic PIV, (b) Tilted PIV and (c) Stereo-PIV measurements at different blade angles of RU01. Highlighted in pink: noisy zone.

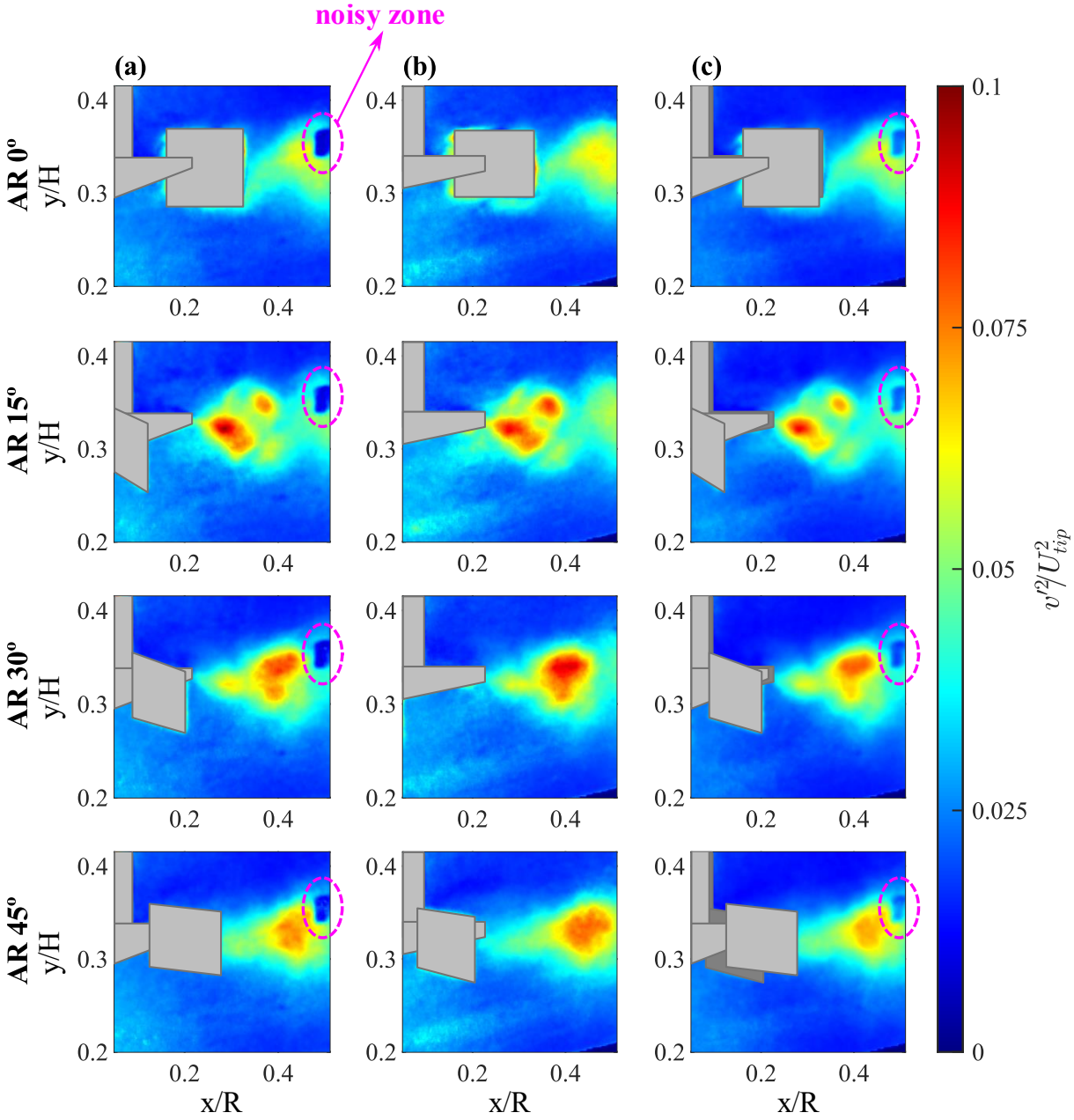

Table 5.2: Maximum values of the rms of the axial velocity fluctuations obtained from Classic PIV, Tilted PIV and Stereo-PIV measurements at different blade angles of RU01 and RU02.

Impeller	AR (°)	Classic PIV	Tilted PIV	Stereo-PIV
RU01	0	$0.06 \times U_{tip}^2$	$0.06 \times U_{tip}^2$	$0.06 \times U_{tip}^2$
	15	$0.10 \times U_{tip}^2$	$0.09 \times U_{tip}^2$	$0.09 \times U_{tip}^2$
	30	$0.08 \times U_{tip}^2$	$0.09 \times U_{tip}^2$	$0.08 \times U_{tip}^2$
	45	$0.08 \times U_{tip}^2$	$0.08 \times U_{tip}^2$	$0.07 \times U_{tip}^2$
RU02	0	$0.06 \times U_{tip}^2$	$0.07 \times U_{tip}^2$	$0.06 \times U_{tip}^2$
	15	$0.10 \times U_{tip}^2$	$0.10 \times U_{tip}^2$	$0.10 \times U_{tip}^2$
	30	$0.10 \times U_{tip}^2$	$0.12 \times U_{tip}^2$	$0.10 \times U_{tip}^2$
	45	$0.10 \times U_{tip}^2$	$0.11 \times U_{tip}^2$	$0.10 \times U_{tip}^2$

Analogous observations were made for the rms of the velocity fluctuations of the flow promoted by PBT. The fields of the rms of the radial velocity fluctuations are set out in Figure 5.5 (PBT01) and Figure A.5 of the APPENDIX A (PBT02). We can observe higher values for the fluctuations obtained by Tilted PIV than the results obtained by the other approaches for all blade angles. In Table 5.3, the maximum values verified for each angle-resolved measurements confirmed this observation. The results obtained from Classic and Stereo-PIV presented a maximum variation of 20% for PBT01 at AR 67.5°. The comparison between Classic and Tilted PIV showed a maximum variation of 67% for PBT02 at AR 67.5°. Moreover, the results of Tilted and Stereo-PIV allowed to verified deviations of 50% for PBT01 at AR 22.5° and AR 45° and for PBT02 at AR 0°.

The fields of the rms of the axial velocity fluctuations of the flow induced by PBT01 and PBT02 were displayed in Figure 5.6 and Figure A.6 of the APPENDIX A, respectively. As already verified for the flow generated by the Rushton turbines, the results showed similar fields for all the approaches considered in this work. This can be also verified in the comparison of the maximum values of the rms of the axial velocity fluctuations for each angle-resolved measurement, presented in Table 5.4. For Classic and Stereo-PIV measurements, we can observe variations of less than 17%. For Classic and Tilted PIV data, this variation reaches only 14%, and for Tilted and Stereo-PIV the maximum variation was 20% for PBT01 and PBT02 at AR 67.5°.

Figure 5.5: Root-mean-square of the radial velocity fluctuations obtained from (a) Classic PIV, (b) Tilted PIV and (c) Stereo-PIV measurements at different blade angles of PBT01. Highlighted in pink: noisy zone.

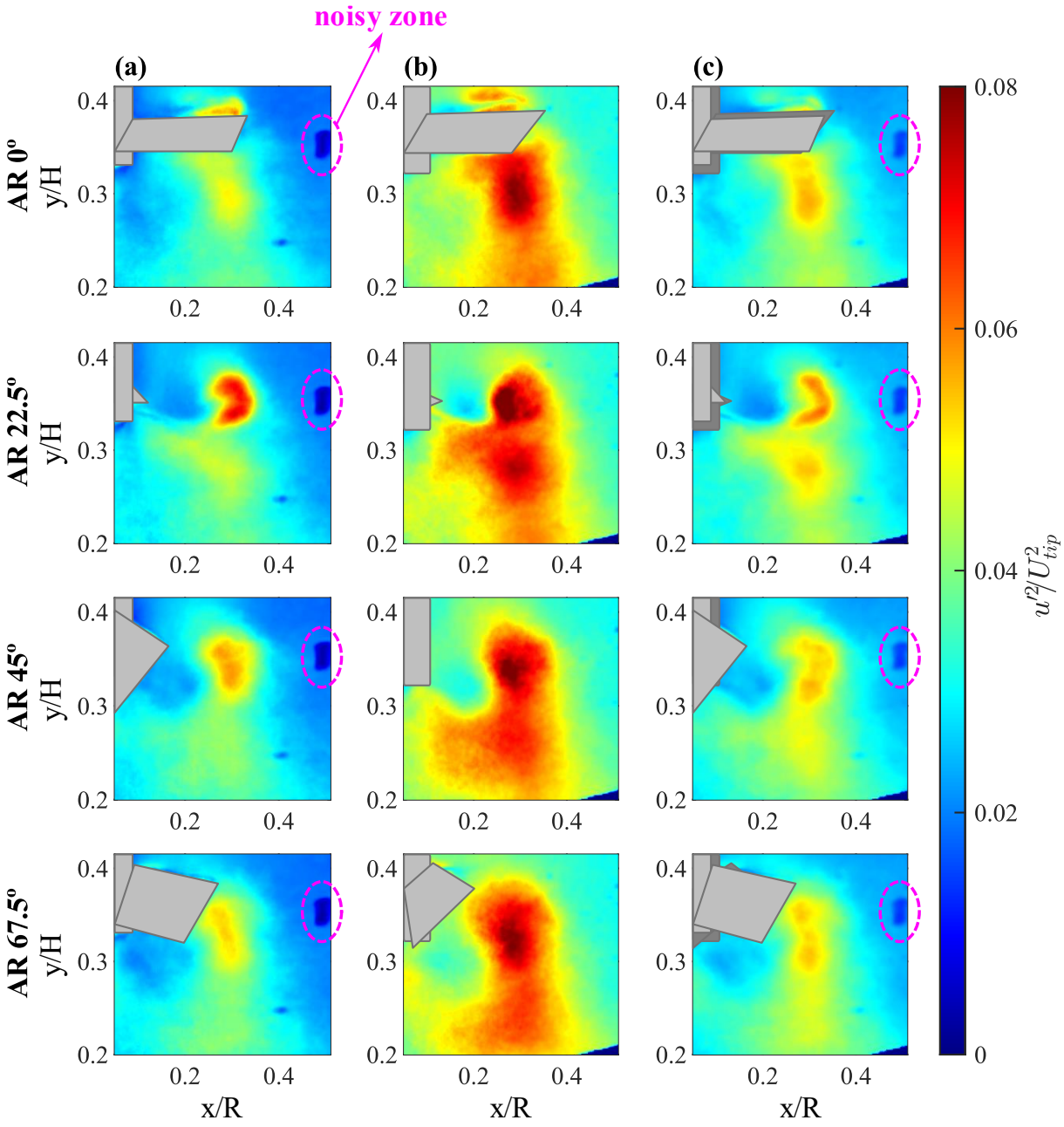

Table 5.3: Maximum values of the rms of the radial velocity fluctuations obtained from Classic PIV, Tilted PIV and Stereo-PIV measurements at different blade angles of PBT01 and PBT02.

Impeller	AR (°)	Classic PIV	Tilted PIV	Stereo-PIV
PBT01	0	$0.06 \times U_{tip}^2$	$0.08 \times U_{tip}^2$	$0.06 \times U_{tip}^2$
	15	$0.07 \times U_{tip}^2$	$0.09 \times U_{tip}^2$	$0.06 \times U_{tip}^2$
	30	$0.06 \times U_{tip}^2$	$0.09 \times U_{tip}^2$	$0.06 \times U_{tip}^2$
	45	$0.05 \times U_{tip}^2$	$0.08 \times U_{tip}^2$	$0.06 \times U_{tip}^2$
PBT02	0	$0.08 \times U_{tip}^2$	$0.12 \times U_{tip}^2$	$0.08 \times U_{tip}^2$
	15	$0.09 \times U_{tip}^2$	$0.13 \times U_{tip}^2$	$0.09 \times U_{tip}^2$
	30	$0.07 \times U_{tip}^2$	$0.11 \times U_{tip}^2$	$0.08 \times U_{tip}^2$
	45	$0.06 \times U_{tip}^2$	$0.10 \times U_{tip}^2$	$0.07 \times U_{tip}^2$

Figure 5.6: Root-mean-square of the axial velocity fluctuations obtained from (a) Classic PIV, (b) Tilted PIV and (c) Stereo-PIV measurements at different blade angles of PBT01. Highlighted in pink: noisy zone.

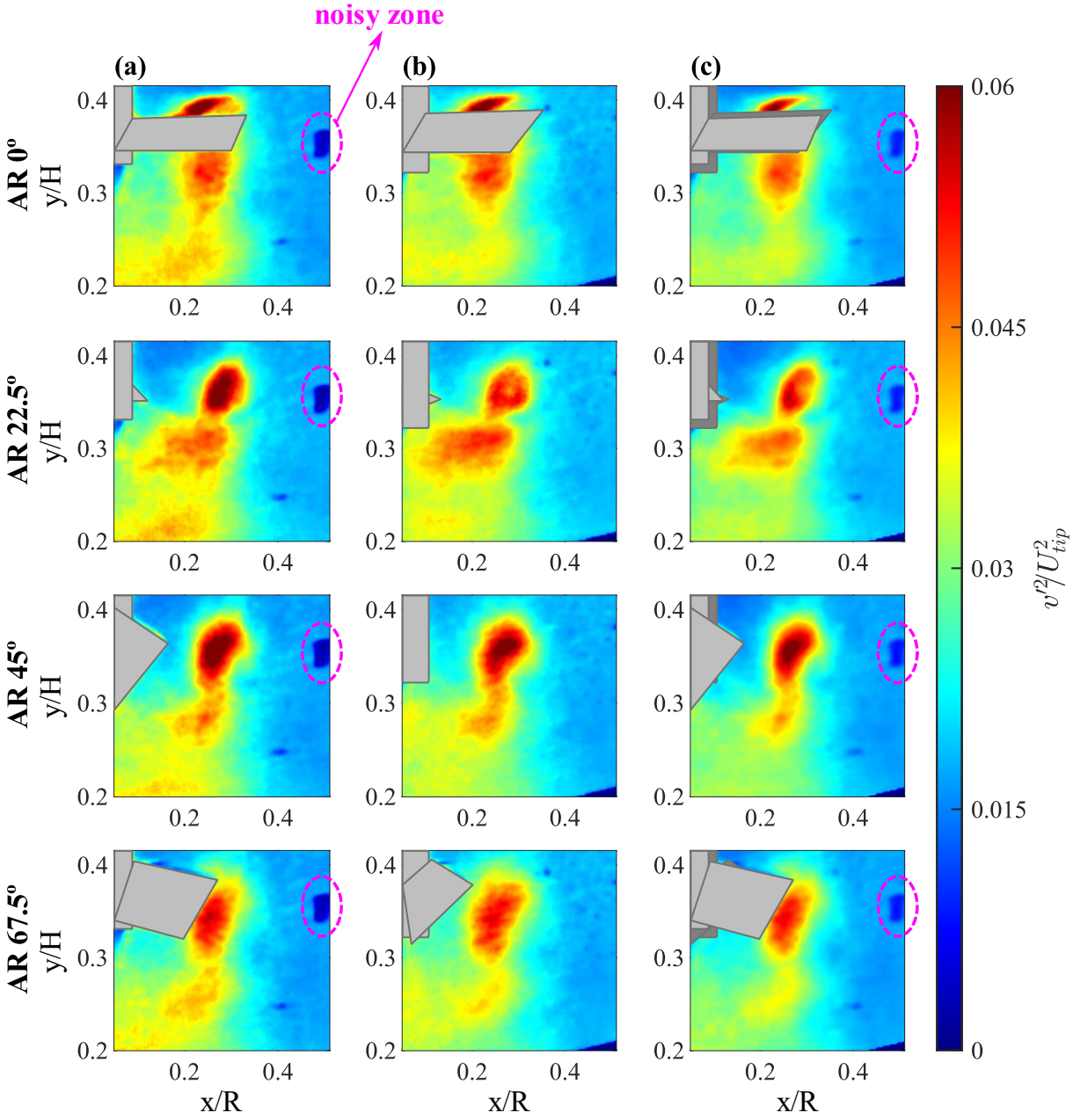

Table 5.4: Maximum values of the rms of the axial velocity fluctuations obtained from Classic PIV, Tilted PIV and Stereo-PIV measurements at different blade angles of PBT01 and PBT02.

Impeller	AR (°)	Classic PIV	Tilted PIV	Stereo-PIV
PBT01	0	$0.07 \times U_{tip}^2$	$0.07 \times U_{tip}^2$	$0.06 \times U_{tip}^2$
	15	$0.07 \times U_{tip}^2$	$0.06 \times U_{tip}^2$	$0.06 \times U_{tip}^2$
	30	$0.07 \times U_{tip}^2$	$0.07 \times U_{tip}^2$	$0.07 \times U_{tip}^2$
	45	$0.06 \times U_{tip}^2$	$0.06 \times U_{tip}^2$	$0.05 \times U_{tip}^2$
PBT02	0	$0.07 \times U_{tip}^2$	$0.07 \times U_{tip}^2$	$0.06 \times U_{tip}^2$
	15	$0.07 \times U_{tip}^2$	$0.06 \times U_{tip}^2$	$0.06 \times U_{tip}^2$
	30	$0.07 \times U_{tip}^2$	$0.07 \times U_{tip}^2$	$0.07 \times U_{tip}^2$
	45	$0.06 \times U_{tip}^2$	$0.06 \times U_{tip}^2$	$0.05 \times U_{tip}^2$

What emerges from the results reported here is that the higher values of the rms of the radial velocity fluctuations verified for the flow induced by all the impellers are the result of the acquisition of the more tilted camera (camera 1), that obtained the in-plane and out-of-plane displacement, as described in Figure 4.2. Thus, the higher values are the combination of the radial and the out-of-plane contributions on the rms of the velocity fluctuations.

In addition, the variation of the camera position applied in the Tilted PIV approach did not influence the acquisition of the axial component, because in this direction the results from the different approaches were very similar. It is important to observe that all fields of Classic PIV and Stereo PIV data presented a noisy zone at z/H = 0.35 and r/R = 0.49 for the fields of Rushton turbines and at z/H = 0.32 and r/R = 0.49 for the fields of PBT. This zone was caused by a light reflection recorded by camera 2 and were better discussed in Section 5.5.5.

Regarding the phenomenon of turbulence, higher values of velocity fluctuations are an indication of higher turbulence in the region, as turbulent phenomena lead to random variations in velocity that are computed by this parameter. Thus, regions with greater rms of velocity fluctuations present higher turbulence levels than regions where this parameter is lower. In the fields of the radial component (Figure 5.3 and Figure A.3 in APPENDIX A), the region of highest turbulence intensity was close to the impeller tip, in the turbine stream ($0.28 < y/H < 0.36$). This region followed the impeller stream toward the wall and reduced its intensity with the change in the blade angle from AR 15º to AR 30° and to AR 45°. The region

is more concentrated and with higher values than those observed in the fields of the axial component (Figure 5.4 and Figure A.4 in APPENDIX A), in which the turbulence intensity is also higher in the impeller stream, but presents values up to 50% smaller and more spread out across the discharge region.

For flows promoted by the pitched blade turbines, the region of highest turbulent intensity is also close to the impeller tip. However, this region does not change with the velocity component and the blade angle, being located between $0.32 < y/H < 0.37$ and $0.30 < x/R < 0.4$ in all the cases and presenting the same intensity, as can be observed in Figure 5.5 and Figure A.5 in APPENDIX A for the rms of the radial component and in Figure 5.6 and Figure A.6 in APPENDIX A for the rms of the axial component. The intensity of the radial component (Table 5.3) is slightly higher than the axial component (Table 5.4) and may vary by up to 30%.

The higher intensity of turbulence promotes a shorter mixing time between the different substances in a stirred operation. Therefore, the regions with higher levels of turbulence are the most suitable for a feed location. Based on this, we can suggest that the most appropriate feed location is close do the impeller tip, at $0.28 < y/H < 0.36$ for flow promoted by a Rushton turbine and at $0.32 < y/H < 0.37$ and $0.30 < x/R < 0.4$ for the flow induced by a 45° PBT with 4 blades. Moreover, we observed that the blade angle can possibly influence the turbulent intensity for the Rushton turbine, so this variable should be considered on the feed operation.

5.3. Pseudo-isotropic Approximation Analysis

In order to evaluate the application of the pseudo-isotropic approximation, we analyzed the percentual contribution of each rms of the velocity fluctuations on the turbulent kinetic energy estimation. This contribution was computed as the ratio between the velocity fluctuations and the TKE estimated for each vector in the field of view, considering angle-resolved measurements from the Stereo-PIV approach.

The percentual contribution of the rms of the velocity fluctuations of the flow induced by RU01 and RU02 are showed in Figure 5.7 and Figure A.7 of the APPENDIX A, respectively. For both impellers, in the region of eddies formation, at AR 15°, AR 30º and AR 45º, the radial component presented higher values than the other components due to the energy transfer induced by the impeller. For RU01, the maximum values in this region were 54% (AR 15°), 51% (AR 30°) and 52% (AR 45°). For RU02, in turn, the maximum values were 54% (AR 15º), 55% (AR 30º) and 50 % (AR 45º). The axial component, in general, presented higher values in the region close do the impeller tip, with a maximum of 55% at AR 30° for RU01 and of 51% at the same blade angle for RU02.

Regarding the out-of-plane component, for RU02 we observed a region of high percentages at AR 15º, near the impeller tip. The maximum value of the contribution in this region reached 73%. At first, we thought it could be a noisy region, but we found that this region had SNR values greater than 1.75, which indicated good quality measurements (BARBUTTI *et al*., 2021; RANADE *et al*., 2001). In addition, this region did not have high 3C reconstruction error values. Therefore, this set of evidence revealed that the higher results are not associated with noisy values. However, it is important to mention that the out-of-plane component is more sensible than the other components because it is obtained from a reconstruction process. The quality of the measurements was better discussed in Section 5.5 of this work.

Figure 5.7: Percentual contribution of the root-mean-square of the (a) radial, (b) axial and (c) out-of-plane velocity fluctuations on the TKE obtained from Stereo-PIV measurements for different blade angles of RU01. Highlighted in pink: noisy zone.

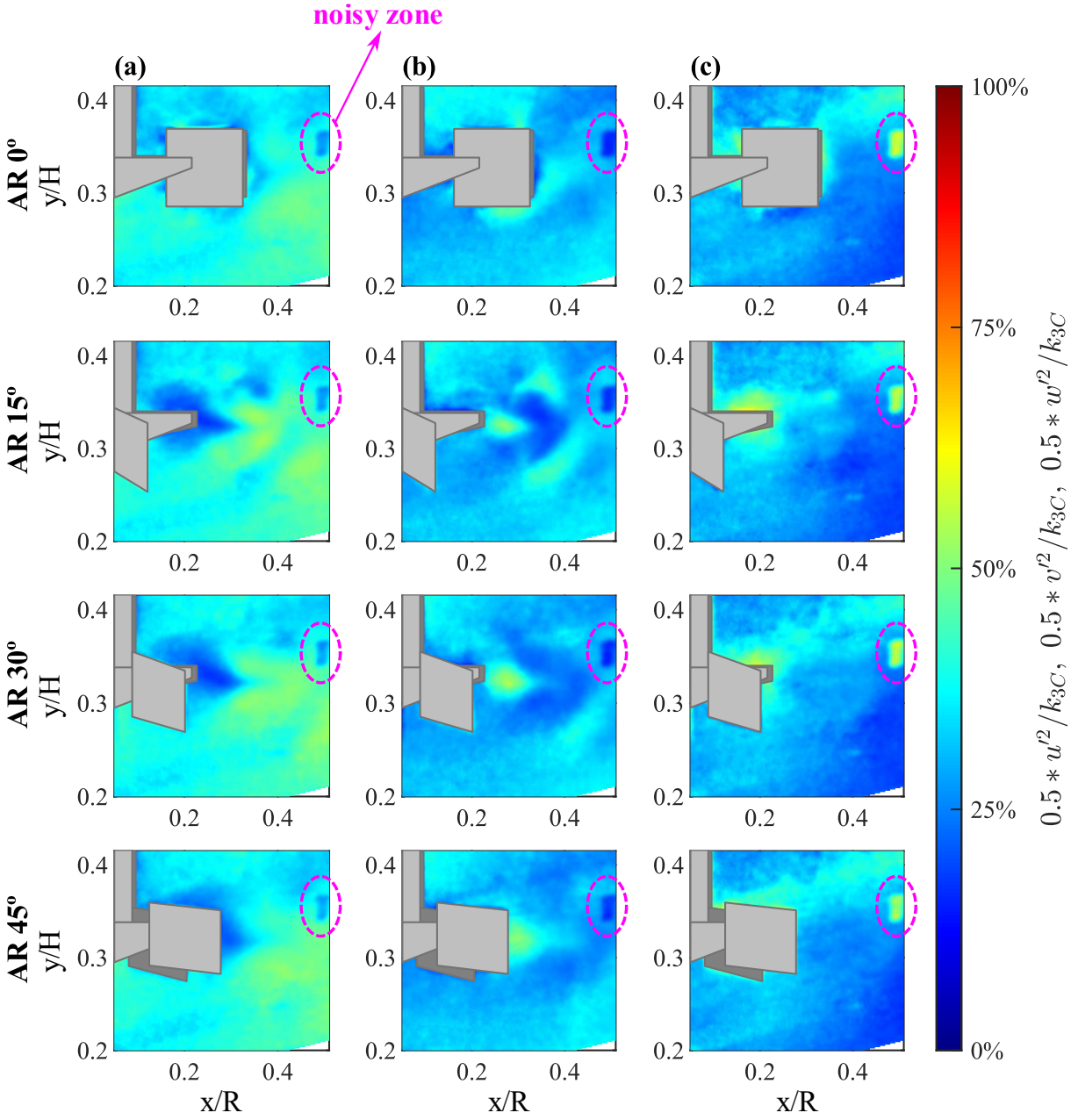

The percentual contribution on the TKE values of each root-mean-square of the velocity fluctuations is shown in Figure 5.8 for PBT01 and Figure A.8 of the APPENDIX A for PBT02. The radial component showed a higher contribution in regions above and below the impeller, reaching 57% at all blade angles for PBT01 and 59% at AR 45° and AR 6.5 for PBT02 in the discharge region ($y/H > 0.27$ and $x/R > 0.32$). The axial component presented contributions, on average, between 28% and 35% for PBT01 and between 29% and 36% for PBT02. The out-of-plane component, in turn, indicated contributions between 20% and 31% for PBT01 and 19% and 29% for PBT02.

The pseudo-isotropic approximation assumes that the out-of-plane component can be estimated as the arithmetic mean of the other two components. Based on this concept, for a successful application of this approximation, it is expected that the percentual contributions of each component would be similar. However, for both impellers, the contributions differ from each other and vary along the field of view, especially in the discharge region. The different contributions of each component may indicate that the pseudo-isotropic approximation is not suitable on the estimative of TKE in this region.

These results corroborate to other studies that evaluated the isotropy of the flow induced by Rushton turbine and also verified discrepancies among the rms of the velocity fluctuations (LEE; YIANNESKIS, 1998; LI; BAO; GAO, 2011; MONTANTE *et al*., 1999; SHARP; ADRIAN, 2001). Similar observations were also made by Delafosse *et al*. (2011) regarding the flow induced by a axial Mixel TTP impeller; by Unadkat *et al*. (2011), when studying the flow promoted by a sawtooth impeller; and by Liang *et al*. (2018), that investigated the flow generated by flat-rigid, flexible and curved-rigid impellers.

However, there are also some studies that found out diverse conclusions. Chung *et al*. (2007) evaluated the flow promoted by a 45° PBT with 6 blades and Bugay *et al* (2002) assessed the flow induced by a hydrofoil Lightnin A310 impeller. Both groups verified that the components presented similar contributions to the TKE estimation so the flow could be considered isotropy. Thus, for a better understanding of the consideration of the pseudo-isotropic approximation on the estimation of TKE we must evaluate its applicability in PIV measurements. This issue was better discussed in Section 5.4.2.

It is important to notice that the noisy zone can be observed for all fields described in this section at $z/H = 0.35$ and $r/R = 0.49$ for the fields of Rushton turbines and at $z/H = 0.32$ .and $r/R = 0.49$ for the fields of PBT. More details about this were discussed in the Section 5.5.5.

Figure 5.8: Percentual contribution of the root-mean-square of the (a) radial, (b) axial and (c) out-of-plane velocity fluctuations on the TKE obtained from Stereo-PIV measurements for different blade angles of PBT01. Highlighted in pink: noisy zone.

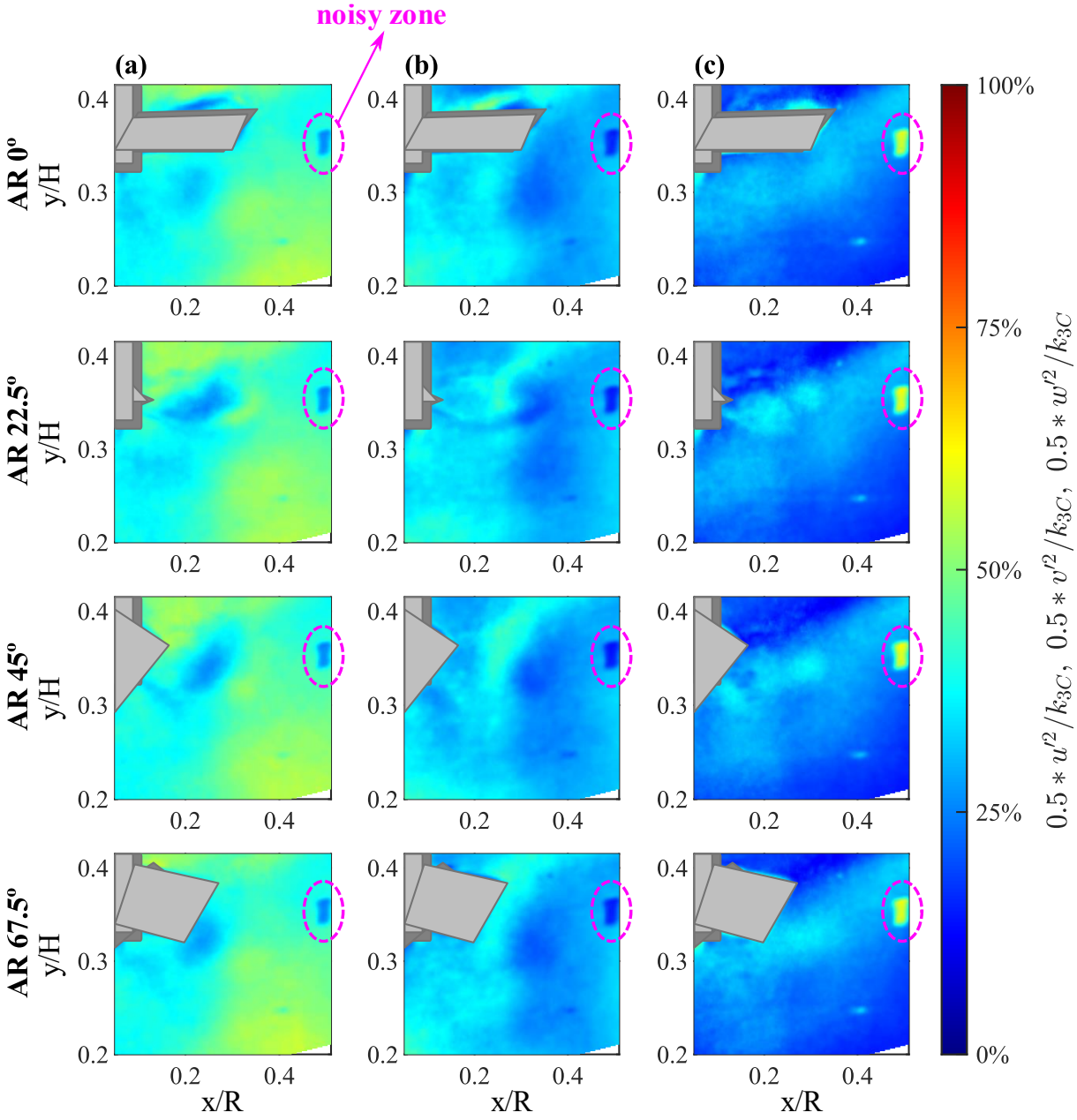

5.4. Turbulent Kinetic Energy

In this section we discuss the estimation of the turbulent kinetic energy (TKE) by the different PIV approaches. Firstly, we analyzed the fields obtained by Stereo-PIV, considering the rms of all three velocity fluctuations (radial, axial, and out-of-plane components). Secondly, we assessed the fields computed by Classic PIV regarding the pseudo-isotropic approximation, that is, taking into account the rms of the radial and axial velocity fluctuations and assuming that the rms of the out-of-plane velocity fluctuations is the arithmetic mean of the other two components. Finally, we evaluated the fields obtained by Tilted PIV. In this case, we considered that the radial component is a combination of the in-plane and out-of-plane motion. Thus, the TKE was estimated by two methods: regarding only the rms of the axial and combined-radial velocity fluctuations and considering the pseudo-isotropic approximation. This section finishes with a critical comparison among all the results and the main conclusions regarding the performance, advantages and disadvantages of each approach.

5.4.1. Stereo-PIV Measurements

The turbulent kinetic energy fields for the flow induced by the Rushton turbine normalized by the square of the impeller tip velocity (U_{tip}^2) are showed in Figure 5.9 for (a) RU01 and (b) RU02. For both impellers, it was verified that turbulent kinetic energy is concentrated in the eddies formation region. The eddies begin in the region near the impeller blade, at AR 0º, and move radially, as observed at AR 15º, AR 30º and AR 45º. The maximum value of k_{3C} was $0.16 \times U_{tip}^2$ at AR 30º for RU01 and $0.22 \times U_{tip}^2$ at the same blade angle for RU02. Similar results were reported by Lee and Yianneskis (1998). Besides, Li *et al.* (2013) verified a maximum value of $0.22 \times U_{tip}^2$ at AR 30º when analyzing the flow promoted by the same type of impeller.

The results also showed that the increase in 20% of the diameter led to higher TKE values. The maximum TKE observed in the flow induced by RU02 is 37.5% greater than the maximum verified in the flow promoted by RU01. As already analyzed in the velocity components fields (Section 5.1) the eddies formation regions of the larger impeller (RU02) seemed to have a higher offset among the angle resolved measurements. We can verify, for example, that for RU01 at AR 45° (Figure 5.9a) the center of the turbulent structures is observed in the field of view. However, for RU02 at the same blade angle (Figure 5.9b) this structure is absent because it is already dislocated beyond to the field of view.

Figure 5.9: Normalized turbulent kinetic energy obtained from Stereo-PIV measurements considering all three root-mean-square of the velocity fluctuations for different blade angles of (a) RU01 and (b) RU02.

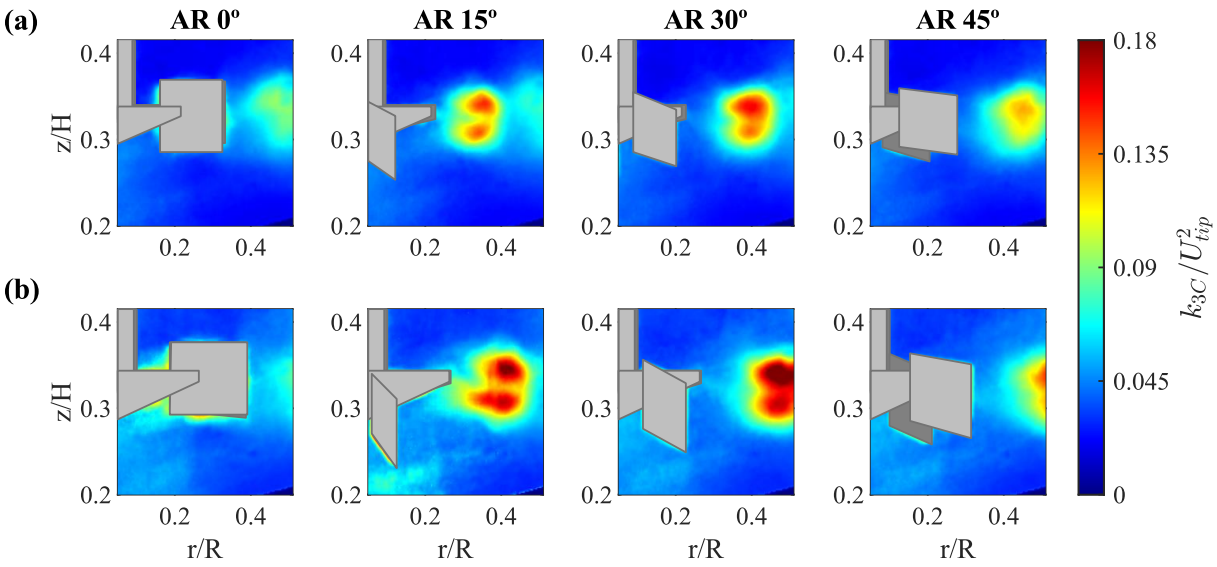

The TKE fields computed from Stereo-PIV measurements performed in the flow promoted by the 4-blade 45º pitched blade turbine (PBT) are presented in Figure 5.10 for (a) PBT01 and (b) PBT02. The TKE values were normalized by U_{tip}^2. For both impellers, the distribution of the turbulent kinetic energy of this flow is also concentrated in the eddies formation region and moves from the suction region, above the impeller at AR 0º, to the discharge region, below the impeller, at AR 67.5º. The TKE fields are in agreement with Khan *et al.*(2006), which observed the trailing vortices detachment between AR 0º and AR 45º when analyzing the flow induced by the same type of impeller. The authors verified TKE values between 0.005 and $0.06 \times U_{tip}^2$ at AR 0º, while our values range from 0.03 to $0.07 \times U_{tip}^2$ for PBT01 and from 0.03 to $0.08 \times U_{tip}^2$ for PBT02 at the same blade angle. Hockey and Nouri (1996) also found similar fields when analyzing the same blade angles of this work using Laser Doppler Velocimeter (LDV) measurements, with a maximum value of $0.11 \times U_{tip}^2$ at AR 45º. In our fields, the maximum TKE value was $0.08 \times U_{tip}^2$ at AR 45º for PBT01 and $0.11 \times U_{tip}^2$ at AR 22.5º for PBT02. The small variations from one work to another can be associated with differences in the geometry of the experimental apparatus and in the processing procedure.

Figure 5.10: Normalized turbulent kinetic energy obtained from Stereo-PIV measurements considering all three root-mean-square of the velocity fluctuations for different blade angles of (a) PBT01 and (b) PBT02.

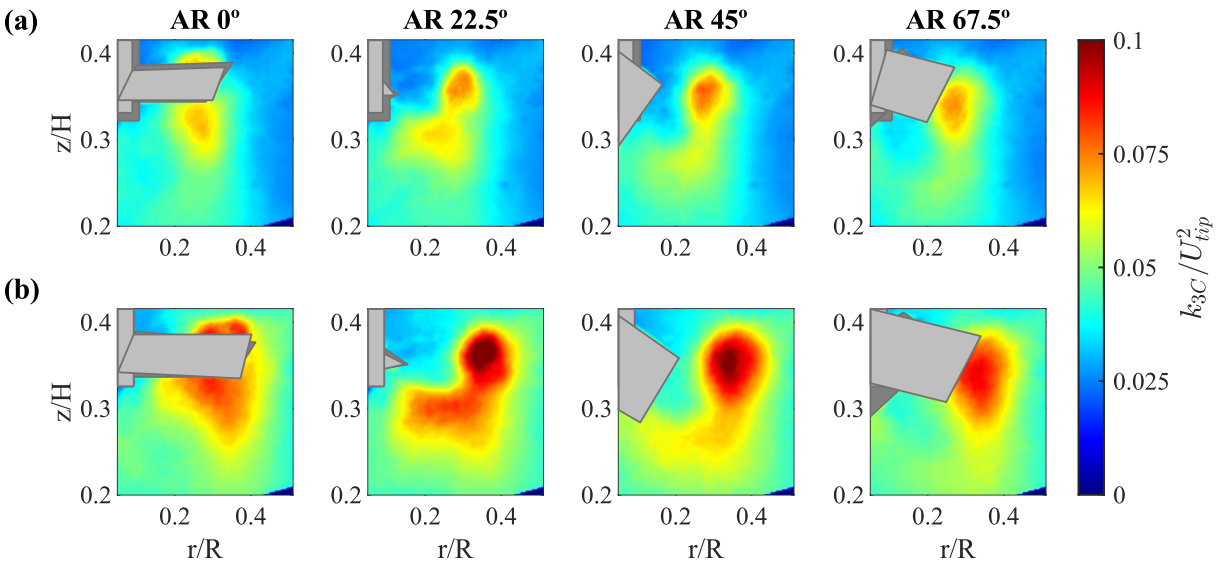

Regarding the variation in the diameter of the impeller, the results indicated that an increase in the PBT diameter also led to higher values of TKE. The enhance of 20% in the diameter caused an increase of 37.5% in the maximum value of TKE. However, we did not observe the offset difference of the eddies formation regions as verified in the flow induced by the Rushton turbines. Nevertheless, we verified that the maximum value changed from the AR 45º for PBT01 (Figure 5.10a) to the AR 22.5º for PBT02 (Figure 5.10b). This probably occurs because the higher values of the larger impeller promoted an anticipation of the maximum turbulent structures' formation.

5.4.2. Classic PIV Measurements Considering the Pseudo-isotropic Approximation

In this section we assess the estimation of the turbulent kinetic energy from Classic PIV measurements registered by camera 2 (Figure 4.1). The normalized TKE fields of the flow induced by the Rushton turbines are displayed in Figure 5.11 for (a) RU01 and (b) RU02. Regarding the flow pattern, the application of this approach led to observations similar to those obtained from Stereo-PIV measurements for both impellers. The maximum TKE value was $0.16 \times U_{tip}^2$ at AR 30º for RU01 and $0.20 \times U_{tip}^2$ at AR 30º for RU02, which agree with the maximum values verified from Stereo-PIV, in Figure 5.9 for (a) RU01 and (b) RU02. The fields were also comparable with those of Li *et al.* (2011) and Fan *et al.* (2022), that investigated the flow generated by the Rushton turbine from Classic PIV measurements and employed the

pseudo-isotropic approximation. However, both works verified lower TKE values, with a maximum of $0.10 \times U_{tip}^2$.

Figure 5.11: Normalized turbulent kinetic energy obtained from Classic PIV measurements considering pseudo-isotropic approximation for different blade angles of (a) RU01 and (b) RU02. Highlighted in pink: noisy zone.

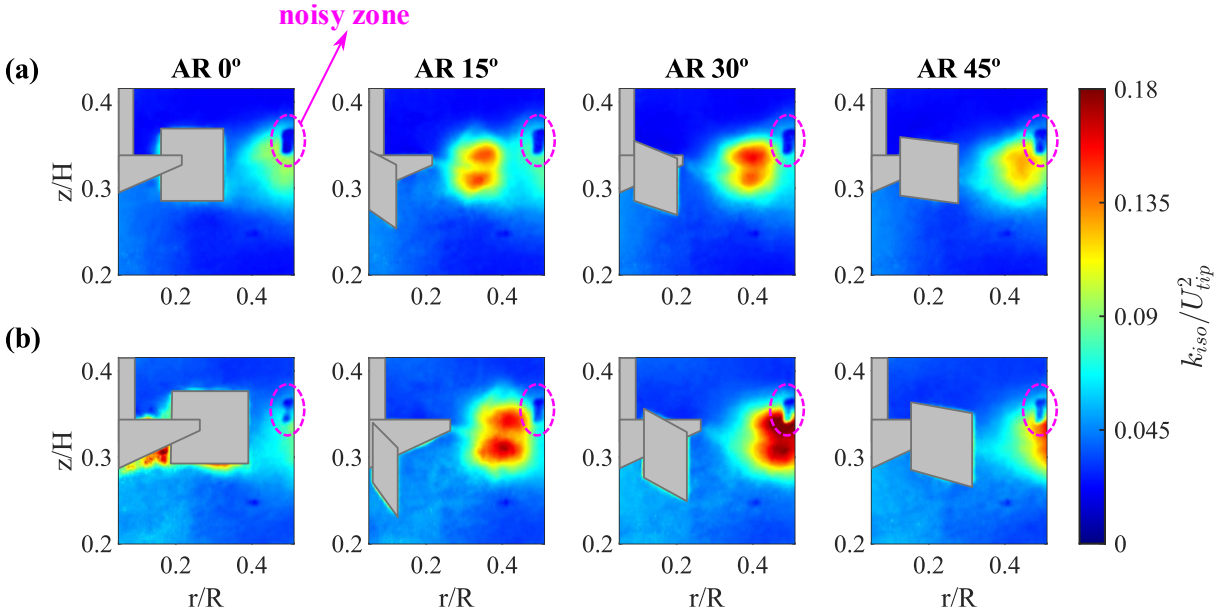

The TKE fields estimated from Classic PIV measurements of the flow promoted by the PBT considering the pseudo-isotropic approximation are presented in Figure 5.12 for (a) PBT01 and (b) PBT02. The flow presented similar behavior of the fields estimated from Stereo-PIV measurements, in Figure 5.10 for (a) PBT01 and (a) PBT02, with a pattern predominantly axial with a slight deviation downwards the tank. The higher TKE values corresponded to the drag vortices movement from the suction zone at AR 0º to the discharge zone at AR 67.5º. The same finding was also reported by Gabriele *et al.* (2009), Alonzo-Garcia *et al.* (2019) and Khan *et al.* (2006) when estimating TKE fields of the flow induced by the PBT from Classic PIV measurements considering the pseudo-isotropic approximation. We verified a maximum TKE value of $0.10 \times U_{tip}^2$ at AR 22.5º for PBT01 and $0.13 \times U_{tip}^2$ at the same blade angle for PBT02, which is very close to the value of $0.08 \times U_{tip}^2$ and $0.11 \times U_{tip}^2$observed from Stereo-PIV measurements for PBT01 and PBT02, respectively. Comparison with literature data for the same impeller type and considering the pseudo-isotropic approximation on the TKE estimation shows similar results despite differences in the tank size, impeller diameter and processing. Ge *et al.* (2014) verified a maximum of $0.10 \times U_{tip}^2$ at AR 0º, while our data presented a maximum

of $0.09 \times U_{tip}^2$ for PBT01 and $0.10 \times U_{tip}^2$ for PBT02 at the same blade angle. Recently, Savari *et al.* (2022) observed a maximum of $0.11 \times U_{tip}^2$ at AR 45º, we reported, at the same blade angle, maximum values of $0.09 \times U_{tip}^2$. for PBT01 and $0.11 \times U_{tip}^2$ for PBT02.

Figure 5.12: Normalized turbulent kinetic energy obtained from Classic PIV measurements considering pseudo-isotropic approximation for different blade angles of (a) PBT01 and (b) PBT02. Highlighted in pink: noisy zone.

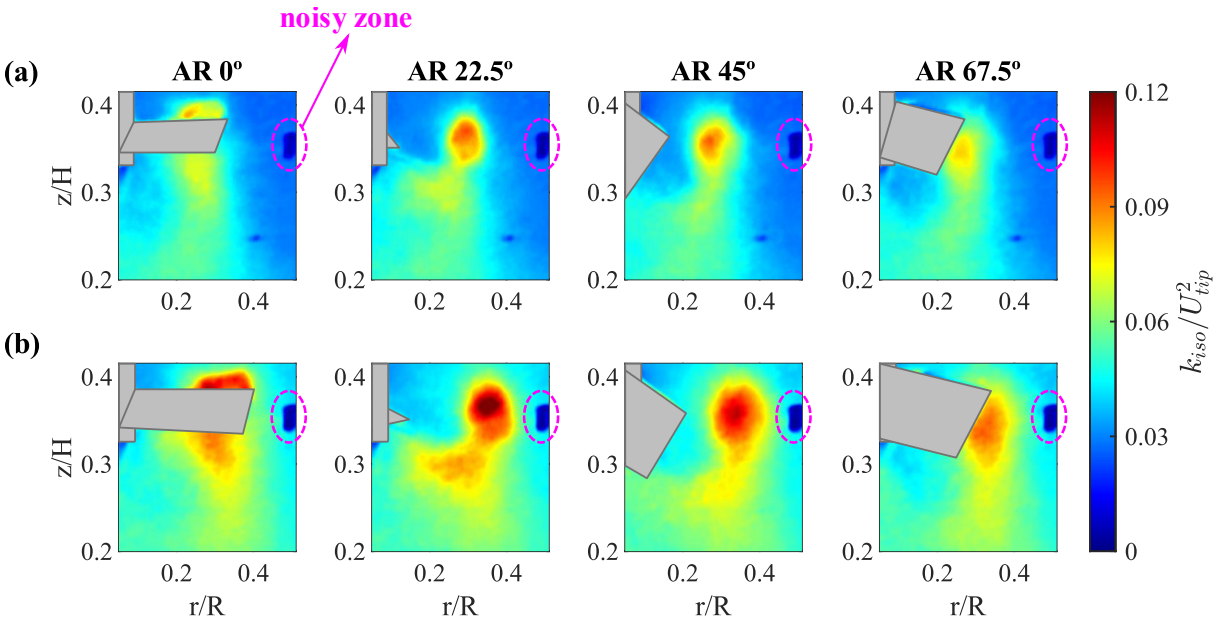

Slight variations between the TKE computed considering the pseudo-isotropic approximation and the one estimated from Stereo-PIV measurements can be better observed in Figure 5.13, that presents the relative difference between k_{3C} and k_{iso} for the flows generated by (a) RU01, (b) RU02, (c) PBT01 and (d) PBT02. We observed that the divergences in general are between 0% and 25% for all fields and blade angles, excepted in the noisy zone, where a higher difference was already expected since this zone appeared only in the TKE fields obtained from Classic PIV. For RU01, we also verified a region with higher values close to the impeller tip at AR 15º. This is the same region where higher values of the percentual contribution of the out-of-plane component were noted (Figure A.7).

Figure 5.13: Relative difference between the TKE values obtained from Stereo-PIV (k_{3C}) and Classic PIV considering pseudo-isotropic approximation (k_{iso}) for different blade angles of (a) RU01, (b) RU02, (c) PBT01 and (d) PBT02. Highlighted in pink: noisy zone.

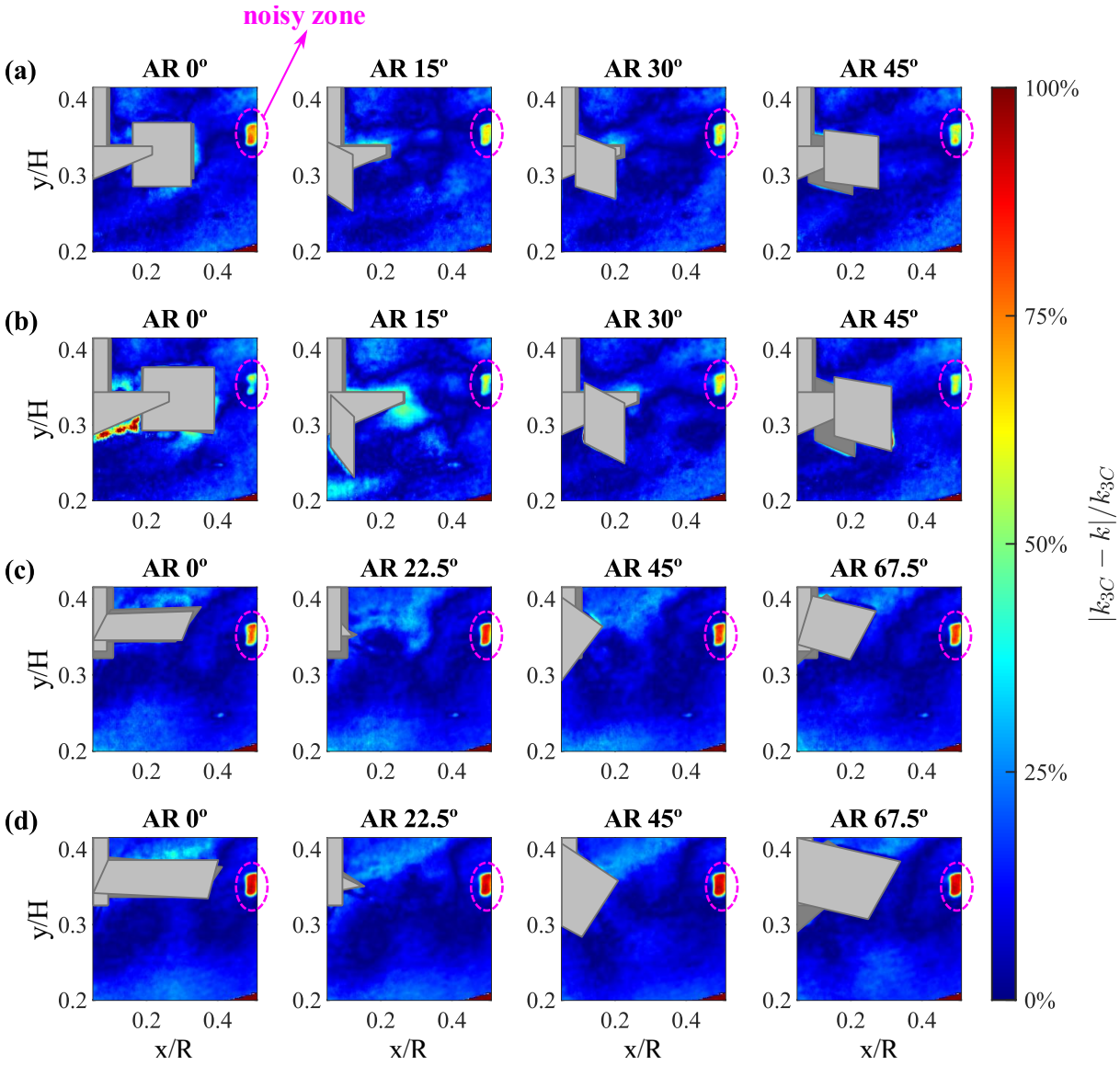

In this section, we verified that the approach considering Classic PIV data and the pseudo-isotropic approximation led to similar results of TKE that the approach regarding Stereo-PIV measurements for different flow patterns and independent experiments. Thus, it was possible to obtain TKE fields with good quality from Classic PIV data combined with the pseudo-isotropic approximation, which is simpler and requires lower operating and processing costs compared to Stereo-PIV data. Also, it is important to observe that because there is a lack of knowledge of the out-of-plane component, the employment of the Classic PIV approach only works suitable when the pseudo-isotropic approximation is considered.

5.4.3. Tilted PIV Measurements

In the following, we present the results obtained from Tilted PIV measurements performed with camera 1 as described in Figure 4.1. The turbulent kinetic energy fields estimated from Tilted PIV measurements considering (a) the pseudo-isotropic approximation ($k_{iso_{tPIV}}$) and (b) axial and combined-radial components (k_{2C}) for the flow promoted by Rushton turbines are displayed in Figure 5.14 for RU01 and in Figure 5.15 for RU02. The first observation is that the greater inclination of the camera did not influence the analysis of the flow pattern promoted by the impellers, because the radial turbulent kinetic energy stream moving from the region near the impeller (at AR 0º) to the side limit of the observation field (at AR 45º) could be clearly observed for both considerations. Also, the movement is similar to the one verified from Stereo-PIV (Figure 5.9) and from Classic PIV measurements (Figure 5.11).

The TKE fields considering the pseudo-isotropic approximation (Figure 5.14a and Figure 5.15a) seem to show overestimated results compared with the TKE computed from Stereo-PIV and Classic PIV data. The maximum value observed was $0.22 \times U_{tip}^2$ at AR 30º for RU01 and $0.29 \times U_{tip}^2$ at AR 30º for RU02, which is 37.5% and 45% higher than the values verified from the other datasets, respectively. On the other hand, the fields estimated by axial and combined-radial components (Figure 5.14b and Figure 5.15b) led to values similar to the ones obtained from Stereo-PIV and Classic PIV. The maximum verified was $0.15 \times U_{tip}^2$ at AR 30º for RU01 and $0.19 \times U_{tip}^2$ at AR 30º for RU02, which agrees with the maximums described earlier in this work.

Figure 5.14: Normalized turbulent kinetic energy obtained from Tilted PIV measurements considering (a) pseudo-isotropic approximation ($k_{iso_{tPIV}}$) and (b) axial and combined-radial components (k_{2C}) for different blade angles of RU01.

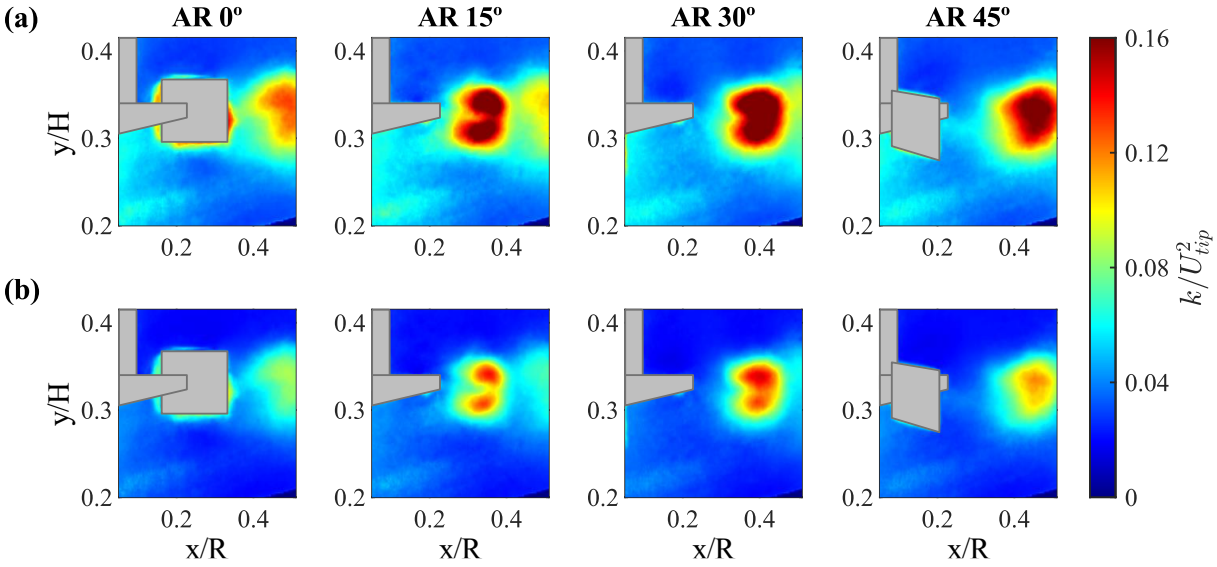

Figure 5.15: Normalized turbulent kinetic energy obtained from Tilted PIV measurements considering (a) pseudo-isotropic approximation ($k_{iso_{tPIV}}$) and (b) axial and combined-radial components (k_{2C}) for different blade angles of RU02.

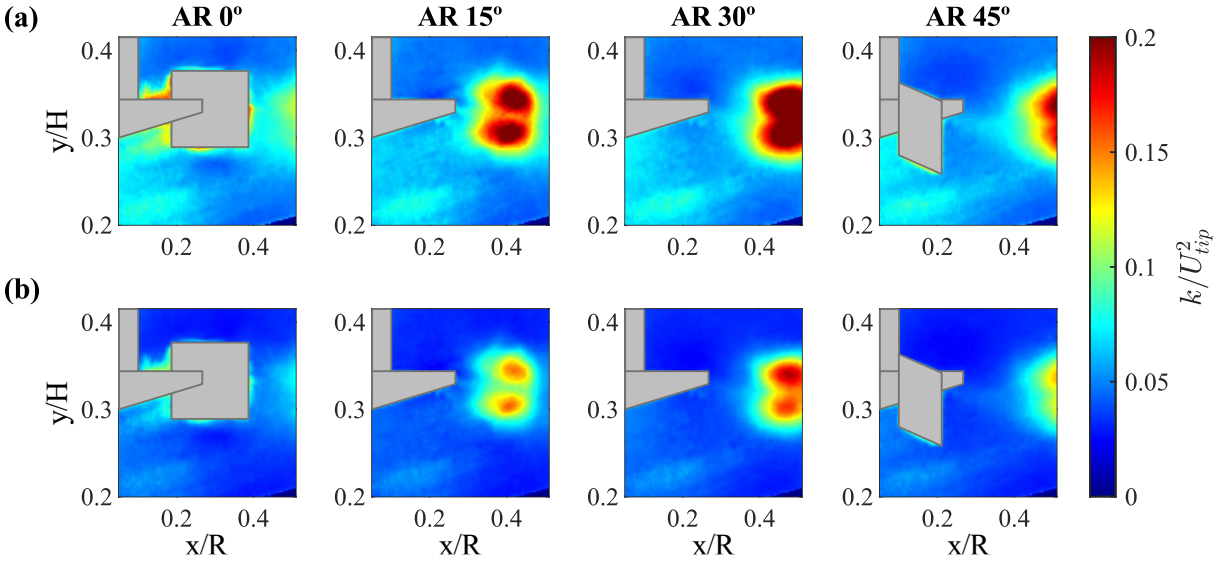

The relative difference between the TKE values estimated from Stereo-PIV and Tilted PIV measurements are shown in Figure 5.16 for RU01 and Figure 5.17 for RU02. The fields computed with the pseudo-isotropic approximation (Figure 5.16a and Figure 5.17a) presented differences, in general, between 32% and 53% for RU01 and between 28% and 54% for RU02 in most of the fields, which can be explained due to overestimating of the TKE inherent to the approximation. On the other hand, the fields computed directly by the two

measured components (Figure 5.16b and Figure 5.17b) demonstrated relative differences, in general, between 3% and 18% for RU01 and between 3% and 25% for RU02 considering all the blade angles. For RU02, a small region with higher values can be observed at AR 15º; however, is it the same region verified in the relative differences between Stereo-PIV and Classic PIV measurements (Figure 5.13b), which was correlated with the higher values of the percentual contribution of the out-of-plane component (Figure A.7c).

Figure 5.16: Relative difference between the TKE values obtained from Stereo-PIV and Tilted PIV measurements considering (a) pseudo-isotropic approximation ($k_{iso_{tPIV}}$) and (b) axial and combined-radial components (k_{2C}) for different blade angles of RU01.

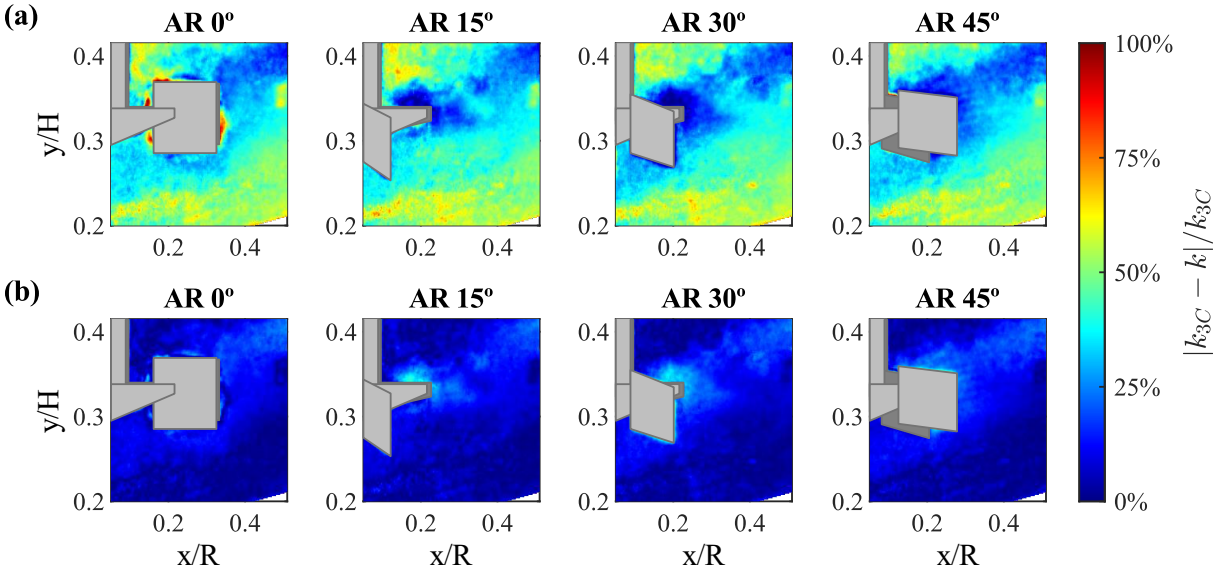

Figure 5.17: Relative difference between the TKE values obtained from Stereo-PIV and Tilted PIV measurements considering (a) pseudo-isotropic approximation ($k_{iso_{tPIV}}$) and (b) axial and combined-radial components (k_{2C}) for different blade angles of RU02.

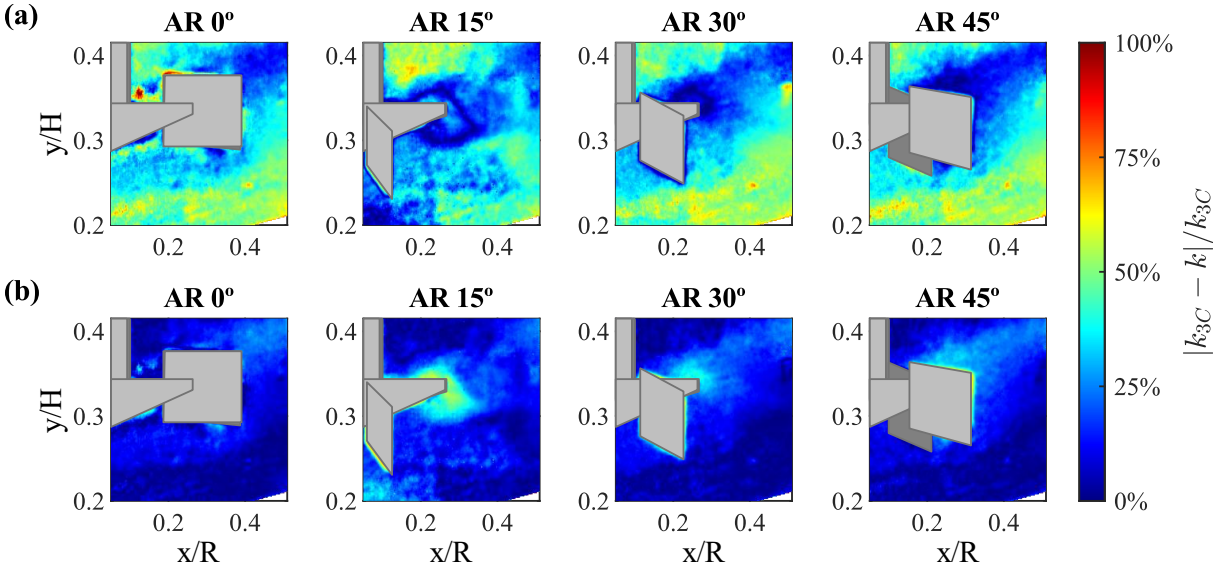

Similar results were verified when analyzing the relative difference between the TKE estimated from Classic PIV and Tilted PIV data (Figure 5.18 for RU01 and Figure 5.19 for RU02). We verified that the relative differences for the TKE fields estimated considering the pseudo-isotropic approximation (Figure 5.18a and Figure 5.19a) varied, in general, from 26% to 48% for RU01 and from 25% to 55% for RU02. However, for the TKE fields computed directly from axial and combined-radial components (Figure 5.18b and Figure 5.19b), the relative differences altered only from 8% to 22% for RU01 and between 8% and 25% for RU02. It is important to notice that, in the fields of the Figure 5.18 and Figure 5.19, the noisy zone can be observed because it appeared in the TKE fields obtained from Classic PIV measurements, but it is not verified in the fields obtained from Tilted PIV data.

Figure 5.18: Relative difference between the TKE values obtained from Classic PIV considering pseudo-isotropic approximation (k_{iso}) and Tilted PIV measurements considering (a) pseudo-isotropic approximation ($k_{iso\,tPIV}$) and (b) axial and combined-radial components (k_{2C}) for different blade angles of RU01. Highlighted in pink: noisy zone.

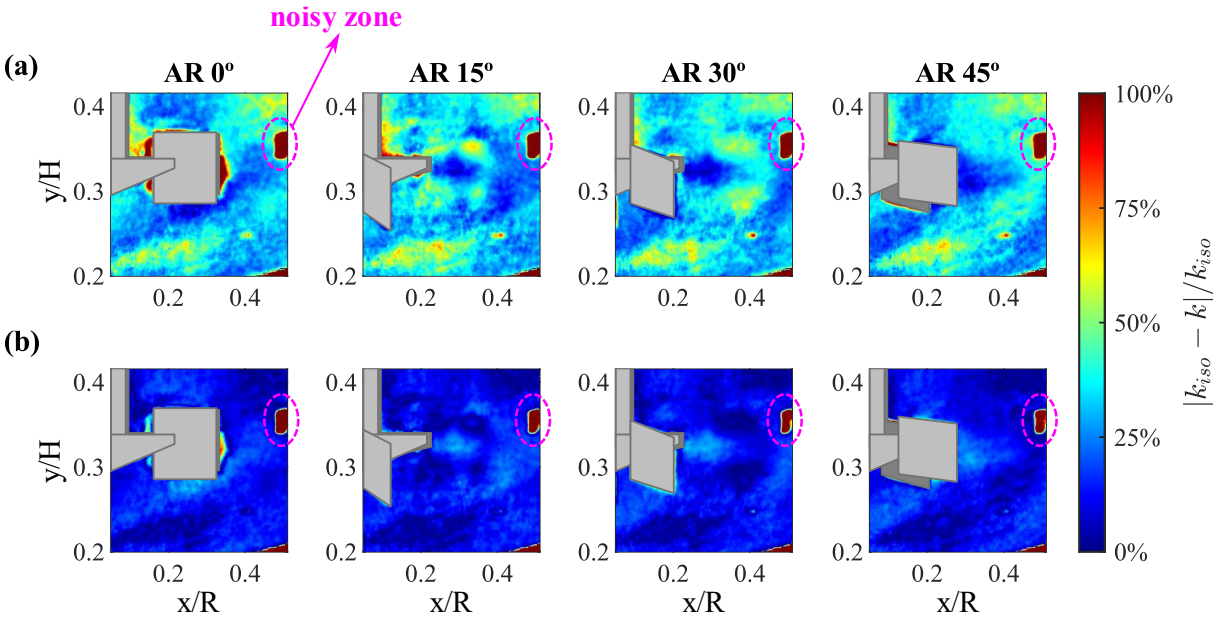

Figure 5.19: Relative difference between the TKE values obtained from Classic PIV considering pseudo-isotropic approximation (k_{iso}) and Tilted PIV measurements considering (a) pseudo-isotropic approximation ($k_{iso_{tPIV}}$) and (b) axial and combined-radial components (k_{2C}) for different blade angles of RU02. Highlighted in pink: noisy zone.

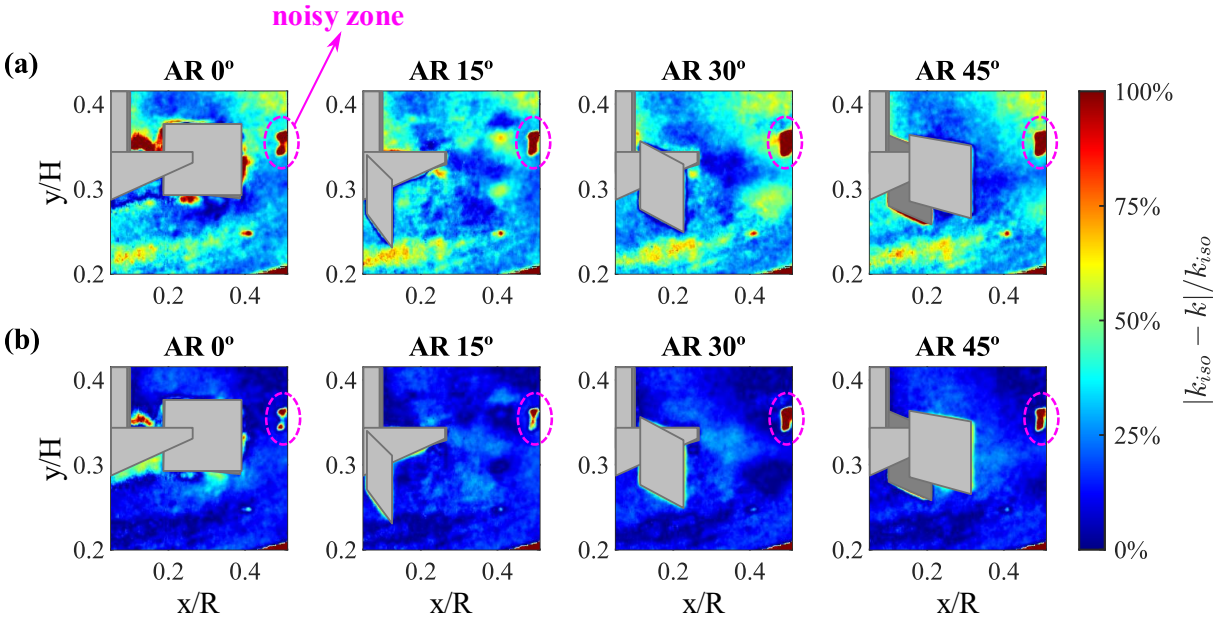

The turbulent kinetic energy fields estimated from Tilted PIV measurements considering (a) pseudo-isotropic approximation ($k_{iso_{tPIV}}$) and (b) axial and combined-radial components (k_{2C}) of the flow generated by the PBT are displayed in Figure 5.20 for PBT01 and in Figure 5.21 for PBT02. Analogously to the assessment of the flow promoted by the Rushton turbines, the more tilted position of the camera did not affect the visualization of the axial and slightly inclined flow pattern promoted by the PBT. In addition, there was also no effect on the evaluation of the region with the highest TKE, which follows the movement of the drag vortices.

The maximum values observed were $0.11 \times U_{tip}^2$ at AR 22.5º for PBT01 and $0.15 \times U_{tip}^2$ at AR 22.5º for PBT02, both regarding the method $k_{iso_{tPIV}}$. Thus, the estimation considering the pseudo-isotropic approximation ($k_{iso_{tPIV}}$) overestimated the TKE values. In fact, for PBT01, the maximum value is 37.5% and 10% higher than observed from Stereo-PIV and Classic PIV, respectively. Also, for PBT02, the maximum value raised 36% and 15% when compared to the maximum value observed in Stereo-PIV and Classic PIV data. On the other hand, the estimation regarding axial and combined-radial components (k_{2C}) showed a maximum value of $0.07 \times U_{tip}^2$ at AR 22.5º for PBT01 and $0.10 \times U_{tip}^2$ at AR 22.5º for PBT02, in agreement with the data obtained from Stereo-PIV and Classic PIV measurements.

Figure 5.20: Normalized turbulent kinetic energy obtained from Tilted PIV measurements considering (a) pseudo-isotropic approximation ($k_{iso_{tPIV}}$) and (b) axial and combined-radial components (k_{2C}) for different blade angles of PBT01.

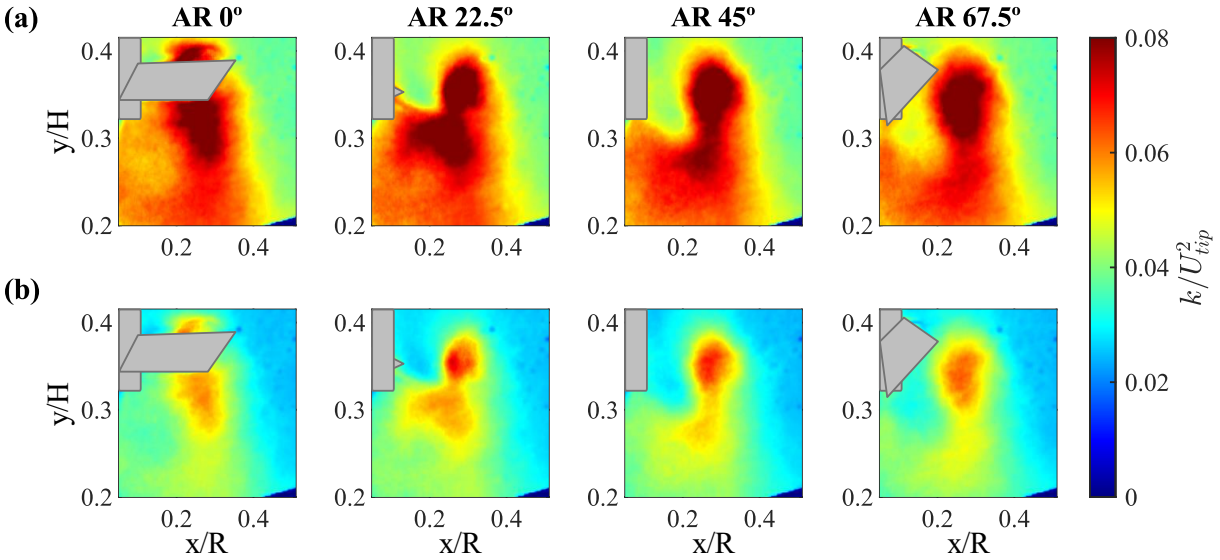

Figure 5.21: Normalized turbulent kinetic energy obtained from Tilted PIV measurements considering (a) pseudo-isotropic approximation ($k_{iso_{tPIV}}$) and (b) axial and combined-radial components (k_{2C}) for different blade angles of PBT02.

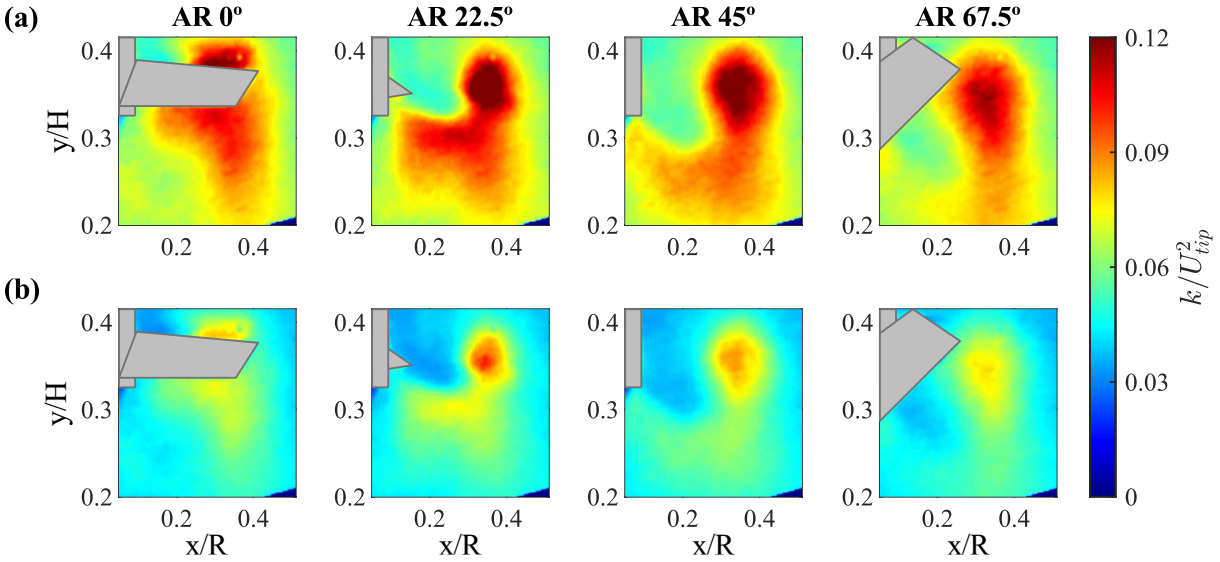

The relative difference between the TKE computed from Stereo-PIV measurements and the estimated (a) considering the pseudo-isotropic approximation ($k_{iso_{tPIV}}$) and (b) axial and combined-radial components (k_{2C}) are displayed in Figure 5.22 and Figure 5.23 for PBT01 and PBT02, respectively. Clearly, the second consideration led to values much closer to those obtained from Stereo-PIV measurements than the pseudo-isotropic approximation. The percentage differences are between 3% and 14% for all the blade angles over most of the fields

and considering both impellers. The pseudo-isotropic approximation, in turn, led to differences, in general, between 34% and 54% for PBT01 and 35% and 56% for PBT02 for all blade angles. Greater discrepancies were found in the region above the impeller, where the relative difference can reach 90% at AR 0° for PBT01 and 87% at the same blade angle for PBT02.

Figure 5.22: Relative difference between the TKE values obtained from Stereo-PIV and Tilted PIV measurements considering (a) pseudo-isotropic approximation ($k_{iso_{tPIV}}$) and (b) axial and combined-radial components (k_{2C}) for different blade angles of PBT01.

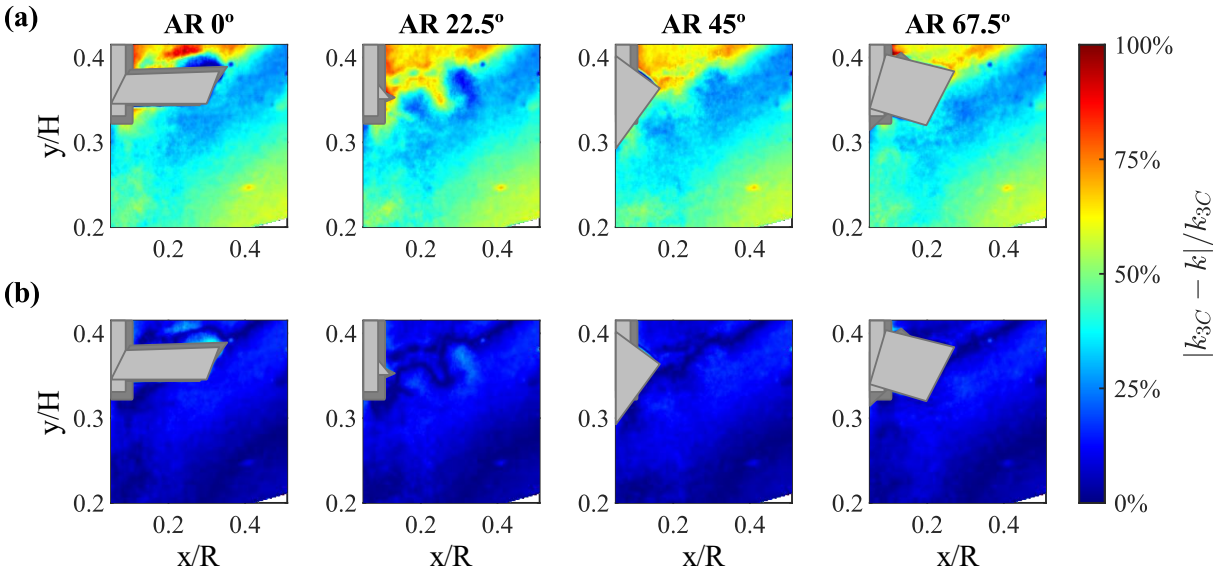

Figure 5.23: Relative difference between the TKE values obtained from Stereo-PIV and Tilted PIV measurements considering (a) pseudo-isotropic approximation ($k_{iso_{tPIV}}$) and (b) axial and combined-radial components (k_{2C}) for different blade angles of PBT02.

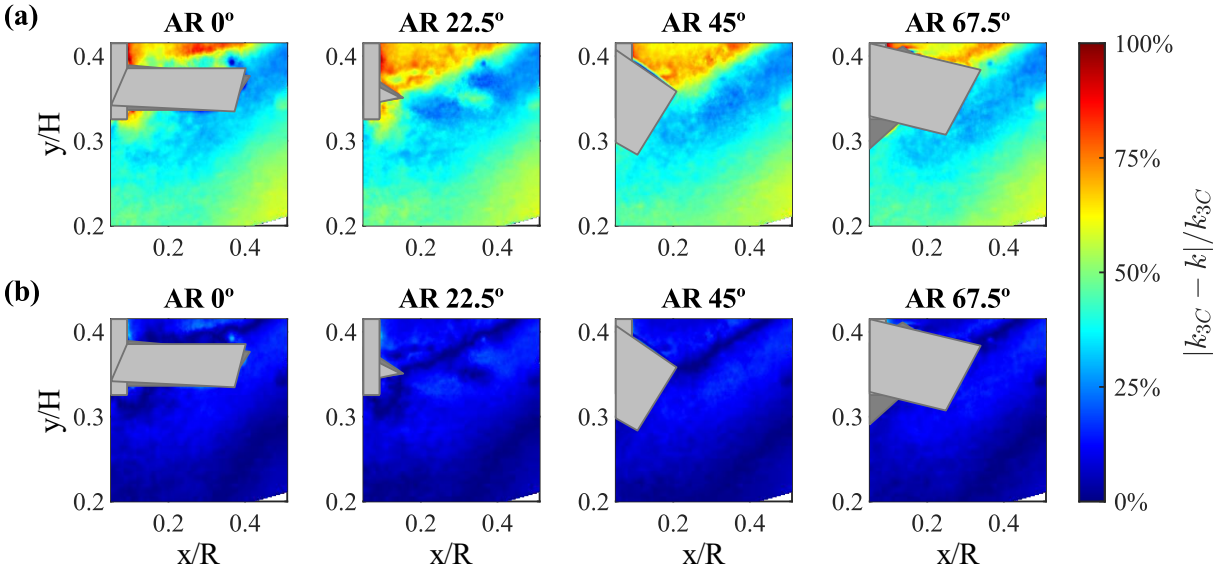

Similarly, we verified that the comparison between the TKE values estimated from Classic PIV and Tilted PIV also led to comparable results (Figure 5.24 for PBT01 and Figure 5.25 for PBT02). The relative differences between the TKE values are between 23% and 42% for PBT01 and 26% and 42% for PBT02 when the fields compared k_{iso} and $k_{iso_{tPIV}}$, while the fields that set against k_{iso} and k_{2C} showed results between 7% and 21% for both impellers. Analogous to the fields obtained from the flow promoted by the Rushton turbines, the noisy zone can be observed in this case because it is only present in Classic PIV measurements.

Figure 5.24: Relative difference between the TKE values obtained from Classic PIV considering pseudo-isotropic approximation (k_{iso}) and Tilted PIV measurements considering (a) pseudo-isotropic approximation ($k_{iso_{tPIV}}$) and (b) axial and combined-radial components (k_{2C}) for different blade angles of PBT01. Highlighted in pink: noisy zone.

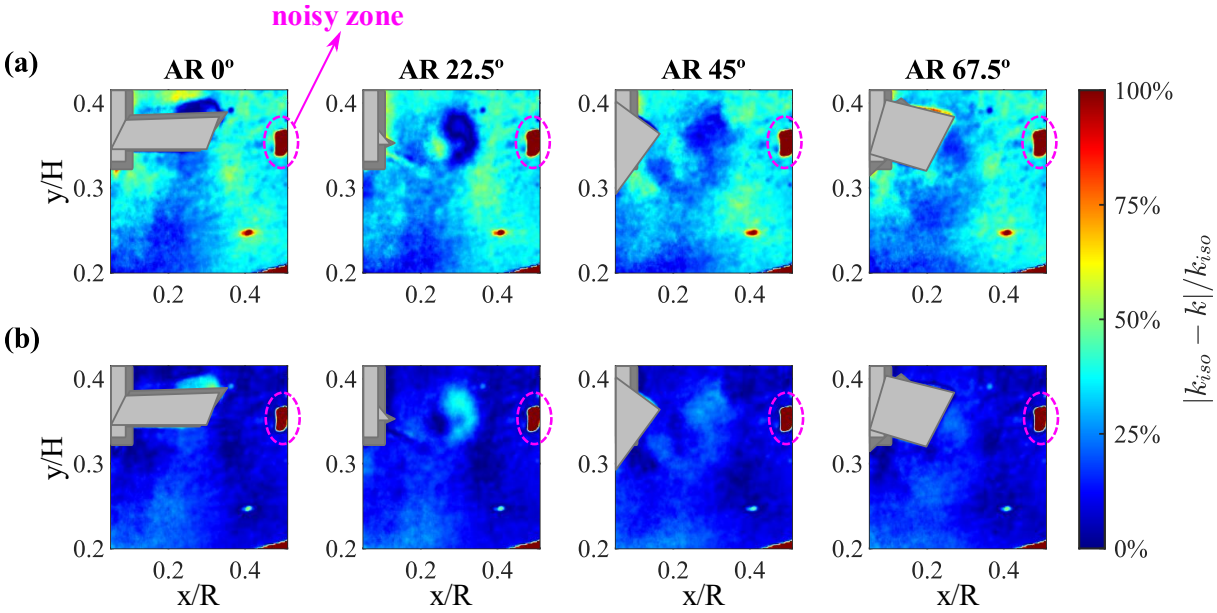

Figure 5.25: Relative difference between the TKE values obtained from Classic PIV considering pseudo-isotropic approximation (k_{iso}) and Tilted PIV measurements considering (a) pseudo-isotropic approximation ($k_{iso_{tPIV}}$) and (b) axial and combined-radial components (k_{2C}) for different blade angles of PBT02. Highlighted in pink: noisy zone.

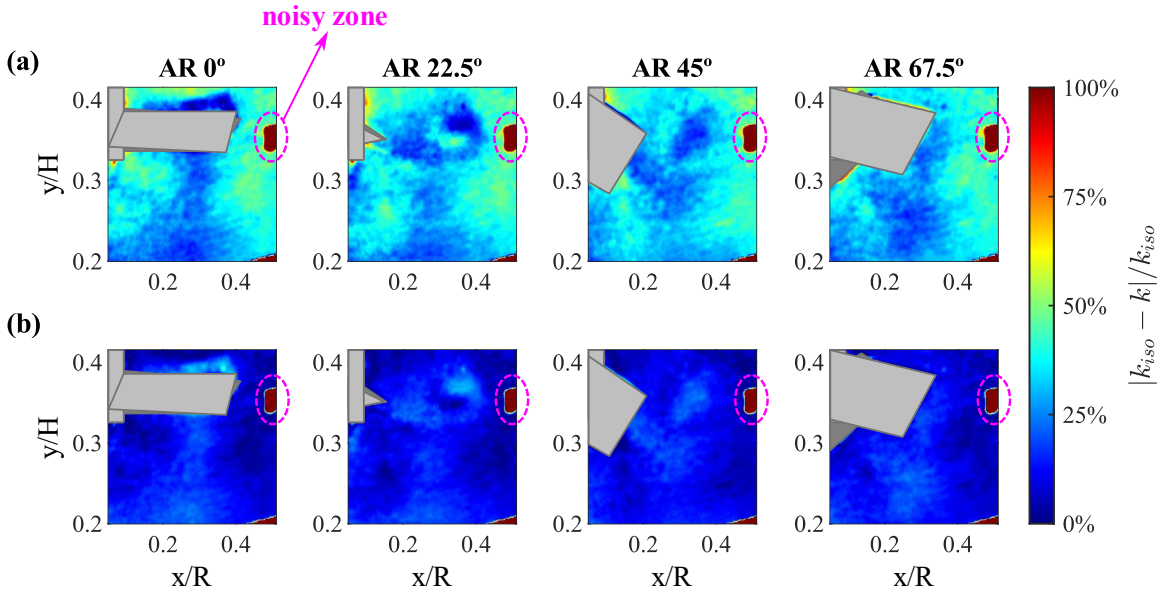

For the purpose to carry out a more in-depth quantitative comparison, horizontal profiles of the normalized turbulent kinetic energy estimated by the three approaches presented in this work were evaluated for the flow promoted by all the impellers. Figure 5.26 and Figure 5.27 shows the profiles for RU01 and RU02, while Figure 5.28 and Figure 5.29 presents the profiles for PBT01 and PBT02. We select one axial position above the impeller (y/H = 0.39 for the Rushton impellers and y/H = 0.39 for the pitched blade turbines), two positions on the impeller stream (y/H = 0.34 and y/H = 0.30 for Rushton turbines; y/H = 0.35 and y/H = 0.29 for pitched blade turbines) and one position below the impeller (y/H = 0.24 for all impellers). In these figures, the impeller and shaft are not masked, so different lines mark the limit of the impeller blades for each approach: Classic PIV (camera 2) and Tilted PIV (camera 1). If the lines are not present, it means that the impeller is not interfering the image record.

Figure 5.26: Comparison of normalized turbulent kinetic energy axial profiles estimated from the approaches Stereo-PIV considering all three root-mean-square of the velocity fluctuations, Classic PIV regarding pseudo-isotropic approximation and Tilted PIV considering axial and combined-radial components for different blade angles of RU01. The left side of the lines is a noisy region due to the presence of the impeller.

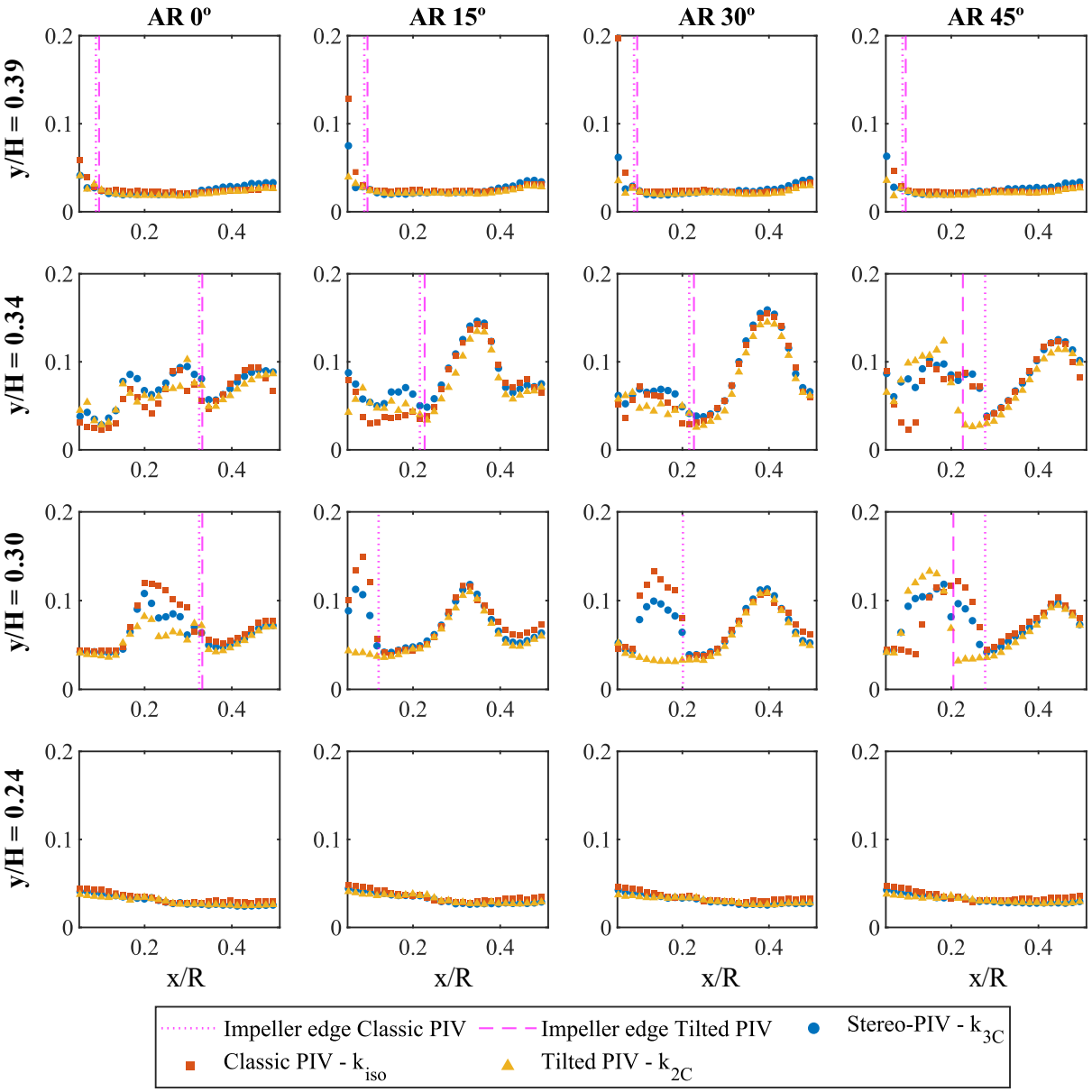

Figure 5.27: Comparison of normalized turbulent kinetic energy axial profiles estimated from the approaches Stereo-PIV considering all three root-mean-square of the velocity fluctuations, Classic PIV regarding pseudo-isotropic approximation and Tilted PIV considering axial and combined-radial components for different blade angles of RU02. The left side of the lines is a noisy region due to the presence of the impeller.

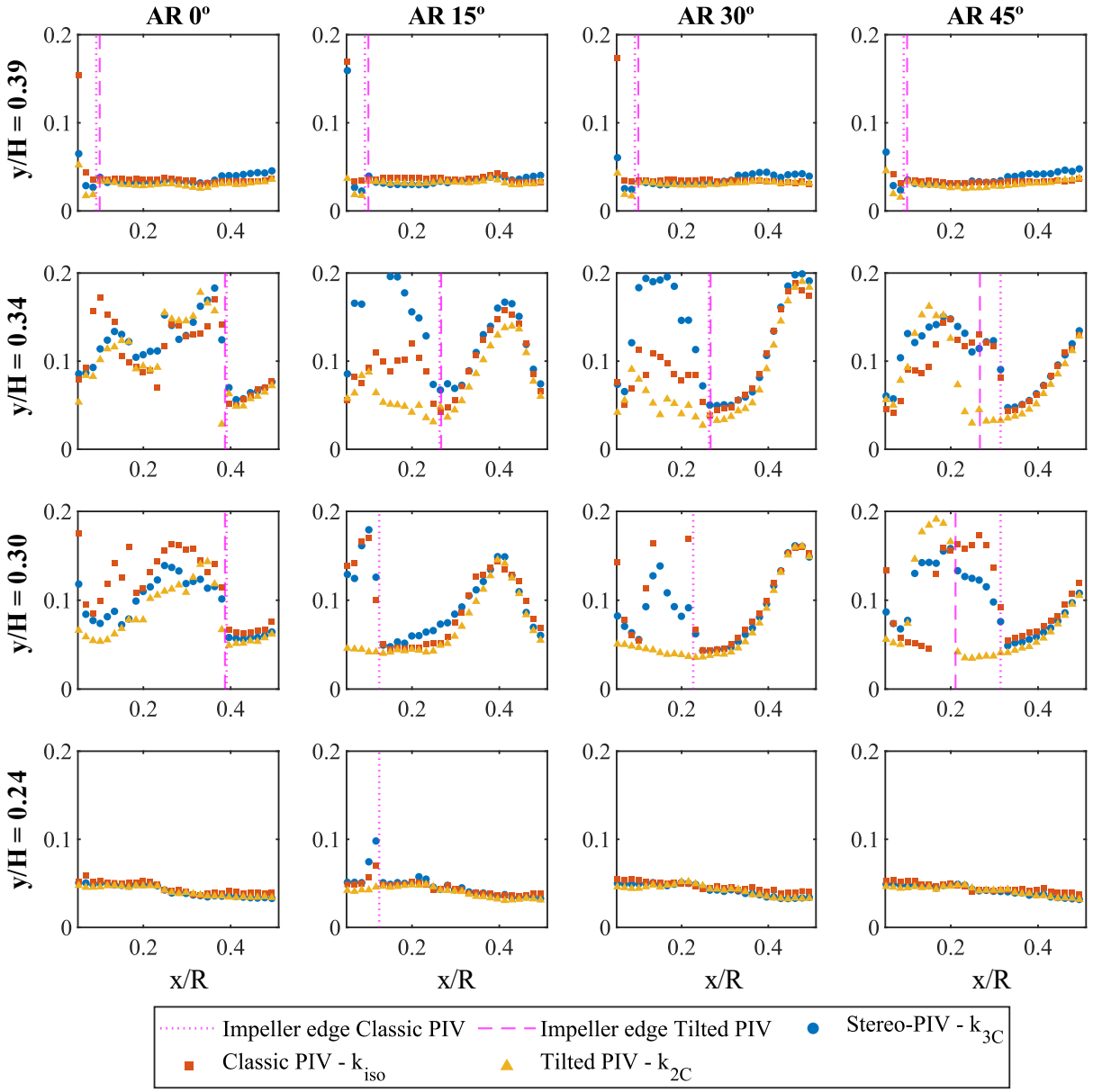

Figure 5.28: Comparison of normalized turbulent kinetic energy axial profiles estimated from the approaches Stereo-PIV considering all three root-mean-square of the velocity fluctuations, Classic PIV regarding pseudo-isotropic approximation and Tilted PIV considering axial and combined-radial components for different blade angles of PBT01. The left side of the lines is a noisy region due to the presence of the impeller.

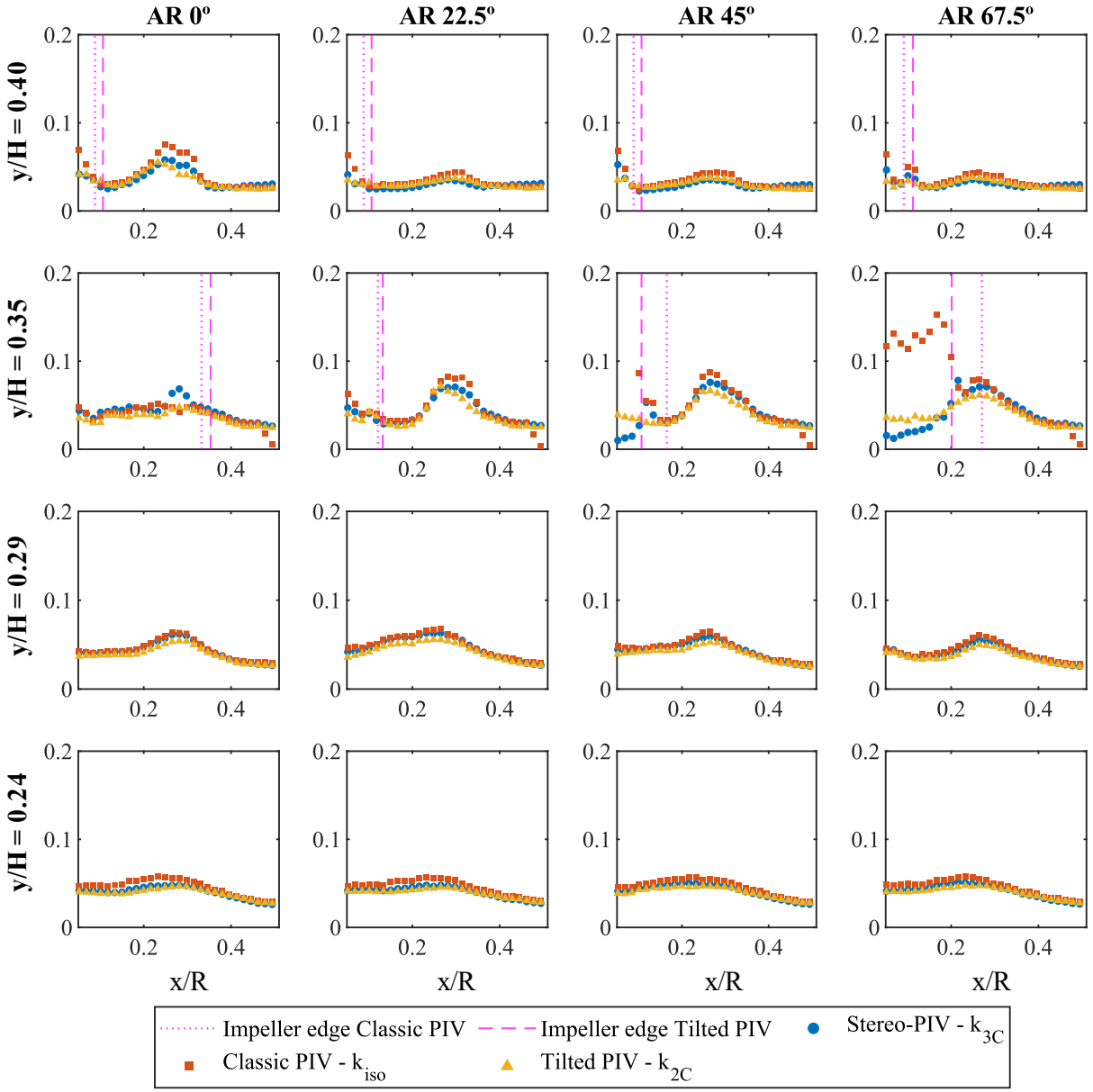

Figure 5.29: Comparison of normalized turbulent kinetic energy axial profiles estimated from the approaches Stereo-PIV considering all three root-mean-square of the velocity fluctuations, Classic PIV regarding pseudo-isotropic approximation and Tilted PIV considering axial and combined-radial components for different blade angles of PBT02. The left side of the lines is a noisy region due to the presence of the impeller.

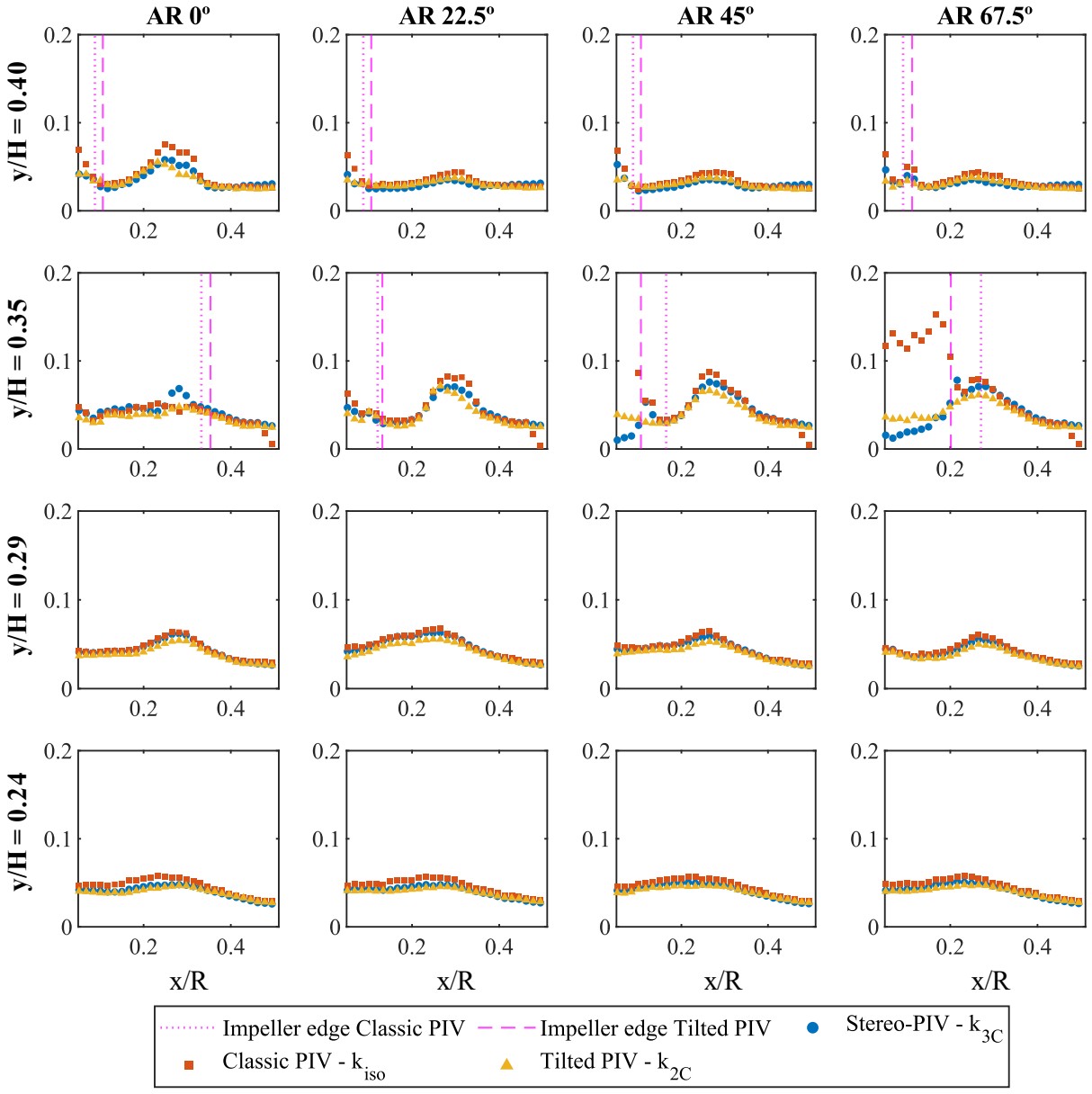

We can observe a lack of spatial coherence between the regions on the left and right side of the lines in all figures that the lines are present. Deviations among values on the left side are large and erratic, while on the right side they are small and smooth. As we ensure the statistical convergence of the results with 1000 pairs of images, we can confirm that the lack of coherence is not correlated with sampling errors, but with noisy sources due to the presence of the impeller and shaft. The highest differences between the cameras optical accesses are at AR 30° and AR 45º for the Rushton turbines and at AR 45º and AR 67.5º for the pitched blade turbines. In these situations, the access of Tilted PIV is, in general, larger than of Classic PIV, because the limit of the impeller blade is at a smaller distance in relation to the shaft.

On the region after the impeller edges (right side), for all selected positions the differences among the approaches are very small. It confirms that all approaches were able to satisfactorily estimate the distribution of turbulent kinetic energy in the stirred tank, even considering independent experiments and different flow patterns. It is also important to emphasize that the measurements were obtained simultaneously, thus minimizing systematic errors of the equipment.

In addition to the analysis discussed in this section, we verified that Tilted PIV approach has the advantage of acquiring images from a perspective that reduces the distortion caused by the rounded tank wall. This was observed during the calibration procedure based on the work of Soloff *et al.* (1997), in which the identification of the points in the calibration target was easier for the camera 1 (Tilted PIV). On the other hand, the image of the points recorded by the camera 2 (Classic PIV) presented a small elongation, demanding an increase of tolerance in the identification procedure (Figure 5.30). More details about these observations can be found in the study of Barbutti *et al.* (2020).

Besides, we verified that the tilted position allows acquiring the effect of the out-of-plane component on the turbulent kinetic energy, avoiding the consideration of the pseudo-isotropic approximation on the estimation from Tilted PIV data. Tilted PIV can be an appropriate approach in situations of difficult optical access, in which the more inclined position may furtherance the implementation of PIV techniques. The approach can be employed, for example, in industrial applications, when only a small field of visualization is available to display the laser light sheet and the camera to acquire images.

Figure 5.30: Raw images of the calibration target for the camera 1 (Cam 1) and camera 2 (Cam 2) highlighting two regions: close to the shaft (R1) and near the tank's wall (R2).

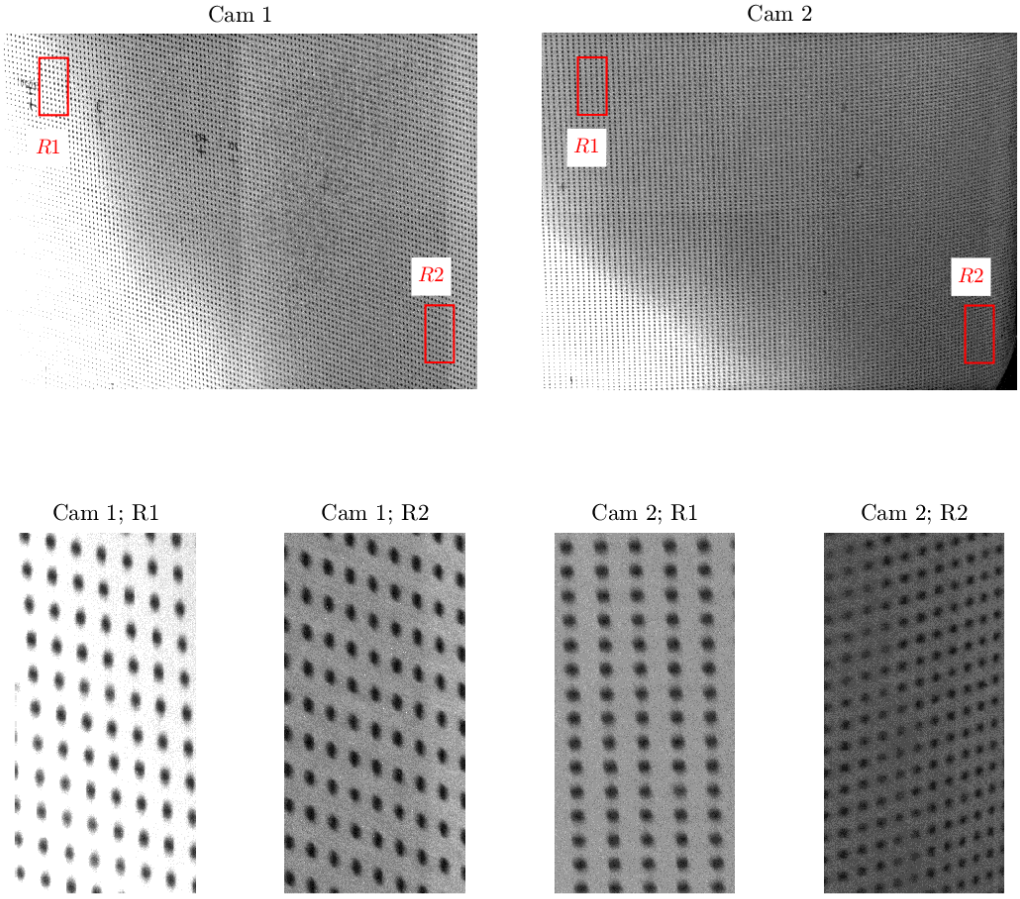

Source: Barbutti *et al.* (2020).

The combination of the cameras at different positions compensated the misleading in the noisy zone related to the light reflections from different parts of the equipment and led to more robust Stereo-PIV data. In fact, we can observe in Figure 5.28 and Figure 5.29 that the axial profile at y/H = 0.35 encompassed some results of the noisy zone after x/R = 0.46. It is possible to verify that the Stereo-PIV presented valid results because they are coherent with the value before this zone. Tilted PIV approach presented results vary similar to the values verified for Stereo-PIV data. However, the results showed that Classic PIV approach failed to estimate the TKE values in this area due to the lack of information originated in the reflection registered by the camera 2. Figure 5.26-29 also highlighted the high difficulty of using the Stereo-PIV approach, since it is not possible to simultaneously guarantee quality acquisitions by both cameras in the same region with different perspectives. Moreover, Tilted and Classic PIV can be used as complementary approaches when, for example, the effect of baffle position is investigated, due to the different optical accesses.

5.5. Quality of PIV Measurements

The quality of the PIV measurements is crucial to validate the phenomena observed in the analysis of the flows promoted by the impellers in the stirred tank. The quality analysis of Stereo-PIV, Classic PIV and Tilted PIV measurements were performed by evaluating the signal-to-noise ratio (SNR), the 3C reconstruction error and the uncertainty quantification. This section presents the results and critical discussion of this assessment.

5.5.1. Signal-to-noise Ratio

The time-averaged signal-to-noise ratio (SNR) fields of the measurements performed by camera 2 and camera 1 of the flow promoted by the RU01, RU02, PBT01 and PBT02 are shown in Figure 5.31, Figure 5.32, Figure 5.33 and Figure 5.34, respectively. For both Rushton turbines, the fields of camera 2 presented values between 1.3 and 2.0 at all blade angles. Camera 1, in turn, showed ratios between 1.7 and 3.4, with higher values in the region above the impellers. The fields of the flow induced by PBT01 displayed results between 1.2 and 1.8 for camera 2, and between 1.3 and 2.2 for camera 1. We can also observe that the fields for PBT02 varied from 1.3 to 2.1 for camera 2 and from 1.5 to 3.7 for camera 1.

Hain and Kähler (2007) commented in their work on multiframe PIV that numerical studies indicate ratios of about 2.0 reliably avoid spurious vectors. Roy *et al.* (2010) defined SNR as a measure of the confidence of the most probable vector compared to the second most probable vector. The authors considered that values above 1.2 indicate a good degree of confidence when assessing the flow structures in a tank stirred by a PBT. Xue *et al.* (2014) also considered that the value of 1.2 is generally used as a threshold for the detectability of true displacements. Barbutti *et al.* (2021) found noise below 0.5% for threshold between 1.75 and 2.5. However, thresholds above 2.5 showed large valid vectors losses. Based on these analyses and considering the results observed in the SNR fields, we verified that both cameras presented robust measurements and good quality in all experiments carried out in this work.

Figure 5.31: Time-averaged signal-to-noise ratio (SNR) of (a) camera 2 and (b) camera 1 acquisitions for different blade angles of RU01. Highlighted in pink: noisy zone.

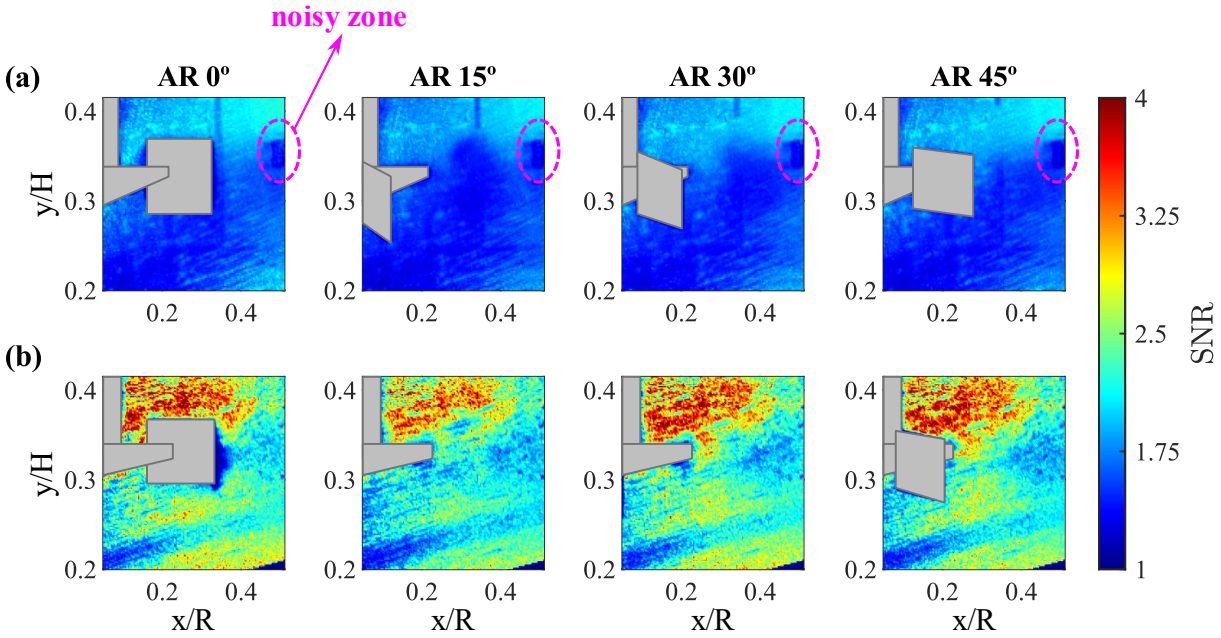

Figure 5.32: Time-averaged signal-to-noise ratio (SNR) of (a) camera 2 and (b) camera 1 acquisitions for different blade angles of RU02. Highlighted in pink: noisy zone.

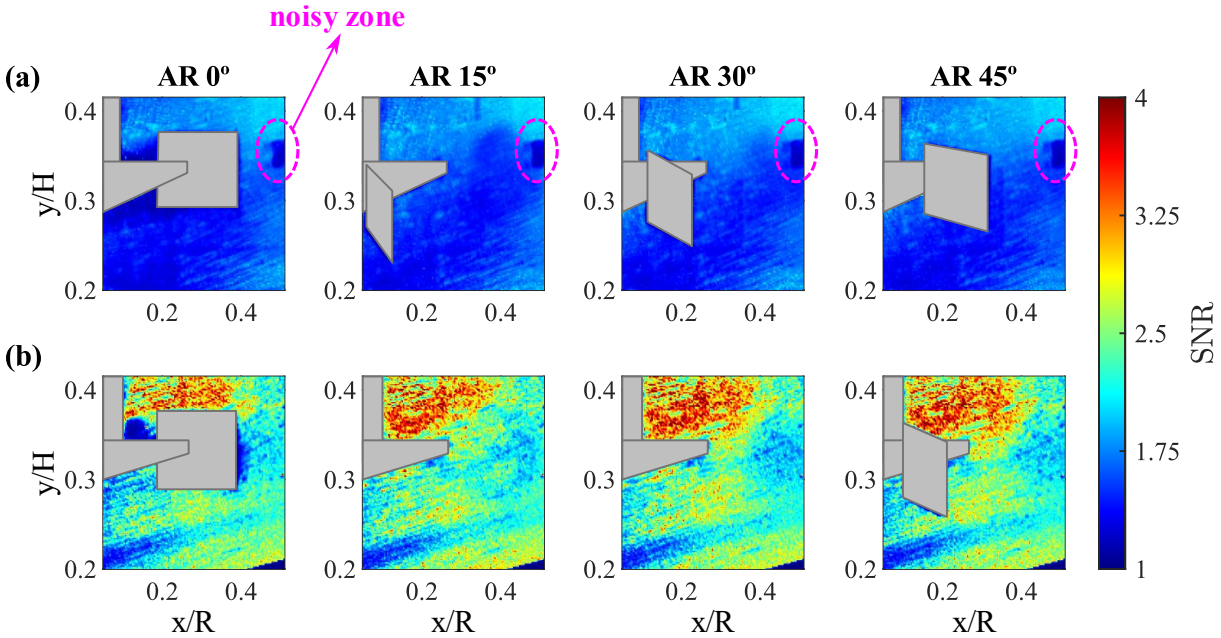

Figure 5.33: Time-averaged signal-to-noise ratio (SNR) of (a) camera 2 and (b) camera 1 acquisitions for different blade angles of PBT01. Highlighted in pink: noisy zone.

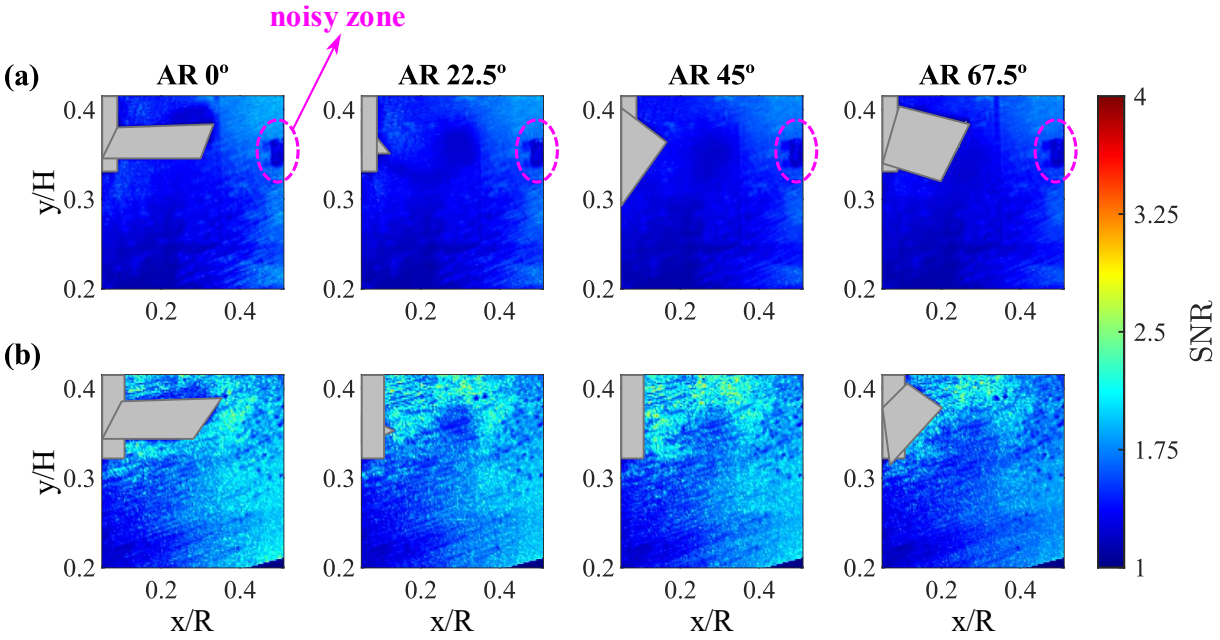

Figure 5.34: Time-averaged signal-to-noise ratio (SNR) of (a) camera 2 and (b) camera 1 acquisitions for different blade angles of PBT02. Highlighted in pink: noisy zone.

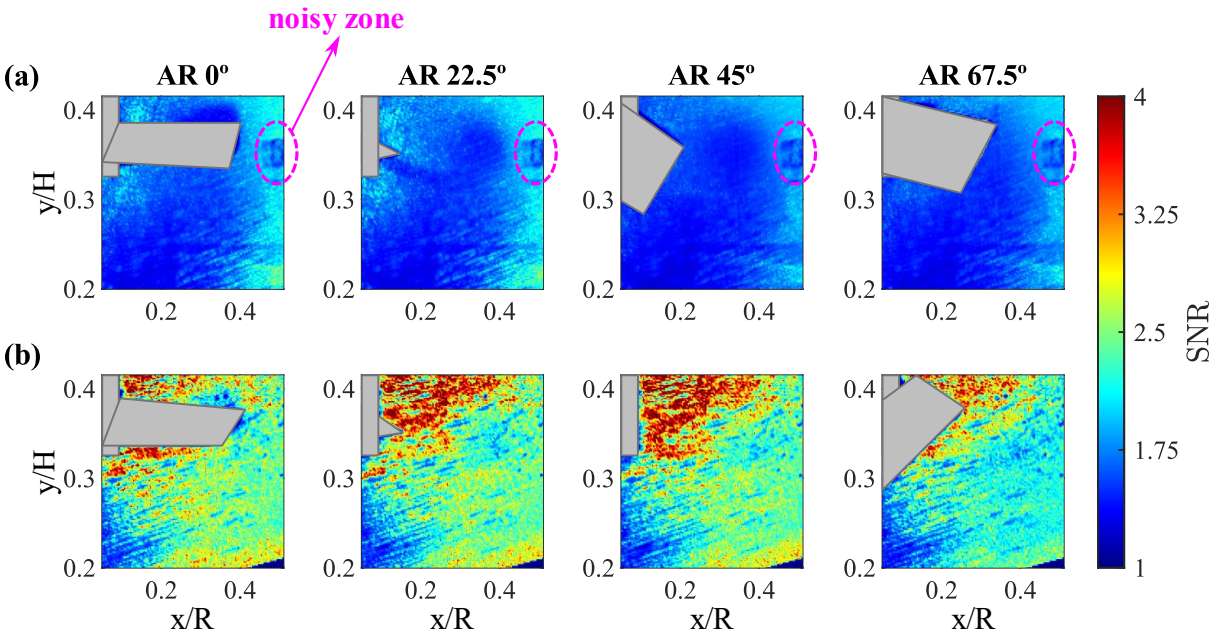

5.5.2. 3C Reconstruction Error

The 3C reconstruction error fields of Stereo-PIV measurements are presented Figure 5.35 for the flow generated by the (a) RU01, (b) RU02, (c) PBT01 and (d) PBT02. It was verified for all blade angles that the 3C reconstruction errors were below 2.5 pixels. The error observed for the Rushton impellers is smaller than for the PBT impellers probably due to the lower rotational speed, which leads to smaller velocity fluctuations.

Figure 5.35: Time-averaged 3C reconstruction error of Stereo-PIV measurements for different blade angles of (a) RU01, (b) RU02, (c) PBT01 and (d) PBT02. Highlighted in pink: noisy zone.

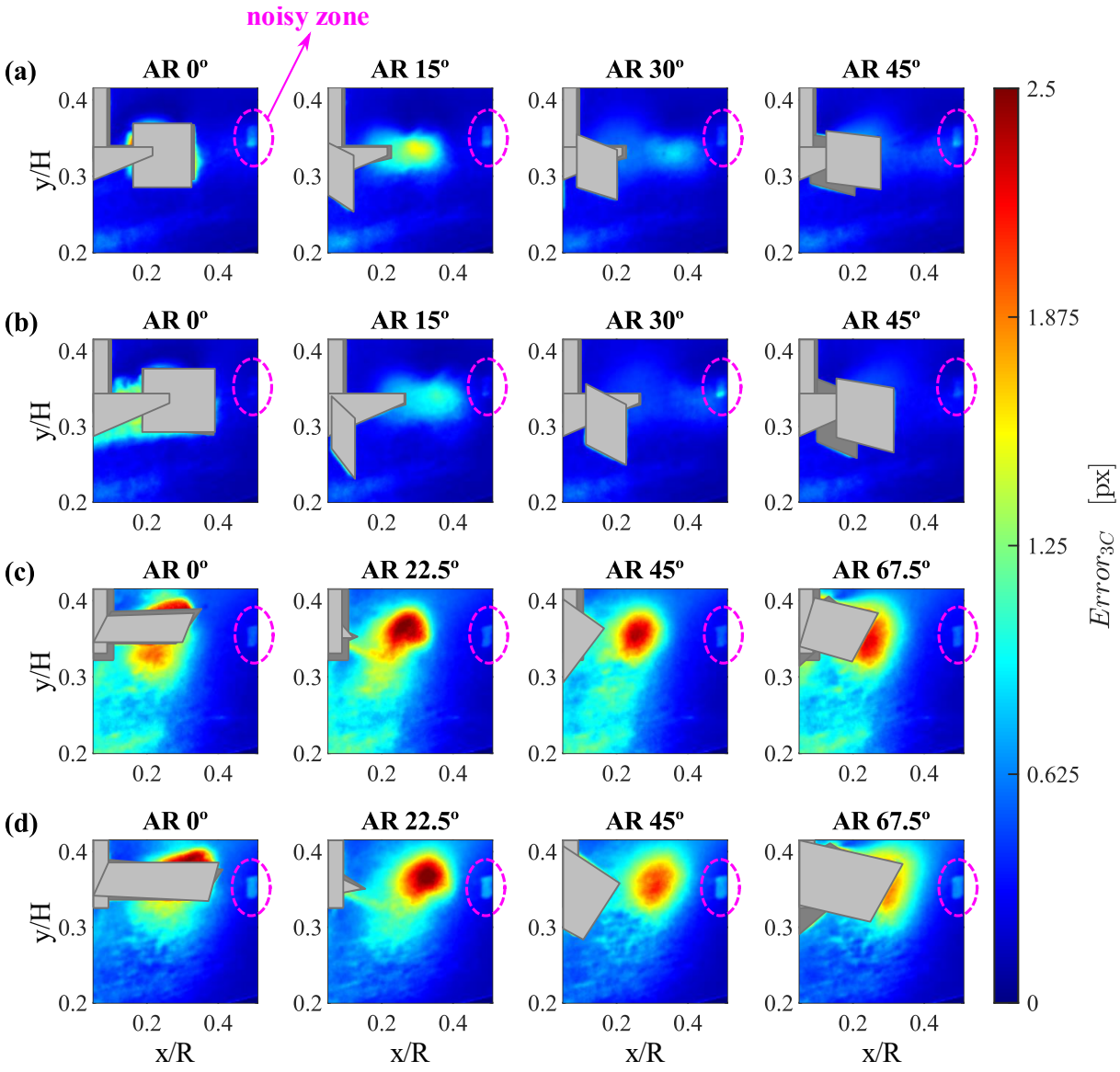

5.5.3. Kolmogorov Scales

The values of the Kolmogorov length scale K_η, integral length scale I_l and the experimental length scale L_{exp} are presented in Table 5.5. It is also possible to observe in this table the values of the power input P and the mean energy dissipation rate $\overline{\varepsilon}$. The power input was obtained in previous works of our research group (AYALA et al., 2022; FREITAS, 2020) by experimental curves of power input as a function of the impeller rotational speed. It is also important to remember that the experimental length scale is the final spatial resolution of the interrogation windows in image processing.

Table 5.5: Comparison among the Kolmogorov (K_η), integral (I_L)and experimental (L) length scales.

Impeller	P (W)	$\overline{\varepsilon}$ (m²/s³)	$K_\eta(\times 10^{-5}\ m)$	$l_l(\times 10^{-1}\ m)$	$L_{exp}\ (\times 10^{-4}\ m)$
RU01	47.75	0.96	3.21	1.72	5.20
RU02	36.48	0.73	3.43	1.81	5.20
PBT01	68.48	1.37	2.93	2.48	5.20
PBT02	61.03	1.22	3.02	2.68	5.20

The results showed that the spatial resolution employed in this work was able to measure the most energize eddies because the experimental scale is lower than the integral scale, which is related to the energetic phenomenon. However, the spatial resolution was not able to reach the smallest eddies, associated with the Kolmogorov scales, because this scale is one order of magnitude lower than the experimental scale. The turbulent kinetic energy is defined as the half of the trace of the Boussinesq-Reynolds tensor. This tensor ultimately stems from momentum transfer by the velocity fluctuations field (POPE, 2000). Thus, in order to properly measure the turbulent kinetic energy, it is not necessary to obtain the smallest eddies, but only the eddies related to the larger scales (SILVEIRA NETO, 2020).

The proper accuracy of the turbulent kinetic energy measurements can also be observed when we take into account the Helland's three-dimensional power spectrum density (PSD) of turbulent kinetic energy (TKE) presented by Saarenrinne et al. (2001). The percentage of correct TKE values for each impeller is shown in Table 5.6. These values were obtained from Figure 4.7 considering the values of the wave number and the Kolmogorov length scale. It is possible to verify that all set of experiments were able to measure at least 97% of correct TKE values.

Table 5.6: Percentage of correct values of TKE in function of the wave number and spatial resolution, according to Helland's three-dimensional energy spectrum.

Impeller	$\lambda_N\ (1/m)$	Δ/K_η	Percentage of correct TKE values (%)
RU01	0.39	16	~98%
RU02	0.42	15	~98%
PBT01	0.35	18	~97%
PBT02	0.36	17	~98%

Another important variable to ensure accuracy is time. The values of the Kolmogorov time scale (K_τ), integral time scale (I_t) and experimental time scale (t_{exp}) are described in Table 5.7. It is important to notice that in this study the experimental time scale is considered the interframe time of PIV measurements. The results showed that the interframe time used in this work enable the acquisition of all time scales of turbulence because the experimental time scale is one order of magnitude lower than the smallest time scales.

Table 5.7: Comparison among Kolmogorov (K_τ), integral (I_t) and experimental (t_{exp}) time scales.

Impeller	P (W)	$\overline{\varepsilon_T}$ (m²/s³)	$K_\tau\ (\times 10^{-4}\ s)$	$I_t(\times 10^{-1}\ s)$	$t_{exp}(\times 10^{-5}\ s)$
RU01	47.75	0.96	10.2	3.14	1.0
RU02	36.48	0.73	11.7	3.56	1.0
PBT01	68.48	1.37	8.56	3.55	1.0
PBT02	61.03	1.22	9.07	3.89	1.0

5.5.4. Uncertainty Quantification

Figure 5.36 compares the uncertainty of the TKE measured from (a) Stereo-PIV measurements (k_{3C}), (b) Classic PIV data considering pseudo-isotropic approximation (k_{iso}) and (c) Tilted PIV measurements regarding axial and combined-radial components (k_{2C}) for the flow induced by RU01. It was verified that most of the field presented uncertainty values lower than 1.0×10^{-3}. All fields at AR 15º and the fields of Stereo PIV and Tilted PIV at AR 30º presented a small region with higher uncertainty values close to the impeller discharge region. The maximum value was observed for Tilted PIV at AR 15º ($0.31 < x/R < 0.42$, $0.31 < y/H < 0.35$) and it was $1.3 \times 10^{-2} \times U_{tip}^2$,.

Similar observations were made in the fields of the uncertainty of TKE for the flow promoted by RU02 (Figure 5.37). For Tilted PIV at AR 15º, we also observed a region with the higher values, with a maximum of $9.3 \times 10^{-3} \times U_{tip}^2$. This region was also verified in the 3C reconstruction error for both impellers (Figure 5.35a-b). It may be related to a region of concentration of drag vortices, which present greater instabilities. Despite this, the maximum TKE value in this same region range reached a maximum of $0.09 \times U_{tip}^2$ for RU01 and $0.05 \times U_{tip}^2$ for RU02, so the uncertainty quantities correspond to 13.9% and 18.6% of the TKE values. This region, however, could not be associated with the differences observed in the TKE fields obtained by the three datasets, so the Tilted PIV measurements have led to a characterization equally valid than the one obtained from Stereo-PIV and Classic PIV data.

Figure 5.36: Uncertainty of TKE obtained from (a) Stereo-PIV measurements (k_{3C}), (b) Classic PIV data considering pseudo-isotropic approximation (k_{iso}) and (c) Tilted PIV measurements regarding axial and combined-radial components (k_{2C}) for different blade angles of RU01. The values were normalized by U_{tip}^2.

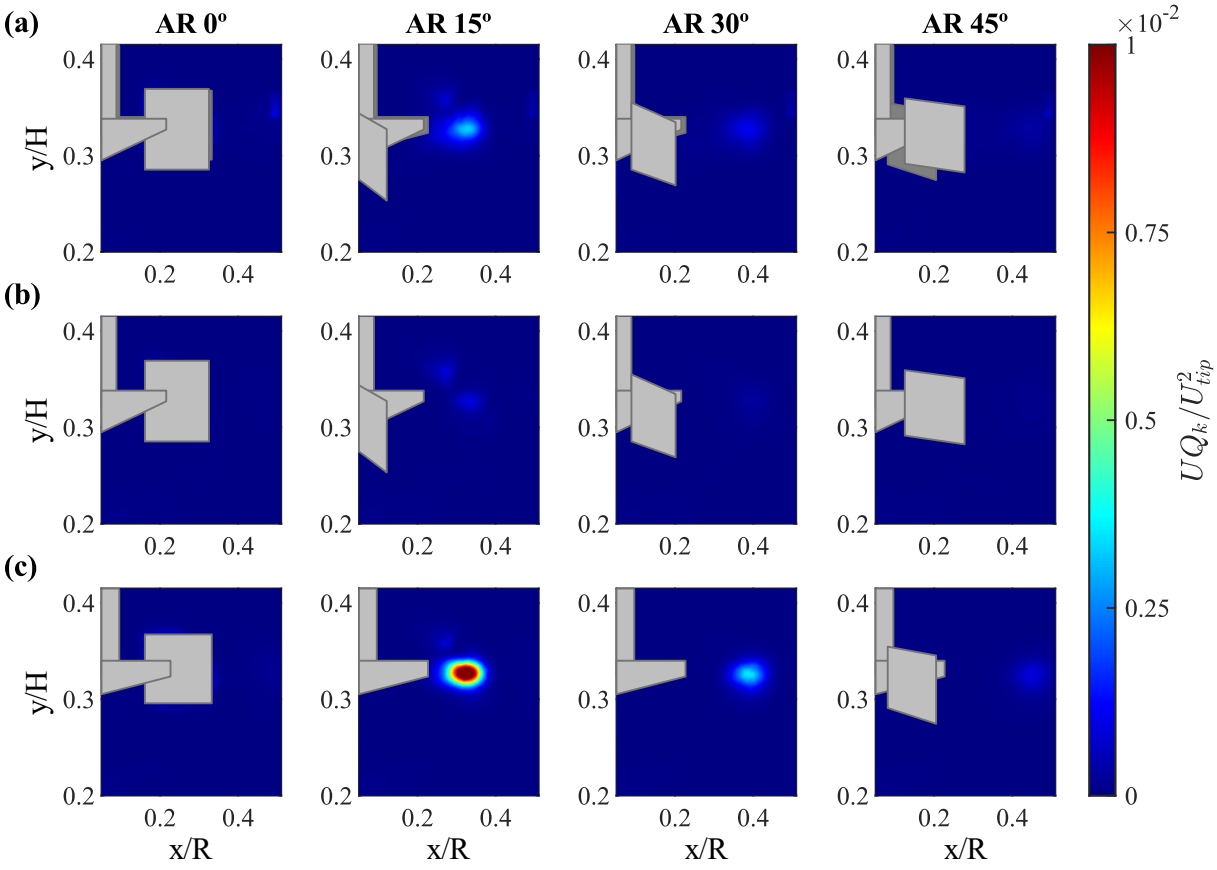

Figure 5.37: Uncertainty of TKE obtained from (a) Stereo-PIV measurements (k_{3C}), (b) Classic PIV data considering pseudo-isotropic approximation (k_{iso}) and (c) Tilted PIV measurements regarding axial and combined-radial components (k_{2C}) for different blade angles of RU02. The values were normalized by U_{tip}^2.

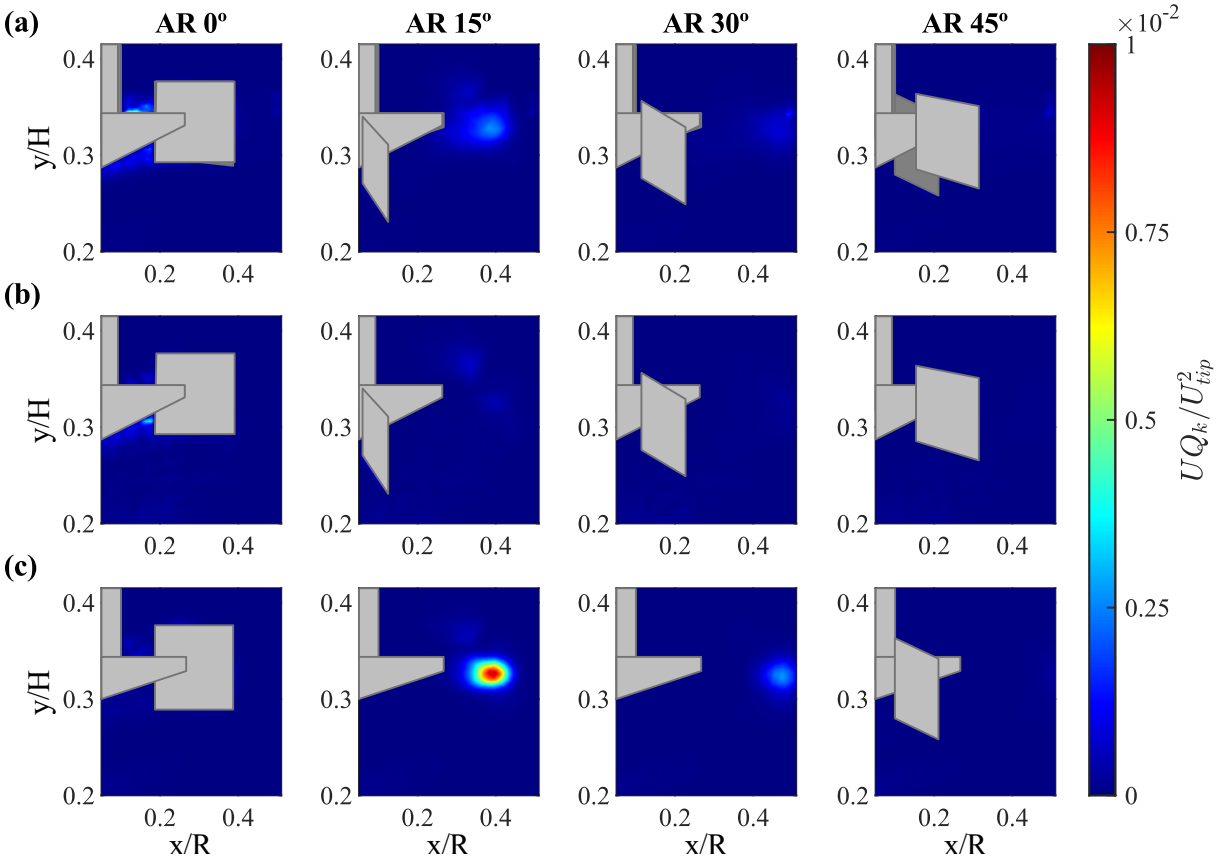

The good quality of the Stereo-PIV measurements can also be verified in the case of the flow promoted by the pitched blade turbines (Figure 5.38 for PBT01 and Figure 5.39 for PBT02). Most of the fields exhibit values below of $1.0 \times 10^{-3} \times U_{tip}^2$, except in the region of eddies formation, which has higher uncertainty values. This region moves from the zone above the impeller, at AR 0º, to the zone below it, at AR 67.5º. The maximum uncertainty quantities can be observed in the region above the impeller ($0.13 < r/R < 0.32$, $0.35 < z/H < 0.39$) at AR 0º for all impellers and PIV approaches. For PBT01, the maximum value was $6.9 \times 10^{-3} \times U_{tip}^2$ for Stereo-PIV data, while for PBT02 the maximum of $5.2 \times 10^{-3} \times U_{tip}^2$ were verified for the Classic PIV measurements. These maximum values corresponding of 16% and 8.8% of the TKE value estimated at the same region, which is relatively small. Also, it is important to notice that the regions in which we observed higher uncertainty quantities are very different from the regions with higher differences between the TKE estimated from Stereo-PIV, Classic PIV and

Tilted PIV, so these uncertainties did not affect the conclusion of the similarity of the results obtained in all approaches.

The comparison between the uncertainty quantities obtained from all PIV approaches indicates that the region in which the higher uncertainties were observed is similar and presents the same order of magnitude when the results of the same impeller are analyzed. Consequently, the higher values must be more associated with the unstable nature of the turbulent flow than with problems in the configuration of the cameras. Furthermore, the uncertainty values were low for all approaches considered due not only to the proper processing of the fields, but also to the guarantee of convergence resulting from the use of 1000 pairs of images.

Figure 5.38: Uncertainty of TKE obtained from (a) Stereo-PIV measurements (k_{3C}), (b) Classic PIV data considering pseudo-isotropic approximation (k_{iso}) and (c) Tilted PIV measurements regarding axial and combined-radial components (k_{2C}) for different blade angles of PBT01. The values were normalized by U_{tip}^2.

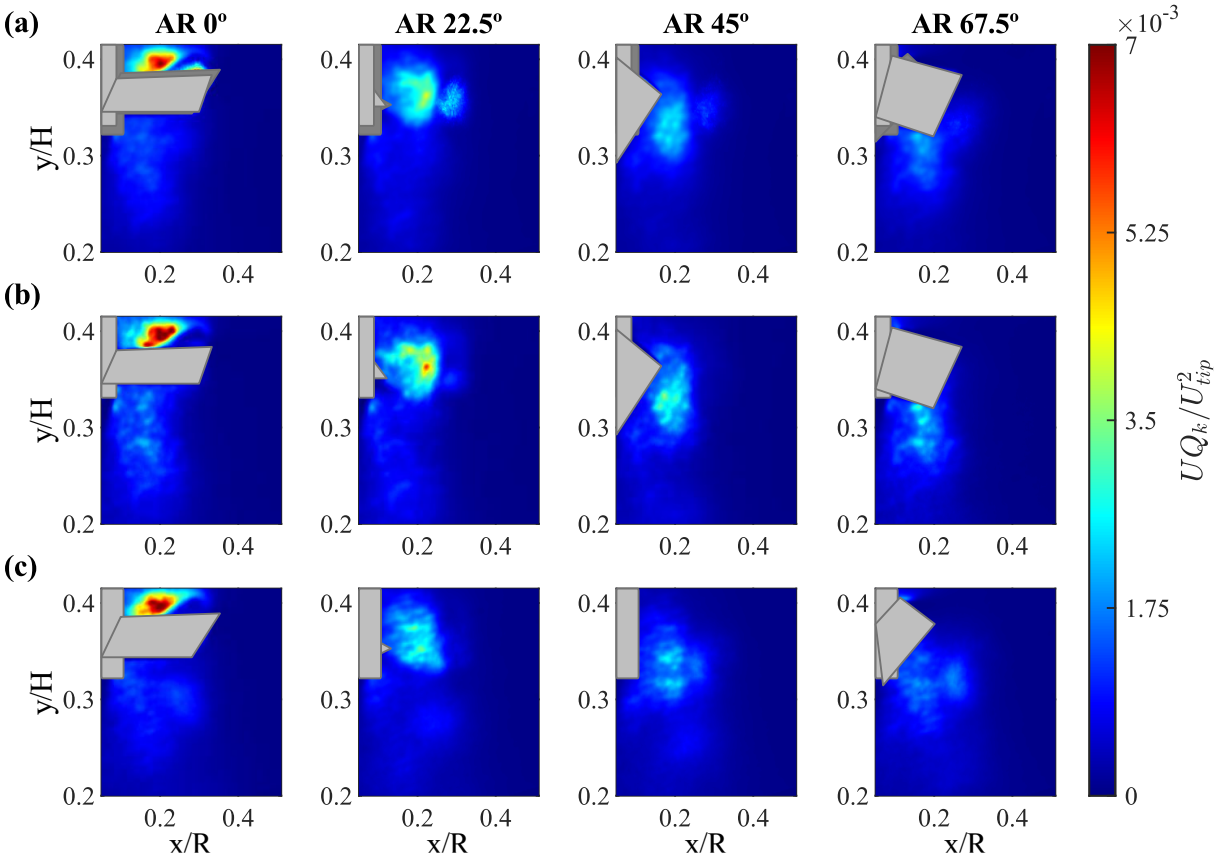

Figure 5.39: Uncertainty of TKE obtained from (a) Stereo-PIV measurements (k_{3C}), (b) Classic PIV data considering pseudo-isotropic approximation (k_{iso}) and (c) Tilted PIV measurements regarding axial and combined-radial components (k_{2C}) for different blade angles of PBT02. The values were normalized by U_{tip}^2.

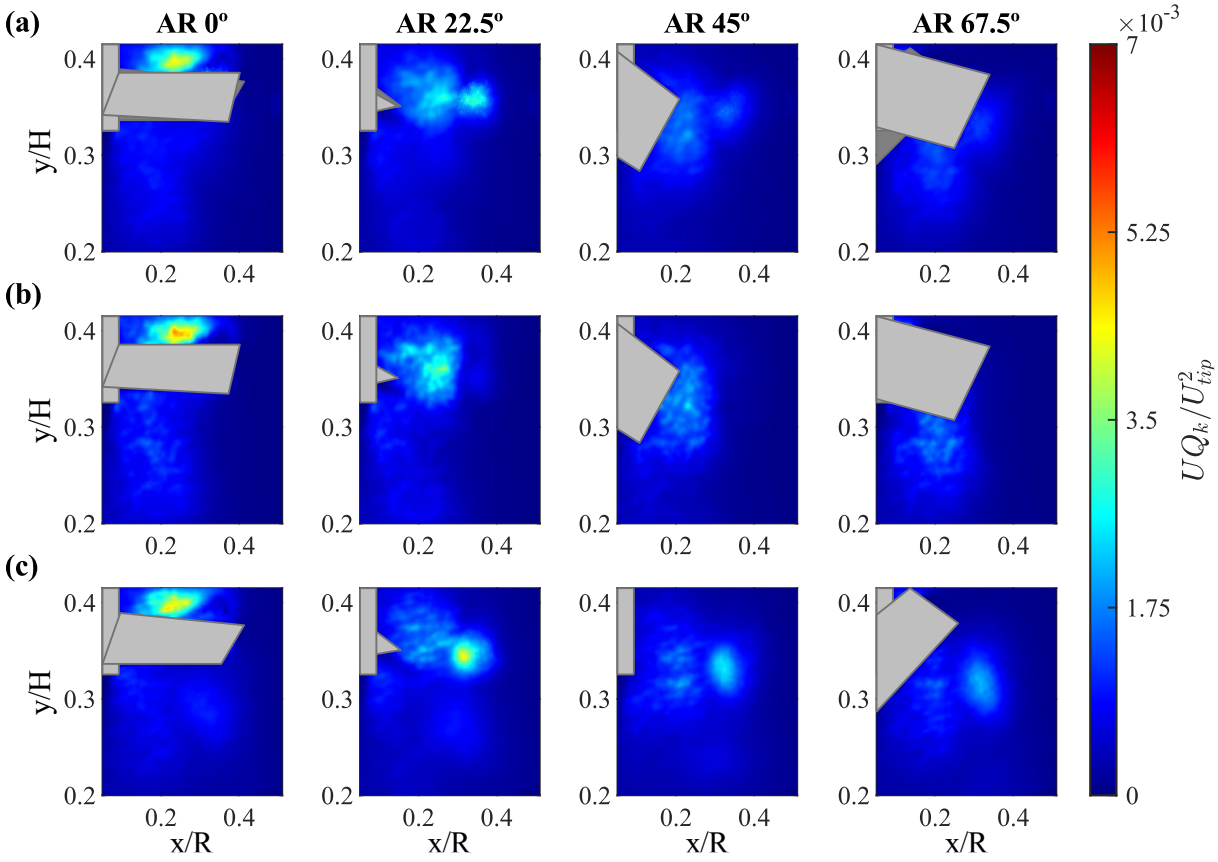

5.5.5. The noisy zone

The noisy zone located at y/H = 0.35 and x/R = 0.49 in the Rushton turbines fields and at y/H = 0.32 and x/R = 0.49 in the pitched blade turbines fields can be observed in different parameters where the data from camera 2 are employed. This noisy effect was present in the signal-to-noise ratio (SNR) for camera 2 (Figure 5.31 to Figure 5.34) as a region with lower SNR values and in the 3C reconstruction error of Stereo-PIV measurements (Figure 5.35) as a region with higher error. It was also verified in the rms of the radial and axial velocity fluctuations obtained from Classic PIV and Stereo-PIV data for all impellers and blade angles (Section 5.2). Consequently, we can also verify this zone in the percentual contribution of the rms of the velocity fluctuations (Section 5.3) and in the TKE estimation from Classic PIV measurements (Section 5.4.2).

The noisy zone is probably caused by a reflection of the light sheet in the impeller, shaft, baffles or in the tank wall that was registered by the camera 2. The raw images, in fact, showed that the zone appears only for camera 2, in the records of all impellers, except the

impeller PBT01 (Section 4.3). The processing attempted to correct the zone; however, it created a region with lack of information. Consequently, the parameters with higher order (e.g., rms of the velocity fluctuations) cannot be properly computed, which led to a zone with sharp variations.

Nevertheless, the noisy zone was not observed for all recorded images, then it is not a systematic deviation. As a result, it was only observed for the radial and out-of-plane velocity component of the flow induced by the Rushton impellers (Figure 5.1 and Figure A.1 in APPENDIX A) in a region with eddies formation and high velocity gradients. For the flow generated by the 45º pitched blade turbines, the region presented a more stable fluid dynamics, than the processing procedure was able to satisfactory reconstruct the components and the noisy zone is not present (Figure 5.2 and Figure A.2 in APPENDIX A). It is important to notice that we were concerned about obtaining high quality PIV measurements, thus, based on the study of Scharnowski, Sciacchitano and Kähler (2019), we reduced the effects of the loss-of-correlation parameters by choosing an optimum interframe time and light sheet thickness. Moreover, the processing procedure were designed to control and reduce the image noise level in order to minimize the post-processing stage, which can lead to smoothing and artificial fields.

The more tilted camera (camera 1) did not present problem caused by reflection that was observed in Classic PIV measurements, obtained by camera 2, although the recordings were made simultaneously. This can be observed not only in the TKE fields presented in Section 5.4.3, but also in the fields of the rms of the radial and axial velocity fluctuations obtained from Tilted PIV (Section 5.2). Also, the raw imagens record by camera 1 for all the impellers (Figure 4.3 to Figure 4.6) and the signal-to-noise ratio (SNR) for Tilted PIV (camera 1 in Figure 5.31 to Figure 5.34) did not show the noisy zone. Based on this, Tilted PIV can be a suitable approach in situations that need a more robust noise control.

Another surprisingly fact is that Tilted PIV measurements also promoted a compensation mechanism of the noisy zone on the 3C reconstruction because we did not verify its effect in the TKE fields obtained from Stereo-PIV (Section 5.4.1). A schematic of the reconstruction of the out-of-plane displacement from the two in-plane displacements are set out in Figure 5.40. The particle image displacement between two light pulses can be determined by the Equation (5.1 in the radial direction and by Equation (5.2 in axial direction (PRASAD; ADRIAN, 1993; RAFFEL et al., 2018):

$$x_i' - x_i = -M\left(d_x + d_z\frac{x_i'}{z_0}\right) \tag{5.1}$$

$$y_i' - y_i = -M\left(d_y + d_z\frac{y_i'}{z_0}\right) \tag{5.2}$$

where M is the magnification factor, d_x, d_y and d_z are the particle displacements in radial, axial and out-of-plane directions and z_0 is the distance between the image plane and the lens.

Figure 5.40: Schematic of the reconstruction of the particle displacements in radial (d_x), axial (d_y) and out-of-plane (d_z) directions from Stereo-PIV measurements.

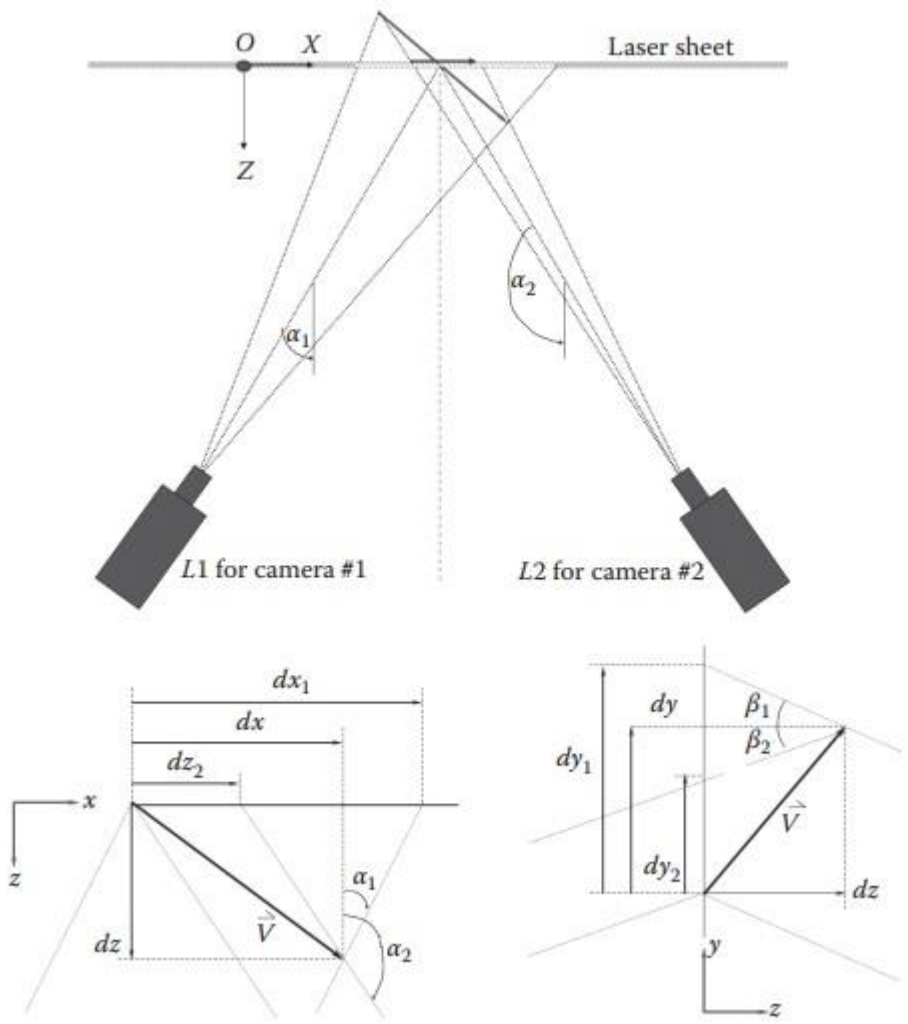

Source: Hu (2013).

The relation between the location of the corresponding image in the image plane (sensor) due to the recording of a particle at two different positions is obtained by Equation (5.3 for plane x-z and Equation (5.4 for plane y-z (RAFFEL et al., 2018):

$$\tan\alpha = \frac{x_i'}{z_0} \tag{5.3}$$

$$\tan\beta = \frac{y_i'}{z_0} \tag{5.4}$$

The velocity components measured by the camera 1 are given by (RAFFEL et al., 2018):

$$U_1 = \frac{x_i' - x_i}{M\Delta t} \tag{5.5}$$

$$V_1 = \frac{y_i' - y_i}{M\Delta t} \tag{5.6}$$

And the velocity components measured by camera 2, U_2 and V_2, can be described in a similar way. Thus, the three velocity components an (U, V, W) are reconstructed from the four measured values obtained by the two cameras from Stereo-PIV measurements (RAFFEL et al., 2018):

$$U = \frac{U_1\tan\alpha_2 + U_2\tan\alpha_1}{\tan\alpha_1 + \tan\alpha_2} \tag{5.7}$$

$$V = \frac{V_1\tan\beta_2 + V_2\tan\beta_1}{\tan\beta_2 + \tan\beta_1} \tag{5.8}$$

$$W = \frac{U_1 - U_2}{\tan\alpha_1 + \tan\alpha_2} = \frac{V_1 - V_2}{\tan\beta_2 + \tan\beta_1} \tag{5.9}$$

In the noisy zone, there is a lack of information regarding the particle image displacement registered by camera 2. However, the tilted camera was able to promote a mechanism on the 3C reconstruction that compute the out-of-plane component with only the

data obtained by this camera and allowed the accurate estimation of the TKE fields obtained from Stereo-PIV with errors below 0.95 pixels in the noisy zone (Figure 5.35).

6. FINAL CONSIDERATIONS

6.1. Conclusions

In this work we improve the estimation of the turbulent kinetic energy by employing a novel particle image velocimetry approach, named Tilted PIV, in which the measurements were made by one camera positioned 45° from the light sheet. The performance of this novel approach was compared with Classic PIV and Stereo-PIV measurements of two different flow patterns in a stirred tank, promoted by Rushton turbines and 45° pitched blade turbines with two different diameters.

Based on the results, Tilted PIV was able to acquire images of the flow from a perspective that reduced the distortion caused by the curvature of the tank and presented a larger optical access than the less tilted camera. The approach also reduced the demand for noise control in processing because it avoided the light reflection problem observed in Classic PIV measurements. In post-processing, it also promoted a compensation mechanism of the light reflection problem on the 3C reconstruction of the TKE fields obtained from Stereo-PIV data. Moreover, Tilted PIV satisfactorily acquired the effect of the out-of-plane component on turbulent kinetic energy and estimated its distribution in the region close to the impellers, avoiding the consideration of pseudo-isotropic approximation.

The changing in camera position was evaluated by the fields of the root-mean-square (rms) of the velocity fluctuations. These fields allowed us to verify higher values of the rms of the radial velocity fluctuations obtained by Tilted PIV for the flow induced by all the impellers. For the Rushton turbines, the highest deviation between Classic and Tilted PIV were 60% for RU01 at AR 45° and between Stereo and Tilted PIV were 54% for RU02 at AR 45°. For 45º pitched blade turbines, the comparison between Classic and Tilted PIV showed a maximum variation of 67% for PBT02 at AR 67.5° and the results of Stereo and Tilted PIV presented deviations of 50% for PBT01 at AR 22.5° and AR 45° and for PBT02 at AR 0°. These results were related to the more tilted camera, that acquired the combination of the radial and the out-of-plane contributions on the rms of the velocity fluctuations.

The rms of the axial velocity fields, in turn, showed similar results for all the approaches considered in this work. For the Rushton turbines, the highest deviation between Classic and Stereo-PIV was 10% for RU01 at AR 15° and among Classic, Tilted and Stereo-PIV was 20% for RU02 at AR 30°. For 45º pitched blade turbines, we observed variations of less than 17% between Classic and Stereo-PIV measurements. For Classic and Tilted PIV data, this variation reaches only 14%, and for Tilted and Stereo-PIV the maximum variation was 20%

for PBT01 and PBT02 at AR 67.5°. Therefore, the variation of the camera position applied in the Tilted PIV approach did not influence the acquisition of the axial component, since the two cameras are in the same x-z plane.

In the fields of the root-mean-square (rms) of the velocity fluctuations we also analyzed the regions with higher levels of turbulence, that are the most suitable for a feed location. Based on the results, we can suggest that the most appropriate feed location is close do the impeller tip, at $0.28 < y/H < 0.36$ for flow promoted by Rushton turbine and at $0.32 < y/H < 0.37$ and $0.30 < x/R < 0.4$ for the flow induced by 45º PBT with 4 blades. Moreover, we observed that the blade angle can possibly influence the turbulent intensity for Rushton turbine, so this variable should be considered on the feed operation. However, more investigations are necessary to validate this information.

Regarding the impeller geometry, we verified that an increase of 20% in impeller diameter led to small growths in the velocity components for the flows induced by the Rushton turbines, which can be considered insignificant to account for effects on agitation and mixing efficiency. However, for the flows generated by 45º pitched blade turbines, a 20% increase in the diameter promoted a 27.2% rise in the maximum value of the radial component, a 6.5% decrease in the maximum value of the axial component, and an enhance of 17.6% in the maximum value of the out-of-plane component. Thus, in this case, we verified that the diameter variation has more influence on the radial component than on the other components, probably because the difference in impeller geometry occurs in the radial direction.

The Stereo-PIV measurements were in good agreement with literature. The Rushton turbines presented a radial flow pattern, with a predominance of the radial component in relation to the axial and out-of-plane components. The maximum absolute values were $0.76 \times U_{tip}$ for the radial component, $0.26 \times U_{tip}$ for the axial component, and $0.37 \times U_{tip}$ for the out-of-plane component for RU01 and $0.77 \times U_{tip}$ for the radial, $0.28 \times U_{tip}$ for the axial and $0.39 \times U_{tip}$ for the out-of-plane component for RU02, both impellers at AR 30°.

The 45° pitched blade turbines showed that the axial velocity component predominated the flow, influenced by the radial and out-of-plane components in the discharge zone below the impeller. For the PBT01, the highest absolute value of the radial component was $0.44 \times U_{tip}$ at AR 22.5º in the trailing vortices area. The maximum absolute value of the axial component was $0.61 \times U_{tip}$, at AR 0º in the suction region. For the out-of-plane velocity component, the uppermost absolute value was $0.34 \times U_{tip}$ at AR 0° in the discharge region at AR 0º. For the PBT02, the highest absolute values were observed in the same regions, however,

the maximum values were $0.56 \times U_{tip}$ at AR 22.5° for the radial component, $0.57 \times U_{tip}$ at AR 0° for the axial component and $0.40 \times U_{tip}$ at AR 0° for the out-of-plane component. The out-of-plane component presented significant values for both flow patterns, especially in the flow induced by the Rushton turbines, thus, this component is relevant for the understanding of the fluid dynamics in stirred tanks.

The pseudo-isotropic approximation assumes that the out-of-plane component in the turbulent kinetic energy computation can be estimated as the arithmetic mean of the other two components. Based on this concept, it is expected that the percentual contributions of each rms of the velocity fluctuations on the turbulent kinetic energy estimation would be similar. However, for both impellers, it was observed that the contributions differ from each other and vary along the field of view, especially in the discharge region. For RU01, the maximum values in this region were 54% (AR 15°), 51% (AR 30°) and 52% (AR 45°). For RU02, in turn, the maximum values were 54% (AR 15º), 55% (AR 30º) and 50 % (AR 45º). The axial component, in general, presented higher values in the region close do the impeller tip, with a maximum of 55% at AR 30° for RU01 and of 51% at the same blade angle for RU02. For the 45º pitched blade turbines, the radial component showed a higher contribution in regions above and below the impeller, reaching 57% at all blade angles for PBT01 and 59% at AR 45° and AR 6.5 for PBT02 in the discharge region ($y/H > 0.27$ and $x/R > 0.32$). The axial component presented contributions, on average, between 28% and 35% for PBT01 and between 29% and 36% for PBT02. The out-of-plane component, in turn, indicated contributions between 20% and 31% for PBT01 and 19% and 29% for PBT02.

The different contributions of each component may indicate that the pseudo-isotropic approximation is not suitable on the estimative of TKE in this region. However, the TKE fields estimated with the pseudo-isotropic approximation from Classic PIV data presented very similar fields to those observed from Stereo-PIV data. In addition, comparison of our results with Stereo-PIV, Classic PIV and 3D measurements techniques from literature for the same impellers also presented good agreement. Thus, the question regarding the limitations of applying the pseudo-isotropic approximation is still not well clarified. It seems that there is a tradeoff between the variation on the rms of the velocity fluctuations for the different components and the suitable use of the pseudo-isotropic approximation. More investigations are necessary related to this topic, especially in more complex and highly anisotropic flows.

The turbulent kinetic energy estimated from the approaches Stereo-PIV considering all three root-mean-square of the velocity fluctuations, Classic PIV regarding pseudo-isotropic

approximation and Tilted PIV considering axial and combined-radial components presented very similar results. The maximum values of TKE were $0.16 \times U_{tip}^2$ at AR 30º for RU01 and $0.22 \times U_{tip}^2$ at the same blade angle for RU02. For the 45º pitched blade turbines, the maximum TKE value was $0.08 \times U_{tip}^2$ at AR 45º for PBT01 and $0.11 \times U_{tip}^2$ at AR 22.5º for PBT02. Regarding the variation in the diameter of the impeller, the results showed that an increase of 20% in the diameter caused an increase of 37.5% in the maximum value of TKE for both types of impellers (Rushton and PBT).

Finally, the good quality of the measurements of all approaches were supported by the signal-to-noise ratio, the 3C reconstruction error and the quantification of uncertainty analysis. The results observed in the SNR fields are between 1.2 and 3.7, which is an indication of robust measurements for all experiments carried out in this work according to the literature. The 3C reconstruction error presented values below 2.5 pixels. For interrogation windows of 18×18 pixels we have 0.1% error per vector, which is very low. In the quantification of uncertainty analysis, we verify, in general, values lower than 1.0×10^{-3}. Some regions presented higher values, but it does not compromise the study's conclusions.

6.2. Future Work

As mentioned in the Introduction (Section 1), this work is just a small part of a large project between the LACEM research group and *Petróleo Brasileiro S/A* company. Thus, the continuity of this work concerns its application within the context of the project to optimize the homogenization of crude oil storage tanks and minimize the formation of sludge.

However, the novel approach presented here can serve not only the context of this project but has the potential to solve optical access and noise control problems in other situations involving PIV measurements, such as in industrial applications when only a small field of view is available to arrange the light sheet and acquire images. Thus, future work also needs to take into account the expansion of the novel approach application to other contexts in order to contribute to the development of methodologies for analyzing fluid dynamic phenomena. Based on this, further studies are necessary to verify the application of the novel approach for estimating more complex turbulent parameters, such as energy dissipation rate (EDR).

Another topic that deserves a deeper investigation is the question regarding the limitations of applying the pseudo-isotropic approximation. It seems that there is a tradeoff between the variation on the rms of the velocity fluctuations for the different components and the suitable use of the pseudo-isotropic approximation. More investigations are necessary to verify if there is a limit on how different that rms of the velocity fluctuations can be and still provide suitable results on the TKE estimation considering the pseudo-isotropic approximation. This study can be done in more complex and highly anisotropic flows, where the differences on the rms of the velocity fluctuations are higher.

Finally, a limitation of the Tilted PIV approach is related to the fact the measurements performed in this way compute radial and out-of-plane components together. In this work, we didn’t attempt to separate the components and work with them individually. More studies can be made to promote this separation in image processing through geometric and statistical investigations. This could probably enhance Tilted PIV applications because the approach would be an alternative to Stereo-PIV measurements on the evaluation of the out-of-plane component fields.

7. REFERENCES

ADRIAN, R. J. Image shifting technique to resolve directional ambiguity in double-pulsed velocimetry. **Applied Optics**, v. 25, n. 21, p. 3855, 1986.

ADRIAN, R. J.; WESTERWEEL, J. **Particle Image Velocimetry**. New York: Cambridge University Press, 2011.

ALBERINI, F. et al. Comparison between 3-D-PTV and 2-D-PIV for determination of hydrodynamics of complex fluids in a stirred vessel. **Chemical Engineering Science**, v. 171, p. 189–203, 2017.

ALCAMO, R. et al. Large-eddy simulation of turbulent flow in an unbaffled stirred tank driven by a Rushton turbine. **Chemical Engineering Science**, 5th International Symposium on Mixing in Industrial Processes (ISMIP5). v. 60, n. 8, p. 2303–2316, 1 abr. 2005.

ALONZO-GARCIA, A. et al. On the performance of different RANS based models to describe the turbulent flow in an agitated vessel using non-structured grids and PIV validation. **Brazilian Journal of Chemical Engineering**, v. 36, n. 1, p. 361–382, 2019.

AMARAL, R. D. L. et al. A novel method based on the Otsu threshold for instantaneous elimination of light reflection in PIV images. **Measurement Science and Technology**, v. 33, n. 2, 1 fev. 2022.

AYALA, J. S. et al. Two-dimensional shear rate field and flow structures of a pseudoplastic fluid in a stirred tank using particle image velocimetry. **Chemical Engineering Science**, v. 248, p. 117198, 2022.

AYALA, J. S. **Avaliação das medidas 2D-PIV na operação de agitação de fluidos newtoniano e não newtoniano**. Tese de Doutorado—Campinas: Universidade Estadual de Campinas, 26 maio 2022.

BALDI, S.; YIANNESKIS, M. On the Direct Measurement of Turbulence Energy Dissipation in Stirred Vessels with PIV. **Industrial and Engineering Chemistry Research**, v. 42, n. 26, p. 7006–7016, 2003.

BALDI, S.; YIANNESKIS, M. On the quantification of energy dissipation in the impeller stream of a stirred vessel from fluctuating velocity gradient measurements. **Chemical Engineering Science**, v. 59, n. 13, p. 2659–2671, 2004.

BARBUTTI, A. D. et al. **Compensation of Image Distortion on PIV Measurements of a Stirred Tank**. 12th Spring School on Transition and Turbulence. **Anais**...Blumenau: Associação Brasileira de Engenharia e Ciências Mecânicas, 2020.

BARBUTTI, A. D. et al. A New Field Correction Method For PIV Measurements Based On Mutual Information: Case Study On A Stirred Tank Flow. **Measurement**, v. 186, n. August, p. 110130, 2021.

BARBUTTI, A. D. **PIV optimization in the investigation of turbulent flow in a stirred tank**. Dissertação de Mestrado—Campinas, SP: Universidade Estadual de Campinas, 15 dez. 2021.

BATES, R. L.; FONDY, P. L.; FENIC, J. G. Impeller Characteristics and Power. Em: UHL, V. W.; GRAY, J. B. (Eds.). **Mixing - Theory and Practice**. New York: Academic Press, 1966. p. 111–178.

BERTRAND, M. et al. Mixing Study in an Unbaffled Stirred Precipitator Using LES Modelling. **International Journal of Chemical Engineering**, v. 2012, p. 1–11, 2012.

BRŮHA, T.; PROCHÁZKA, P.; URUBA, V. Investigation of Low-Frequency Phenomena within Flow Pattern in Standard Mixing Vessel Induced by Pitched Blade Impeller. **Processes**, v. 9, n. 3, p. 545, 19 mar. 2021.

BRUNAZZI, E. et al. Screening Tool to Evaluate the Levels of Local Anisotropy of Turbulence in Stirred Vessels. **Industrial & Engineering Chemistry Research**, v. 44, n. 15, p. 5836–5844, 1 jul. 2005.

BUGAY, S.; ESCUDIÉ, R.; LINÉ, A. Experimental analysis of hydrodynamics in axially agitated tank. **AIChE Journal**, v. 48, n. 3, p. 463–475, mar. 2002.
CALLUAUD, D.; DAVID, L. Stereoscopic particle image velocimetry measurements of the flow around a surface-mounted block. **Experiments in Fluids**, v. 36, n. 1, p. 53–61, 1 jan. 2004.

CHUNG, K. H. K.; BARIGOU, M.; SIMMONS, M. J. H. Reconstruction of 3-D flow field inside miniature stirred vessels using a 2-D PIV technique. **Chemical Engineering Research and Design**, v. 85, n. 5 A, p. 560–567, 2007.

CHUNG, K. H. K.; SIMMONS, M. J. H.; BARIGOU, M. Angle-resolved particle image velocimetry measurements of flow and turbulence fields in small-scale stirred vessels of different mixer configurations. **Industrial and Engineering Chemistry Research**, v. 48, n. 2, p. 1008–1018, 2009.

CREMASCO, MARCO AURELIO. **Operações Unitárias em Sistemas Particulados e Fluidomecânicos**. [s.l.] Editora Edgard Blucher, 2012.

DE LAMOTTE, A. et al. Investigating the effects of hydrodynamics and mixing on mass transfer through the free-surface in stirred tank bioreactors. **Chemical Engineering Science**, v. 172, p. 125–142, 2017.

DELAFOSSE, A. et al. Estimation of the turbulent kinetic energy dissipation rate from 2D-PIV measurements in a vessel stirred by an axial Mixel TTP impeller. **Chemical Engineering Science**, v. 66, n. 8, p. 1728–1737, 2011.

DELBRIDGE, J. N. et al. Power, mixing and flow dynamics of the novel Allegro™ stirred tank reactor. **Chemical Engineering Science**, v. 271, p. 118545, maio 2023.

DERKSEN, J. J.; DOELMAN, M. S.; VAN DEN AKKER, H. E. A. Three-dimensional LDA measurements in the impeller region of a turbulently stirred tank. **Experiments in Fluids**, v. 27, n. 6, p. 522–532, 4 nov. 1999.

DIETERLE, L.; WEICHERT, R. Particle image velocimetry applied to microstructures in turbulent flows. Em: RODI, W.; BERGELES, G. (Eds.). **Engineering turbulence modelling and experiments 3: proceedings of the Third International Symposium on Engineering Turbulence Modelling and Measurements, Heraklion-Crete, Greece, 27-29 May, 1996**. Elsevier series in thermal and fluid sciences. Amsterdam ; New York: Elsevier, 1996. p. 391–400.

DUCCI, A.; YIANNESKIS, M. Direct determination of energy dissipation in stirred vessels with two-point LDA. **AIChE Journal**, v. 51, n. 8, p. 2133–2149, 2005.

EDWARDS, M. F.; BAKER, M. R. A review of liquid mixing equipment. Em: HARNBY, N.; EDWARDS, M. F.; NIENOW, A. W. (Eds.). **Mixing in the Process Industries**. [s.l.] Elsevier, 1992. p. 118–136.

ELSINGA, G. E. **Tomographic particle image velocimetry and its application to turbulent boundary layers**. Tese de Doutorado—Delft: Technische Universiteit Delft, 2008.
ESCUDIÉ, R.; LINÉ, A. Experimental analysis of hydrodynamics in a radially agitated tank. **AIChE Journal**, v. 49, n. 3, p. 585–603, 2003.

ESCUDIÉ, R.; LINÉ, A. Analysis of turbulence anisotropy in a mixing tank. **Chemical Engineering Science**, v. 61, n. 9, p. 2771–2779, maio 2006.

FAN, Y. et al. Effects of baffle on flow structure and cyclic variation in stirred tanks with Rushton turbine. **AIP Advances**, v. 12, n. 1, 1 jan. 2022.

FANG, J.; LING, X.; SANG, Z. F. Experimental and Numerical Studies of the Flow Field in a Stirred Tank Equipped with Multiple Side-Entering Agitators. **Chemical Engineering and Technology**, v. 34, n. 10, p. 1619–1629, 2011.

FREITAS, L. F. DE L. E. **Características Turbulentas de um Tanque Agitado com Medidas PIV 2C-2D**. Dissertação de Mestrado—Campinas: Universidade Estadual de Campinas, 2020.

FROST, W.; MOULDEN, T. H. (EDS.). **Handbook of Turbulence: Volume 1 Fundamentals and Applications**. Boston, MA: Springer US, 1977.

GABRIELE, A. et al. Use of PIV to measure turbulence modulation in a high throughput stirred vessel with the addition of high Stokes number particles for both up- and down-pumping configurations. **Chemical Engineering Science**, v. 66, n. 23, p. 5862–5874, 2011.

GABRIELE, A.; NIENOW, A. W.; SIMMONS, M. J. H. Use of angle resolved PIV to estimate local specific energy dissipation rates for up- and down-pumping pitched blade agitators in a stirred tank. **Chemical Engineering Science**, v. 64, n. 1, p. 126–143, 2009.

GALLETTI, C. et al. A Study of Reynolds Stresses, Triple Products and Turbulence States in a Radially Stirred Tank with 3-D Laser Anemometry. **Chemical Engineering Research and Design**, v. 82, n. 9, p. 1214–1228, set. 2004.

GE, C. Y. et al. CFD simulation and PIV measurement of the flow field generated by modified pitched blade turbine impellers. **Chemical Engineering Research and Design**, v. 92, n. 6, p. 1027–1036, 2014.

GENCK, W. J. et al. Liquid-Solid Operations and Equipment. Em: GREEN, D. W.; PERRY, R. H. (Eds.). **Perry's Chemical Engineers' Handbook**. [s.l.] McGraw-Hill Companies, Inc., 2008. p. 151.

GÓMEZ, C.; BENNINGTON, C. P. J.; TAGHIPOUR, F. Investigation of the flow field in a rectangular vessel equipped with a side-entering agitator. **Journal of Fluids Engineering, Transactions of the ASME**, v. 132, n. 5, p. 0511061–05110613, 2010.

GUIDA, A.; NIENOW, A. W.; BARIGOU, M. The effects of the azimuthal position of the measurement plane on the flow parameters determined by PIV within a stirred vessel. **Chemical Engineering Science**, v. 65, n. 8, p. 2454–2463, 2010.

HAIN, R.; KÄHLER, C. J. Fundamentals of multiframe particle image velocimetry (PIV). **Experiments in Fluids**, v. 42, n. 4, p. 575–587, 23 mar. 2007.

HARTMANN, H. et al. Assessment of large eddy and RANS stirred tank simulations by means of LDA. **Chemical Engineering Science**, v. 59, n. 12, p. 2419–2432, jun. 2004.

HINSCH, K. D. Three-dimensional particle velocimetry. **Measurement Science and Technology**, v. 6, n. 6, p. 742–753, 1995.

HOCKEY, R. M.; NOURI, J. M. Turbulent flow in a baffled vessel stirred by a 60º pitched blade impeller. **Chemical Engineering Science**, v. 51, n. 19, p. 4405–4421, out. 1996.

HOQUE, M. M. et al. Analysis of turbulence energy spectrum by using particle image velocimetry. **Procedia Engineering**, v. 90, p. 320–326, 2014.

HU, H. Stereo Particle Imaging Velocimetry Techniques: Technical Basis, System Setup, and Application. Em: ZHANG, S. (Ed.). **Handbook of 3D Machine Vision: Optical Metrology and Imaging**. Boca Raton: CRC Press, 2013. p. 71–100.

JÄHRLING, K. et al. Particle Image Velocimetry Compared to CFD Simulation of Stirred Vessels with Helical Coils. **Chemie Ingenieur Technik**, v. 89, n. 4, p. 401–408, abr. 2017.

JOAQUIM JUNIOR, C. F. et al. **Agitação e Mistura na Indústria**. Rio de Janeiro, RJ: LTC - Livros Técnicos e Científicos Editora S.A., 2007.

KEANE, R. D.; ADRIAN, R. J. Theory of cross-correlation analysis of PIV images. **Applied Scientific Research**, v. 49, n. 3, p. 191–215, 1992.

KHAN, F. R. **Investigation of turbulent flows and instabilities in a stirred vessel using particle image velocimetry**. Tese de Doutorado—[s.l.] Loughborough University, 2005.

KHAN, F. R.; RIELLY, C. D.; BROWN, D. A. R. Angle-resolved stereo-PIV measurements close to a down-pumping pitched-blade turbine. **Chemical Engineering Science**, v. 61, n. 9, p. 2799–2806, 2006.

KHAN, F. R.; RIELLY, C. D.; HARGRAVE, G. K. A multi-block approach to obtain angle-resolved PIV measurements of the mean flow and turbulence fields in a stirred vessel. **Chemical Engineering and Technology**, v. 27, n. 3, p. 264–269, 2004.

KILANDER, J.; RASMUSON, A. Energy dissipation and macro instabilities in a stirred square tank investigated using an le PIV approach and LDA measurements. **Chemical Engineering Science**, v. 60, n. 24, p. 6844–6856, 2005.

KIM, B. J.; SUNG, H. J. A further assessment of interpolation schemes for window deformation in PIV. **Experiments in Fluids**, v. 41, n. 3, p. 499–511, 2006.

KOLMOGOROV, A. N. The local structure of turbulence in incompressible viscous fluid for very large Reynolds numbers. **Proceedings of the Royal Society of London. Series A: Mathematical and Physical Sciences**, v. 434, n. 1890, p. 9–13, 8 jul. 1991.

KRESTA, S. Turbulence in stirred tanks: anisotropic, approximate, and applied. **The Canadian Journal of Chemical Engineering**, v. 76, n. 3, p. 563–576, jun. 1998.

KRESTA, S. M.; BRODKEY, R. S. Turbulence in Mixing Applications. Em: PAUL, E. L.; ATIEMO-OBENG, V. A.; KRESTA, S. M. (Eds.). **Handbook of Industrial Mixing**. 1. ed. [s.l.] Wiley, 2003. p. 19–87.

KRESTA, S. M.; WOOD, P. E. The flow field produced by a pitched blade turbine: Characterization of the turbulence and estimation of the dissipation rate. **Chemical Engineering Science**, v. 48, n. 10, p. 1761–1774, 1993.

LAINE, Q. et al. Experimental study of velocity and turbulence fields in a square mixer-settler tank: Comparison of shake the box PTV and 2D2C PIV. **Chemical Engineering Science**, v. 275, p. 118636, jul. 2023.

LAMARQUE, N. et al. Large-eddy simulation of the turbulent free-surface flow in an unbaffled stirred tank reactor. **Chemical Engineering Science**, v. 65, n. 15, p. 4307–4322, ago. 2010.

LEE, H. et al. The effect of perspective error on 2D PIV Measurements of homogeneous isotropic turbulence. **Experiments in Fluids**, v. 63, n. 8, p. 122, 2 ago. 2022.

LEE, K. C.; BORRETT, N. A.; YIANNESKIS, M. Turbulence Structure and Isotropy in Stirred Vessels. Em: GUPTA, B. S.; IBRAHIM, S. (Eds.). **Mixing and Crystallization**. Dordrecht: Springer Netherlands, 2000. p. 29–42.

LEE, K. C.; YIANNESKIS, M. Turbulence Properties of the Impeller Stream of a Rushton Turbine. **AIChE Journal**, v. 44, n. 1, p. 13–24, jan. 1998.

LI, Z. et al. Stereo-PIV experiments and large eddy simulations of flow fields in stirred tanks with Rushton and curved-blade turbines. **AIChE Journal**, v. 59, n. 10, p. 3986–4003, out. 2013.

LI, Z.; BAO, Y.; GAO, Z. PIV experiments and large eddy simulations of single-loop flow fields in Rushton turbine stirred tanks. **Chemical Engineering Science**, v. 66, n. 6, p. 1219–1231, 2011.

LIANG, Y. et al. Turbulent flow field in a stirred vessel agitated by an impeller with flexible blades. **AIChE Journal**, v. 64, n. 11, p. 4148–4161, nov. 2018.

LIU, X. et al. Particle Image Velocimetry Study of Turbulence Characteristics in a Vessel Agitated by a Dual Rushton Impeller. **Chinese Journal of Chemical Engineering**, v. 16, n. 5, p. 700–708, 2008.

LUMLEY, J. L. Computational Modeling of Turbulent Flows. Em: YIH, C.-S. (Ed.). **Advances in Applied Machanics**. London: Academic Press, 1978. v. 18p. 123–176.

MACHADO, M. B. et al. Impeller characterization and selection: Balancing efficient hydrodynamics with process mixing requirements. **AIChE Journal**, v. 58, n. 8, p. 2573–2588, ago. 2012.

MARTÍNEZ-DELGADILLO, S. A. et al. Analysis of the turbulent flow and trailing vortices induced by new design grooved blade impellers in a baffled tank. **Chemical Engineering Journal**, v. 358, n. July, p. 225–235, 2019.

MENDOZA-ESCAMILLA, V. X. et al. Effect of Modified Impellers with Added Leading Edges Flanges on Pumping Efficiency in Agitated Tanks. **Industrial & Engineering Chemistry Research**, v. 62, n. 1, p. 535–544, 11 jan. 2023.

MICHELETTI, M. et al. On spatial and temporal variations and estimates of energy dissipation in stirred reactors. **Chemical Engineering Research and Design**, v. 82, n. 9 SPEC. ISS., p. 1188–1198, 2004.

MÖLLER, S. V.; SILVESTRINI, J. H. Turbulência: Fundamentos. Em: **Coleção Cadernos de Turbulência.** Rio de Janeiro: Associação Brasileira de Ciências Mecânicas–ABCM, 2004. v. 4p. 32.

MONTANTE, G. et al. An experimental study of double-to-single-loop transition in stirred vessels. **The Canadian Journal of Chemical Engineering**, v. 77, n. 4, p. 649–659, 1999.

MONTANTE, G. et al. Numerical simulations of the dependency of flow pattern on impeller clearance in stirred vessels. **Chemical Engineering Science**, v. 56, n. 12, p. 3751–3770, 2001.

MORY, M. **Fluid mechanics for chemical engineering**. London : Hoboken, NJ: ISTE ; Wiley, 2011.

PERRARD, M. et al. Characterisation of the Turbulence in a Stirred Tank Using Particle Image Velocimetry. Em: VAN DEN AKKER, H. E. A.; DERKSEN, J. J. (Eds.). **10th European Conference on Mixing**. Delft: Elsevier Science B.V., 2000. p. 345–352.

PINHO, F. T. et al. Turbulent flow in stirred vessels agitated by a single, low-clearance hyperboloid impeller. **Chemical Engineering Science**, v. 55, n. 16, p. 3287–3303, ago. 2000.

POPE, S. B. **Turbulent Flows**. United Kingdom: Cambridge University Press, 2000.
PRASAD, A. K. Stereoscopic particle image velocimetry. **Experiments in Fluids**, v. 29, n. 2, p. 103–116, 7 ago. 2000.

PRASAD, A. K.; ADRIAN, R. J. Stereoscopic particle image velocimetry applied to liquid flows. **Experiments in Fluids**, v. 15, n. 1, p. 49–60, jun. 1993.

PRASAD, A. K.; JENSEN, K. Scheimpflug stereocamera for particle image velocimetry in liquid flows. **Applied Optics**, v. 34, n. 30, p. 7092–7099, 1995.

RAFFEL, M. et al. **Particle Image Velocimetry**. Cham: Springer International Publishing, 2018.

RANADE, V. V. et al. Trailing vortices of Rushton turbine: PIV measurements and CFD simulations with snapshots approach. **Chemical Engineering Research and Design**, v. 79, n. 1, p. 3–12, 2001.

ROY, S.; ACHARYA, S.; CLOETER, M. D. Flow structure and the effect of macro-instabilities in a pitched-blade stirred tank. **Chemical Engineering Science**, v. 65, n. 10, p. 3009–3024, maio 2010.

RUTHERFORD, K. et al. Hydrodynamic characteristics of dual Rushton impeller stirred vessels. **AIChE Journal**, v. 42, n. 2, p. 332–346, 1996.

SAARENRINNE, P.; PIIRTO, M.; ELORANTA, H. Experiences of turbulence measurement with PIV. **Measurement Science and Technology**, v. 12, n. 11, p. 1904–1910, 2001.

SAVARI, C.; LI, K.; BARIGOU, M. Multiscale wavelet analysis of 3D Lagrangian trajectories in a mechanically agitated vessel. **Chemical Engineering Science**, v. 260, 12 out. 2022.

SCARANO, F. Iterative image deformation methods in PIV. **Measurement Science and Technology**, v. 13, n. 13, p. 1–19, 2002.

SCHÄFER, M. et al. Trailing vortices around a 45° pitched-blade impeller. **AIChE Journal**, v. 44, n. 6, p. 1233–1246, 1998.

SCHARNOWSKI, S.; KÄHLER, C. J. On the loss-of-correlation due to PIV image noise. **Experiments in Fluids**, v. 57, n. 7, p. 119, jul. 2016.

SCHARNOWSKI, S.; KÄHLER, C. J. Particle image velocimetry - Classical operating rules from today's perspective. **Optics and Lasers in Engineering**, v. 135, n. November 2019, p. 106185, 2020.

SCHARNOWSKI, S.; SCIACCHITANO, A.; KAHLER, C. J. On the universality of Keane & Adrian's valid detection probability in PIV. **Measurement Science and Technology**, v. 30, n. 3, 2019.

SCIACCHITANO, A.; WIENEKE, B. PIV uncertainty propagation. **Measurement Science and Technology**, v. 27, n. 8, p. 84006, 2016.

SHARP, K. V.; ADRIAN, R. J. PIV Study of small-scale flow structure around a Rushton turbine. **AIChE Journal**, v. 47, n. 4, p. 766–778, 2001.

SHEKHAR, C. et al. Stereo-PIV measurement of turbulence characteristics in a flow mixer. **Journal of Visualization**, v. 15, n. 4, p. 293–308, 5 nov. 2012.

SHENG, J.; MENG, H.; FOX, R. O. A large eddy PIV method for turbulence dissipation rate estimation. **Chemical Engineering Science**, v. 55, n. 20, p. 4423–4434, 2000.

SILVA, P. T. DA. **Estudo do escoamento em um tanque agitado por PIV e CFD**. Dissertação de Mestrado—Campinas, SP: Universidade Estadual de Campinas, 17 dez. 2020.

SILVEIRA NETO, A. DA. **Escoamento Turbulentos: Análise Física e Modelagem Teórica**. [s.l.] Grafica Composer, 2020.

SOLOFF, S. M.; ADRIAN, R. J.; LIU, Z. C. Distortion compensation for generalized stereoscopic particle image velocimetry. **Measurement Science and Technology**, v. 8, n. 12, p. 1441–1454, 1997.

SOUZA, J. F. A. D. et al. Uma revisão sobre a turbulência e sua modelagem. **Revista Brasileira de Geofísica**, v. 29, n. 1, p. 21–41, mar. 2011.

STELMACH, J. et al. Turbulent energy dissipation rate and turbulence scales in the blade region of a self-aspirating disk impeller. **Journal of Applied Fluid Mechanics**, v. 12, n. 3, p. 715–728, 2019.

STELMACH, J. et al. Efficiency of PBT Impellers with Different Blade Cross-Sections. **Energies**, v. 15, n. 2, p. 585, 14 jan. 2022.

UNADKAT, H. **Investigation of turbulence modulation in solid-liquid suspensions using FPIV and micromixing experiments**. Tese de Doutorado—[s.l.] Loughborough University, 2010.

UNADKAT, H.; RIELLY, C. D.; NAGY, Z. K. PIV study of the flow field generated by a sawtooth impeller. **Chemical Engineering Science**, v. 66, n. 21, p. 5374–5387, 2011.

VIRGINIA POLYTECHNIC INSTITUTE AND STATE UNIVERSITY. **prana**. , 2015. Disponível em: <https://github.com/aether-lab/prana/tree/master>. Acesso em: 3 out. 2023.

WANG, C. et al. PIV investigation of the flow features of double and single 45° up-pumping pitched blade turbines in a square tank. **The Canadian Journal of Chemical Engineering**, v. 96, n. 3, p. 788–799, mar. 2018.

WANG, G. et al. Estimation of the dissipation rate of turbulent kinetic energy: A review. **Chemical Engineering Science**, v. 229, 2021.

WANG, H. et al. Effect of impeller type and scale-up on spatial distribution of shear rate in a stirred tank. **Chinese Journal of Chemical Engineering**, v. 42, p. 351–363, fev. 2022.

WESTERWEEL, J.; ELSINGA, G. E.; ADRIAN, R. J. Particle Image Velocimetry for Complex and Turbulent Flows. **Annual Review of Fluid Mechanics**, v. 45, n. 1, p. 409–436, 2013.

WESTERWEEL, J.; SCARANO, F. Universal outlier detection for PIV data. **Experiments in Fluids**, v. 39, n. 6, p. 1096–1100, 2005.

WIENEKE, B. Stereo-PIV using self-calibration on particle images. **Experiments in Fluids**, v. 39, n. 2, p. 267–280, 2005.

WU, H.; PATTERSON, G. K. Laser-Doppler measurements of turbulent-flow parameters in a stirred mixer. **Chemical Engineering Science**, v. 44, n. 10, p. 2207–2221, 1 jan. 1989.

WYROBNIK, T. A. et al. Engineering characterization of the novel Bach impeller for bioprocessing applications requiring low power inputs. **Chemical Engineering Science**, v. 252, p. 117263, abr. 2022.

XUE, Z.; CHARONKO, J. J.; VLACHOS, P. P. Particle image velocimetry correlation signal-to-noise ratio metrics and measurement uncertainty quantification. **Measurement Science and Technology**, v. 25, n. 11, 2014.

YEOH, S. L.; PAPADAKIS, G.; YIANNESKIS, M. Numerical Simulation of Turbulent Flow Characteristics in a Stirred Vessel Using the LES and RANS Approaches with the Sliding/Deforming Mesh Methodology. **Chemical Engineering Research and Design**, v. 82, n. 7, p. 834–848, jul. 2004.

YOON, J. H.; LEE, S. J. Direct comparison of 2D PIV and stereoscopic PIV measurements. **Measurement Science and Technology**, v. 13, n. 10, p. 1631–1642, 2002.

ZAMIRI, A.; CHUNG, J. T. Numerical evaluation of turbulent flow structures in a stirred tank with a Rushton turbine based on scale-adaptive simulation. **Computers & Fluids**, v. 170, p. 236–248, jul. 2018.

ZHANG, Y. et al. Transitional flow in a Rushton turbine stirred tank. **AIChE Journal**, v. 63, n. 8, p. 3610–3623, ago. 2017.

ZHAO, J.; GAO, Z.; BAO, Y. Effects of the Blade Shape on the Trailing Vortices in Liquid Flow Generated by Disc Turbines. **Chinese Journal of Chemical Engineering**, v. 19, n. 2, p. 232–242, abr. 2011.

ZHOU, G.; KRESTA, S. M. Distribution of Energy Between Convective and Turbulent-Flow for 3 Frequently Used Impellers. **Chemical Engineering Research & Design**, v. 74, n. 3, p. 379–389, 1996.

APPENDIX A. Supplementary Figures

Figure A.1: (a) Radial, (b) axial and (c) out-of-plane time-averaged velocity components obtained from Stereo-PIV measurements at different blade angles of RU02. Highlighted in pink: noisy zone.

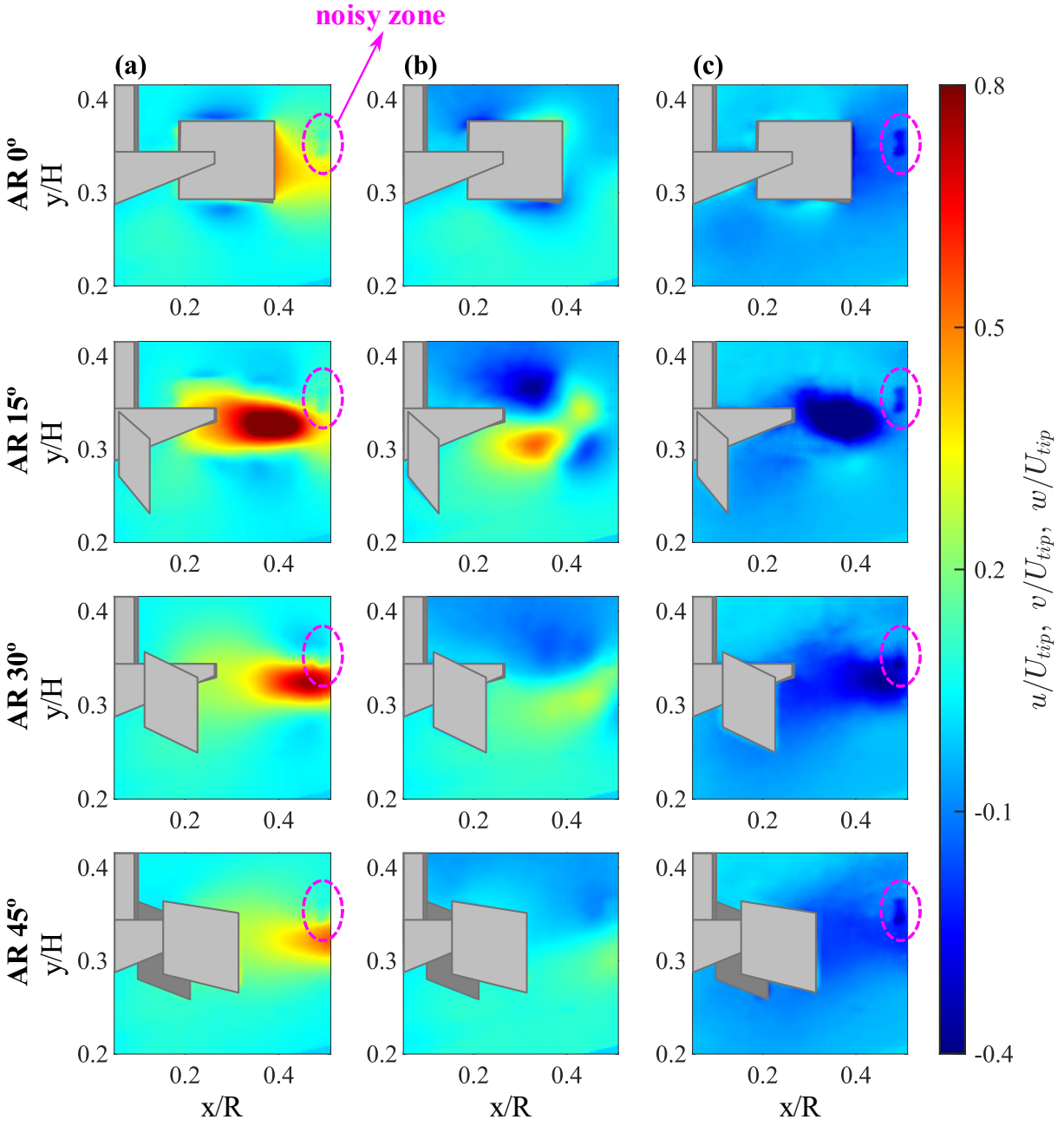

Figure A.2: (a) Radial, (b) axial and (c) out-of-plane time-averaged velocity components obtained from Stereo-PIV measurements at different blade angles of PBT02.

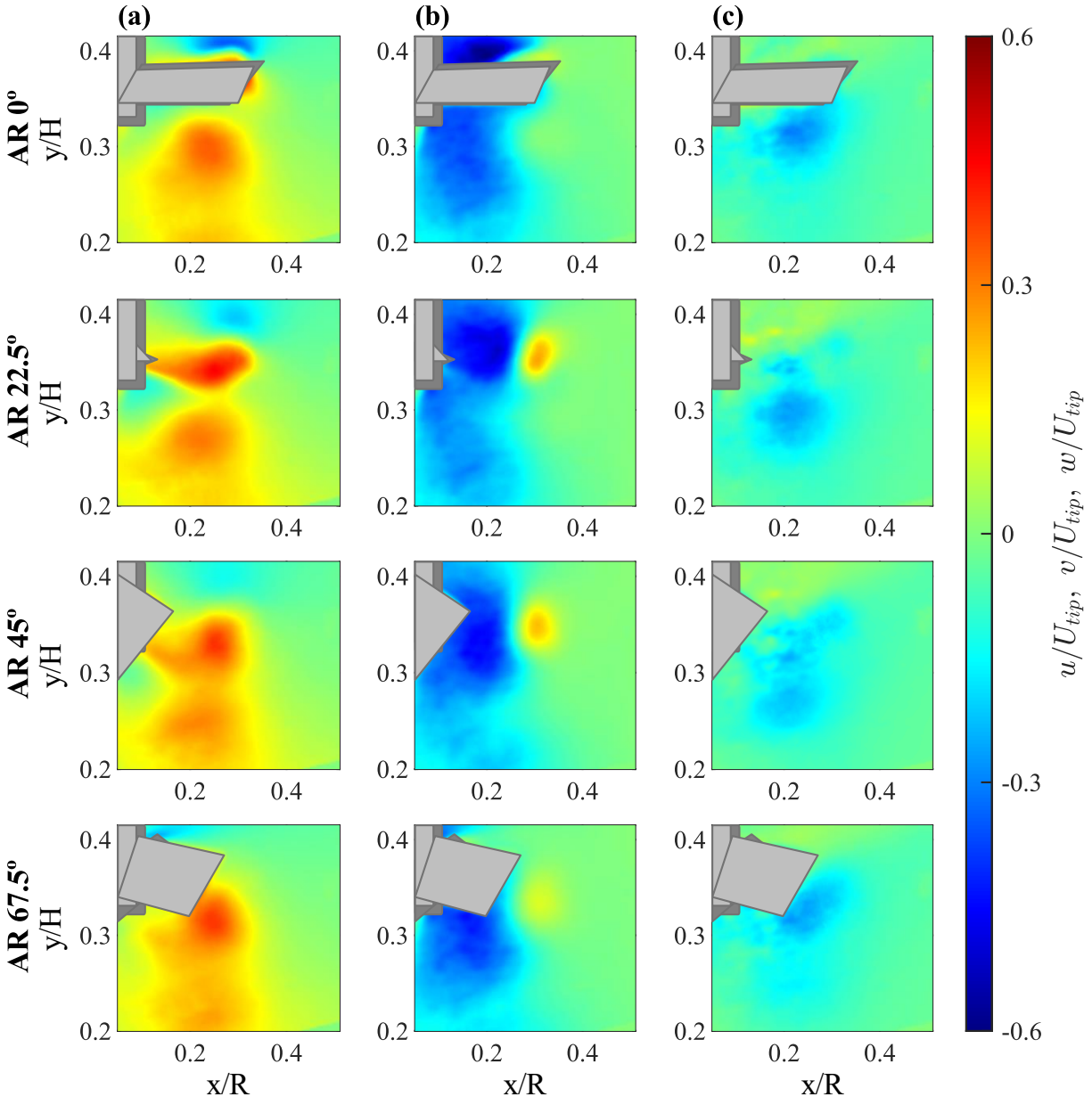

Figure A.3: Root-mean-square of the radial velocity fluctuations obtained from (a) Classic PIV, (b) Tilted PIV and (c) Stereo-PIV measurements at different blade angles of RU02. Highlighted in pink: noisy zone.

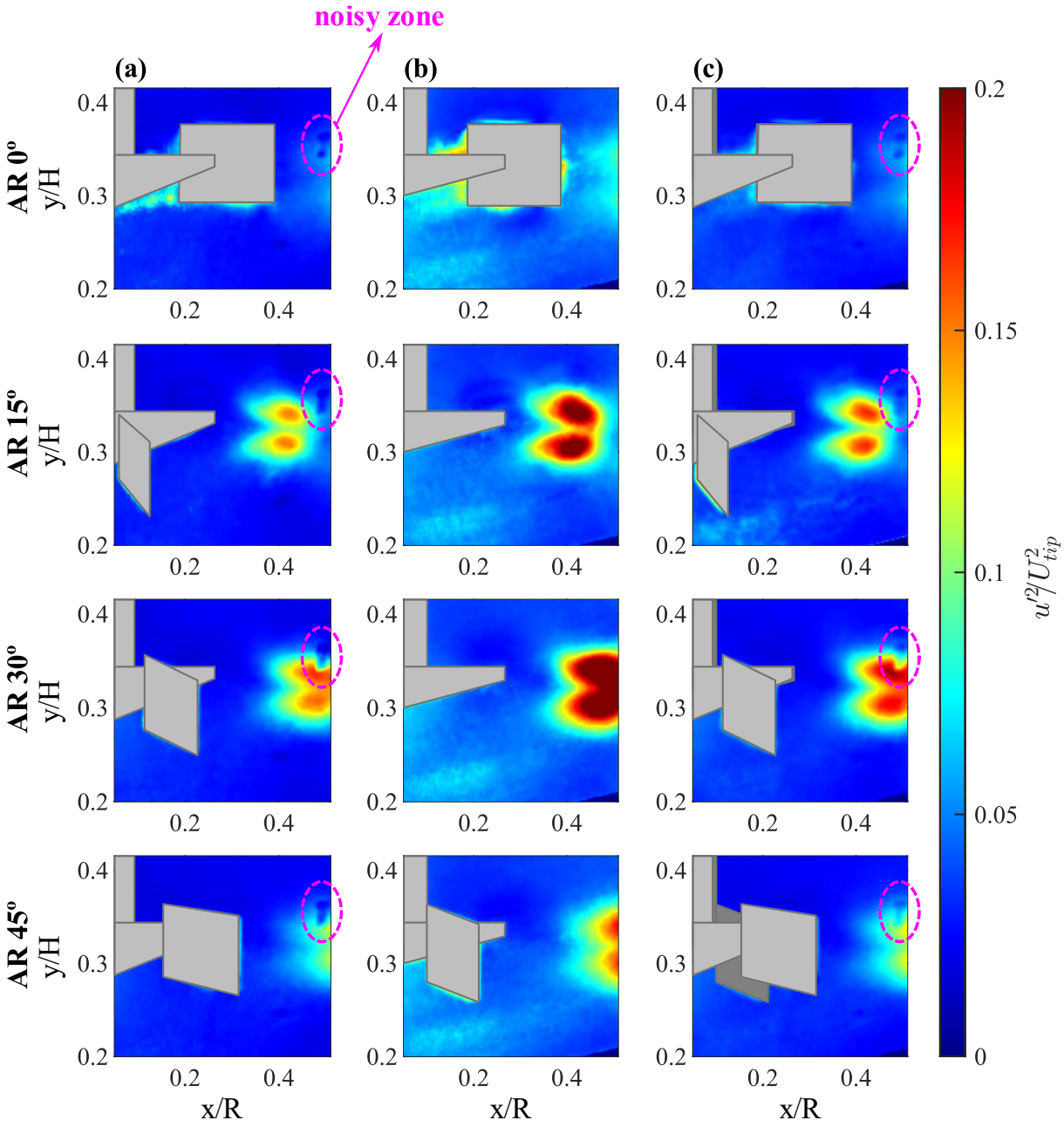

Figure A.4: Root-mean-square of the axial velocity fluctuations obtained from (a) Classic PIV, (b) Tilted PIV and (c) Stereo-PIV measurements at different blade angles of RU02. Highlighted in pink: noisy zone.

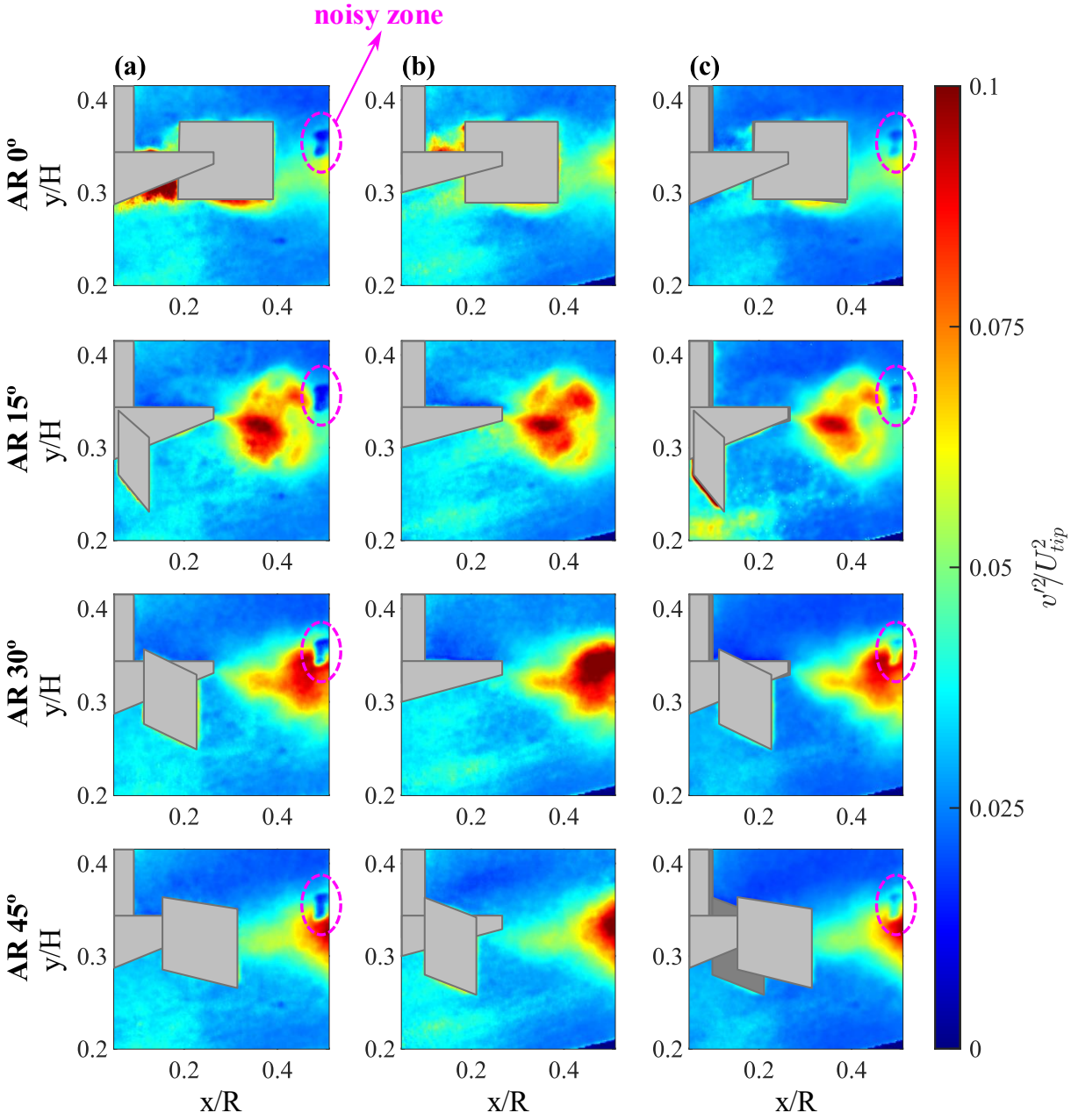

Figure A.5: Root-mean-square of the radial velocity fluctuations obtained from (a) Classic PIV, (b) Tilted PIV and (c) Stereo-PIV measurements at different blade angles of PBT02. Highlighted in pink: noisy zone.

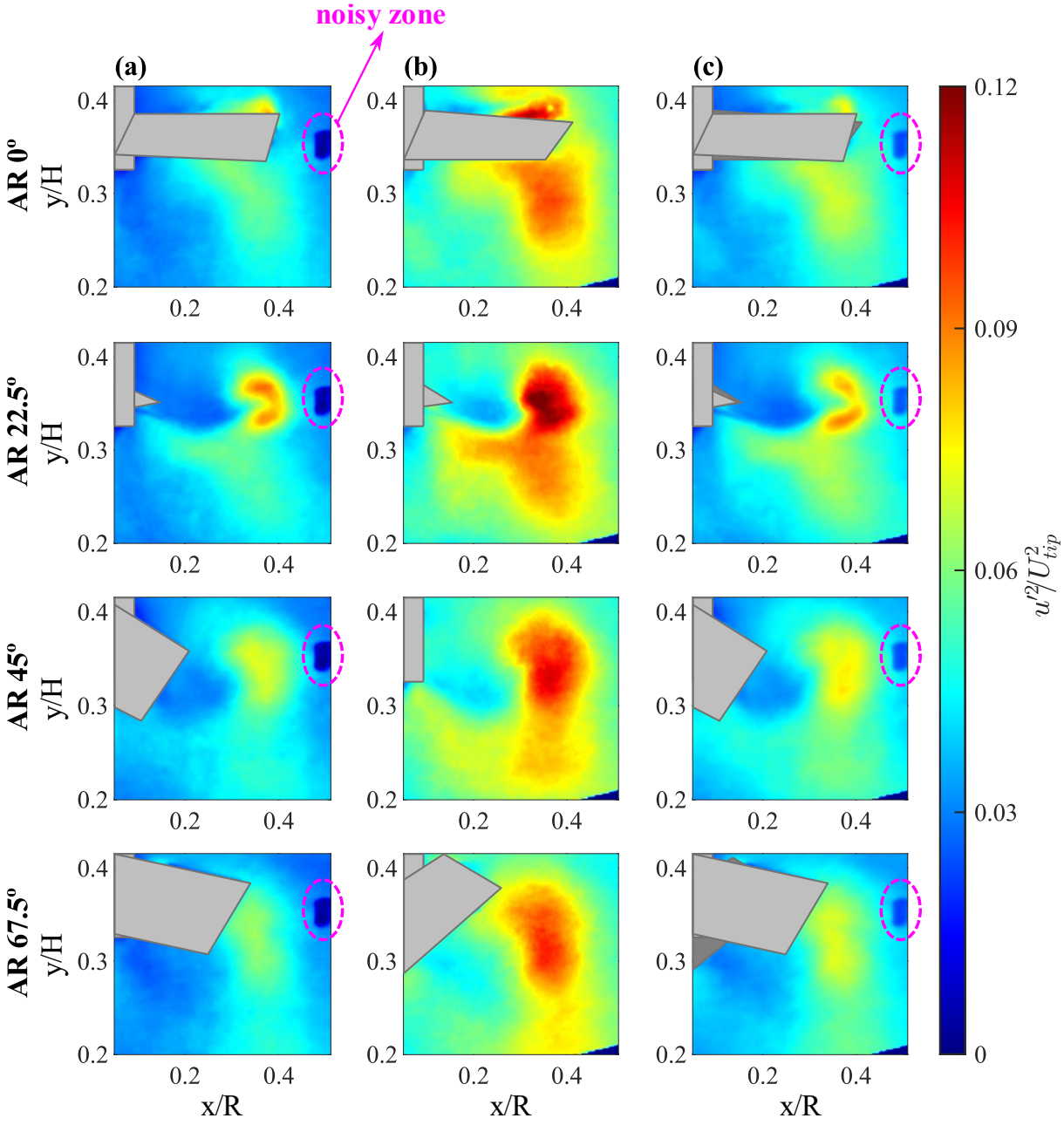

Figure A.6: Root-mean-square of the axial velocity fluctuations obtained from (a) Classic PIV, (b) Tilted PIV and (c) Stereo-PIV measurements at different blade angles of PBT02. Highlighted in pink: noisy zone.

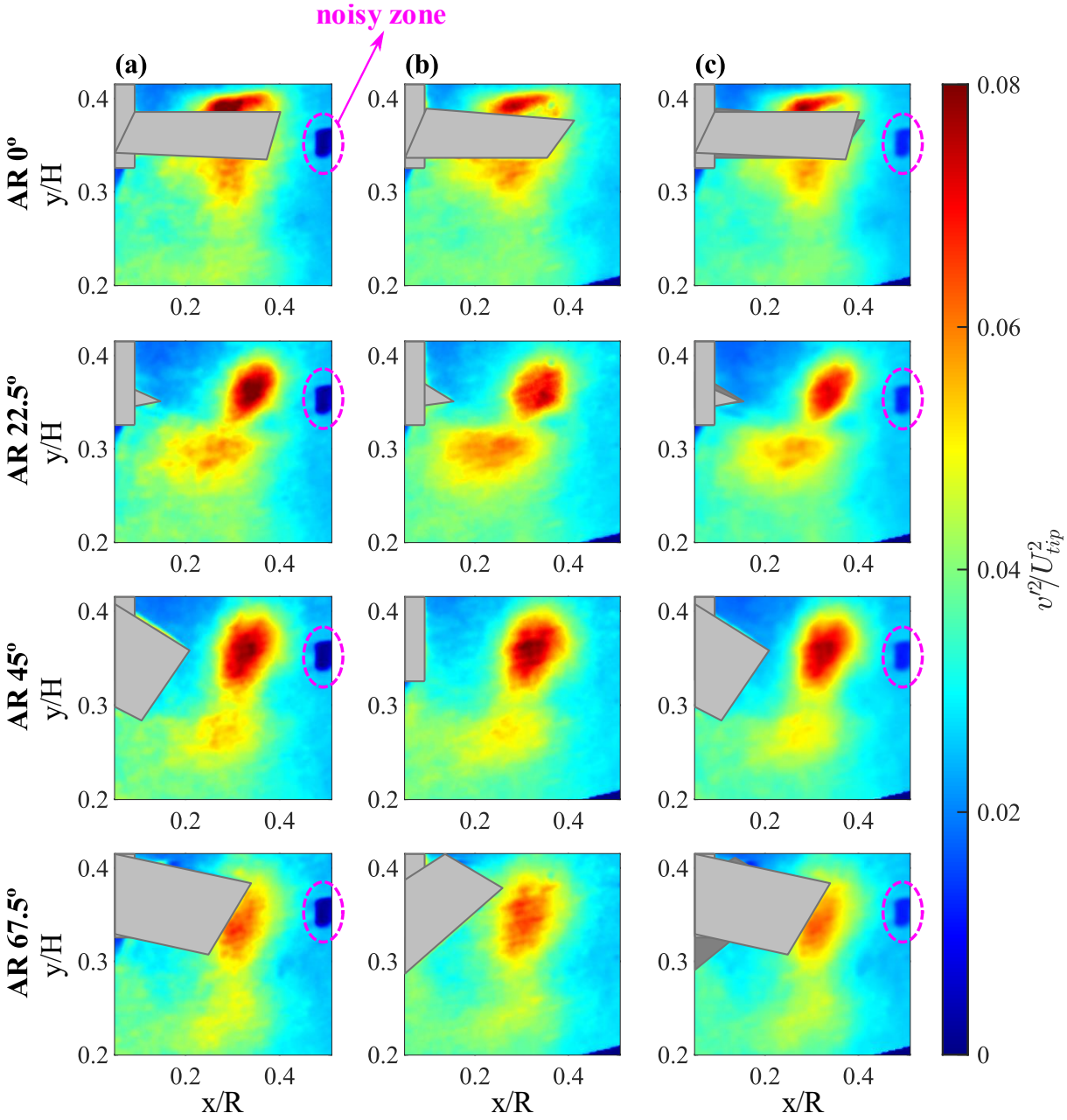

Figure A.7: Percentual contribution of the root-mean-square of the (a) radial, (b) axial and (c) out-of-plane velocity fluctuations on the TKE obtained from Stereo-PIV measurements for different blade angles of RU02. Highlighted in pink: noisy zone.

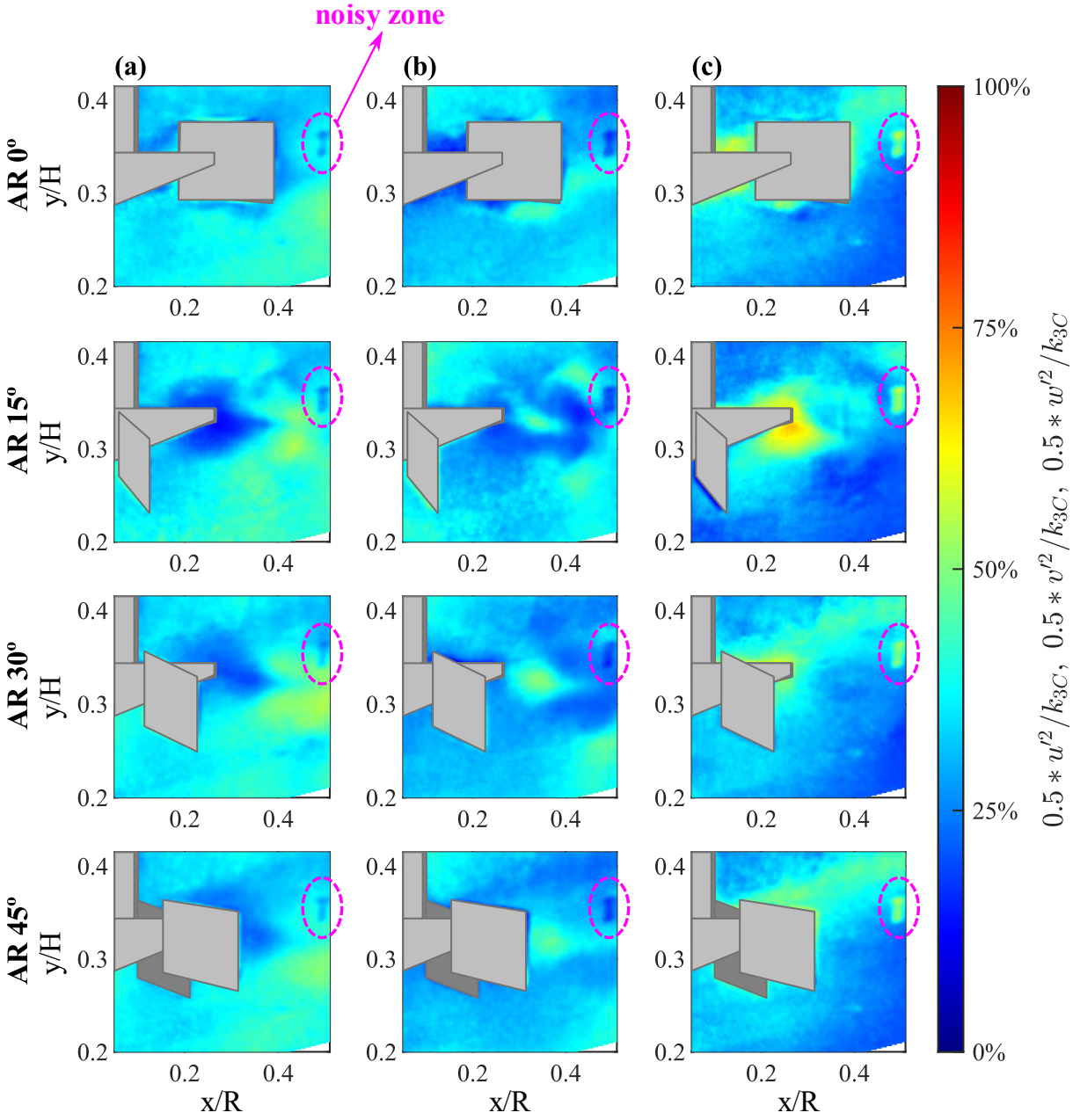

Figure A.8: Percentual contribution of the root-mean-square of the (a) radial, (b) axial and (c) out-of-plane velocity fluctuations on the TKE obtained from Stereo-PIV measurements for different blade angles of PBT02. Highlighted in pink: noisy zone.

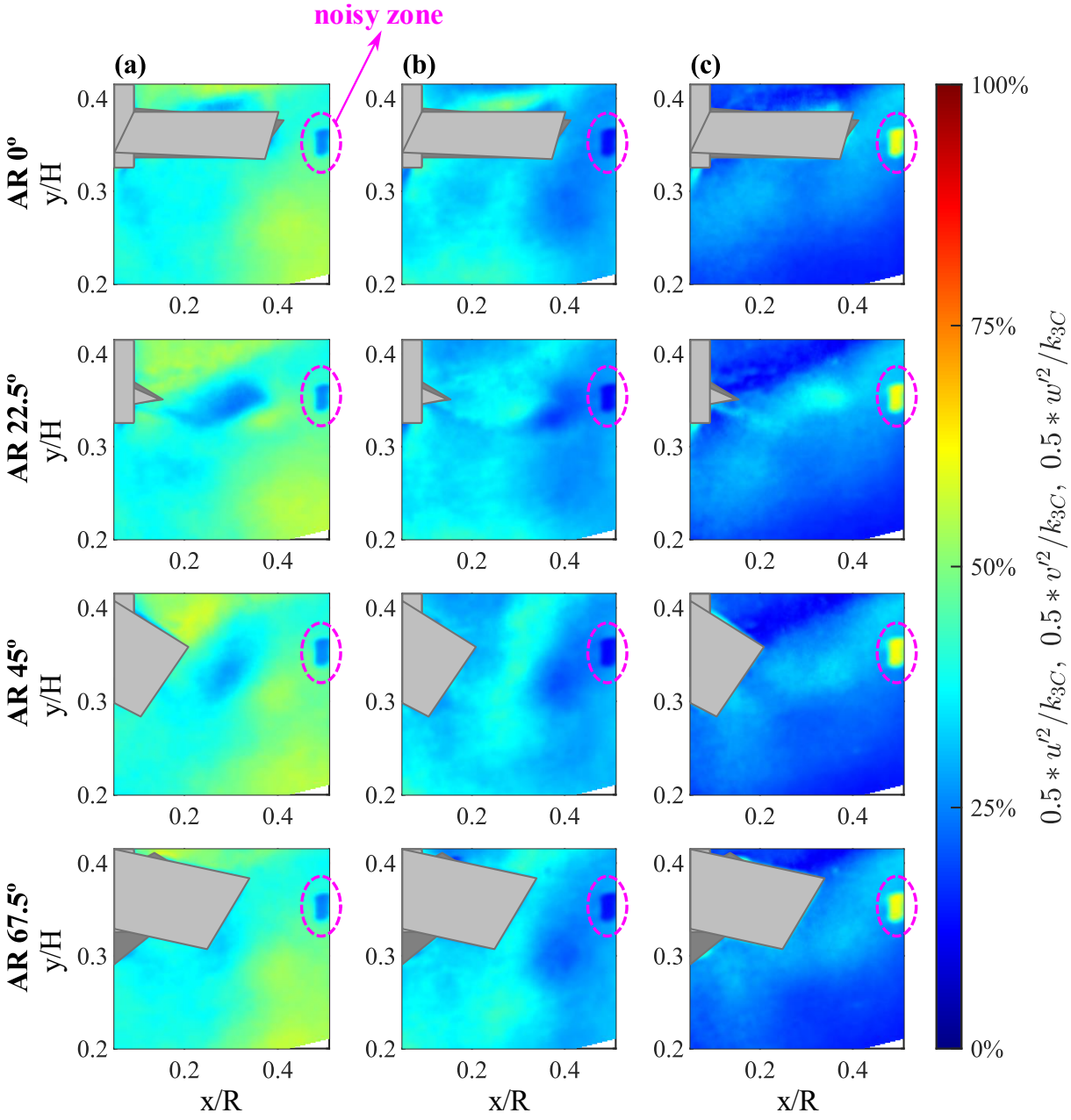

APPENDIX B. Publications and Participation in Scientific Events

PEER- REVIEWED PUBLICATIONS

De Mitri, A. G.; Amaral, R. de L.; Moura, H. L. de; Ayala, J. S.; Nunhez, J. R.; Castilho, G. J. de. Tilted PIV: a Novel Approach for Estimating the Turbulent Kinetic Energy in Stirred Tanks. *Measurement*, 113112, DOI:10.1016/j.measurement.2023.113112

CONFERENCE PROCEDINGS

Mitri, A. G. De; Amaral, R. de L; Moura, H. L. de; Castilho, Guilherme J. de. Turbulent Kinetic Energy in Stirred Tanks Estimated with an Alternative Approach: Tilted PIV. In: *The 11th International Conference on Multiphase Flow* (ICMF 2023), 2023, Kobe. ICMF-2023 Abstract Book, 2023**.**

Mitri, A. G. De; Amaral, R. de L.; Ayala, J. S.; Moura, H. L. de; Castilho, Guilherme J. de. Classic PIV and Stereo-PIV Techniques in the Analysis of Turbulent Flow in a Stirred Tank. In: *The 7th World Congress on Momentum, Heat and Mass Transfer*, 2022, Lisboa, Portugal, 2022.DOI:10.11159/icmfht22.152

Ayala, J.; **Mitri, A. G. De**; Moura, H. L. de; Amaral, R. de L.; Espina, G.; Castilho, G. J. de. Flow Structures of a Pseudoplastic Fluid in a Stirred Tank Using Particle Image Velocimetry. In: *The 7th World Congress on Momentum, Heat and Mass Transfer*, 2022, Lisboa, Portugal, 2022. DOI:10.11159/icmfht22.153

Portella, M.; **De Mitri, A. G.**; Moura, H.; Amaral, R. de L.; Nunhez, J. R.; Castilho, G. J. de. Investigation of the Pseudo-Isotropic Approximation of a Turbulent Flow in a Stirred Tank. In: *26th International Congress of Mechanical Engineering*, 2021, Florianópolis, Brasil. Proceedings of the 26th International Congress of Mechanical Engineering, 2021. DOI:10.26678/ABCM.COBEM2021.COB2021-0996

Barbutti, A.; **De Mitri, A. G.**; Ayala, J. S.; Amaral, R. de L.; Moura, H.; Nunhez, J. R.; Castilho, Guilherme J. de. Compensation of Image Distortion on PIV Measurements of a Stirred Tank. In: *12th Spring School on Transition and Turbulence*, 2020, Blumenau, Brasil. Proceedings of the 12th Spring School on Transition and Turbulence, 2020. DOI://10.26678/ABCM.EPTT2020.EPT20-0101

PARTICIPATION IN EVENTS

11th International Conference on Multiphase Flow (ICMF 2023), 04/2023

Oral presentation of the work “Turbulent Kinetic Energy in Stirred Tanks Estimated with an Alternative Approach: Tilted PIV”.

7th International Conference on Multiphase Flow and Heat Transfer (ICMFHT 22), 02/2022

Virtual presentation of the work “Classic PIV and Stereo-PIV Techniques in the Analysis of Turbulent Flow in a Stirred Tank”.

26th International Congress of Mechanical Engineering (COBEM 2021), 11/2021

Co-authorship in the work “Investigation of the Pseudo-Isotropic Approximation of a Turbulent Flow in a Stirred Tank”.

Course “Basics of Computational Fluid Dynamics and Applications” (course load: 4h).

XII Escola de Primavera de Transição e Turbulência (EPTT 2020), 09/2020

Co-authorship in the work “Compensation of Image Distortion on PIV Measurements of a Stirred Tank”.